

Shielding Benchmark Tests of JENDL-3

March 1994

日本原子力研究所

Japan Atomic Energy Research Institute

日本原子力研究所研究成果編集委員会

委員長 佐竹 宏文 (理事)

委 員

阿部 哲也 (核融合工学部)	斎藤 実 (材料試験炉部)
荒 克之 (原子炉工学部)	佐伯 正克 (先端基礎研究センター)
新井 英彦 (環境・資源利用研究部)	新藤 雅美 (材料研究部)
飯田 浩正 (原子力船研究開発室)	数土 幸夫 (原子炉工学部)
岩本 昭 (先端基礎研究センター)	館盛 勝一 (燃料サイクル安全工学部)
江草 茂則 (材料開発部)	立川 圓造 (燃料研究部)
数又 幸生 (材料研究部)	土橋敬一郎 (原子炉工学部)
菊地 章 (ホット試験室)	平林 孝圀 (バックエンド技術部)
工藤 博司 (先端基礎研究センター)	前田 彦祐 (炉心プラズマ研究部)
國谷 実 (企画室)	松井 浩 (保健物理部)
鴻坂 厚夫 (原子炉安全工学部)	武藤 康 (高温工学部)
古平 恒夫 (研究炉部)	山本 巧 (核融合装置試験部)
小林 義威 (環境安全研究部)	吉沢 清 (技術情報部)

Japan Atomic Energy Research Institute

Board of Editors

Hirofumi Satake (Chief Editor)

Tetsuya Abe	Katsuyuki Ara	Hidehiko Arai
Shigenori Egusa	Takakuni Hirabayashi	Hiromasa Iida
Akira Iwamoto	Yukio Kazumata	Akira Kikuchi
Yoshii Kobayashi	Atsuo Kohsaka	Tsuneo Kodaira
Hiroshi Kudo	Minoru Kuniya	Hikosuke Maeda
Hiroshi Matsui	Yasushi Muto	Masakatsu Saeki
Minoru Saito	Yukio Sudo	Masami Shindo
Enzo Tachikawa	Shoichi Tachimori	Keichiro Tsuchihashi
Takumi Yamamoto	Kiyoshi Yoshizawa	

JAERI レポートは、日本原子力研究所が研究成果編集委員会の審査を経て不定期に公開している研究報告書です。

入手の問合わせは、日本原子力研究所技術情報部情報資料課 (〒319-11 茨城県那珂郡東海村) あて、お申しこしてください。なお、このほかに財団法人原子力弘済会資料センター (〒319-11 茨城県那珂郡東海村日本原子力研究所内) で複写による実費頒布をおこなっております。

JAERI reports are reviewed by the Board of Editors and issued irregularly.

Inquiries about availability of the reports should be addressed to Information Division, Department of Technical Information, Japan Atomic Energy Research Institute, Tokai-mura, Naka-gun, Ibaraki-ken 319-11, Japan.

©Japan Atomic Energy Research Institute, 1994

編集兼発行 日本原子力研究所
印刷 いばらき印刷 (株)

Shielding Benchmark Tests of JENDL-3

Masayoshi KAWAI^{*1}, Akira HASEGAWA^{*2}, Kohtaro UEKI^{*3},
Naoki YAMANO^{*4}, Kenji SASAKI^{*5}, Yoshihiro MATSUMOTO^{*6},
Morio TAKEMURA^{*7}, Nobuo OHTANI^{*8} and Kiyoshi SAKURAI^{*9}

Shielding Integral Test Working Group
Japanese Nuclear Data Committee
Japan Atomic Energy Research Institute
Tokai-mura, Naka-gun, Ibaraki-ken

(Received October 12, 1992)

Abstract

The integral test of neutron cross sections for major shielding materials in JENDL-3 has been performed by analyzing various shielding benchmark experiments. For the fission-like neutron source problem, the following experiments are analyzed: (1) ORNL Broomstick experiments for oxygen, iron and sodium, (2) ASPIS deep penetration experiments for iron, (3) ORNL neutron transmission experiments for iron, stainless steel, sodium and graphite, (4) KfK leakage spectrum measurements from iron spheres, (5) RPI angular neutron spectrum measurements in a graphite block. For D-T neutron source problem, the following two experiments are analyzed: (6) LLNL leakage spectrum measurements from spheres of iron and graphite, and (7) JAERI-FNS angular neutron spectrum measurements on beryllium and graphite slabs. Analyses have been performed using the radiation transport codes: ANISN (1D Sn), DIAC(1D Sn), DOT3.5(2D Sn) and MCNP(3D point Monte Carlo). The group cross sections for Sn transport calculations are generated with the code systems PROF-GROUCH-G/B and RADHEAT-V4. The point-wise cross sections for MCNP are produced with NJOY. For comparison, the analyses with JENDL-2 and ENDF/B-IV have been also carried out. The calculations using JENDL-3 show overall agreement with the experimental data as well as those with ENDF/B-IV. Particularly, JENDL-3 gives better results than JENDL-2 and ENDF/B-IV for sodium. It has been concluded that JENDL-3 is very applicable for fission and fusion reactor shielding analyses.

Keywords: Integral Tests, Shielding, Neutron, Benchmark, Transmission, Cross Section, Beryllium, Graphite, Oxygen, Sodium, Iron, JENDL-3, ENDF/B-IV, DIAC, PROF-GROUCH-G/B, RADHEAT-V4, NJOY, ANISN, DOT3.5, MCNP

*1 Toshiba Corp.

*2 Department of Reactor Engineering, JAERI

*3 Ship Research Institute

*4 Sumitomo Atomic Energy Industries, Ltd.

*5 Mitsubishi Atomic Power Industries, Inc.

*6 Mitsui Engineering & Ship Building Co., Ltd.

*7 Kawasaki Heavy Industries, Ltd.

*8 Power Reactor and Nuclear Fuel Development Corp.

*9 Nuclear Safety Research Center, JAERI

JENDL-3 遮蔽ベンチマークテスト

日本原子力研究所 シグマ研究委員会

Shielding 積分テストワーキンググループ

川合 将義^{*1}・長谷川 明^{*2}・植木紘太郎^{*3}
山野 直樹^{*4}・佐々木研治^{*5}・松本 誠弘^{*6}
竹村 守雄^{*7}・大谷 暢夫^{*8}・桜井 淳^{*9}

(1992 年 10 月 12 日受理)

要 旨

JENDL-3 に格納されている主要な遮蔽物質の中性子断面積に対する積分テストを種々の遮蔽ベンチマーク問題を解析することにより実施した。核分裂中性子源問題として、次の実験を解析した。(1)ORNL における酸素、鉄、ナトリウムに対するブルームスティック実験、(2)ASPIS における鉄に対する深層透過実験、(3)ORNL における鉄、ステンレススチール、ナトリウム、グラファイトに対する中性子透過実験、(4)KfK における鉄球からの漏洩スペクトル測定、(5)RPI におけるグラファイトブロックからの角度依存中性子スペクトル測定。D-T 中性子源問題としては以下の2つの実験を解析した。(6)LLNL におけるグラファイト、鉄球からの漏洩スペクトル測定、(7)原研-FNS におけるベリリウム、グラファイトからの角度依存中性子スペクトル測定。解析は一次元 S_N 輸送計算コード ANISN, DIAC, 二次元 S_N 輸送計算コード DOT 3.5 および三次元ポイントモンテカルロコード MCNP を用いて実施した。 S_N 輸送計算に用いた群定数は PROF-GROUCH-G/B および RADHEAT-V4 コードシステムで作成した。MCNP で用いたポイントワイズ断面積は NJOY で作成した。比較のため、JENDL-2 および ENDF/B-IV を用いた解析も実施した。JENDL-3 を用いた計算は ENDF/B-IV を用いたものと同様に、全体的に実験値と良い一致を示した。特に、ナトリウムに関して JENDL-3 は JENDL-2 および ENDF/B-IV より良い結果を与えた。これらの結果より、JENDL-3 は核分裂炉および核融合炉の遮蔽解析に対して十分な適用性を持つことが結論された。

-
- * 1 株式会社 東芝
 - * 2 原研, 原子炉工学部
 - * 3 運輸省船舶技術研究所
 - * 4 住友原子力工業株式会社
 - * 5 三菱原子力工業株式会社
 - * 6 三井造船株式会社
 - * 7 川崎重工業株式会社
 - * 8 動力炉核燃料開発事業団
 - * 9 原研, 安全性試験研究センター

Contents

1. Introduction	1
2. Method of Analyses	3
2.1 General Description	3
2.2 Preparation of Cross-section Libraries	4
2.2.1 JSSTD L-295n-104 γ : a Common Nuclear Group Cross-section Library by PROF-GROUCH-G/B	5
2.2.2 SSL90A/B: Standard Group Constants for Safety Analysis of Radiation Shielding	13
2.2.3 FSXLIB-J3: A Point-wise Cross-section Library for MCNP	19
3. Shielding Analyses	25
3.1 Total Cross-section Check in MeV Energy Range by the Broomstick Experiments	25
3.1.1 Outline of Experiments	25
3.1.2 Calculation Method	25
3.1.3 Results	26
3.1.4 Summary	33
3.2 WINFRITH-ASPIS Iron Experiments	34
3.2.1 Outline of Experiments	34
3.2.2 Calculation Method	34
3.2.3 Results	37
3.2.4 Summary	41
3.3 ORNL Iron and Stainless Steel Experiments	51
3.3.1 Outline of Experiments	51
3.3.2 Calculation Method	55
3.3.3 Results by DOT Calculation	61
3.3.4 Results by MCNP Calculation	67
3.4 KfK Iron Experiments	69
3.4.1 Outline of Experiments	69
3.4.2 Calculation Method	69
3.4.3 Results by DIAC Calculation	71
3.5 ORNL Sodium Experiments	76
3.5.1 Outline of Experiments	76
3.5.2 Calculation Method	77
3.5.3 Results	79
3.6 RPI Graphite Experiments	87
3.6.1 Outline of Experiments	87
3.6.2 Calculation Method	88
3.6.3 Results	88
3.7 ORNL Graphite Experiments	99
3.7.1 Outline of Experiments	99
3.7.2 Calculation Method	99
3.7.3 Results	99
3.8 LLNL Iron and Graphite Experiments	101
3.8.1 Outline of Experiments	101
3.8.2 Calculation Method	102
3.8.3 Results	103

3.9 JAERI-FNS Beryllium and Graphite Experiments	106
3.9.1 Outline of Experiments	106
3.9.2 Calculation Method	107
3.9.3 Results	108
4. Discussions	115
4.1 Iron	115
4.2 Sodium	120
4.3 Graphite	122
4.4 Oxygen	123
4.5 Stainless Steel	124
4.6 Beryllium	124
5. Conclusion	125
Acknowledgments	126
References	127

目 次

1. 序	1
2. 解析方法	3
2.1 概 要	3
2.2 断面積ライブラリの準備	4
2.2.1 JSSTD _L -295 n-104 γ : PROF-GROUCH-G/B による共通群定数ライブラリ	5
2.2.2 SSL 90 A/B: 放射線遮蔽安全解析における標準群定数セット	13
2.2.3 FSXLIB-J3: MCNP 用ポイントワイズ断面積ライブラリ	19
3. 遮蔽解析	25
3.1 Broomstick 実験による MeV エネルギー領域の全断面積の検討	25
3.1.1 実験の概要	25
3.1.2 計算方法	25
3.1.3 結 果	26
3.1.4 まとめ	33
3.2 WINFRITH-ASPIS 鉄実験	34
3.2.1 実験の概要	34
3.2.2 計算方法	34
3.2.3 結 果	37
3.2.4 まとめ	41
3.3 ORNL 鉄およびステンレススチール実験	51
3.3.1 実験の概要	51
3.3.2 計算方法	55
3.3.3 DOT 計算による結果	61
3.3.4 MCNP 計算による結果	67
3.4 KfK 鉄実験	69
3.4.1 実験の概要	69
3.4.2 計算方法	69
3.4.3 DIAC 計算による結果	71
3.5 ORNL ナトリウム実験	76
3.5.1 実験の概要	76
3.5.2 計算方法	77
3.5.3 結 果	79
3.6 RPI グラファイト実験	87
3.6.1 実験の概要	87
3.6.2 計算方法	88
3.6.3 結 果	88
3.7 ORNL グラファイト実験	99
3.7.1 実験の概要	99
3.7.2 計算方法	99
3.7.3 結 果	99
3.8 LLNL 鉄およびグラファイト実験	101
3.8.1 実験の概要	101
3.8.2 計算方法	102
3.8.3 結 果	103

3.9 原研-FNS ベリリウムおよびグラファイト実験	106
3.9.1 実験の概要	106
3.9.2 計算方法	107
3.9.3 結 果	108
4. 議 論	115
4.1 鉄	115
4.2 ナトリウム	120
4.3 グラファイト	122
4.4 酸 素	123
4.5 ステンレススチール	124
4.6 ベリリウム	124
5. 結 言	125
謝 辞	126
参考文献	127

List of Tables

Table 2.1	Summary of analysis methods for shielding benchmark tests of JENDL-3
Table 2.2.1-1	Group cross-section library processing specification
Table 2.2.1-2	Neutron group boundaries considered in the JSSTD L system
Table 2.2.1-3	Gamma-ray group boundaries considered in the JSSTD L system
Table 2.2.1-4	Developed utility codes in the JSSTD L system
Table 2.2.1-5	JSSTD L-295 processed nuclides
Table 2.2.1-6	Processing outline for group cross-section library generation
Table 2.2.1-7	JSSTD L-295n-104 γ library neutron group structures
Table 2.2.1-8	JSSTD L-295n-104 γ library gamma-ray group structures
Table 2.2.2-1	Specifications of group cross section library processing
Table 2.2.2-2	Processed nuclides in the SSL90A/B library
Table 2.2.2-3	Energy group structure of neutrons (SSL90A: 120 groups)
Table 2.2.2-4	Energy group structures of neutrons (SSL90B: 22 groups) and gamma-rays (SSL90A and SSL90B: 18 groups)
Table 2.2.3-1	Contents of FSXLIB-J3 library based on JENDL-3 ²⁴⁾
Table 3.1-1	Statistics of C/E values for the oxygen Broomstick experiment
Table 3.1-2	Statistics of C/E values for the sodium Broomstick experiment
Table 3.1-3	Statistics of C/E values for the iron Broomstick experiment
Table 3.2-1	Reactions used in axial attenuation profile measurements
Table 3.2-2	Summary of C/E values for the axial attenuation profile
Table 3.3-1	Composition of the slabs in atoms/barn-cm
Table 3.3-2	Bonner ball description
Table 3.3-3	Experimental configurations for the iron transmission measurements
Table 3.3-4	Experimental configurations for the stainless steel transmission measurements
Table 3.3-5	Energy group structure used in the ORNL iron and stainless steel benchmark calculations
Table 3.3-6	Bonner ball detector response functions
Table 3.3-7	Calculated results and C/E values of the ORNL iron experiments
Table 3.3-8	Calculated results and C/E values of the ORNL stainless steel experiments
Table 3.4-1	Energy group structure and the energy spectrum of ²⁵² Cf neutron source used in the KfK benchmark calculation
Table 3.4-2	Nuclide compositions for the KfK iron experiments
Table 3.4-3	C/E values for selected energy ranges from 63.25 keV to 5.238 MeV for the KfK iron experiments
Table 3.4-4	C/E values for selected energy ranges from 63.25 keV to 1.0 MeV for the KfK iron experiments
Table 3.5-1	Atomic number densities for materials used in the ORNL sodium benchmark experiments
Table 3.5-2	DOT3.5 calculational condition
Table 3.5-3	Comparison of Bonner ball responses behind 10-ft-thick sodium and their C/E values
Table 3.5-4	Average C/E values of Bonner ball responses
Table 3.5-5	Comparison of Bonner ball responses behind 15-ft-thick sodium and their C/E values
Table 3.5-6	Average C/E values of Bonner ball responses for 10-ft-thick sodium
Table 3.6-1	Composition of materials
Table 3.6-2	Normalized total leakage spectrum from target
Table 3.6-3	Cumulative probability for source angular distribution

Table 3.7-1 C/E values of Bonner ball responses calculated with DOT3.5 for the ORNL graphite benchmark experiments

List of Figures

- Fig. 1** Flow of shielding benchmark tests of JENDL-3
- Fig. 2.2.2-1** Cross-section generation flow in the RADHEAT-V4 code system
- Fig. 2.2.3-1** Compilation code system for the MCNP data library²⁴⁾
- Fig. 3.1-1** A schematic of the Broomstick experimental arrangement²⁾
- Fig. 3.1-2** Calculated and experimental transmitted spectra and their C/E profiles for an oxygen sample
- Fig. 3.1-3** Total cross section of oxygen
- Fig. 3.1-4** Calculated and experimental transmitted spectra and their C/E profiles for a sodium sample
- Fig. 3.1-5** Total cross section of sodium
- Fig. 3.1-6** Calculated and experimental transmitted spectra and their C/E profiles for an iron sample (20.3 cm thick)
- Fig. 3.1-7** Calculated and experimental transmitted spectra and their C/E profiles for an iron sample (30.5 cm thick)
- Fig. 3.2-1** R-Z geometrical model adopted for the ASPIS analysis
- Fig. 3.2-2** Concept of the next event sphere annular surface crossing estimator
- Fig. 3.2-3** Neutron dose equivalent attenuation characteristics for various materials
- Fig. 3.2-4** Detector cross section used in the analysis
(group averaged data in the BERMUDA-121 group structures and the sensitive energy ranges to each detector for the reaction rate in the attenuation profile calculation)
- Fig. 3.2-5** Comparison of the measured and calculated reaction rate attenuation profiles along the main axis
- Fig. 3.2-6** Comparison of C/E values for the reaction rate attenuation profile along the main axis
- Fig. 3.2-7** Comparison of calculated flux profiles with the RADAK unfolded spectrum measurement and C/E values at the 22.9 cm position
- Fig. 3.2-8** Comparison of calculated flux profiles with the RADAK unfolded spectrum measurement and C/E values at the 57.1 cm position
- Fig. 3.2-9** Comparison of calculated flux profiles with the RADAK unfolded spectrum measurement and C/E values at the 85.7 cm position
- Fig. 3.2-10** Comparison of calculated flux profiles with the RADAK unfolded spectrum measurement and C/E values at the 114.3 cm position
- Fig. 3.2-11** Comparison of energy spectra between the MCNP calculation and measurement at the 22.54 cm depth in the shield and C/E values
- Fig. 3.2-12** Comparison of energy spectra between the MCNP calculation and measurement at the 56.83 cm depth in the shield and C/E values
- Fig. 3.2-13** Comparison of energy spectra between the MCNP calculation and measurement at the 85.41 cm depth in the shield and C/E values
- Fig. 3.2-14** Comparison of energy spectra between the MCNP calculation and measurement at the 113.98 cm depth in the shield and C/E values
- Fig. 3.3-1** Experimental configuration for the 4-1/4-in.-dia. collimator used for the measurements made behind iron slabs and 12-in.-thick stainless steel³⁾
- Fig. 3.3-2** Experimental configuration for the 15-1/4-in.-dia. collimator used for the measurements made behind 18-in.-thick stainless steel³⁾
- Fig. 3.3-3** Neutron beam source spectrum on the centerline at the outside edge of the 4-1/4-in.-dia. collimator
- Fig. 3.3-4** Two-dimensional calculation model (iron slabs)

- Fig. 3.3-5** Two-dimensional calculation model (stainless steel 30.9 cm thickness)
- Fig. 3.3-6** Two-dimensional calculation model (stainless steel 46.6 cm thickness)
- Fig. 3.3-7** Neutron energy spectrum at ($r=401.32$ cm, $z=107.95$ cm) behind 10.287-cm (4.05-in.) thick iron slab
- Fig. 3.3-8** Neutron energy spectrum at ($r=294.64$ cm, $z=294.64$ cm) behind 10.287-cm (4.05-in.) thick iron slab
- Fig. 3.3-9** Neutron energy spectrum at ($r=381.0$ cm, $z=102.87$ cm) behind 30.81-cm (12.13-in.) thick iron slab
- Fig. 3.3-10** Neutron energy spectrum at ($r=279.4$ cm, $z=279.4$ cm) behind 30.81-cm (12.13-in.) thick iron slab
- Fig. 3.3-11** Neutron energy spectrum at ($r=25.4$ cm, $z=30.48$ cm) behind 31.115-cm (12.25-in.) thick iron slab
- Fig. 3.3-12** Neutron energy spectrum at ($r=25.4$ cm, $z=30.48$ cm) behind 30.91-cm (12.17-in.) thick stainless steel slab
- Fig. 3.3-13** Comparison of energy spectra between the MCNP calculation and measurement in the energy range from 60 keV to 1.5 MeV on the centerline behind 12-in.-thick iron slab
- Fig. 3.3-14** Comparison of energy spectra between the MCNP calculation and measurement above 800 keV on the centerline behind 12-in.-thick iron slab
- Fig. 3.4-1** Configuration of the KfK iron benchmark experiment
- Fig. 3.4-2** Calculation model for the KfK iron benchmark problem
- Fig. 3.4-3** Energy spectra of neutrons from the KfK iron sphere having a 15 cm diameter
- Fig. 3.4-4** Energy spectra of neutrons from the KfK iron sphere having a 20 cm diameter
- Fig. 3.4-5** Energy spectra of neutrons from the KfK iron sphere having a 25 cm diameter
- Fig. 3.4-6** Energy spectra of neutrons from the KfK iron sphere having a 30 cm diameter
- Fig. 3.4-7** Energy spectra of neutrons from the KfK iron sphere having a 35 cm diameter
- Fig. 3.4-8** Energy spectra of neutrons from the KfK iron sphere having a 40 cm diameter
- Fig. 3.5-1** Experimental configuration for 15-ft-thick sodium sample using the 15.25 in. dia. collimator⁴⁾
- Fig. 3.5-2** Experimental configuration for 10-ft-thick sodium sample using the 15.25 in. dia. collimator (taken from Fig. 16.5 in JAERI-M 7843, p.174 (1978)).
- Fig. 3.5-3** Calculational RZ model of 10-ft-thick sodium
- Fig. 3.5-4** Calculational RZ model of 15-ft-thick sodium
- Fig. 3.5-5** Neutron spectra at 12 in. behind 10-ft-thick sodium
- Fig. 3.5-6** Axial traverse of Bonner ball responses behind 10-ft-thick sodium
- Fig. 3.5-7** Radial traverse of Bonner ball responses at 24 in. distant behind 10-ft-thick sodium
- Fig. 3.5-8** Comparison of C/E values for Bonner ball responses in the case of 10-ft-thick sodium
- Fig. 3.5-9** Axial traverse of Bonner ball responses behind the 15-ft-thick sodium
- Fig. 3.5-10** Radial traverse of 3 in. Bonner ball responses at 24 in. distant behind 15-ft-thick sodium
- Fig. 3.5-11** Comparison of C/E values for Bonner ball responses in the case of 15-ft-thick sodium
- Fig. 3.6-1** Schematic experimental layout⁷⁾
- Fig. 3.6-2** Graphite stack for neutron spectrum measurement⁷⁾
- Fig. 3.6-3** Depleted uranium target
- Fig. 3.6-4** Calculational model for one-dimensional sphere geometry
- Fig. 3.6-5** Fast neutron angular spectra at 0 deg. and $r=20.3$ cm
- Fig. 3.6-6** Fast neutron angular spectra at 0 deg. and $r=35.6$ cm
- Fig. 3.6-7** Fast neutron angular spectra at 0 deg. and $r=50.8$ cm
- Fig. 3.6-8** Fast neutron angular spectra at 0 deg. and $r=66.0$ cm
- Fig. 3.6-9** Neutron angular spectra at 30 deg. and $r=20.3$ cm

- Fig. 3.6-10** Neutron angular spectra at 16.6 deg. and $r=35.6\text{cm}$
- Fig. 3.6-11** Neutron angular spectra at 34.8 deg. and $r=35.6\text{cm}$
- Fig. 3.6-12** Neutron angular spectra at 58.9 deg. and $r=35.6\text{cm}$
- Fig. 3.6-13** Neutron angular spectra at 11.5 deg. and $r=50.8\text{cm}$
- Fig. 3.6-14** Neutron angular spectra at 23.6 deg. and $r=50.8\text{cm}$
- Fig. 3.6-15** Neutron angular spectra at 36.9 deg. and $r=50.8\text{cm}$
- Fig. 3.6-16** Flux angular distribution at $r=50.8\text{ cm}$, $E=1.0\text{ MeV}$
- Fig. 3.6-17** Flux angular distribution at $r=50.8\text{ cm}$, $E=2.0\text{ MeV}$
- Fig. 3.6-18** Flux angular distribution at $r=50.8\text{ cm}$, $E=5.0\text{ MeV}$
- Fig. 3.7-1** Configuration of the ORNL graphite benchmark experiment
- Fig. 3.7-2** Comparison of neutron energy spectra of the ORNL graphite experiment (36.3 cm behind the slabs of graphite 60.96 cm + B_4C 6.5 cm + lead 15.24 cm)
- Fig. 3.8-1** Schematic drawing of the experimental setup⁹⁾
- Fig. 3.8-2** Geometry of the spherical iron targets⁹⁾
- Fig. 3.8-3** Comparison of energy spectrum between the LLNL experiments and the MCNP calculations with JENDL-3 for 0.9 mfp ($r=4.46\text{ cm}$) of iron at 30°
- Fig. 3.8-4** Comparison of energy spectrum between the LLNL experiments and the MCNP calculations with JENDL-3 for 2.9 mfp ($r=13.41\text{ cm}$) of iron at 30°
- Fig. 3.8-5** Comparison of energy spectrum between the LLNL experiments and the MCNP calculations with JENDL-3 for 4.8 mfp ($r=22.30\text{ cm}$) of iron at 30°
- Fig. 3.8-6** Comparison of energy spectrum between the LLNL experiments and the MCNP calculations with JENDL-3 for 1.3 mfp ($r=10.16\text{ cm}$) of carbon at 30°
- Fig. 3.8-7** Comparison of energy spectrum between the LLNL experiments and the MCNP calculations with JENDL-3 for 2.9 mfp ($r=20.96\text{ cm}$) of carbon at 30°
- Fig. 3.9-1** Layout of target, assembly, collimator and detector¹⁰⁾
- Fig. 3.9-2** Experimental assembly with pseudo-cylindrical shape made of rectangular blocks
- Fig. 3.9-3** Calculational model of the FNS experiment by using modified subroutine TALLYD in the MCNP code
- Fig. 3.9-4** MCNP Calculation/Experiment (C/E) ratio of fluxes integrated over three energy regions for the 15.24-cm-thick assembly;
(a) above 0.01 MeV, (b) above 1.0 MeV, (c) above 10.0 MeV
- Fig. 3.9-5** Comparison of beryllium angular fluxes between the FNS experiments and the MCNP calculations with JENDL-3 and ENDF/B-IV for 15.24-cm-thick;
(a) 0.0 deg., (b) 12.2 deg., (c) 24.9 deg., (d) 41.8 deg., (e) 66.8 deg.
- Fig. 3.9-6** MCNP Calculation/Experiment (C/E) ratio of fluxes integrated over three energy regions for the 20.24-cm-thick assembly;
(a) above 0.01 MeV, (b) above 1.0 MeV, (c) above 10.0 MeV
- Fig. 3.9-7** Comparison of graphite angular fluxes between the FNS experiments and the MCNP calculations with JENDL-3 and ENDF/B-IV for 20.24-cm-thick;
(a) 0.0 deg., (b) 12.2 deg., (c) 24.9 deg., (d) 41.8 deg., (e) 66.8 deg.
- Fig. 4.1-1** Comparison of total cross sections for natural iron between JENDL-3 and ENDF/B-IV in the energy range from 1 MeV to 1.1 MeV
- Fig. 4.1-2** Comparison of elastic and total inelastic scattering cross sections for natural iron between JENDL-3 and ENDF/B-IV (1-1.2 MeV)
- Fig. 4.1-3** Comparison of total cross sections for natural iron between JENDL-3 and ENDF/B-IV in the energy range from 800 keV to 1 MeV
- Fig. 4.1-4** Comparison of elastic and total inelastic scattering cross sections for natural iron between JENDL-3 and ENDF/B-IV (0.8-1.0 MeV)

- Fig. 4.1-5** Comparison of total cross sections for natural iron between JENDL-3 and ENDF/B-IV in the energy range from 4 keV to 100 keV
- Fig. 4.1-6** Comparison of group-wise elastic scattering cross sections for natural iron between JENDL-3 and ENDF/B-IV in the JSSTD library
- Fig. 4.1-7** Comparison of group-wise inelastic scattering cross sections for natural iron between JENDL-3 and ENDF/B-IV in the JSSTD library
- Fig. 4.2-1** Comparison of evaluated and experimental total cross sections for sodium
- Fig. 4.2-2** Comparison of neutron spectra at the source and the opposite side positions
- Fig. 4.2-3** Comparison of inelastic scattering cross section for sodium of JENDL-3 with JENDL-2 and ENDF/B-IV
- Fig. 4.4-1** Total cross section of oxygen for JENDL-3 and ENDF/B-IV

1. Introduction

The third version of the Japanese Evaluated Nuclear Data Library (JENDL-3) was compiled¹⁾ in 1989 aiming at general applications such as fission, fusion, shielding and nuclear safety analyses in the fuel cycle. The general purpose file of JENDL-3 contains neutron nuclear data for 324 nuclides. In the JENDL-3 evaluation, a lot of effort has been devoted to improving the reliability of resonance- and high-energy data for fusion neutronics and shielding calculations, by applying some advanced nuclear theoretical models and the recent experimental data of resonance parameters and energy-angle double-differential cross sections (DDX). Various benchmark tests have been made to verify the applicability of JENDL-3 for various fields. In this report, the results of integral tests of neutron cross sections for major shielding materials have been presented.

The shielding benchmark tests of neutron cross sections in JENDL-3 have been performed as one of the activities of Shielding Integral Test Working Group of the Japanese Nuclear Data Committee (JNDC) to clarify the applicability of JENDL-3 for shielding analyses. The shielding benchmark experiments for beryllium, carbon, oxygen, sodium, iron and stainless steel with a fission-like neutron source and with a D-T neutron source have been analyzed. Adopted shielding benchmarks are characterized with a good geometry and a well description of the experimental methods and results, as follows:

- 1) ORNL Broomstick experiments²⁾ for oxygen, iron and sodium to check total cross sections,
- 2) ORNL neutron transmission experiments of iron and stainless steel blocks³⁾ (10 to 90 cm thick) and sodium cylinder⁴⁾ (3 and 4.6 m long) using a collimated neutron beam source from the TSF reactor,
- 3) WINFRITH deep penetration experiments⁵⁾ (140 cm thick iron) using a fission neutron source from the ASPIS converter of the NESTOR reactor,
- 4) KfK leakage neutron spectrum measurements⁶⁾ from iron spheres (15 to 40 cm dia.) with a ²⁵²Cf neutron source,
- 5) RPI angular neutron spectrum measurements⁷⁾ (Profio's experiment) in a graphite block of 132 × 152 × 152 cm³ using a photo-neutron source with the time-of-flight method,
- 6) ORNL neutron transmission experiments of a graphite block⁸⁾ (10 to 60 cm thick) using a broad neutron beam source from the TSF reactor,
- 7) LLNL leakage neutron spectrum measurements⁹⁾ (Hansen's experiment) from spheres with a few mean-free-path thick graphite and iron using the LLNL D-T neutron source,
- 8) JAERI-FNS angular neutron spectrum measurements¹⁰⁾ on beryllium (15.24 cm thick) and graphite (20.24 cm thick) slabs using the FNS D-T neutron source.

The analyses have been performed, as shown in **Fig. 1**, by using ANISN¹¹⁾ (1D Sn), DIAC¹²⁾ (1D Sn), and DOT3.5¹³⁾ (2D Sn) transport codes with more than 100 energy groups. The group cross sections are generated from an evaluated nuclear data library with the cross-section processing code systems, PROF-GROUCH-G/B¹⁴⁾ and RADHEAT-V4¹⁵⁾ developed at JAERI. Bondarenko-type self-shielding factors¹⁶⁾ are employed for calculating the effective macroscopic cross sections. Continuous energy Monte Carlo calculations are also made using MCNP¹⁷⁾ with cross sections produced by NJOY83¹⁸⁾. The calculated results have been compared with the experimental data and with those calculated using the other nuclear data files of ENDF/B-IV¹⁹⁾ and JENDL-2²⁰⁾.

In the following chapters, the details of the benchmark tests are described. Chapter 2 describes analysis methods. The calculated results, compared with the experimental data for individual experiments are presented in Chapter 3. In Chapter 4, the applicability of cross sections for each material in JENDL-3 is discussed by summarizing the results.

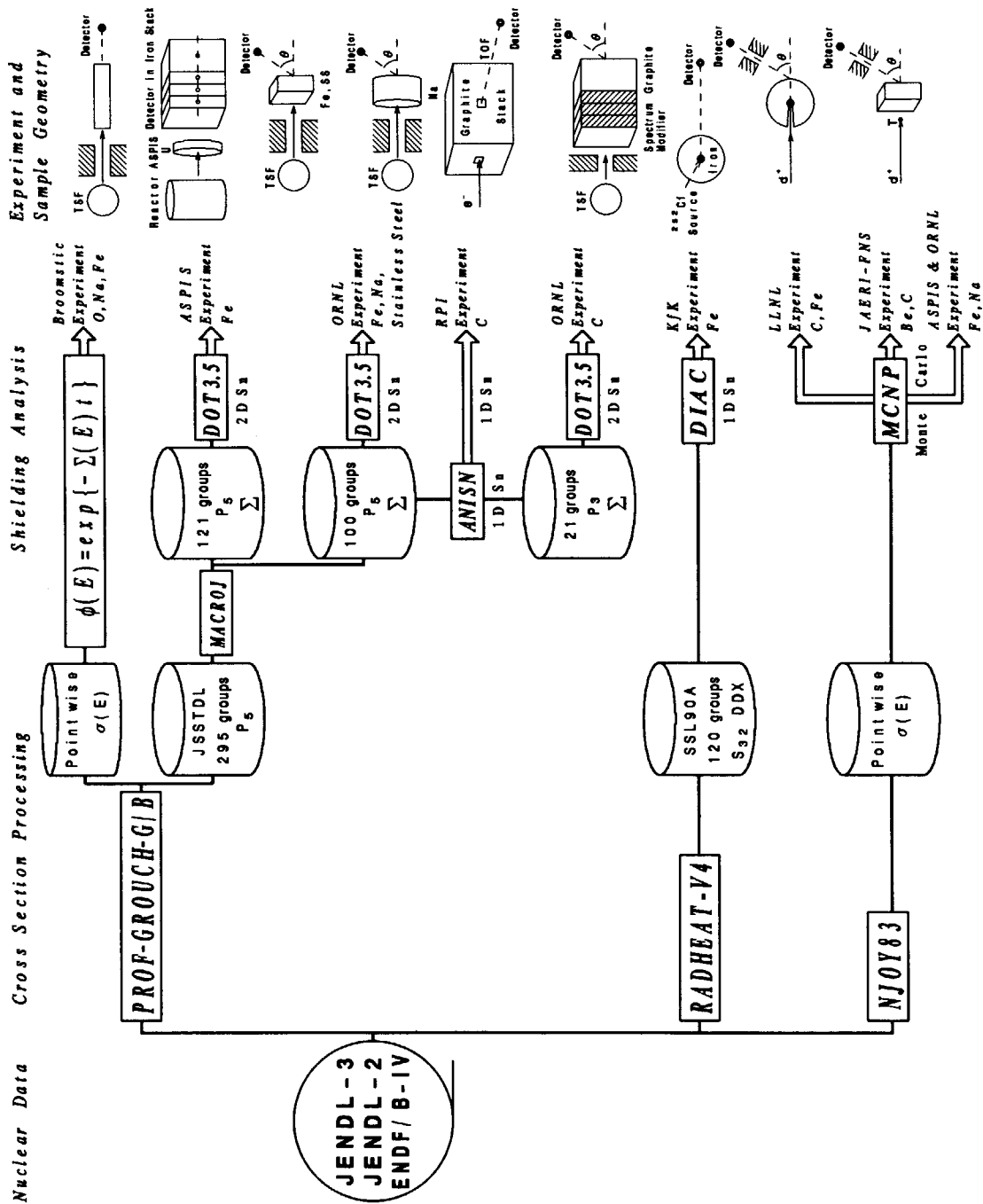


Fig. 1 Flow of shielding benchmark tests of JENDL-3

2. Method of Analyses

2.1 General Description

In benchmark test of the cross sections, attention must be given so as not to cause serious errors due to the use of improper analysis methods such as rough modeling, approximation of transport theory and rudeness of the cross-section treatments. For neutron transport calculations, one-dimensional Sn codes, DIAC and ANISN, two-dimensional one, DOT3.5, and continuous energy Monte Carlo code, MCNP were employed. A combination of the calculation model and computer code used for analyses of the individual shielding experiments are summarized in **Table 2.1**. They were selected by taking into consideration both experimental geometry and anisotropy of the neutron source. For example, to analyze the KfK experiments for iron, which were made with spherical samples and a ^{252}Cf fission source at the center, a one-dimensional spherical model and DIAC were employed, while the LLNL experiments which were made with a sample of spherical geometry were analyzed with MCNP so as to rigorously simulate a three-dimensional effect due to a beam hole and anisotropy of neutron source. For the analyses of the ORNL transmission experiments, a two-dimensional model and DOT3.5 were used. For estimating neutron fluxes at the detector positions behind the installation, an auxiliary code, SPACETRAN²¹⁾, was also utilized by using leakage angular fluxes calculated with DOT3.5.

For the Sn calculation, the number of discrete ordinates and the order of anisotropy of the scattering matrices play an important role in estimating the neutron fluxes. In the present study, one-dimensional Sn

Table 2.1 Summary of analysis methods for shielding benchmark tests of JENDL-3

Experiments	Sample geometry	Compared data	Calculation model and computer code
ORNL-Broomstick experiments	Sticks of oxygen, sodium and iron	$\phi(E)$ behind stick	Analytic formula
ORNL experiments	Slabs of iron and stainless steel cylinder of sodium	$\phi(E)$, Bonner ball responses behind sample	R-Z model, DOT3.5, 100 groups, S8-P5 MCNP (NESX estimator, weight window)
ASPIS experiments	Slab of iron	$\phi(E)$, Activation foil in iron stack	R-Z model, DOT3.5, 121 groups, S8-P5 MCNP (NESX estimator, weight window)
KfK experiments	Sphere of iron	Leakage energy spectrum	Sphere, DIAC, 120 groups, S32 DDX
RPI experiments	Stack of graphite blocks	Extracted $\phi(E, \theta)$	Sphere, ANISN, 100 groups, S32-P5
ORNL experiments	Slab of graphite with SM*	$\phi(E)$, Bonner ball responses	R-Z model, DOT3.5, 21 groups, S12-P3
LLNL experiments	Spheres of graphite and iron	Leakage energy spectrum	3D model, MCNP (NESX estimator, weight window)
JAERI-FNS experiments	Slabs of beryllium and graphite	Leakage $\phi(E, \theta)$	3D model, MCNP (Point detector estimator)

*) SM is the spectrum modifier to simulate the leakage neutron energy spectrum from the radial blanket of a sodium cooled fast breeder reactor.

calculations with DIAC were made with an S32 approximation (33 discrete polar angles to the main axis) and with rigorous treatment of the scattering matrices by an energy-angle double-differential presentation. ANISN calculation was made with an S32-P5 approximation. Two-dimensional calculation with DOT3.5 was carried out with an S8 (48 discrete angles per hemisphere) and P5 approximation, except for the case of the ORNL transmission experiments with graphite which was analyzed with an S12-P3 approximation. The number of energy groups was as much as about one hundred, which was thought to be sufficient for obtaining accurate results which considered to be practical.

For the MCNP calculation, the next event surface crossing (NESX) estimators and neutron source generation routines were copied into the MCNP code. The estimator more efficiently scores the neutron fluxes than the estimator which scores the trajectories of real particles or the point estimator which scores contributions from all events of real particles with the last collision method. In the calculation, an importance-sampling-technique was employed according to the weight window method.

The group cross sections were generated from evaluated nuclear data library by using the cross-section processing code systems, PROF-GROUCH-G/B and RADHEAT-V4, developed at JAERI. Bondarenko-type self-shielding factors were employed to calculate the effective macroscopic cross sections. Point-wise cross sections were also generated using NJOY83 for the MCNP calculations. The calculated results using JENDL-3 were compared with the experimental data and with those calculated by using the other nuclear data files of JENDL-2 and ENDF/B-IV. In the following sections, the preparations of the cross sections for the benchmark tests are presented.

2.2 Preparation of Cross-section Libraries

For the purpose of an integral test of the evaluated neutron nuclear data in JENDL-3, cross sections used for the transport calculations should be prepared by using an appropriate cross-section processing code which adopts the state-of-the-art treatments such as point-wise cross-section generation from resonance parameters, estimation of Doppler broadening and resonance self-shielding factors of each reaction.

The resonance self-shielding effect plays an important role in evaluating the neutron penetration characteristics in shielding materials. The nature of the resonance self-shielding effect essentially depends on both energy and space. On the contrary, the Bondarenko-type resonance self-shielding factor of multi-group cross sections is only considered by the energy spectrum change in the materials, so that uncertainty is contained in the self-shielding factor, although the uncertainty becomes less as the group number increases. In the treatment of the scattering anisotropy in the group-to-group transfer matrix, most of processing codes adopt the finite Legendre expansion method, that cannot reproduce the rigorous correlation between energy and angle. To avoid those uncertainties, several transport codes which use continuous energy treatment and energy-angle double differential cross sections (DDXs) have been developed.

Nevertheless, it is a fact that most of the shielding calculations are performed using multi-group transport codes, so the accuracy of the conventional method should also be confirmed in the same ways as the sophisticated method.

For the above reason, three cross section libraries were generated by different processing codes and used in the present benchmark tests. The first is the JSSTD library²²⁾ generated by the PROF-GROUCH-G/B code system. This library was produced as the common group constants with JENDL-3, that has 295 neutron energy groups and the scattering anisotropy is considered up to the P5 components. The second is the SSL90 library²³⁾ produced by the RADHEAT-V4 code system. This library was produced as standard group constants for safety analysis regarding radiation shielding. The feature of this library is that the scattering matrix is considered with the DDX form instead of the finite Legendre expansion. The RADHEAT-V4 and the prototype version were also used to verify the evaluated nuclear data in

JENDL-1 and JENDL-2. The third library is the point-wise cross-section library FSXLIB-J3²⁴⁾ for MCNP generated by the NJOY83 and MACROS codes. The feature of this library is that the cross sections are stored with a point-wise form which is directly applicable to the continuous energy Monte Carlo code MCNP. The following sections, the detailed descriptions for these cross-section libraries and the methods of generation are presented.

2.2.1 JSSTD-295n-104 γ : a Common Nuclear Group Cross-section Library by PROF-GROUCH-G/B

This library is a common group cross-section library based on JENDL-3 recently developed in JAERI under the cooperation of the Working Group on Standard Group Constants affiliated by the Subcommittee of Group Constants of JNDC (Japanese Nuclear Data Committee). This work was started according to a recommendation²⁵⁾ despatched to the JNDC (Proposal on Post-JENDL-3 Activity Program for JNDC, 1986) by the Nakazawa Committee. In this proposal, it is highly promoted that JNDC should supply the commonly usable group cross-section library for primary data users like fast or fusion reactor designers at the same time the JENDL-3 is released.

Up to now shielding and criticality calculations have been performed in different calculation paths using the different group constants libraries, i.e., in different group structures and data sources due to the characteristics of the calculations involved. Finer group structure is inevitably necessary for the shielding or fusion reactor calculations but a relatively coarse group structure is sufficient for the criticality calculations. Hence, there have been many requests for supplying a common library applicable both for the criticality and shielding or fusion calculations. Users are also very keen about using the latest nuclear data.

Responding to these requests, specifications for the common group constants were chosen. In **Table 2.2.1-1** specifications of the JSSTD system are shown. From the discussions in the working group, most users insist on maintaining their own group structure which has been so far used. Therefore, a universal group structure which was composed of 295 groups was decided to cover almost all group structures used in Japan, as seen in **Tables 2.2.1-2** and **2.2.1-3**, so as to produce their own required group structure library from a master library. It was also decided to produce a macroscopic cross-section data file directly acceptable in the design codes most frequently used such as ANISN¹¹⁾, DOT¹³⁾ or MORSE²⁶⁾. Resonance

Table 2.2.1-1 Group cross-section library processing specification

Items	Specifications
Group structure	Neutron : 295 20 MeV-- 1.0×10^{-5} eV Gamma : 104 50 MeV--1 keV
Weighting spectrum	Maxwellian from 1.0×10^{-5} to 0.3224 eV, the rest is 1/E
Resonance reconstruction tolerance	0.1%
Self-shielding factor	
Temperature grid	300, 600, 900, 2100 Kelvin
σ_0 grid	0, 0.1778, 1, 10, 10^2 , 10^3 , 10^4 , 10^5 , 10^6 barns
Reactions	Total, elastic, capture, fission
Anisotropic P_l order	5
Photon production data	Total = fission + capture + except fission and capture

Table 2.2.1-2 Neutron group boundaries considered in the JSSTD L system

Library name	Groups
JSD-100	100
JSD-1000	100
BERMUDA-121	121
FNS-125	125
VITAMIN-C	171
VITAMIN-J (E+C)	175
GICX-42	42
ABBN-25	25
JFS-New	70
GAM-123 (fast only)	92
MGCL-137 (fast only)	91
WIMS-69 (fast only)	28

Table 2.2.1-3 Gamma-ray group boundaries considered in the JSSTD L system

Library name	Groups
CSEWG-94	94
LANL-12	12
STEINER-21	21
STRAKER-22	22
LANL-48	48
LANL-24	24
BERMUDA-36	36
HONEYCOMB-15	15

self-shielding factors were also considered for primary reactions. Scattering matrices were calculated up to the P5 components and were stored independently for elastic and inelastic scattering so as to use the different self-shielding factors. For secondary γ production cross sections, data are stored for the following 4 reactions, i.e., total, capture ((n, γ) MT:102 only), fission (MT:18), other than capture and fission ((n,n') + (n,p) + (n, α) + ...), to reflect self-shielding factors for capture and fission reactions in neutrons. Gamma-ray transport cross-sections are generated by GAMLEG-JR²⁷⁾.

A utility routine was developed to enhance the portability of this system to other sites or machines. Routines for group collapsing and for generating region dependent macroscopic cross sections were also developed and released with the library. In **Table 2.2.1-4**, all of the routines developed are shown.

Up to now, cross sections for 63 nuclides from the JENDL-3 general purpose file¹⁾ were processed and stored into the JSSTD L library. Gamma-ray data are furnished for 32 nuclides out of 63 processed nuclides. Almost all nuclides available for γ production data in JENDL-3 were processed. A detailed list of processed nuclides is given in **Table 2.2.1-5**. For processing of the JENDL-3 neutron and γ production cross section, the PROF-GROUCH-G/B¹⁴⁾ system and its utility codes were used. Actual processing codes used are shown in **Table 2.2.1-6**.

Table 2.2.1-4 Developed utility codes in the JSSTD L system

Code name		
Neutron-lib.	Gamma-lib.	Function
CONVJSS	CONVJGG	Format conversion code Binary \leftrightarrow EBCDIC
CONDNSJ	CONDNSJG	Collapsing code to any broad group 295 \leftrightarrow User specified group (JSD100, BERMUDA-121, etc)
MACROJ	MACROJG	Region dependent macroscopic cross-section creation for ANISN, DOT, MORSE codes.

Table 2.2.1-5 JSSTD L-295 processed nuclides

Order	Gamma	Z	ch	A	MAT	NCODE	Comment
1	G	1	H	1	3011	117	
2		1	H	2	3012	127	
3		2	He	3	3021	237	
4		2	He	4	3022	247	
5	G	3	Li	6	3031	367	
6	G	3	Li	7	3032	377	
7	G	4	Be	9	3041	497	
8	G	5	B	10	3051	507	
9	G	5	B	11	3052	517	
10	G	6	C	12	3061	607	
11	G	7	N	14	3072	707	
12	G	8	O	16	3081	807	
13		9	F	19	3091	907	
14	G	11	Na	23	3111	1107	
15	G	12	Mg	0	3120	1207	
16	G	13	Al	27	3131	1307	
17	G	14	Si	0	3140	1407	
18		15	P	31	3151	1507	
19		16	S	0	3160	1607	
20		19	K	0	3190	1907	
21	G	20	Ca	0	3200	2007	
22	G	22	Ti	0	3220	2207	
23		23	V	51	3231	2307	
24	G	24	Cr	0	3240	2407	
25	G	25	Mn	55	3251	2557	
26	G	26	Fe	0	3260	2607	
27	G	28	Ni	0	3280	2807	
28	G	29	Cu	0	3290	2907	
29		31	Ga	0	3100	3108	ENDF/B-VI
30	G	40	Zr	0	3400	4007	
31	G	41	Nb	93	3411	4137	
32	G	42	Mo	0	3420	4207	
33		48	Cd	0	3480	4807	
34	G	63	Eu	0	3630	6307	
35	G	72	Hf	0	3720	7207	
36	G	73	Ta	81	3731	7307	
37	G	74	W	0	3740	7407	
38	G	82	Pb	0	3820	8207	
39	G	83	Bi	209	3831	8397	
40		90	Th	232	3905	9027	
41		92	U	233	3922	9237	
42		92	U	234	3923	9247	
43	G	92	U	235	3924	9257	
44		92	U	236	3925	9267	
45	G	92	U	238	3926	9287	
46		93	Np	237	3931	9377	

Table 2.2.1-5 (continued)

Order	Gamma	Z	ch	A	MAT	NCODE	Comment
47	G	93	Np	239	3932	9397	
48		94	Pu	236	3941	9467	
49		94	Pu	238	3942	9487	
50		94	Pu	239	3943	9497	
51		94	Pu	240	3944	9407	
52		94	Pu	241	3945	9417	
53		94	Pu	242	3946	9427	
54		95	Am	241	3951	9517	
55		95	Am	242m	3953	9597	
56		95	Am	243	3954	9537	
57		96	Cm	242	3962	9627	
58		96	Cm	243	3963	9637	
59		96	Cm	244	3964	9647	
60		96	Cm	245	3965	9657	
61		96	Cm	246	3966	9667	
62		96	Cm	247	3967	9677	
63		96	Cm	248	3968	9687	

N.B.

Gamma : G means data given

Z : Atomic number

ch : Chemical symbol

A : Mass number

MAT : MAT number of JENDL-3

NCODE: Code number in the JSSTD L library

Energy boundaries of the JSSTD L-295n-104 γ library are given in **Table 2.2.1-7** and **2.2.1-8**, for neutron and gamma-ray groups, respectively.

In these benchmark tests, working data libraries of the JSD-100²⁸⁾ or JSD-1000²⁹⁾ group structure, referred to JSSTD L-100 or JSSTD L-1000 respectively, were produced from the master library of JSSTD L-295 and used for the analyses.

Table 2.2.1-6 Processing outline for group cross-section library generation

Process	Code used	Process comments
Reprocessing	LINEAR RECENT-J SIGMA1	Linearized data generation Resonance reconstruction for 0. K Doppler broadened cross-section
Processing	Prof. GROUCH-G/B	Group averaging process Self-shielding factor calculation Group transfer matrices calculation
Postprocessing	GLIBMK	Group library compilation

Table 2.2.1-7 JSTDL-295n-104 γ library neutron group structures

TABLE OF NEUTRON ENERGY GROUP STRUCTURE

GROUP	UP-ENERGY	LETHAGY	DELTA-U	GROUP	UP-ENERGY	LETHAGY	DELTA-U	GROUP	UP-ENERGY	LETHAGY	DELTA-U
1	1.96403E+07	-3.38527E-01	1.25001E-01	41	1.08120E+07	2.58400E-01	1.55757E-02	81	4.00570E+06	1.23647E+00	1.62916E-02
2	1.73325E+07	-2.13526E-01	2.49969E-02	42	1.06449E+07	2.73978E-01	1.24989E-02	82	4.00000E+06	1.25276E+00	2.12109E-02
3	1.69046E+07	-1.88529E-01	2.50020E-02	43	1.05127E+07	2.86473E-01	3.11530E-03	83	3.91605E+06	1.27397E+00	6.24998E-02
4	1.64872E+07	-1.63527E-01	1.56613E-02	44	1.04800E+07	2.89588E-01	1.56757E-02	84	3.67879E+06	1.33647E+00	6.25010E-02
5	1.62310E+07	-1.47866E-01	1.55851E-02	45	1.03170E+07	3.05264E-01	1.56299E-02	85	3.45590E+06	1.39897E+00	3.74981E-02
6	1.59800E+07	-1.32281E-01	1.56411E-02	46	1.01570E+07	3.20894E-01	1.55780E-02	86	3.32871E+06	1.43647E+00	2.50012E-02
7	1.57320E+07	-1.16640E-01	3.11316E-03	47	1.00000E+07	3.36472E-01	5.00005E-02	87	3.24652E+06	1.46147E+00	2.49979E-02
8	1.56831E+07	-1.13526E-01	1.24989E-02	48	9.51229E+06	3.86472E-01	1.24996E-02	88	3.16637E+06	1.48647E+00	3.75033E-02
9	1.54083E+07	-1.01028E-01	1.56366E-02	49	9.39413E+06	3.98972E-01	8.56643E-03	89	3.04982E+06	1.52397E+00	1.24982E-02
10	1.52400E+07	-8.53910E-02	1.55905E-02	50	9.31400E+06	4.07530E-01	2.89340E-02	90	3.01194E+06	1.53647E+00	4.99986E-02
11	1.50120E+07	-6.97926E-02	6.26124E-03	51	9.04837E+06	4.36472E-01	2.49995E-02	91	2.86505E+06	1.58647E+00	5.00000E-02
12	1.49183E+07	-6.35314E-02	9.38141E-03	52	8.82497E+06	4.61471E-01	2.50001E-02	92	2.72532E+06	1.63647E+00	1.25021E-02
13	1.47790E+07	-5.41499E-02	1.56231E-02	53	8.60708E+06	4.86472E-01	3.75002E-02	93	2.69146E+06	1.64897E+00	3.74997E-02
14	1.45499E+07	-3.85268E-02	1.56477E-02	54	8.29029E+06	5.23972E-01	3.53932E-03	94	2.59240E+06	1.68647E+00	2.50014E-02
15	1.43240E+07	-2.28792E-02	9.34964E-03	55	8.26100E+06	5.27511E-01	8.96028E-03	95	2.52839E+06	1.71147E+00	1.12920E-02
16	1.41907E+07	-1.35295E-02	6.27024E-03	56	8.18731E+06	5.36472E-01	5.00000E-02	96	2.50000E+06	1.72277E+00	1.37055E-02
17	1.41020E+07	-7.25931E-03	1.56516E-02	57	7.78801E+06	5.86472E-01	5.00006E-02	97	2.46597E+06	1.73647E+00	3.32981E-02
18	1.38830E+07	8.39136E-03	3.08046E-03	58	7.40818E+06	6.36472E-01	1.25006E-02	98	2.38521E+06	1.76977E+00	4.20554E-03
19	1.38403E+07	1.14724E-02	8.73002E-03	59	7.31615E+06	6.48973E-01	3.74993E-02	99	2.37520E+06	1.77398E+00	4.19793E-03
20	1.37200E+07	2.02022E-02	3.76802E-03	60	7.04688E+06	6.86472E-01	2.50003E-02	100	2.36525E+06	1.77817E+00	8.29991E-03
21	1.36684E+07	2.39700E-02	1.25007E-02	61	6.87289E+06	7.11472E-01	2.49997E-02	101	2.34570E+06	1.78647E+00	1.66966E-02
22	1.34986E+07	3.64705E-02	3.16088E-03	62	6.70320E+06	7.36472E-01	1.66706E-02	102	2.30686E+06	1.80317E+00	3.33029E-02
23	1.34560E+07	3.96316E-02	1.55785E-02	63	6.59238E+06	7.53143E-01	1.41123E-02	103	2.23130E+06	1.83647E+00	4.99992E-02
24	1.32480E+07	5.52102E-02	1.56717E-02	64	6.50000E+06	7.67255E-01	6.71791E-03	104	2.12248E+06	1.88647E+00	1.25020E-02
25	1.30420E+07	7.08823E-02	1.56096E-02	65	6.45648E+06	7.73973E-01	1.24995E-02	105	2.09611E+06	1.89897E+00	3.74958E-02
26	1.28400E+07	8.64919E-02	1.56198E-02	66	6.37628E+06	7.86472E-01	4.99992E-02	106	2.01897E+06	1.93647E+00	2.50109E-02
27	1.26410E+07	1.02111E-01	9.36258E-03	67	6.06531E+06	8.36472E-01	5.00003E-02	107	1.96910E+06	1.96148E+00	2.49910E-02
28	1.25232E+07	1.11474E-01	6.26400E-03	68	5.76950E+06	8.86472E-01	1.25018E-02	108	1.92050E+06	1.98647E+00	2.61125E-02
29	1.24450E+07	1.17738E-01	1.56290E-02	69	5.69782E+06	8.98974E-01	3.74979E-02	109	1.87100E+06	2.01258E+00	1.13902E-02
30	1.22520E+07	1.33367E-01	3.10641E-03	70	5.48812E+06	9.36471E-01	2.50015E-02	110	1.84981E+06	2.02397E+00	1.24952E-02
31	1.22140E+07	1.36474E-01	1.24980E-02	71	5.35261E+06	9.61473E-01	2.49988E-02	111	1.82684E+06	2.03647E+00	5.00023E-02
32	1.20623E+07	1.40972E-01	1.56495E-02	72	5.22046E+06	9.86471E-01	2.35411E-02	112	1.73774E+06	2.08647E+00	4.99997E-02
33	1.18750E+07	1.64621E-01	1.56161E-02	73	5.09900E+06	1.01001E+00	1.39605E-02	113	1.65299E+06	2.13647E+00	1.25039E-02
34	1.16910E+07	1.80230E-01	6.23791E-03	74	5.02831E+06	1.02397E+00	1.24995E-02	114	1.63245E+06	2.14898E+00	3.74979E-02
35	1.16103E+07	1.86476E-01	9.36523E-03	75	4.96587E+06	1.03647E+00	4.99985E-02	115	1.57327E+06	2.18647E+00	2.50053E-02
36	1.15100E+07	1.95841E-01	1.56290E-02	76	4.72367E+06	1.08647E+00	4.9594E-02	116	1.53354E+06	2.21148E+00	2.49912E-02
37	1.13315E+07	2.11471E-01	1.56090E-02	77	4.51600E+06	1.13143E+00	5.04153E-03	117	1.49569E+06	2.23647E+00	3.75072E-02
38	1.11560E+07	2.27079E-01	9.39326E-03	78	4.49329E+06	1.13647E+00	1.25008E-02	118	1.44063E+06	2.27398E+00	1.24960E-02
39	1.10517E+07	2.36473E-01	6.23569E-03	79	4.43747E+06	1.14897E+00	6.24994E-02	119	1.42274E+06	2.28647E+00	1.61124E-02
40	1.09830E+07	2.42708E-01	1.56920E-02	80	4.16862E+06	1.21147E+00	2.49991E-02	120	1.40000E+06	2.30258E+00	3.38892E-02

Table 2.2.1-7 (Continued)

TABLE OF NEUTRON ENERGY GROUP STRUCTURE

GROUP	UP-ENERGY	LETHAGY	DELTA-U	GROUP	UP-ENERGY	LETHAGY	DELTA-U	GROUP	UP-ENERGY	LETHAGY	DELTA-U
121	1.35335E+06	2.33647E+00	4.99972E-02	161	2.984691E+05	3.84807E+00	4.29748E-03	201	4.65000E+04	5.70736E+00	4.11168E-03
122	1.20735E+06	2.38647E+00	1.25065E-02	162	2.97211E+05	3.85237E+00	9.10222E-03	202	4.63092E+04	5.71147E+00	1.25001E-01
123	1.27135E+06	2.39890E+00	3.74978E-02	163	2.94518E+05	3.86147E+00	2.49977E-02	203	4.08672E+04	5.83647E+00	1.25012E-01
124	1.22456E+06	2.43648E+00	2.50044E-02	164	2.87247E+05	3.88647E+00	1.48956E-02	204	3.60652E+04	5.96148E+00	4.99878E-02
125	1.19432E+06	2.46148E+00	2.49933E-02	165	2.83000E+05	3.90137E+00	3.51074E-02	205	3.43067E+04	6.01147E+00	7.50005E-02
126	1.16484E+06	2.48647E+00	3.75066E-02	166	2.73237E+05	3.93647E+00	2.50104E-02	206	3.18278E+04	6.08647E+00	1.10397E-01
127	1.12196E+06	2.52398E+00	1.24935E-02	167	2.66488E+05	3.96148E+00	7.49900E-02	207	2.85011E+04	6.19687E+00	1.46145E-01
128	1.10803E+06	2.53647E+00	4.62034E-02	168	2.47235E+05	4.03647E+00	5.00009E-02	208	2.80076E+04	6.21148E+00	3.94876E-02
129	1.05800E+06	2.58268E+00	3.80691E-03	169	2.35177E+05	4.08647E+00	4.99968E-02	209	2.70001E+04	6.25097E+00	3.55005E-02
130	1.05398E+06	2.58648E+00	4.99869E-02	170	2.23708E+05	4.13647E+00	5.00030E-02	210	2.60584E+04	6.28647E+00	5.00007E-02
131	1.00359E+06	2.63647E+00	4.17018E-02	171	2.12797E+05	4.18647E+00	2.50098E-02	211	2.47875E+04	6.33647E+00	2.49998E-02
132	9.61640E+05	2.67817E+00	3.33083E-02	172	2.07541E+05	4.21148E+00	2.49891E-02	212	2.41755E+04	6.36147E+00	2.50003E-02
133	9.30137E+05	2.71148E+00	2.49910E-02	173	2.02419E+05	4.23647E+00	1.20225E-02	213	2.35786E+04	6.38647E+00	7.49998E-02
134	9.07180E+05	2.73647E+00	5.00004E-02	174	2.00000E+05	4.24850E+00	3.79771E-02	214	2.18749E+04	6.46147E+00	1.72869E-02
135	8.62366E+05	2.78647E+00	5.00002E-02	175	1.92547E+05	4.28647E+00	5.00020E-02	215	2.15000E+04	6.47876E+00	1.07715E-01
136	8.20850E+05	2.83647E+00	2.57287E-02	176	1.83156E+05	4.33647E+00	4.99965E-02	216	1.93045E+04	6.58647E+00	1.25010E-01
137	8.00000E+05	2.86220E+00	2.42709E-02	177	1.74224E+05	4.38647E+00	5.00000E-02	217	1.70360E+04	6.71148E+00	1.24988E-01
138	7.80817E+05	2.88647E+00	5.00002E-02	178	1.65727E+05	4.43647E+00	2.50136E-02	218	1.50344E+04	6.83647E+00	2.50000E-01
139	7.42736E+05	2.93647E+00	2.50004E-02	179	1.61633E+05	4.46148E+00	2.49891E-02	219	1.17008E+04	7.08647E+00	9.99962E-02
140	7.24391E+05	2.96148E+00	2.49911E-02	180	1.57644E+05	4.48647E+00	4.99975E-02	220	1.05946E+04	7.18647E+00	5.77595E-02
141	7.06312E+05	2.98647E+00	5.00000E-02	181	1.49956E+05	4.53647E+00	5.00040E-02	221	1.00000E+04	7.24423E+00	9.22447E-02
142	6.72055E+05	3.03647E+00	4.99992E-02	182	1.42642E+05	4.58647E+00	1.15703E-02	222	9.11802E+03	7.33647E+00	2.50001E-01
143	6.39279E+05	3.08647E+00	5.00000E-02	183	1.41000E+05	4.59805E+00	3.84165E-02	223	7.10174E+03	7.58647E+00	2.50000E-01
144	6.08101E+05	3.13647E+00	4.99993E-02	184	1.35686E+05	4.63647E+00	5.00040E-02	224	5.53084E+03	7.83647E+00	1.73473E-01
145	5.78444E+05	3.18647E+00	2.17477E-02	185	1.29068E+05	4.68647E+00	2.50103E-02	225	4.65000E+03	8.00994E+00	7.65277E-02
146	5.60000E+05	3.20822E+00	3.26331E-03	186	1.25880E+05	4.71148E+00	2.49920E-02	226	4.30742E+03	8.08647E+00	1.49998E-01
147	5.64156E+05	3.21148E+00	2.49908E-02	187	1.22773E+05	4.73648E+00	4.99940E-02	227	3.70744E+03	8.23647E+00	5.21363E-02
148	5.50232E+05	3.23647E+00	4.99998E-02	188	1.16786E+05	4.78647E+00	5.00025E-02	228	3.51910E+03	8.28861E+00	4.78639E-02
149	5.23397E+05	3.28647E+00	4.57322E-02	189	1.11090E+05	4.83647E+00	1.05171E-01	229	3.35463E+03	8.33647E+00	1.00002E-01
150	5.00000E+05	3.32200E+00	4.26713E-03	190	1.00000E+05	4.94164E+00	1.98291E-02	230	3.03539E+03	8.43647E+00	9.99979E-02
151	4.97871E+05	3.33647E+00	1.00001E-01	191	9.80366E+04	4.96147E+00	1.25002E-01	231	2.74654E+03	8.53647E+00	4.99999E-02
152	4.50492E+05	3.36647E+00	2.50098E-02	192	8.65169E+04	5.08647E+00	4.75003E-02	232	2.61259E+03	8.58647E+00	5.00011E-02
153	4.39365E+05	3.46148E+00	7.49903E-02	193	8.25034E+04	5.13397E+00	3.70987E-02	233	2.48517E+03	8.63647E+00	1.00002E-01
154	4.07622E+05	3.53647E+00	1.88875E-02	194	7.94987E+04	5.17107E+00	4.04109E-02	234	2.24867E+03	8.73647E+00	4.10863E-03
155	4.00000E+05	3.55355E+00	3.11244E-02	195	7.63501E+04	5.21148E+00	5.86896E-02	235	2.23945E+03	8.74058E+00	4.07625E-02
156	3.87742E+05	3.58647E+00	4.99990E-02	196	7.19981E+04	5.27017E+00	6.63011E-02	236	2.15000E+03	8.78134E+00	5.51293E-02
157	3.68832E+05	3.63647E+00	7.50102E-02	197	6.73794E+04	5.33647E+00	1.25010E-01	237	2.03648E+03	8.8647E+00	2.50000E-01
158	3.42178E+05	3.71148E+00	2.49898E-02	198	5.94615E+04	5.46148E+00	4.99803E-02	238	1.50461E+03	9.08647E+00	1.60696E-01
159	3.33733E+05	3.73647E+00	1.00000E-01	199	5.65622E+04	5.51147E+00	7.50002E-02	239	1.42510E+03	9.19257E+00	1.43900E-01
160	3.01974E+05	3.83647E+00	1.16012E-02	200	5.24752E+04	5.58647E+00	1.20808E-01	240	1.23410E+03	9.33647E+00	2.10342E-01

Table 2.2.1-7 (Continued)

TABLE OF NEUTRON ENERGY GROUP STRUCTURE											
GROUP	UP-ENERGY	LETHAGY	DELTA-U	GROUP	UP-ENERGY	LETHAGY	DELTA-U	GROUP	UP-ENERGY	LETHAGY	DELTA-U
241	1.00000E+03	9.54681E+00	3.96602E-02	281	2.38237E+00	1.55865E+01	1.02628E-01				
242	9.61116E+02	9.58647E+00	5.80652E-02	282	2.15000E+00	1.56091E+01	1.47373E-01				
243	9.06898E+02	9.64454E+00	1.91935E-01	283	1.85539E+00	1.58365E+01	2.49999E-01				
244	7.48518E+02	9.83647E+00	2.49999E-01	284	1.44498E+00	1.60865E+01	2.50001E-01				
245	5.82947E+02	1.00865E+01	2.26059E-01	285	1.12535E+00	1.63365E+01	1.18094E-01				
246	4.65000E+02	1.03125E+01	2.39424E-02	286	1.00000E+00	1.64546E+01	1.31904E-01				
247	4.53999E+02	1.03365E+01	2.12020E-01	287	8.76425E-01	1.65865E+01	2.50001E-01				
248	3.67262E+02	1.05485E+01	3.79799E-02	288	6.82560E-01	1.68365E+01	2.50001E-01				
249	3.53575E+02	1.05865E+01	2.50002E-01	289	5.31578E-01	1.70865E+01	1.33813E-01				
250	2.75364E+02	1.08365E+01	2.49999E-01	290	4.65000E-01	1.72203E+01	1.16186E-01				
251	2.14454E+02	1.10865E+01	2.50000E-01	291	4.13994E-01	1.73365E+01	2.50018E-01				
252	1.67017E+02	1.13365E+01	1.15977E-01	292	3.22413E-01	1.75865E+01	4.05196E-01				
253	1.48728E+02	1.14524E+01	1.34023E-01	293	2.15000E-01	1.79917E+01	7.65467E-01				
254	1.30073E+02	1.15865E+01	2.50000E-01	294	1.00000E-01	1.87572E+01	4.60517E+00				
255	1.01301E+02	1.18365E+01	1.29261E-02	295	1.00000E-03	2.33623E+01	4.60516E+00				
256	1.00000E+02	1.18494E+01	2.37075E-01	296	1.00001E-05	2.79675E+01	0.0				
257	7.88932E+01	1.20865E+01	4.39439E-02								
258	7.55014E+01	1.21304E+01	2.06056E-01								
259	6.1421E+01	1.23365E+01	2.45811E-01								
260	4.80520E+01	1.25823E+01	4.18770E-03								
261	4.78512E+01	1.25865E+01	2.86438E-02								
262	4.65000E+01	1.26151E+01	2.21358E-01								
263	3.72665E+01	1.28365E+01	2.49999E-01								
264	2.90232E+01	1.30865E+01	4.66630E-02								
265	2.77000E+01	1.31331E+01	2.03336E-01								
266	2.26033E+01	1.33365E+01	5.00431E-02								
267	2.15000E+01	1.33865E+01	1.99955E-01								
268	1.76035E+01	1.35865E+01	9.75111E-02								
269	1.59680E+01	1.36840E+01	1.52490E-01								
270	1.37096E+01	1.38365E+01	2.50005E-01								
271	1.06770E+01	1.40865E+01	6.50688E-02								
272	1.00000E+01	1.41520E+01	1.23763E-02								
273	9.87700E+00	1.41644E+01	1.72113E-01								
274	8.31529E+00	1.43365E+01	2.50001E-01								
275	6.47595E+00	1.45865E+01	2.49999E-01								
276	5.04348E+00	1.48365E+01	8.12292E-02								
277	4.65000E+00	1.49177E+01	1.50573E-01								
278	4.00000E+00	1.50683E+01	1.81995E-02								
279	3.92786E+00	1.50865E+01	2.50000E-01								
280	3.05902E+00	1.53365E+01	2.49999E-01								

Table 2.2.1-8 JSSTD-295n-104 γ library gamma-ray group structures

TABLE OF GAMMA ENERGY GROUP STRUCTURE

GROUP	UP-ENERGY	LETHAGY	DELTA-U	GROUP	UP-ENERGY	LETHAGY	DELTA-U	GROUP	UP-ENERGY	LETHAGY	DELTA-U
1	5.00000E+07	1.27297E+00	5.10826E-01	41	2.50000E+06	1.72777E+00	6.91358E-02	81	3.00000E+05	3.84303E+00	1.43101E-01
2	3.00000E+07	7.62140E-01	4.05465E-01	42	2.33300E+06	1.79190E+00	3.62248E-02	82	2.60000E+05	3.98613E+00	1.67054E-01
3	2.00000E+07	3.56675E-01	1.62519E-01	43	2.25000E+06	1.82813E+00	3.80481E-02	83	2.40000E+05	4.15318E+00	9.53102E-02
4	1.70000E+07	1.94156E-01	1.94156E-01	44	2.16600E+06	1.86617E+00	7.97350E-02	84	2.00000E+05	4.24850E+00	5.12933E-02
5	1.40000E+07	0.0	1.54151E-01	45	2.00000E+06	1.94591E+00	6.45305E-02	85	1.90000E+05	4.29979E+00	1.71850E-01
6	1.20000E+07	1.54150E-01	8.70114E-02	46	1.87500E+06	2.01045E+00	6.89929E-02	86	1.60000E+05	4.47164E+00	4.5385E-02
7	1.10000E+07	2.41162E-01	3.70413E-02	47	1.75000E+06	2.07944E+00	5.27982E-02	87	1.50000E+05	4.53618E+00	6.89929E-02
8	1.06000E+07	2.70203E-01	5.82689E-02	48	1.66000E+06	2.13224E+00	3.68140E-02	88	1.40000E+05	4.60517E+00	1.54151E-01
9	1.00000E+07	3.36472E-01	4.60440E-02	49	1.60000E+06	2.16905E+00	6.45305E-02	89	1.20000E+05	4.75932E+00	1.02322E-01
10	9.55000E+06	3.82516E-01	5.93166E-02	50	1.50000E+06	2.23359E+00	5.48082E-02	90	1.00000E+05	4.94164E+00	1.05361E-01
11	9.00000E+06	4.41833E-01	5.71584E-02	51	1.42000E+06	2.28840E+00	3.22032E-02	91	9.00000E+04	5.04700E+00	1.17783E-01
12	8.50000E+06	5.59616E-01	6.06247E-02	52	1.37500E+06	2.32060E+00	3.32748E-02	92	8.00000E+04	5.16479E+00	6.5385E-02
13	8.00000E+06	5.91364E-01	3.17487E-02	53	1.33000E+06	2.35388E+00	6.20354E-02	93	7.50000E+04	5.22932E+00	1.43101E-01
14	7.50000E+06	5.91364E-01	3.27899E-02	54	1.25000E+06	2.41591E+00	4.08220E-02	94	6.50000E+04	5.37243E+00	8.00428E-02
15	7.50000E+06	6.24154E-01	3.39016E-02	55	1.20000E+06	2.45674E+00	6.45305E-02	95	6.00000E+04	5.45247E+00	8.70114E-02
16	7.25000E+06	6.5056E-01	3.50913E-02	56	1.12500E+06	2.52127E+00	1.17783E-01	96	5.50000E+04	5.53948E+00	2.00671E-01
17	7.00000E+06	6.93147E-01	3.63677E-02	57	1.00000E+06	2.63908E+00	1.05361E-01	97	4.50000E+04	5.74015E+00	1.17783E-01
18	6.75000E+06	7.29515E-01	3.77404E-02	58	9.00000E+05	2.74442E+00	3.96653E-02	98	4.00000E+04	5.85793E+00	1.33531E-01
19	6.50000E+06	7.67255E-01	3.92207E-02	59	8.50000E+05	2.78408E+00	4.73462E-02	99	3.50000E+04	5.99146E+00	1.54151E-01
20	6.25000E+06	8.06476E-01	4.08220E-02	60	8.25000E+05	2.83143E+00	3.07717E-02	100	3.00000E+04	6.14561E+00	4.05465E-01
21	6.00000E+06	8.47298E-01	4.25596E-02	61	8.00000E+05	2.86220E+00	6.45385E-02	101	2.00000E+04	6.55108E+00	2.07682E-01
22	5.75000E+06	8.89857E-01	4.44518E-02	62	7.50000E+05	2.92674E+00	6.89929E-02	102	1.50000E+04	6.83874E+00	4.05465E-01
23	5.50000E+06	9.34309E-01	1.83492E-02	63	7.00000E+05	2.99573E+00	3.63677E-02	103	1.00000E+04	7.24423E+00	6.93147E-01
24	5.40000E+06	9.52658E-01	3.77404E-02	64	6.75000E+05	3.03210E+00	3.77404E-02	104	5.00000E+03	7.93738E+00	1.60944E+00
25	5.20000E+06	9.90399E-01	3.92207E-02	65	6.50000E+05	3.06984E+00	3.92207E-02	105	1.00000E+03	9.54681E+00	0.0
26	5.00000E+06	1.02962E+00	6.18754E-02	66	6.25000E+05	3.10986E+00	4.08220E-02				
27	4.70000E+06	1.09149E+00	4.34852E-02	67	6.00000E+05	3.14988E+00	4.25596E-02				
28	4.50000E+06	1.13498E+00	2.24729E-02	68	5.75000E+05	3.19244E+00	4.44518E-02				
29	4.40000E+06	1.15745E+00	4.65200E-02	69	5.50000E+05	3.23689E+00	4.65200E-02				
30	4.20000E+06	1.20397E+00	4.87902E-02	70	5.25000E+05	3.28341E+00	9.56951E-03				
31	4.00000E+06	1.25276E+00	2.53178E-02	71	5.20000E+05	3.29298E+00	1.55042E-02				
32	3.90000E+06	1.27808E+00	2.59755E-02	72	5.12000E+05	3.30849E+00	3.91390E-03				
33	3.80000E+06	1.30406E+00	4.02739E-02	73	5.10000E+05	3.31240E+00	1.98027E-02				
34	3.65000E+06	1.34433E+00	4.19642E-02	74	5.00000E+05	3.33220E+00	1.05361E-01				
35	3.50000E+06	1.38629E+00	4.88902E-02	75	4.50000E+05	3.43756E+00	5.71504E-02				
36	3.33300E+06	1.43518E+00	5.14039E-02	76	4.25000E+05	3.49472E+00	6.06247E-02				
37	3.16600E+06	1.48659E+00	5.38567E-02	77	4.00000E+05	3.55535E+00	6.45385E-02				
38	3.00000E+06	1.54045E+00	5.72761E-02	78	3.75000E+05	3.61989E+00	6.89929E-02				
39	2.83300E+06	1.59772E+00	6.07570E-02	79	3.50000E+05	3.68888E+00	7.41080E-02				
40	2.66600E+06	1.65848E+00	6.42885E-02	80	3.25000E+05	3.76299E+00	8.00428E-02				

2.2.2 SSL90A/B: Standard Group Constants for Safety Analysis of Radiation Shielding

The SSL90A/B library²³⁾ is a common group cross-section library developed at JAERI under the cooperation of Working Group on Shielding Code Evaluation affiliated with the Committee of Nuclear Code Evaluation of JNCC (Japanese Nuclear Code Committee). This library is developed as standard data for use of safety analysis of radiation shielding on nuclear fuel related facilities.

The library was produced by the FAIR-CROSS and the TOWAY modules in the RADHEAT-V4 code system¹⁵⁾, employing JENDL-3¹⁾ and PHOTX-V2³⁰⁾ as evaluated nuclear data files. The system flow of the FAIR-CROSS and the TOWAY modules is shown in Fig. 2.2.2-1. The FAIR-CROSS is a major part in the RADHEAT-V4 system and has many processing subroutines, so that the module is divided into three steps. The ultrafine group cross sections, consisting of 3829 groups, are produced at the beginning stage of FAIR-CROSS Step 1. The fine-group cross sections and Bondarenko-type self-shielding factors¹⁶⁾ of each reaction are generated on the later stage of FAIR-CROSS Step 1. Scattering matrices including up-scattering and atomic displacement cross sections are also produced in this step. Secondary gamma-ray production cross sections are generated by the TOWAY module using the ultrafine group cross sections and nuclear data library, JENDL-3, ENDF/B¹⁹⁾ or POPOP4³¹⁾. Effective neutron and gamma-ray coupled macroscopic cross sections for a homogenized mixture are produced in FAIR-CROSS Step 2. Gamma-ray cross sections are generated using the DLC-136/PHOTX or DLC-15³²⁾ library. Bremsstrahlung data can also be calculated by Step 2. In Step 3, the cross sections of the DDX form are converted into the Legendre expansion ones.

In Table 2.2.2-1, specifications of the library are shown. The SSL90A library contains 43 nuclides and consists of 120 neutron and 18 gamma-ray energy groups. The SSL90B library contains the same nuclides in the SSL90A library, but the energy group structures of 22 neutron and 18 gamma-ray are adopted. A detailed list of processed nuclides is provided in Table 2.2.2-2. The energy group boundaries which were carefully determined so as to satisfy the target accuracy for shielding applications are given in Table 2.2.2-3 and 2.2.2-4, respectively.

Table 2.2.2-1 Specification of group cross section library processing

Items	Contents
Group structure	SSL90A neutrons: 120 and gamma-ray: 18 Neutrons: 10 MeV to 3.307×10^{-5} eV Gamma-ray: 11 MeV to 10 keV SSL90B neutrons: 22 and gamma-ray: 18 Neutrons: 10 MeV to 1.0×10^{-2} eV Gamma-ray: 11 MeV to 10 keV
Weighting spectrum	Maxwellian + 1/E + Fission The MGCL standard spectrum is adopted
Resonance reconstruction tolerance	1.0%
Self-shielding factor	Bondarenko type
Temperature	300 Kelvin
Background cross section, σ_0	0, 1, 10, 10^2 , 10^3 , 10^4 , 10^8 barns
f-table reaction	Total, elastic, capture, fission
Scattering matrix	Double differential cross section (DDX) form
Secondary gamma-ray production data	Fission + capture + inelastic scattering + (n, 2n), (n, 3n) reactions + the other non-elastic reactions

Table 2.2.2-2 Processed nuclides in the SSL90A/B library

Nuclide	SSL90A/B Library MAT No.*	Identification of Contained Data**		
		ULX	INFX	SGRX ⁺
H-1	3011 (J3)	yes	INF FTB ELS	101 (J3)
Li-6	3031 (J3)	yes	INF FTB ELS INS N2N	103 303 (J3)
Li-7	3032 (J3)	yes	INF FTB ELS INS N2N	103 303 (J3)
Be-9	3041 (J3)	yes	INF FTB ELS INS N2N	104 (J3)
B-10	3051 (J3)	yes	INF FTB ELS INS N2N	105 605 305 (J3)
B-11	3052 (J3)	yes	INF FTB ELS INS	105 905 305 (J3)
C-12	3061 (J3)	yes	INF FTB ELS INS	106 306 (J3)
N-14	3071 (J3)	yes	INF FTB ELS INS	107 607 907 (J3)
O-16	3081 (J3)	yes	INF FTB ELS INS	108 208 908 308 (J3)
F-19	3091 (J3)	yes	INF FTB ELS INS	909 109 209 309 (B4)
Na-23	3111 (J3)	yes	INF FTB ELS INS	111 911 311 (J3)
Mg	3120 (J3)	yes	INF FTB ELS INS N2N	112 912 (J3)
Al-27	3131 (J3)	yes	INF FTB ELS INS	113 613 213 913 313 (J3)
Si	3140 (J3)	yes	INF FTB ELS INS N2N	114 614 214 914 314 (J3)
K	3190 (J3)	yes	INF FTB ELS INS N2N	119 619 219 319 (B4)
Ca	3200 (J3)	yes	INF FTB ELS INS N2N	120 220 920 (J3)
Cr	3240 (J3)	yes	INF FTB ELS INS N2N	124 924 (J3)
Mn-55	3251 (J3)	yes	INF FTB ELS INS	125 625 225 325 (J3)
Fe	3260 (J3)	yes	INF FTB ELS INS N2N	926 126 326 (J3)
Co-59	3271 (J3)	yes	INF FTB ELS INS	127 927 (B4)
Ni	3280 (J3)	yes	INF FTB ELS INS N2N	128 928 (J3)
Cu	3290 (J3)	yes	INF FTB ELS INS	129 929 (J3)
Kr-80	1182 (B4)	yes	INF FTB ELS INS	not given
Zr	3400 (J3)	yes	INF FTB ELS INS N2N	140 640 240 340 440 (J3)
Nb-93	3411 (J3)	yes	INF FTB ELS INS N2N	141 641 241 341 441 (J3)
Mo	3420 (J3)	yes	INF FTB ELS INS N2N	142 942 342 (J3)
Cd	3480 (J3)	yes	INF FTB ELS INS N2N	948 148 (J3)
W-182	3741 (J3)	yes	INF FTB ELS INS N2N	174 374 (B4)
W-183	3742 (J3)	yes	INF FTB ELS INS N2N	174 374 (B4)

*) J3 or B4 given in parentheses means JENDL-3 or ENDF/B-IV, respectively.

**) Abbreviations are as follows: ULX: Ultrafine group cross section, INFX: Fine-group cross section, SGRX: Secondary gamma-ray data, INF: Infinite dilution cross section, FTB: f-tables, ELS: Elastic scattering matrix, INS: Inelastic scattering matrix, N2N: (n, 2n) scattering matrix.

+) J3, B4 or P4 given in parentheses means JENDL-3, ENDF/B-IV or POPOP4, respectively. The reaction type is indicated by three digits.

Table 2.2.2-2 (continued)

Nuclide	SSL90A/B Library MAT No.*	Identification of Contained Data**		
		ULX	INFX	SGRX ⁺
W-184	3743 (J3)	yes	INF FTB ELS INS N2N	174 374 (B4)
W-186	3744 (J3)	yes	INF FTB ELS INS N2N	174 374 (B4)
Au-197	1283 (B4)	yes	INF FTB ELS INS N2N	not given
Pb	3820 (J3)	yes	INF FTB ELS INS N2N	182 982 (J3)
U-235	3924 (J3)	yes	INF FTB ELS INS N2N	892 192 992 392 (J3)
U-238	3926 (J3)	yes	INF FTB ELS INS N2N	892 192 992 392 (J3)
Np-237	3931 (J3)	yes	INF FTB ELS INS N2N	not given
Pu-238	3942 (J3)	yes	INF FTB ELS INS N2N	not given
Pu-239	3943 (J3)	yes	INF FTB ELS INS N2N	894 194 394 494 (J3)
Pu-240	3944 (J3)	yes	INF FTB ELS INS N2N	894 194 994 394 (B4)
Pu-241	3945 (J3)	yes	INF FTB ELS INS N2N	194 894 (P4)
Pu-242	3946 (J3)	yes	INF FTB ELS INS N2N	194 894 (P4)
Am-241	3951 (J3)	yes	INF FTB ELS INS N2N	not given
Am-243	3954 (J3)	yes	INF FTB ELS INS N2N	not given

*) J3 or B4 given in parentheses means JENDL-3 or ENDF/B-IV, respectively.

* *) Abbreviations are as follows: ULX: Ultrafine group cross section, INFX: Fine-group cross section, SGRX: Secondary gamma-ray data, INF: Infinite dilution cross section, FTB: f-tables, ELS: Elastic scattering matrix, INS: Inelastic scattering matrix, N2N: (n, 2n) scattering matrix.

+) J3, B4 or P4 given in parentheses means JENDL-3, ENDF/B-IV or POPOP4, respectively. The reaction type is indicated by three digits.

Table 2.2.2-3 Energy group structure of neutrons (SSL90A: 120 groups)

No	Upper Energy (eV)	Lower Energy	Upper Lethargy	No	Upper Energy (eV)	Lower Energy	Upper Lethargy
1	1.00000E+07	8.82497E+06	0.0	62	3.43067E+04	3.18278E+04	5.675
2	8.82497E+06	7.78801E+06	0.125	63	3.18278E+04	2.85124E+04	5.75
3	7.78801E+06	6.87289E+06	0.25	64	2.85124E+04	2.69866E+04	5.86
4	6.87289E+06	6.06531E+06	0.375	65	2.69866E+04	2.60584E+04	5.915
5	6.06531E+06	5.35261E+06	0.5	66	2.60584E+04	2.47875E+04	5.95
6	5.35261E+06	4.72367E+06	0.625	67	2.47875E+04	2.41755E+04	6.0
7	4.72367E+06	4.16862E+06	0.75	68	2.41755E+04	2.35786E+04	6.025
8	4.16862E+06	3.67879E+06	0.875	69	2.35786E+04	2.18749E+04	6.05
9	3.67879E+06	3.24652E+06	1.0	70	2.18749E+04	1.93045E+04	6.125
10	3.24652E+06	2.86505E+06	1.125	71	1.93045E+04	1.50344E+04	6.25
11	2.86505E+06	2.59240E+06	1.25	72	1.50344E+04	1.11936E+04	6.5
12	2.59240E+06	2.38521E+06	1.35	73	1.11936E+04	9.11882E+03	6.795
13	2.38521E+06	2.36525E+06	1.4333	74	9.11882E+03	7.10174E+03	7.0
14	2.36525E+06	2.30685E+06	1.4417	75	7.10174E+03	5.53084E+03	7.25
15	2.30685E+06	2.12248E+06	1.4667	76	5.53084E+03	4.30743E+03	7.5
16	2.12248E+06	1.92050E+06	1.55	77	4.30743E+03	3.70744E+03	7.75
17	1.92050E+06	1.73774E+06	1.65	78	3.70744E+03	3.35463E+03	7.9
18	1.73774E+06	1.53355E+06	1.75	79	3.35463E+03	3.03539E+03	8.0
19	1.53355E+06	1.35335E+06	1.875	80	3.03539E+03	2.74654E+03	8.1
20	1.35335E+06	1.19433E+06	2.0	81	2.74654E+03	2.61259E+03	8.2
21	1.19433E+06	1.05399E+06	2.125	82	2.61259E+03	2.48517E+03	8.25
22	1.05399E+06	9.58472E+05	2.25	83	2.48517E+03	2.24867E+03	8.3
23	9.58472E+05	8.20850E+05	2.345	84	2.24867E+03	2.03468E+03	8.4
24	8.20850E+05	7.24398E+05	2.5	85	2.03468E+03	1.58461E+03	8.5
25	7.24398E+05	6.39279E+05	2.625	86	1.58461E+03	1.23410E+03	8.75
26	6.39279E+05	5.64161E+05	2.75	87	1.23410E+03	9.61117E+02	9.0
27	5.64161E+05	4.97871E+05	2.875	88	9.61117E+02	7.48518E+02	9.25
28	4.97871E+05	4.39369E+05	3.0	89	7.48518E+02	5.82947E+02	9.5
29	4.39369E+05	3.87742E+05	3.125	90	5.82947E+02	4.53999E+02	9.75
30	3.87742E+05	3.68832E+05	3.25	91	4.53999E+02	3.53575E+02	10.0
31	3.68832E+05	3.42181E+05	3.3	92	3.53575E+02	2.75364E+02	10.25
32	3.42181E+05	3.33733E+05	3.375	93	2.75364E+02	2.14454E+02	10.5
33	3.33733E+05	3.01974E+05	3.4	94	2.14454E+02	1.67017E+02	10.75
34	3.01974E+05	2.98500E+05	3.5	95	1.67017E+02	1.30073E+02	11.0
35	2.98500E+05	2.97199E+05	3.51157	96	1.30073E+02	1.01301E+02	11.25
36	2.97199E+05	2.94518E+05	3.51594	97	1.01301E+02	7.88932E+01	11.5
37	2.94518E+05	2.87246E+05	3.525	98	7.88932E+01	6.14421E+01	11.75
38	2.87246E+05	2.74607E+05	3.55	99	6.14421E+01	4.78512E+01	12.0
39	2.74607E+05	2.66491E+05	3.595	100	4.78512E+01	3.72665E+01	12.25
40	2.66491E+05	2.50972E+05	3.625	101	3.72665E+01	2.90232E+01	12.5
41	2.50972E+05	2.35177E+05	3.685	102	2.90232E+01	2.26033E+01	12.75
42	2.35177E+05	2.07543E+05	3.75	103	2.26033E+01	1.76035E+01	13.0
43	2.07543E+05	1.85924E+05	3.875	104	1.76035E+01	1.37096E+01	13.25
44	1.85924E+05	1.61635E+05	3.985	105	1.37096E+01	1.06770E+01	13.5
45	1.61635E+05	1.48464E+05	4.125	106	1.06770E+01	8.31529E+00	13.75
46	1.48464E+05	1.39120E+05	4.21	107	8.31529E+00	6.47595E+00	14.0
47	1.39120E+05	1.31019E+05	4.275	108	6.47595E+00	5.04348E+00	14.25
48	1.31019E+05	1.29715E+05	4.335	109	5.04348E+00	3.92786E+00	14.5
49	1.29715E+05	1.22773E+05	4.345	110	3.92786E+00	3.05902E+00	14.75
50	1.22773E+05	1.11090E+05	4.4	111	3.05902E+00	2.38237E+00	15.0
51	1.11090E+05	9.80366E+04	4.5	112	2.38237E+00	1.85539E+00	15.25
52	9.80366E+04	8.65170E+04	4.625	113	1.85539E+00	1.44498E+00	15.5
53	8.65170E+04	8.27100E+04	4.75	114	1.44498E+00	1.12535E+00	15.75
54	8.27100E+04	7.94669E+04	4.795	115	1.12535E+00	8.76425E-01	16.0
55	7.94669E+04	7.63509E+04	4.835	116	8.76425E-01	6.82560E-01	16.25
56	7.63509E+04	7.19046E+04	4.875	117	6.82560E-01	5.31579E-01	16.5
57	7.19046E+04	6.73795E+04	4.935	118	5.31579E-01	4.13994E-01	16.75
58	6.73795E+04	5.94622E+04	5.0	119	4.13994E-01	1.09624E-01	17.0
59	5.94622E+04	5.24752E+04	5.125	120	1.09624E-01	3.30660E-05	18.328795
60	5.24752E+04	4.08677E+04	5.25	121		3.30660E-05	26.435101
61	4.08677E+04	3.43067E+04	5.5				

Table 2.2.2-4 Energy group structures of neutrons (SSL90B: 22 groups) and gamma-rays (SSL90A and SSL90B: 18 groups)

Neutron				Photon		
No	Upper Energy (eV)	Lower Energy	Upper Lethargy	No	Upper Energy (eV)	Lower Energy
1	1.00000E+07	8.18000E+06	0.0	1	1.1E+07	8.0E+06
2	8.18000E+06	6.36000E+06	0.20089	2	8.0E+06	6.0E+06
3	6.36000E+06	4.96000E+06	0.45256	3	6.0E+06	4.0E+06
4	4.96000E+06	4.06000E+06	0.70118	4	4.0E+06	3.0E+06
5	4.06000E+06	3.01000E+06	0.90140	5	3.0E+06	2.5E+06
6	3.01000E+06	2.46000E+06	1.20065	6	2.5E+06	2.0E+06
7	2.46000E+06	2.35000E+06	1.40242	7	2.0E+06	1.5E+06
8	2.35000E+06	1.83000E+06	1.44817	8	1.5E+06	1.0E+06
9	1.83000E+06	1.11000E+06	1.69827	9	1.0E+06	7.0E+05
10	1.11000E+06	5.50000E+05	2.19823	10	7.0E+05	4.5E+05
11	5.50000E+05	1.11000E+05	2.90042	11	4.5E+05	3.0E+05
12	1.11000E+05	5.94622E+04	4.50081	12	3.0E+05	1.5E+05
13	5.94622E+04	2.60584E+04	5.125	13	1.5E+05	1.0E+05
14	2.60584E+04	1.50344E+04	5.95	14	1.0E+05	7.0E+04
15	1.50344E+04	3.35000E+03	6.5	15	7.0E+04	4.5E+04
16	3.35000E+03	5.83000E+02	8.00138	16	4.5E+04	3.0E+04
17	5.83000E+02	1.01000E+02	9.74991	17	3.0E+04	2.0E+04
18	1.01000E+02	1.07000E+01	11.50298	18	2.0E+04	1.0E+04
19	1.07000E+01	3.06000E+00	13.74785			
20	3.06000E+00	1.12000E+00	14.99968			
21	1.12000E+00	4.14000E-01	16.00477			
22	4.14000E-01	1.00000E-02	16.99998			
23		1.00000E-02	20.72327			

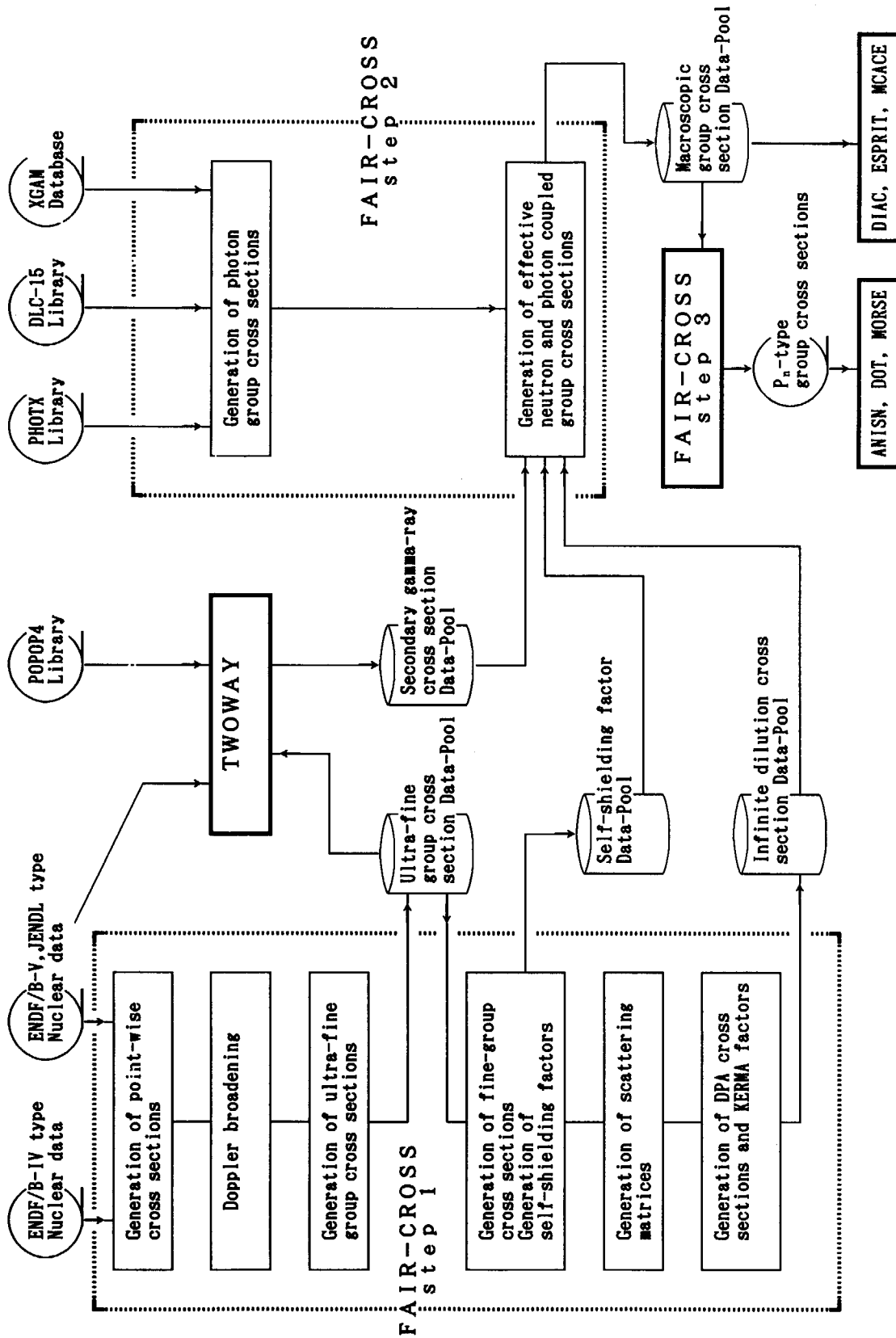


Fig. 2.2.2-1 Cross-section generation flow in the RADHEAT-V4 code system

2.2.3 FSXLIB-J3: A Point-wise Cross-section Library for MCNP

The point-wise cross-section library FSXLIB-J3²⁴⁾ was produced using the cross-section processing code system, NJOY¹⁸⁾, and a compilation code MACROS²⁴⁾ developed at JAERI. The schematic flow of the present code system is given in Fig. 2.2.3-1. The MACROS code includes the following functions: 1) converting the ACE-formatted point-wise cross-sections, which were generated by NJOY-83, to the form of the cross-section library which is directly applicable to the MCNP code¹⁷⁾ and compiling a new library, 2) adding or replacing new cross-section in the library, 3) deleting data from the library, 4) rearranging order of stored data and 5) printing stored data.

The point-wise cross-section library includes the data for 45 nuclides as shown in Table 2.2.3-1. Most of the nuclides were selected referring to the JSD1000²⁹⁾ library which is the DDX type shielding group constants generated by RADHEAT-V4¹⁵⁾ from ENDF/B-IV, and the rest of nuclides were determined from the nuclides specific in fusion neutronics field. Therefore the present library is considered to cover almost all nuclides necessary for shielding design calculations of any kind of facility.

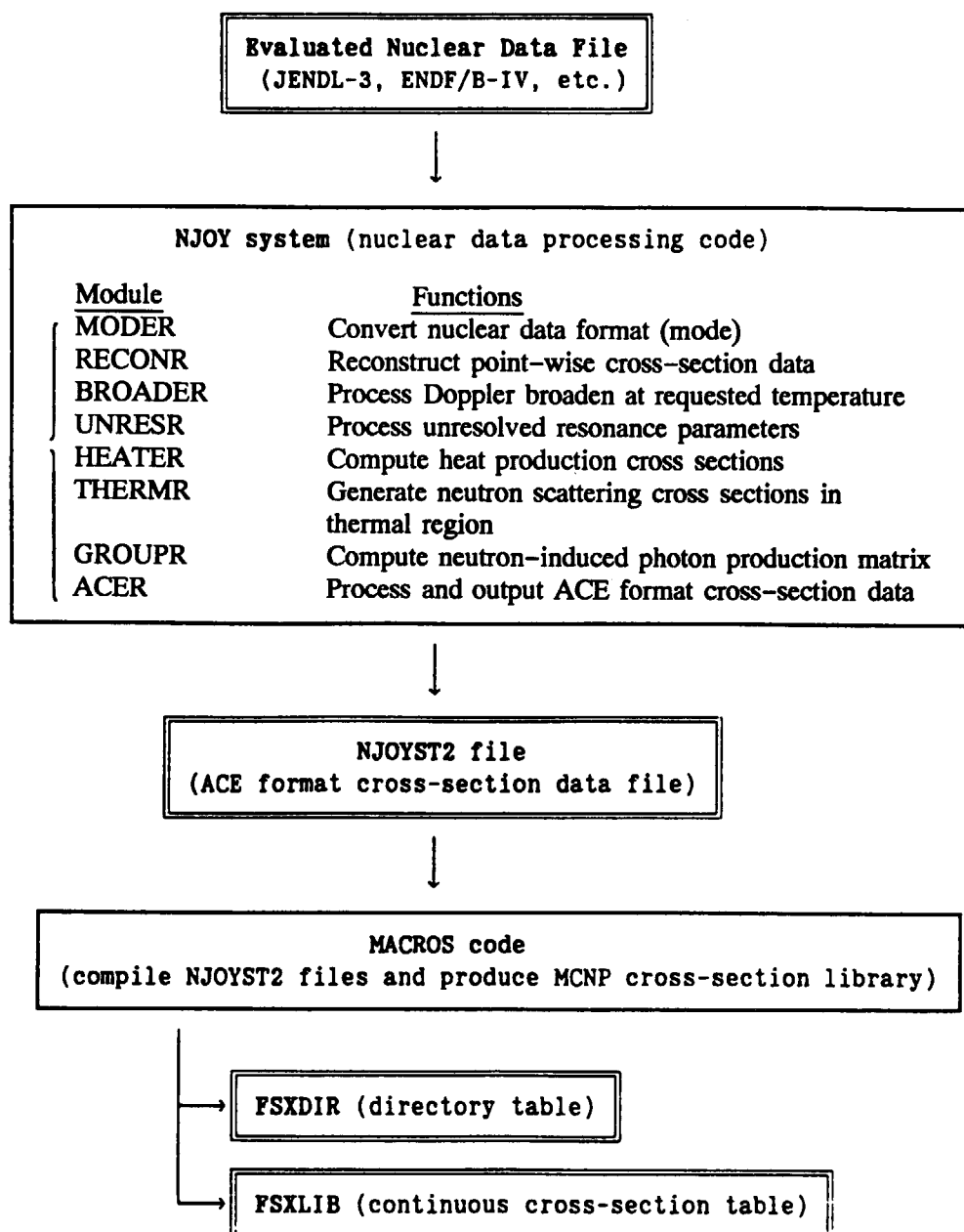


Fig. 2.2.3-1 Compilation code system for the MCNP data library²⁴⁾

Table 2.2.3-1 Contents of FSXLIB-J3 library based on JENDL-3²⁴⁾Description of labels in table

- ZAID** : the nuclide identification number
- FILE** : the name of MCNP cross section libraries
- SOURCE** : the name of evaluated nuclear data file
 'JENDL-3' is the Japanese Evaluated Nuclear Data Library, version 3.
- MAT** : the material identifier for a particular evaluation
- TYPE** : the type of a nuclear data table
 'CONT' indicates a continuous-energy cross section set.
- TEMP** : the temperature (in Kelvin) at which the nuclear data were processed
- GPD** : the secondary gamma-ray production data
 'YES' means that the point-wise energy-dependent gamma production cross section exists.
 'NO' means that the gamma production cross section does not exist.
- LENGTH** : the total length of a particular nuclide in decimal
- NUBAR** : for fissionable material, NUBAR indicates the type of fission nubar data available
 'PROMPT' means that only prompt nubar data are given.
 'TOTAL' means that only total nubar data are given.
 'BOTH' means that prompt and total nubar are given.
- Standard** : Does this nuclide include in the standard library FSXLIB?
 'YES' means that nuclide includes in the standard and expansion FSXLIB.
 'NO' means that nuclide includes only in the expansion FSXLIB.

nuclide [ZAID]	FILE	SOURCE	MAT	TYPE	TEMP (K)	GPD	LENGTH	NUBAR	Stan dard
(Hydrogen)									
1001.34C	FSXLIBJ3	JENDL-3	3011	CONT	300	YES	2422		YES
1002.34C	FSXLIBJ3	JENDL-3	3012	CONT	300	NO	6376		YES
(Helium)									
2003.34C	FSXLIBJ3	JENDL-3	3021	CONT	300	NO	2053		YES
2004.34C	FSXLIBJ3	JENDL-3	3022	CONT	300	NO	3319		YES
(Lithium)									
3006.34C	FSXLIBJ3	JENDL-3	3031	CONT	300	YES	11637		YES
3007.34C	FSXLIBJ3	JENDL-3	3032	CONT	300	YES	19526		YES
(Beryllium)									
4009.34C	FSXLIBJ3	JENDL-3	3041	CONT	300	YES	18522		YES
(Boron)									
5010.34C	FSXLIBJ3	JENDL-3	3051	CONT	300	YES	29462		YES
5011.34C	FSXLIBJ3	JENDL-3	3052	CONT	300	YES	42854		YES
(Carbon)									
6012.34C	FSXLIBJ3	JENDL-3	3061	CONT	300	YES	17833		YES
(Nitrogen)									
7014.34C	FSXLIBJ3	JENDL-3	3071	CONT	300	YES	37816		YES
7015.34C	FSXLIBJ3	JENDL-3	3072	CONT	300	YES	29147		YES
(Oxygen)									
8016.34C	FSXLIBJ3	JENDL-3	3081	CONT	300	YES	43263		YES
(Fluorine)									
9019.34C	FSXLIBJ3	JENDL-3	3091	CONT	300	NO	14188		YES

Table 2.2.3-1 (continued)

nuclide [ZAID]	FILE	SOURCE	MAT	TYPE	TEMP (K)	GPD	LENGTH	NUBAR	Stan dard
(Sodium) 11023.34C	FSXLIBJ3	JENDL-3	3111	CONT	300	YES	43710		YES
(Magnesium) 12000.34C	FSXLIBJ3	JENDL-3	3120	CONT	300	YES	44552		YES
12024.34C	FSXLIBJ3	JENDL-3	3121	CONT	300	NO	11943		NO
12025.34C	FSXLIBJ3	JENDL-3	3122	CONT	300	NO	16032		NO
12026.34C	FSXLIBJ3	JENDL-3	3123	CONT	300	NO	12175		NO
(Aluminum) 13027.34C	FSXLIBJ3	JENDL-3	3131	CONT	300	YES	41884		YES
(Silicon) 14000.34C	FSXLIBJ3	JENDL-3	3140	CONT	300	YES	86018		YES
14028.34C	FSXLIBJ3	JENDL-3	3141	CONT	300	YES	41020		NO
14029.34C	FSXLIBJ3	JENDL-3	3142	CONT	300	YES	37263		NO
14030.34C	FSXLIBJ3	JENDL-3	3143	CONT	300	YES	31540		NO
(Phosphorus) 15031.34C	FSXLIBJ3	JENDL-3	3151	CONT	300	NO	21030		YES
(Sulfur) 16000.33C	FSXLIBJ3	JENDL-3	3160	CONT	300	NO	67590		YES
(Potassium) 19000.34C	FSXLIBJ3	JENDL-3	3190	CONT	300	NO	53108		YES
19039.34C	FSXLIBJ3	JENDL-3	3191	CONT	300	NO	28410		NO
19040.34C	FSXLIBJ3	JENDL-3	3192	CONT	300	NO	8822		NO
19041.34C	FSXLIBJ3	JENDL-3	3193	CONT	300	NO	23107		NO
(Calcium) 20000.34C	FSXLIBJ3	JENDL-3	3200	CONT	300	YES	87797		YES
20040.34C	FSXLIBJ3	JENDL-3	3201	CONT	300	YES	54170		NO
20042.34C	FSXLIBJ3	JENDL-3	3202	CONT	300	NO	31071		NO
20043.34C	FSXLIBJ3	JENDL-3	3203	CONT	300	NO	24682		NO
20044.34C	FSXLIBJ3	JENDL-3	3204	CONT	300	NO	26534		NO
20046.34C	FSXLIBJ3	JENDL-3	3205	CONT	300	NO	3532		NO
20048.34C	FSXLIBJ3	JENDL-3	3206	CONT	300	NO	13615		NO
(Scandium) 21045.34C	FSXLIBJ3	JENDL-3	3211	CONT	300	YES	79926		YES
(Titanium) 22000.34C	FSXLIBJ3	JENDL-3	3220	CONT	300	YES	64044		YES
22046.34C	FSXLIBJ3	JENDL-3	3221	CONT	300	NO	29710		NO
22047.34C	FSXLIBJ3	JENDL-3	3222	CONT	300	NO	29725		NO
22048.34C	FSXLIBJ3	JENDL-3	3223	CONT	300	NO	20242		NO
22049.34C	FSXLIBJ3	JENDL-3	3224	CONT	300	NO	20441		NO
22050.34C	FSXLIBJ3	JENDL-3	3225	CONT	300	NO	16522		NO
(Vanadium) 23051.34C	FSXLIBJ3	JENDL-3	3231	CONT	300	NO	39191		YES

Table 2.2.3-1 (continued)

nuclide [ZAID]	FILE	SOURCE	MAT	TYPE	TEMP (K)	GPD	LENGTH	NUBAR	Stan dard
(Chromium)									
24000.34C	FSXLIBJ3	JENDL-3	3240	CONT	300	YES	117591		YES
24050.34C	FSXLIBJ3	JENDL-3	3241	CONT	300	NO	47312		NO
24052.34C	FSXLIBJ3	JENDL-3	3242	CONT	300	NO	39983		NO
24053.34C	FSXLIBJ3	JENDL-3	3243	CONT	300	NO	31758		NO
24054.34C	FSXLIBJ3	JENDL-3	3244	CONT	300	NO	24481		NO
(Manganese)									
25055.34C	FSXLIBJ3	JENDL-3	3251	CONT	300	YES	201069		YES
(Iron)									
26000.34C	FSXLIBJ3	JENDL-3	3260	CONT	300	YES	144778		YES
26054.34C	FSXLIBJ3	JENDL-3	3261	CONT	300	YES	62131		NO
26056.34C	FSXLIBJ3	JENDL-3	3262	CONT	300	YES	72810		NO
26057.34C	FSXLIBJ3	JENDL-3	3263	CONT	300	YES	60593		NO
26058.34C	FSXLIBJ3	JENDL-3	3264	CONT	300	YES	67076		NO
(Cobalt)									
27059.34C	FSXLIBJ3	JENDL-3	3271	CONT	300	NO	79549		YES
(Nickel)									
28000.34C	FSXLIBJ3	JENDL-3	3280	CONT	300	YES	237991		YES
28058.34C	FSXLIBJ3	JENDL-3	3281	CONT	300	YES	82463		NO
28060.34C	FSXLIBJ3	JENDL-3	3282	CONT	300	YES	103280		NO
28061.34C	FSXLIBJ3	JENDL-3	3283	CONT	300	NO	44481		NO
28062.34C	FSXLIBJ3	JENDL-3	3284	CONT	300	NO	42650		NO
28064.34C	FSXLIBJ3	JENDL-3	3285	CONT	300	NO	41593		NO
(Copper)									
29000.34C	FSXLIBJ3	JENDL-3	3290	CONT	300	YES	170023		YES
29063.34C	FSXLIBJ3	JENDL-3	3291	CONT	300	YES	144647		NO
29065.34C	FSXLIBJ3	JENDL-3	3292	CONT	300	YES	115286		NO
(Zirconium)									
40000.34C	FSXLIBJ3	JENDL-3	3400	CONT	300	YES	160023		YES
40090.34C	FSXLIBJ3	JENDL-3	3401	CONT	300	NO	53750		NO
40091.34C	FSXLIBJ3	JENDL-3	3402	CONT	300	NO	67096		NO
40092.34C	FSXLIBJ3	JENDL-3	3403	CONT	300	NO	53115		NO
40094.34C	FSXLIBJ3	JENDL-3	3405	CONT	300	NO	44262		NO
40096.34C	FSXLIBJ3	JENDL-3	3407	CONT	300	NO	30050		NO
(Niobium)									
41093.34C	FSXLIBJ3	JENDL-3	3411	CONT	300	YES	119152		YES
(Molybdenum)									
42000.34C	FSXLIBJ3	JENDL-3	3420	CONT	300	YES	165448		YES
42092.34C	FSXLIBJ3	JENDL-3	3421	CONT	300	NO	48160		NO
42094.34C	FSXLIBJ3	JENDL-3	3422	CONT	300	NO	41872		NO
42095.34C	FSXLIBJ3	JENDL-3	3423	CONT	300	NO	39992		NO
42096.34C	FSXLIBJ3	JENDL-3	3424	CONT	300	NO	46780		NO
42097.34C	FSXLIBJ3	JENDL-3	3425	CONT	300	NO	42827		NO
42098.34C	FSXLIBJ3	JENDL-3	3426	CONT	300	NO	65873		NO
42100.34C	FSXLIBJ3	JENDL-3	3428	CONT	300	NO	67388		NO
(Silver)									
47000.34C	FSXLIBJ3	JENDL-3	3470	CONT	300	YES	183283		NO

Table 2.2.3-1 (continued)

nuclide [ZAID]	FILE	SOURCE	MAT	TYPE	TEMP (K)	GPD	LENGTH	NUBAR	Stan dard
(Cadmium) 48000.34C	FSXLIBJ3	JENDL-3	3480	CONT	300	YES	153335		YES
(Antimony) 51000.34C	FSXLIBJ3	JENDL-3	3510	CONT	300	NO	76427		NO
(Europium) 63000.34C	FSXLIBJ3	JENDL-3	3630	CONT	300	YES	56669		NO
63151.34C	FSXLIBJ3	JENDL-3	3631	CONT	300	NO	42862		NO
63153.34C	FSXLIBJ3	JENDL-3	3633	CONT	300	NO	39469		NO
(Hafnium) 72000.34C	FSXLIBJ3	JENDL-3	3720	CONT	300	YES	85740		YES
(Tantalum) 73181.34C	FSXLIBJ3	JENDL-3	3731	CONT	300	YES	166522		YES
(Tungsten) 74000.34C	FSXLIBJ3	JENDL-3	3740	CONT	300	YES	199104		YES
74182.34C	FSXLIBJ3	JENDL-3	3741	CONT	300	NO	105858		NO
74183.34C	FSXLIBJ3	JENDL-3	3742	CONT	300	NO	67010		NO
74184.34C	FSXLIBJ3	JENDL-3	3743	CONT	300	NO	95032		NO
74186.34C	FSXLIBJ3	JENDL-3	3744	CONT	300	NO	86861		NO
(Lead) 82000.34C	FSXLIBJ3	JENDL-3	3820	CONT	300	YES	137640		YES
82204.34C	FSXLIBJ3	JENDL-3	3821	CONT	300	YES	55113		NO
82206.34C	FSXLIBJ3	JENDL-3	3822	CONT	300	YES	107986		NO
82207.34C	FSXLIBJ3	JENDL-3	3823	CONT	300	YES	71243		NO
82208.34C	FSXLIBJ3	JENDL-3	3824	CONT	300	YES	38091		NO
(Bismuth) 83209.34C	FSXLIBJ3	JENDL-3	3831	CONT	300	YES	70146		YES
(Thorium) 90232.34C	FSXLIBJ3	JENDL-3	3905	CONT	300	NO	96180	BOTH	YES
(Protactinium) 91233.34C	FSXLIBJ3	JENDL-3	3913	CONT	300	NO	13592	BOTH	NO
(Uranium) 92233.34C	FSXLIBJ3	JENDL-3	3922	CONT	300	NO	33892	BOTH	NO
92234.34C	FSXLIBJ3	JENDL-3	3923	CONT	300	NO	80600	TOTAL	NO
92235.34C	FSXLIBJ3	JENDL-3	3924	CONT	300	YES	62587	BOTH	YES
92236.34C	FSXLIBJ3	JENDL-3	3925	CONT	300	NO	77518	TOTAL	NO
92238.34C	FSXLIBJ3	JENDL-3	3926	CONT	300	YES	235117	BOTH	YES
(Neptunium) 93237.34C	FSXLIBJ3	JENDL-3	3931	CONT	300	NO	47171	BOTH	YES
(Plutonium) 94239.34C	FSXLIBJ3	JENDL-3	3943	CONT	300	YES	128048	BOTH	YES
94240.34C	FSXLIBJ3	JENDL-3	3944	CONT	300	NO	134534	BOTH	YES
94241.34C	FSXLIBJ3	JENDL-3	3945	CONT	300	NO	25107	BOTH	NO
94242.34C	FSXLIBJ3	JENDL-3	3946	CONT	300	NO	58687	TOTAL	NO

Table 2.2.3-1 (continued)

nuclide [ZAID]	FILE	SOURCE	MAT	TYPE	TEMP (K)	GPD	LENGTH	NUBAR	Standard
(Americium)									
95241.34C	FSXLIBJ3	JENDL-3	3951	CONT	300	NO	50430	BOTH	NO
95242.34C	FSXLIBJ3	JENDL-3	3952	CONT	300	NO	13996	BOTH	NO
95243.34C	FSXLIBJ3	JENDL-3	3954	CONT	300	NO	57829	BOTH	NO
(Californium)									
98252.34C	FSXLIBJ3	JENDL-3	3984	CONT	300	NO	32666	BOTH	NO

3. Shielding Analyses

3.1 Total Cross-section Check in MeV Energy Range by the Broomstick Experiments

3.1.1 Outline of Experiments

Broomstick experiments were performed by Straker to investigate the effect of minima in the total neutron cross sections in the MeV energy range for the typical shielding material²⁾.

A schematic of the experiment is shown in **Fig. 3.1-1**. The sample is a cylinder form of 4 inch in diameter and placed so that its axis coincides with the axis of the neutron beam. To reduce the effect of neutron scattering into the sample except through the cylinder top surface, the distance from the neutron source (Tower Shielding Reactor II of ORNL) to the sample is 50 feet and the detector is placed at a position 50 feet from the sample. The neutron beam was confined to a diameter of 3.5 inch by collimators placed between the reactor and sample near the sample position. To reduce air-scattering effects, the reactor and detector were heavily shielded with lead and water, and the reactor beam and detector acceptance were tightly collimated.

The detector is a nominal 2 inch \times 2 inch NE213 scintillator. The unfolding of the pulse-height distributions was accomplished using the FERDOR code.

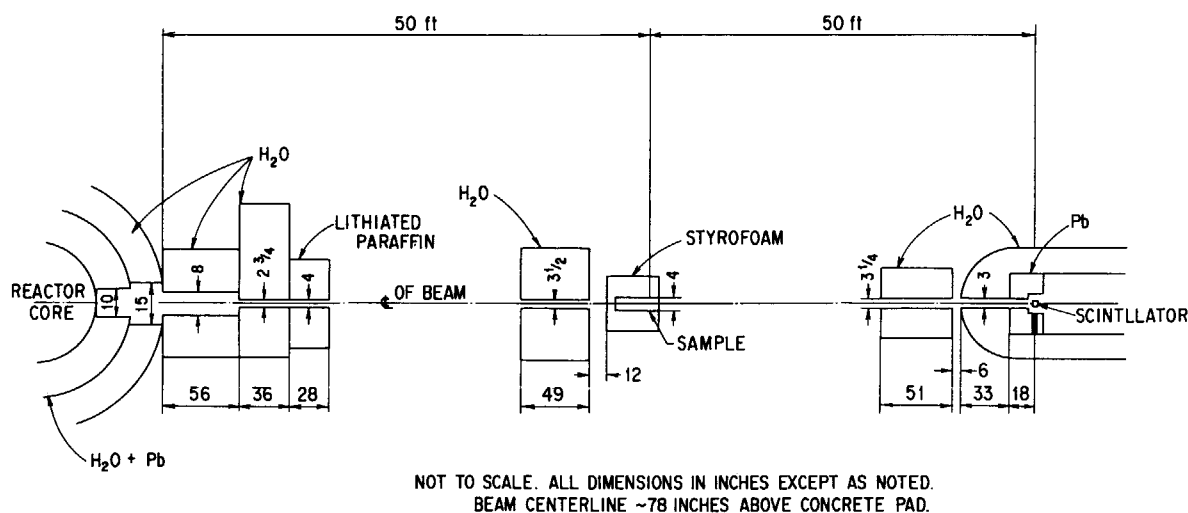


Fig. 3.1-1 A schematic of the Broomstick experimental arrangement²⁾

3.1.2 Calculation Method

As described above, this experiment is performed with a good geometry. Thus, no transport calculations are needed for the analysis. The calculation consists from two parts. The first one is for determining the transmitted uncollided spectrum; here we should not miss the minima of any kind in the total cross section. The second one is to fold the uncollided spectrum calculated from the preceding step with the resolution function of the NE-213 spectrometer system which actually used. Source neutron energy spectrum and detector resolution functions are given in a tabulated form. Indications of these calculations are given in the references³³⁾⁻³⁵⁾. As the results of experiments were only presented in curves, the data were read from these reports to convert them into digital form.

To perform the calculation, we made a code system called WINDOW which accesses the ENDF/B format library. This code calculates the transmitted neutron spectrum, which can be directly compared

with the experimental one, using given functions for source and detector resolutions assigned by the experiment.

To demonstrate the revision history of JENDL data by these benchmark tests, chronological JENDL results are shown, i.e., JENDL-2, JENDL-3PR1,¹ JENDL-3T³⁶⁾,² JENDL-3, as far as available, together with ENDF/B-IV.

3.1.3 Results

3.1.3.1 Oxygen

Thickness : 154.2 cm

Sample condition : Liquid

Testing energy range : 800 keV to 11 MeV

The results are given in **Fig. 3.1-2**, where upper part shows measured spectrum and the calculated ones with JENDL-3, JENDL-3T and ENDF/B-IV; lower part shows the profile of C/E (ratio of calculation to experimental value) of each evaluated data file. In **Table 3.1-1**, statistics of C/E taken over the measured energy region is given for each evaluated data. The first column is an average of C/E, the second is an absolute average of the deviation from C/E=1.0, and the third is a standard deviation (STD), i.e., root mean square.

From this figure and table, we can see the C/E value by ENDF/B-IV is better than JENDL-3T. As the standard deviation is almost the same between the two, the JENDL-3T result is 7 or 8% underestimated from ENDF/B-IV. As for JENDL-3, the standard deviation is better than the rest, especially 2 to 4 MeV energy range, agreement of JENDL-3 result is considerably improved. Yet all of the data underestimate transmission spectra compared with the experiment. Total cross-sections of ENDF/B-IV and JENDL-3 are given in **Fig. 3.1-3**. It is found from this figure that special care was paid to the ENDF/B-IV evaluation especially for the minima as seen in the energy range from 6 to 8 MeV and at 2.5 MeV where the spectrum peaks are seen in **Fig. 3.1-2**. Underestimation of transmitted spectrum suggests that deeper minima of the total cross section in the evaluated data file is recommended, since the total cross section and the transmitted spectrum has an inverse proportional relation.

From these results, we can conclude that the quality of JENDL-3 is nearly the same as ENDF/B-IV, though some improvements are made from JENDL-3T. Still some revision (deeper minima for resonances) is anticipated for the minima of oxygen data. Oxygen data is not available for JENDL-2.

Table 3.1-1 Statistics of C/E values for the oxygen Broomstick experiment

Library	C/E	Abs (1.0-C/E)	STD
JENDL-3	0.736	0.303	0.201
JENDL-3T	0.686	0.353	0.218
ENDF/B-IV	0.756	0.262	0.213

¹JENDL-3PR1: A preliminary version of JENDL-3 specially made for fusion neutronics applications. Only limited nuclides are evaluated.

²JENDL-3T: Temporary version of JENDL-3 made for the benchmark testing prior to the final release.

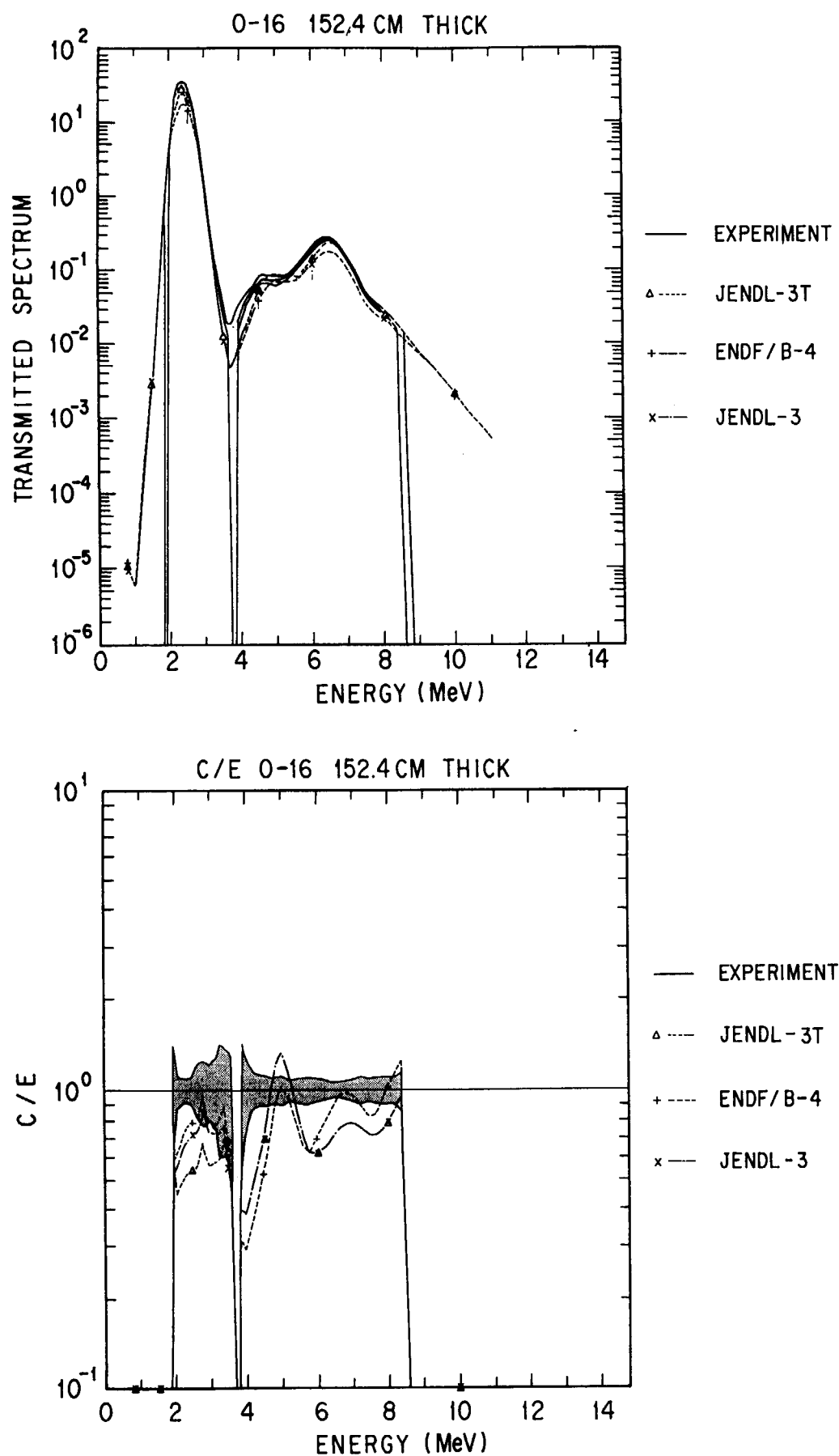


Fig. 3.1-2 Calculated and experimental transmitted spectra and their C/E profiles for an oxygen sample

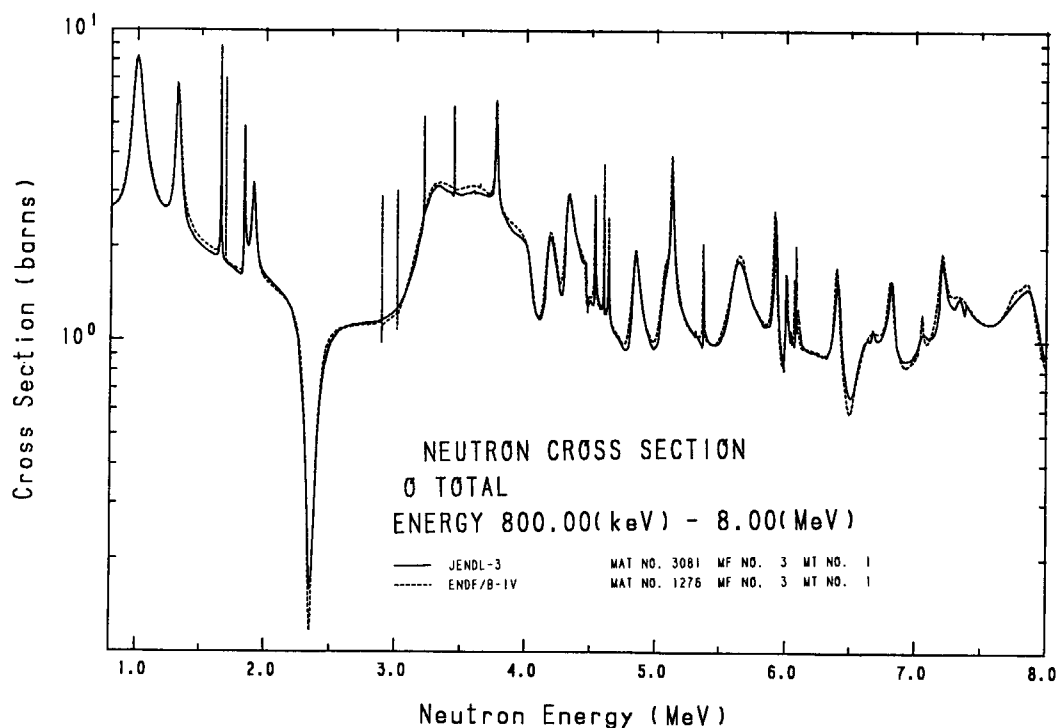


Fig. 3.1-3 Total cross section of oxygen

3.1.3.2 Sodium

Thickness : 60.6 cm

Sample condition : Solid

Testing energy range : 800 keV to 11 MeV

The results are given in **Fig. 3.1-4** and **Table 3.1-2**. The result of JENDL-3T is the same as JENDL-3, since no modifications were made for the total cross sections in this energy range. From this figure and table, we can see the C/E values by all evaluations are overestimated systematically. Again there are no differences between the JENDL-3 and JENDL-2 evaluations. On the other hand, there are clear differences between JENDL-3 and ENDF/B-IV in the energy range from 6 to 10 MeV. In this range, ENDF/B-IV shows a better agreement with the experiment than JENDL-3.

In these results, both ENDF/B-IV and JENDL-3 overestimate the spectrum by about 20% systematically. This implies that the total cross sections in the evaluated data file are relatively small or total cross-section minima are too deep. Total cross-sections of ENDF/B-IV and JENDL-3 are given in **Fig. 3.1-5**. It is recognized from this figure that more careful evaluations are given for ENDF/B-IV tracing resonance structure above 6 MeV. The quality of JENDL-3 data are nearly the same as the ENDF/B-IV below the 6 MeV energy range. The discrepancy between calculation and experiment is fairly large, therefore careful reevaluations are requested.

Table 3.1-2 Statistics of C/E values for the sodium Broomstick experiment

Library	C/E	Abs (1.0-C/E)	STD
JENDL-3	1.243	0.243	0.189
JENDL-3T	1.243	0.243	0.189
JENDL-2	1.242	0.242	0.188
ENDF/B-IV	1.217	0.217	0.215

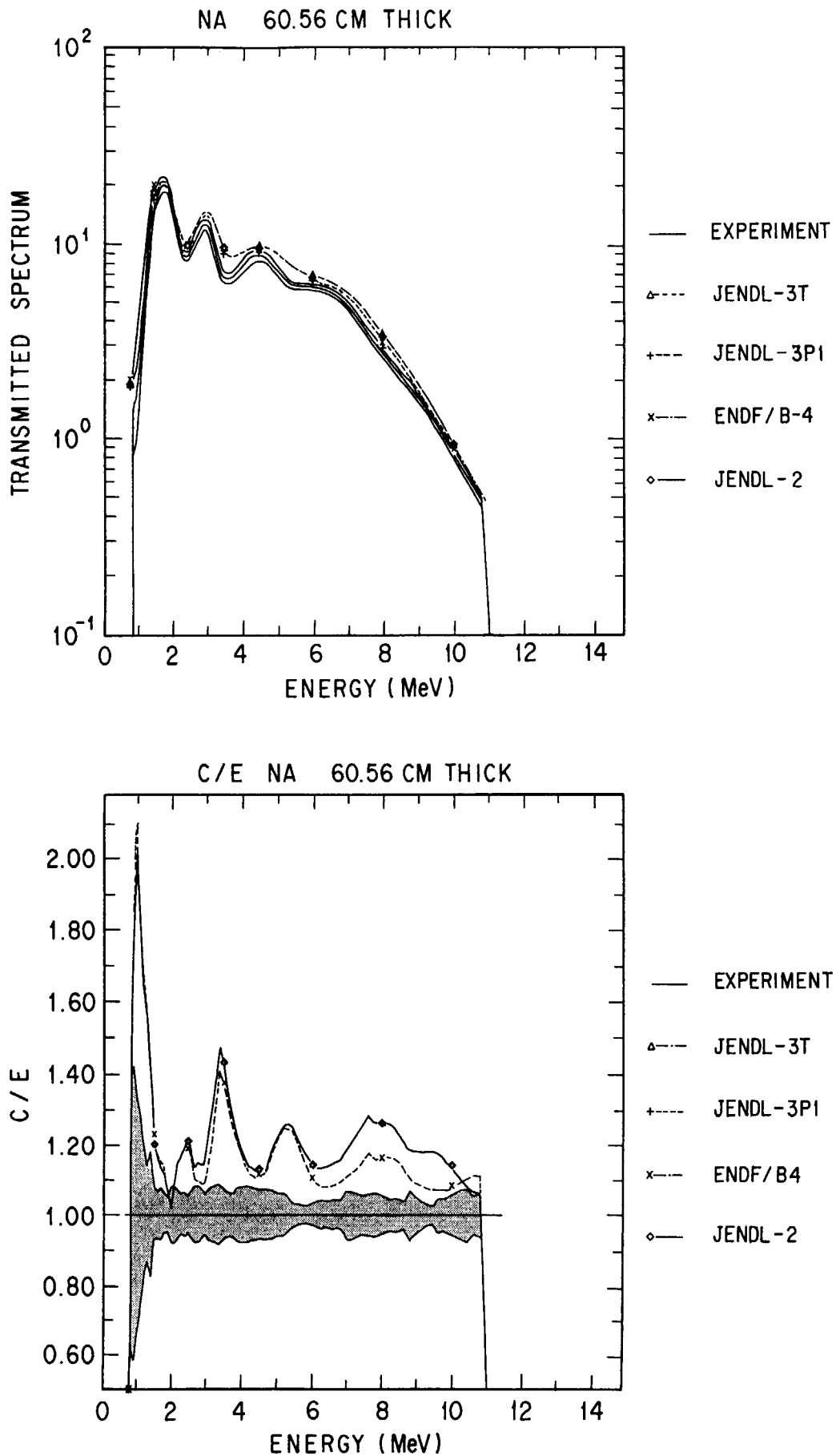


Fig. 3.1-4 Calculated and experimental transmitted spectra and their C/E profiles for a sodium sample

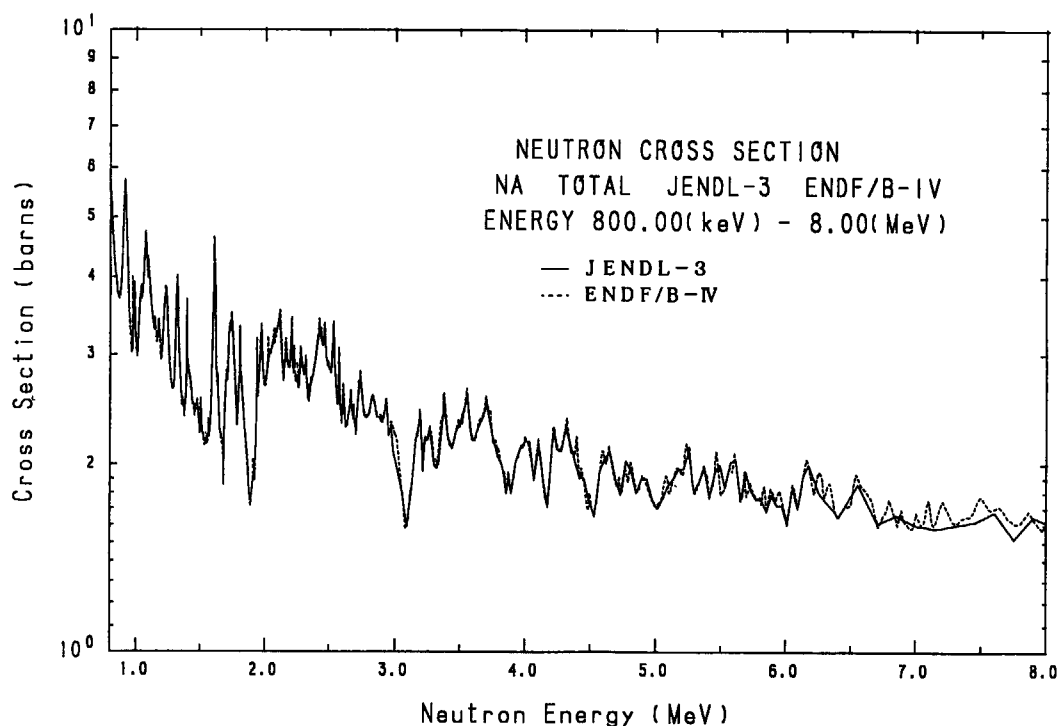


Fig. 3.1-5 Total cross section of sodium

3.1.3.3 Iron

Thickness : a) 20.3 cm b) 30.5 cm
 Sample condition : Solid
 Testing energy range : a) 1.2 - 11.0 MeV b) 1.0 - 8.0 MeV

For this material, there are two experiments with different sample thicknesses. The results are given in Figs. 3.1-6 and 3.1-7, and Table 3.1-3. From these figures and table, we can draw following observations.

1. No clear differences can be seen among older JENDL evaluations except JENDL-3, i.e., JENDL-3T, -3P1, -2.
2. As to the standard deviation for thin sample in Table 3.1-3, the value by ENDF/B-IV (0.086) is much better than the older version of JENDL (0.160), about one half the value of the older JENDL. The average of C/E, however, is not so different between ENDF/B-IV (0.954) and the older JENDL (0.958). JENDL-3 (0.126) is somewhat improved from the view of standard deviations. These results show that the evaluation of JENDL-3 becomes close to ENDF/B-IV

Table 3.1-3 Statistics of C/E values for the iron Broomstick experiment

Library	C/E		Abs (1.0-C/E)		STD	
	a	b	a	b	a	c
JENDL-3	0.927 (0.936)		0.117 (0.204)		0.126 (0.242)	
JENDL-3T	0.958 (0.937)		0.142 (0.219)		0.160 (0.254)	
JENDL-3P1	0.959 (0.935)		0.144 (0.220)		0.163 (0.255)	
JENDL-2	0.959 (0.938)		0.144 (0.219)		0.163 (0.254)	
ENDF/B-IV	0.936 (0.986)		0.092 (0.130)		0.086 (0.176)	

*The values in the parentheses are for the thickness 30.5cm.

a : thickness 20.3cm

b : thickness 30.5cm

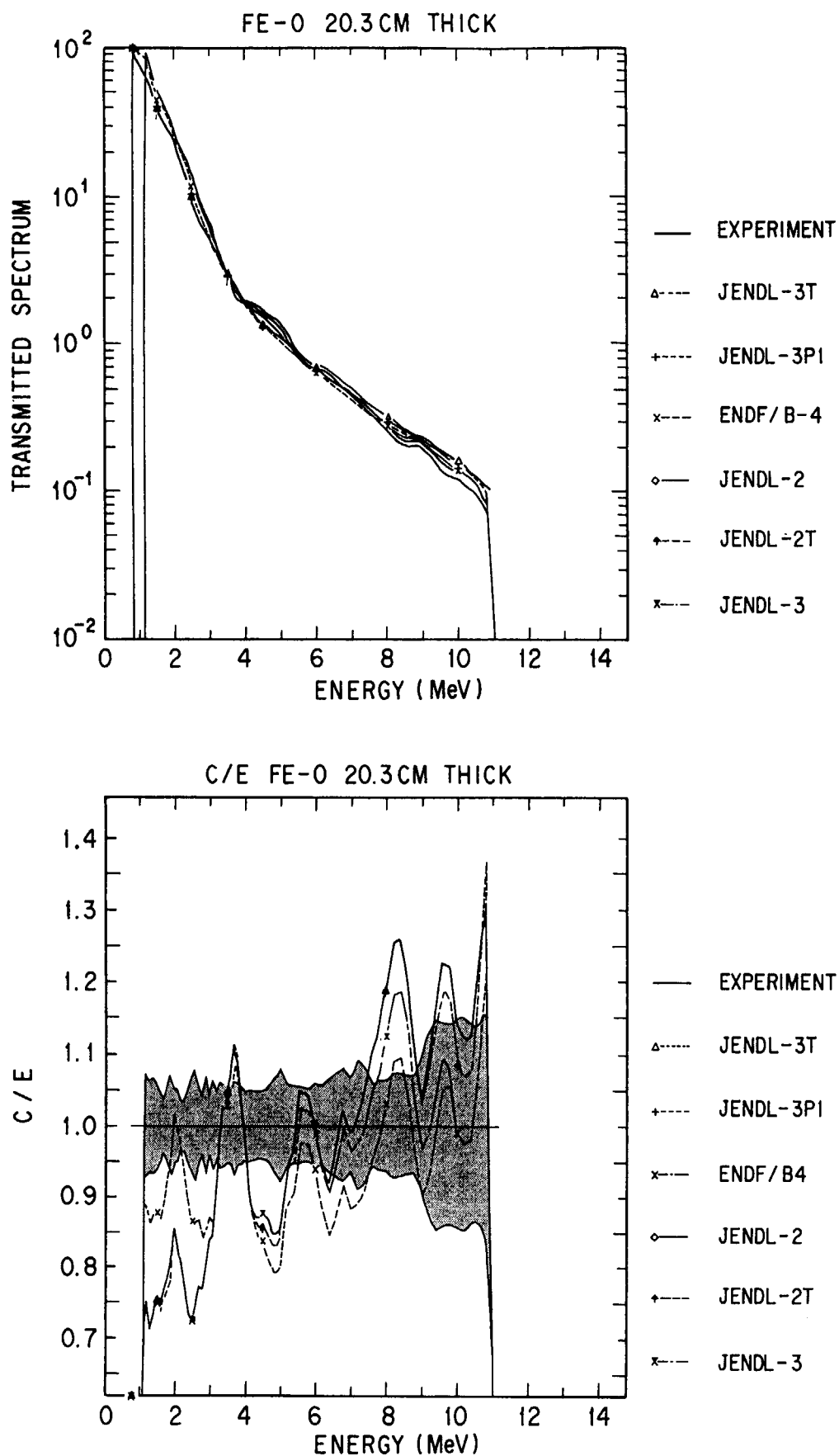


Fig. 3.1-6 Calculated and experimental transmitted spectra and their C/E profiles for an iron sample (20.3 cm thick)

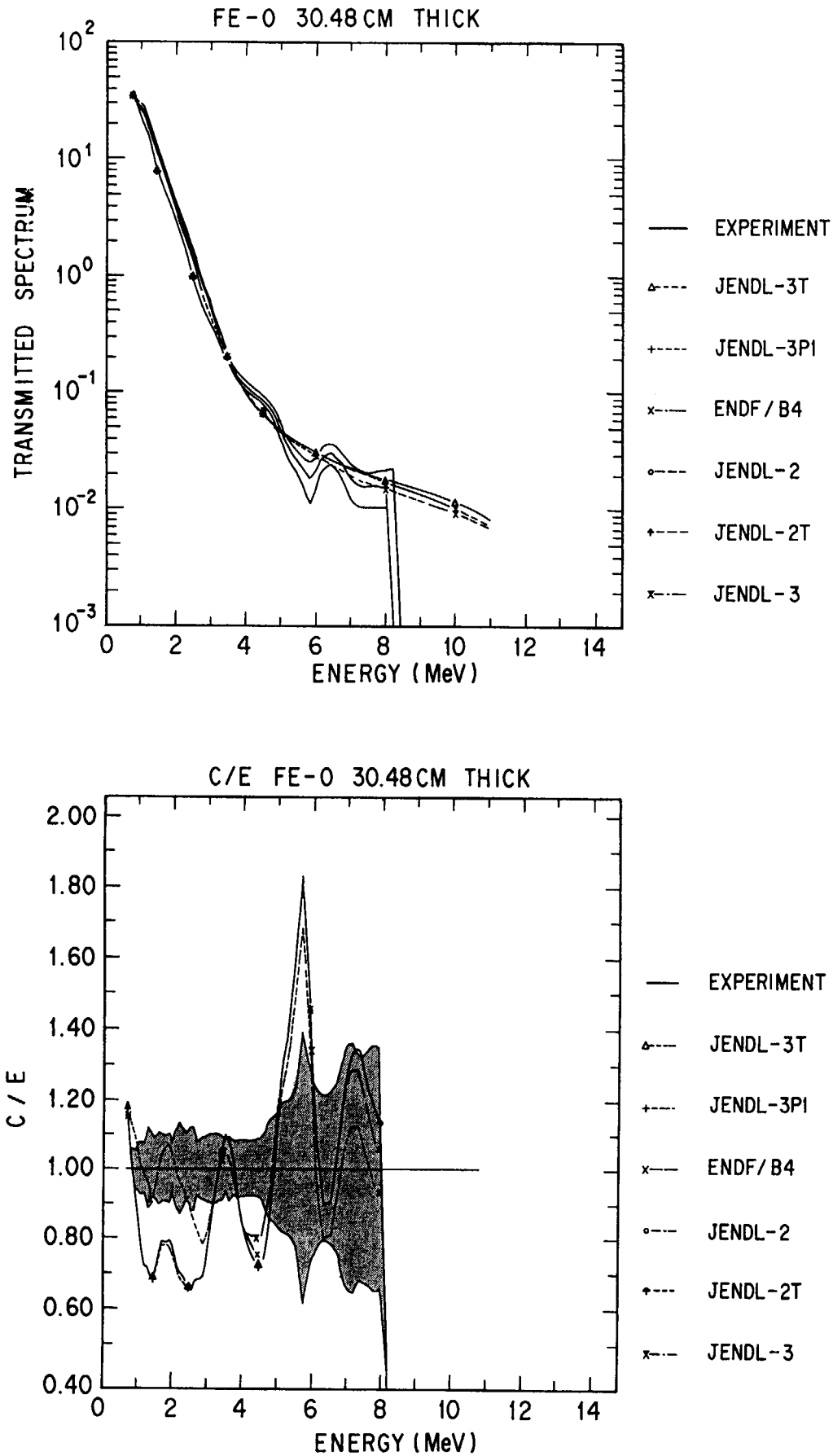


Fig. 3.1-7 Calculated and experimental transmitted spectra and their C/E profiles for an iron sample (30.5 cm thick)

evaluation.

3. For the thick sample case, the agreement of the calculations by ENDF/B-IV with the experiments ($C/E=0.986$) is better than JENDL-3 (0.936).
4. For the JENDL-3T data, C/E profile has some systematic tendency, i.e., C/E increases with energy, while such tendency is not obtained for the ENDF/B-IV case. The values of C/E of JENDL-3, -3T are too small (about 0.7) in the energy range between 1 to 3 MeV compared with the results of ENDF/B-IV, it suggests that the total cross sections are too large or cross-section minima are too shallow. On the contrary for 8 to 10 MeV, the values of C/E of JENDL-3T are too large (about 1.2), i.e., total cross sections are too small or the cross-section minima are too deep. From this information, the high energy part of JENDL-3 was revised and the C/E dependence on energy is a little bit cured in this energy range, but the tendency still remains.

3.1.4 Summary

From this study, the reliability of the total cross section for JENDL-3 data is confirmed. The problems still remaining in JENDL-3 are also pointed out. Those are:

- Oxygen: Total cross section minima for 2 to 8 MeV are rather shallow.
- Sodium: Total cross sections for 2 to 10 MeV are rather small, especially for 6 to 10 MeV.
- Natural iron: Total cross section minima for 1 to 3 MeV are rather shallow (or total cross sections are too large.)

Compared with the results by the older versions of JENDL, i.e., JENDL-2, -3PR1, -3T, no clear revision in total cross-section was found for the tested nuclides. Only oxygen and iron data of JENDL-3 are improved from the older versions. We conclude from this benchmark test that the overall predictability of JENDL-3 is nearly the same as ENDF/B-IV.

3.2 WINFRITH-ASPIS Iron Experiments

3.2.1 Outline of Experiments

This experiment was designed to provide information of benchmark quality for testing of data and calculational methods for deep-penetration profiles by natural iron shielding material.

The experimental configuration is as follows: a low-power natural uranium converter plate (ASPIS), driven by the source reactor, NESTOR, provided a large thin disc source of fission neutrons was placed at the interface of a graphite moderator and extensive iron shield (140 cm thickness)⁵⁾.

Measurements were made for the axial attenuation profiles with three threshold detectors and one low-energy activation detector. The spectra were measured by the spectrometer at four selected positions in the iron shield.

3.2.2 Calculation Method

3.2.2.1 Calculation method by the DOT code

As to the calculational model of the Sn code, we closely follow the model in the report of Carter et al.³⁷⁾ However some modifications were made. The converter plate region was simulated in a straight way, i.e., it was composed of 5 regions as represented by Al-Fe-U-Fe-Al layers. The adopted configuration is shown in Fig. 3.2-1 together with a detailed model of the converter plate in the upper part of the figure.

The volume distributed sources (equivalent radius was 59.3 cm and thickness 0.318 cm) were treated as cross products of energy and space (in the radial direction only) distribution functions. For energy dependence of emitted fission neutrons, U-235 data of ENDF/B-V was used. Average values of source spectrum were calculated and given on each mesh point of the fuel region.

We used the JSSTD 295n-104 γ group cross-section library²²⁾ prepared by the PROF-GROUCH-

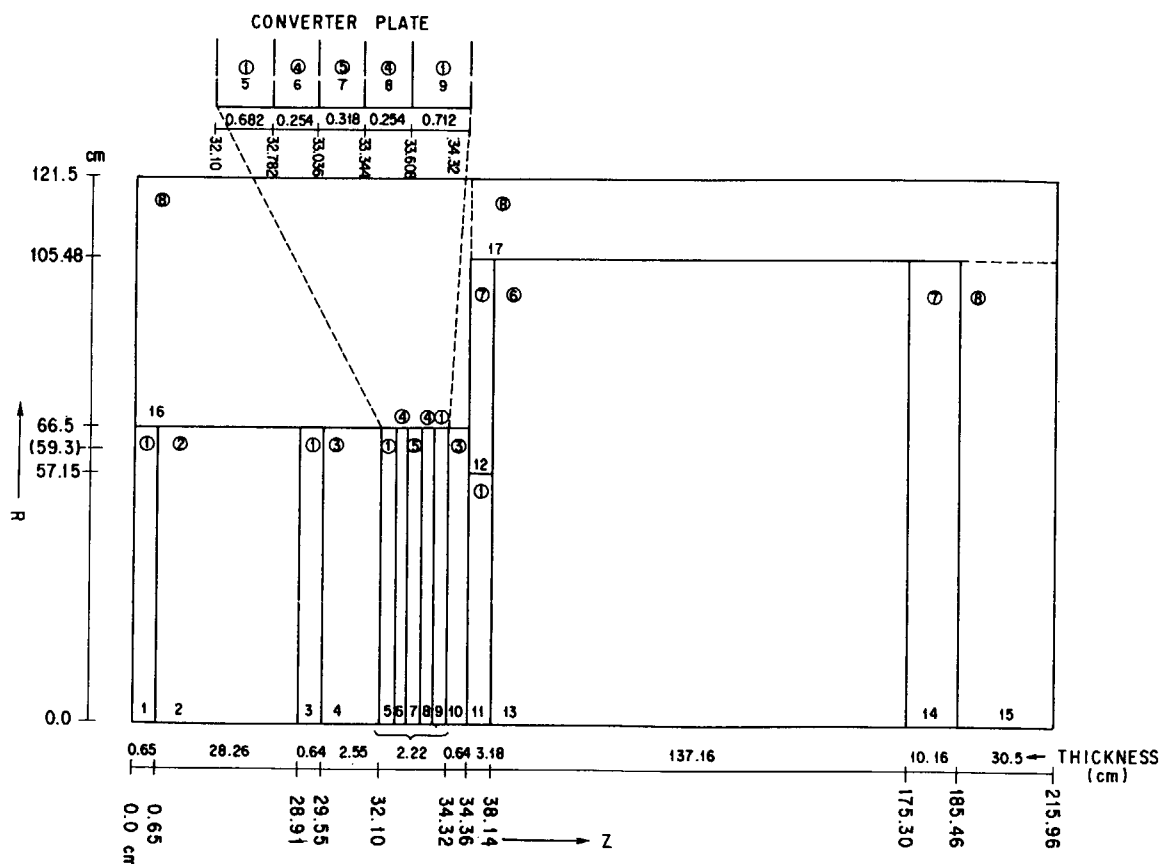


Fig. 3.2-1 R-Z geometrical model adopted for the ASPIS analysis

G/B code¹⁴⁾. For the energy groups, the BERMUDA-121³⁸⁾ group structure was adopted, which is defined as follows, from 16.487 to 1.054 MeV (1-44 groups) a lethargy increment, Δu , is 0.0625, from 1.054 MeV to 19.304 keV (45-76 groups) Δu is 0.125, for the rest of energy down to 0.32241 eV Δu is 0.250 and one thermal group down to 1.0×10^{-5} eV. This energy group structure is in sufficient detail for the ASPIS analysis.

Anisotropy was included up to P5. The weighting functions used for the generation of group cross-section were $1/E$ above 0.32241 eV and Maxwellian below it.

For natural iron in the test region, which is thought as being a nearly pure material, fully shielded cross sections including higher P_1 matrices (i.e., $\sigma_0 = 0$.) were calculated and used by the special option of the PROF-GROUCH-G/B code.

For generating the macroscopic cross-sections for the DOT code, the GLIBMK-MACROJ utility codes²²⁾ were used. The transport calculations were performed by DOT3.5¹³⁾ with the S8-P5 approximation and R-Z geometry with 53×92 meshes. Typical running time was 140 min, required I/O exceeded 200,000 and core memory was about 4 MB per case using FACOM-M/380.

3.2.2.2. Calculation method by the MCNP code

As to the calculational model of the MCNP code¹⁷⁾, we closely followed the experimental configuration by the three-dimensional model. In the MCNP calculation, the following two methods were employed to reduce a fractional standard deviation (FSD) and to obtain results with sufficient accuracy. One is the Next Event Surface Crossing estimator (NESX estimator)³⁹⁾ and the other is the Weight Window Importance Sampling. In this section, the two methods are described.

(a) Next Event Surface Crossing estimator (NESX estimator)

The estimation routines must furnish the bookkeeping routines with the necessary information on particle histories. There are many types of estimators, such as collision density, track length, surface crossing, next event surface crossing (NESX) and point detector. In this study, the NESX estimator was employed intensively to analyze the ASPIS and ORNL (described in Sec. 3.3) experiments with fission neutrons and also to the LLNL experiment (Sec. 3.8) with D-T neutrons. The NESX estimator has been proven to effectively reduce FSD³⁹⁾.

In the NESX estimator, the particles emerging from the collision site were examined as to whether or not they cross any surface detector. If the path is toward a surface detector, the probability that a particle emerging from a collision site will cross the detector surface before its next collision is $\exp(-\eta)$ and the contribution to the fluence is scored with the detector; if there is no detector along the path, the probability is zero. The concept of the NESX estimator is shown in Fig. 3.2-2. This selective scoring

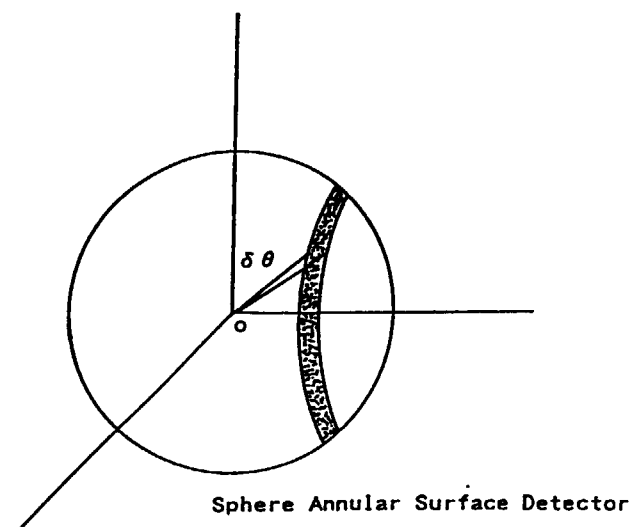


Fig. 3.2-2 Concept of the next event sphere annular surface crossing estimator

procedure of the NESX estimator is more efficient than the procedure of the point detector which scores a contribution from all collisions, because it saves much computer time to calculate the η values in case of the zero probability. In addition, counting statistics by the NESX estimator is better than that by the other type estimators of real particle.

The contribution to the fluence from a collision site in the NESX estimator is described as follows:

$$\Psi = W \exp(-\eta) / (|n \cdot \Omega| \cdot A). \quad (1)$$

where Ψ : contribution to the fluence per collision,

W : weight of the particle,

η : length in mean-free-path unit between the collision site and crossing point,

Ω : unit direction vector of the particle,

n : unit vector normal to the surface at the point where the particle crosses,

A : area of the detector.

The difficulty with this type of estimation is that if a particle crosses the surface at a grazing angle, $|n \cdot \Omega| \rightarrow 0$, a very large contribution to the fluence is encountered, $\Psi \rightarrow \infty$. Accordingly, a linear fluence variation was assumed in the range up to 0.01 in $|n \cdot \Omega|$. If $|n \cdot \Omega| < 0.01$, the value of 0.005 was assigned for $|n \cdot \Omega|$.

Due to introduction of Eq. (1) with the above advantages, a reduction in the FSDs is expected even if the estimator is set in a shield, and also correct scoring is possible for the tightly collimated source neutrons as the ORNL experiment. Accordingly, instead of the point detector estimator, the NESX estimator was newly incorporated in the subroutine TALLYD of the MCNP code.

(b) Weight Window Importance Sampling

As the ASPIS and ORNL benchmark experiments were typical deep penetration problems in the iron shields, the Weight Window Importance Sampling was employed so as to reduce the FSDs in the MCNP calculations.

To determine the Weight Window Importance parameters with an empirical formula, the thick iron shield was divided finely, i.e., each divided iron cell was 10-cm thick, and also the energy region was divided into three intervals, i.e., $0.005 \text{ MeV} < E_n \leq 0.0075 \text{ MeV}$, $0.0075 \text{ MeV} < E_n \leq 0.72 \text{ MeV}$, and $0.72 \text{ MeV} < E_n \leq 14.5 \text{ MeV}$. Those boundary energies were determined as follows:

- (i) 0.0075 MeV = the lowest limit of the measured energy spectra,
- (ii) 0.72 MeV = as shown in **Figs. 3.2-11** and **3.2-12**, energy spectra in the iron slabs drop rapidly above 0.72 MeV ,
- (iii) 14.5 MeV = the maximum energy of fission neutrons from ^{235}U .

The Weight Window Importance in each divided cell was obtained from the following empirical formula newly introduced in this study:

$$W_m = W_0 \cdot f^{m-1}. \quad (2)$$

where W_m : lower weight bound in the m -th cell,

W_0 : initial value of the weight bound,

f : a factor of which depends on the energy, material and thickness.

In the present two iron benchmark calculations, parameter f in Eq. (2) was determined based on the iron neutron dose-rate attenuation experiments summarized in **Fig. 3.2-3**. The following values were actually employed:

- (i) $0.005 \text{ MeV} < E_n \leq 0.0075 \text{ MeV}$: $W_0 = 0.64$, $f = 0.75$,
- (ii) $0.075 \text{ MeV} < E_n \leq 0.72 \text{ MeV}$: $W_0 = 0.31$, $f = 0.6$,
- (iii) $0.72 \text{ MeV} < E_n \leq 14.5 \text{ MeV}$: $W_0 = 0.13$, $f = 0.5$.

As shown in **Fig. 3.2-3**, the neutron dose rate of ^{252}Cf source attenuates by a factor of 0.5 in an iron slab 10-cm thick. The average neutron energy of ^{252}Cf is approximately 2.35 MeV.

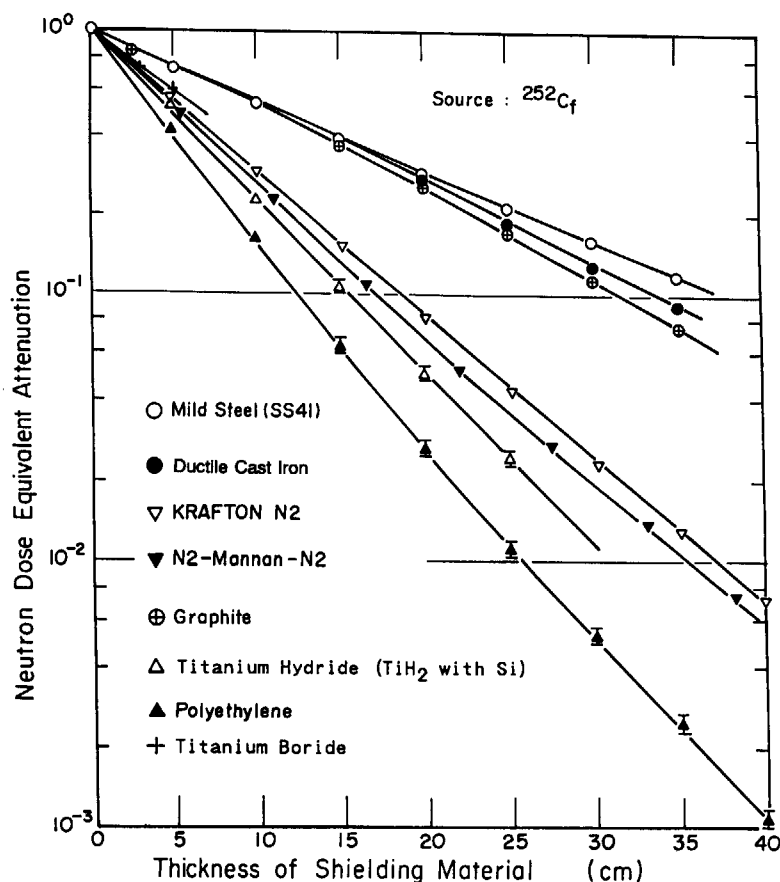


Fig. 3.2-3 Neutron dose equivalent attenuation characteristics for various materials

3.2.3 Results

3.2.3.1 Results by DOT Calculation

To test the applicability of the JENDL-3 data, the JENDL-3T, JENDL-3PR1 and ENDF/B-IV data were also used for comparisons.

1) Analysis for axial attenuation measurements

Measurements were made for the following 4 detectors.

Table 3.2-1 Reactions used in axial attenuation profile measurements

Sensitive energy range	Reactions	Cross-section data
Resonance detector (epi-thermal)	Au(n, γ) Cd covered	\langle ENDF/B-V MAT=1379 \rangle
Threshold detector	Rh-103(n, n')Rh-103m In-115(n, n')In-115m S-32(n, p)P-32	\langle IRDF-82 MAT=4520 \rangle \langle ENDF/B-V MAT=6437 \rangle \langle ENDF/B-V MAT=6439 \rangle

Detector cross sections used in the calculation are shown in the last column of the table listed above. As for the Au detector, self-shielding and Cd covered effects should be taken into account. Self shielding correction of the foil (thickness: 0.052 mm) was made with the Bethe's method⁴⁰⁾. The Cd-covered effect is also considered. Cross-section curves of threshold detectors used in the analysis are shown in Fig. 3.2-4 together with the sensitive energy range of each detector for shallow (6 cm) and deep penetration (64 cm) case.

The results are given in Figs. 3.2-5 and 3.2-6. In the latter figure, C/E values (i.e., ratio of

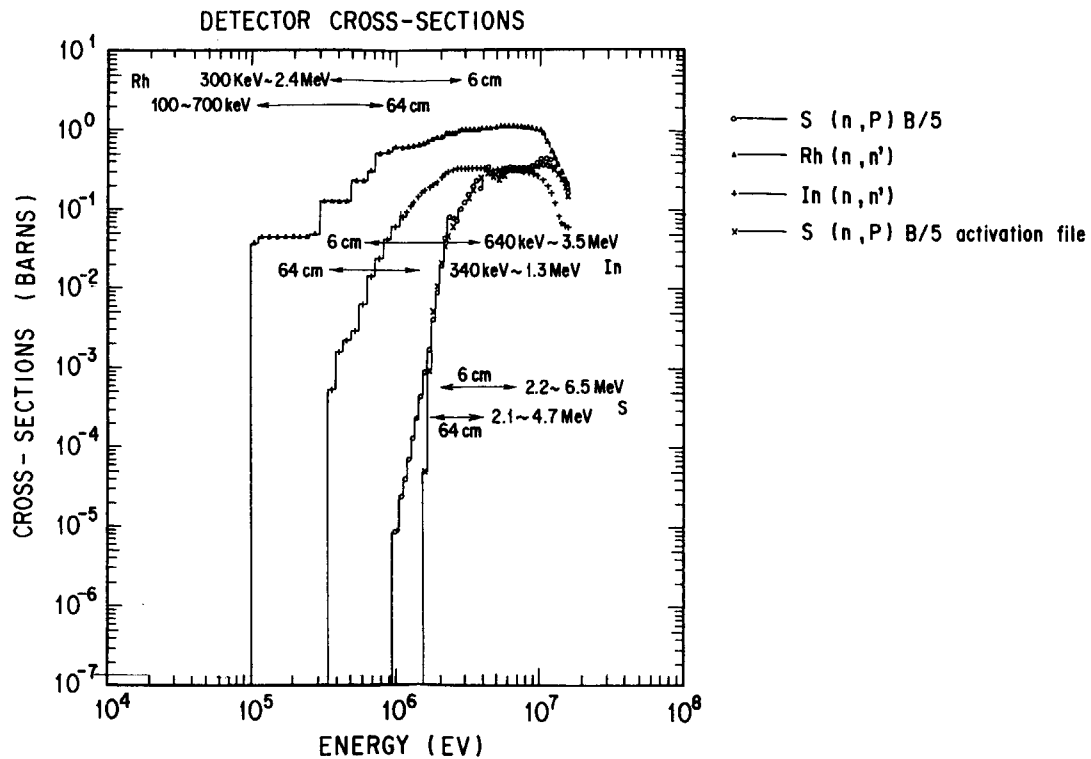


Fig. 3.2-4 Detector cross section used in the analysis
(group averaged data in the BERMUDA-121 group structures and the sensitive energy ranges to each detector for the reaction rate in the attenuation profile calculation)

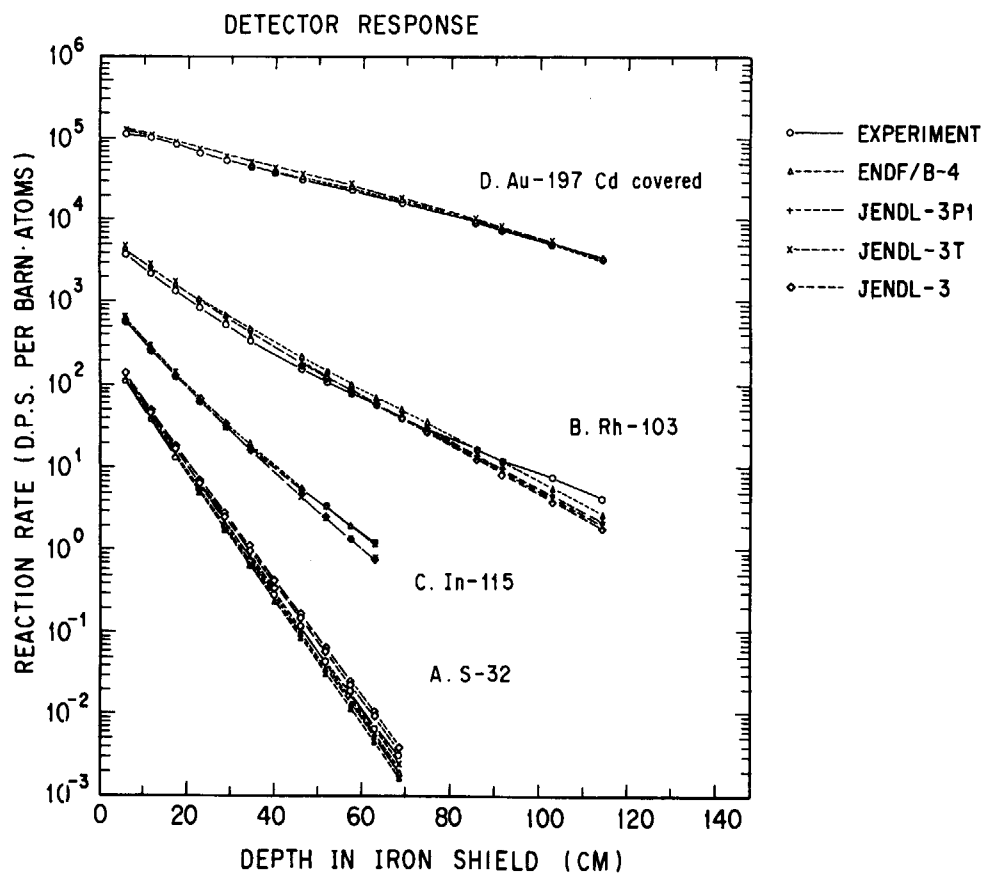


Fig. 3.2-5 Comparison of the measured and calculated reaction rate attenuation profiles along the main axis

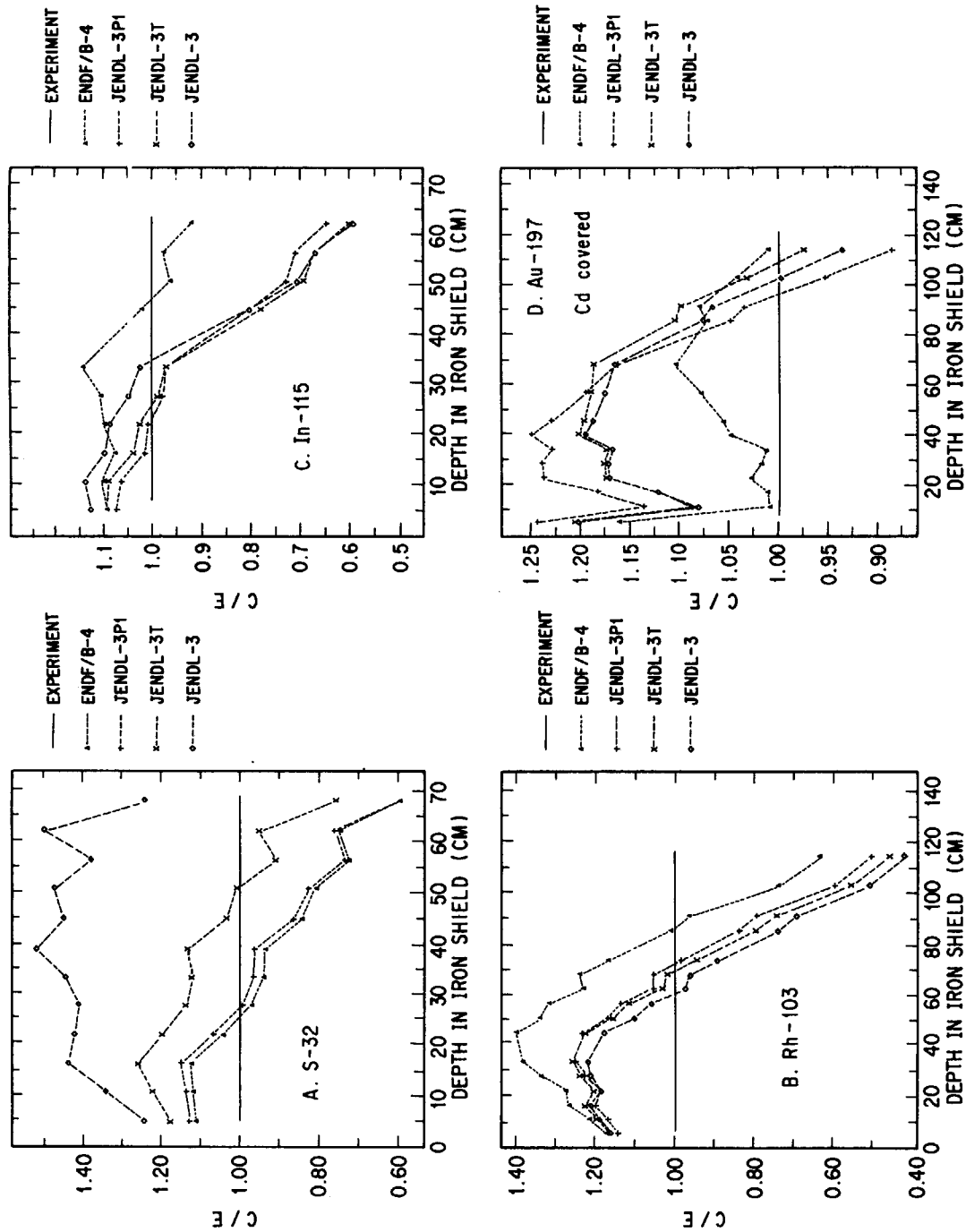


Fig. 3.2-6 Comparison of C/E values for the reaction rate attenuation profile along the main axis

calculation to experiment) are plotted. From **Fig. 3.2-5**, in general all results show a good agreement for the axial attenuation profiles. However, in **Fig. 3.2-6**, for some detectors differences are clearly seen between the results from the JENDL evaluations (JENDL-3, JENDL-3T or -3PR1) and ENDF/B-IV. It reflects the differences of the cross sections of natural iron.

The C/E values for each detector can be summarized as follows.

Table 3.2-2 Summary of C/E values for the axial attenuation profile

Detector cross section	Library			
	JENDL-3	JENDL-3T	JENDL-3PR1	ENDF/B-IV
Au(n, γ) Cd covered	1.2 - 0.9	1.2 - 1.0	1.2 - 0.9	1.1 - 1.0
Rh-103(n, n')Rh-103m	1.2 - 0.4	1.2 - 0.5	1.2 - 0.5	1.4 - 0.6
In-115(n, n')In-115m	1.1 - 0.6	1.1 - 0.6	1.1 - 0.6	1.1 - 0.9
S-32(n, p)P-32	1.5 - 1.2	1.3 - 0.8	1.1 - 0.6	1.1 - 0.6

(a) S-32

The same tendency is observed both for ENDF/B-IV and JENDL-3PR1, i.e., C/E values are greatly underestimated along with the penetration depth. However, for JENDL-3T, the declining tendency with a penetration depth is a little bit cured. In JENDL-3, this tendency is completely changed. No declining tendency along with penetration depth is observed with JENDL-3, but the C/E value is overestimated by 40%.

As seen from **Fig. 3.2-4**, this reaction is very sensitive of high energy spectra, from 2.0 MeV to 5.0 MeV. This suggests that the inelastic scattering cross-section of this energy range, which greatly contributes to the formation of the spectra, is too high in ENDF/B-IV and JENDL-3PR1. Most of the neutrons generated in this energy range are slowed down by these high inelastic scattering. For JENDL-3T, inelastic scattering cross section was only slightly changed so as to reduce the discrepancy. In JENDL-3, the latest version of JENDL, 2 to 4 MeV inelastic scattering cross section is changed considerably from the previous version of JENDL-3T. Thus, an amazing change in the C/E profile is brought out. From the results, however, the modification seems to be overdue.

(b) Rh-103

This detector is sensitive to rather low energy spectrum parts among the threshold detectors used in the experiments. C/E behaviors for all of the evaluated cross sections are nearly the same, and no special data problems need to be revised are pointed out.

(c) In-115

A clear difference is observed between ENDF/B-IV and JENDL (JENDL-3, JENDL-3T and JENDL-3PR1). C/E of ENDF/B-IV is almost flat along with the penetration depth, but the JENDL profile is underestimated. In the energy range from 600 keV to 1.2 MeV, there is no clear difference in the total cross section, but in the elastic and inelastic scattering cross sections some differences are found.

From this fact, it seems that this underestimation is related to the partitioning of scattering cross-sections between elastic and inelastic scattering. This explanation is also supported by the results of the spectrum measurements described afterward.

(d) Au-197 Cd covered

This is the only one resonance detector used in the measurements. Sensitivity to this detector is attributed to only a few Au resonances in the low energies, especially the enormously giant 4.9 eV resonance. As seen from **Fig. 3.2-6**, the C/E value of ENDF/B-IV data shows good results with no clear tendency being seen with the penetration depth. On the other hand, the JENDL-3T and -3PR1 results have a tendency of underestimation with the penetration depth.

2) Flux spectrometer measurements

Comprehensive spectrometer measurements at four selected positions within the iron shield were made, and measured spectra were obtained from unfolding of all these data using the RADAK code.

The results can be shown in **Fig. 3.2-7** to **Fig. 3.2-10**. In each figure, a comparison between experimental and calculated fluxes, and C/E values are shown.

Over-all agreements are rather good in these figures. For shallow penetration (22.8 cm), all calculations overestimate, and underestimation proceeds with the penetration depth but not to a large degree.

For the JENDL (JENDL-3, -3T and -3PR1) data, as mentioned in the In-115 axial attenuation measurement, a clear difference in fluxes from 600 keV to 1.2 MeV are found. Especially the C/E values of JENDL in this energy range are considerably lower than that of ENDF/B-IV (see **Fig. 3.2-8**). This is attributable to the partial assignments between inelastic and elastic scattering cross sections of iron. Reevaluation for the JENDL-3 data are required from this viewpoint.

On the other hand, the agreement by the JENDL evaluations in the energy range of the 24-keV window is much more superior to ENDF/B-IV data (see **Figs. 3.2-8** through **3.2-10**). The window which indicates a wide valley of iron total cross section below the 27-keV resonance is predicted as an interference between the potential scattering and the s-wave resonance at 27 keV. So, the good result for spectrum means the evaluation of resonance parameters of JENDL-3, -3T and -3PR1 is better than ENDF/B-IV.

For deep penetration, underestimation of fluxes in the MeV range (2-5 MeV) appeared in all evaluations except for JENDL-3, i.e., JENDL-3T, -3PR1 and ENDF/B-IV (**Figs. 3.2-8** to **3.2-10**), suggests that the inelastic cross section in this energy range is rather high. This conclusion is also supported by the S-32 axial attenuation measurements results as described above. In JENDL-3, considerable improvements have been made for this 2 to 4 MeV energy range. Spectrum by JENDL-3 is about twice larger than the others as seen in **Fig. 3.2-8**.

3.2.4 Summary

3.2.4.1 Discussion of DOT3.5 results

From this study, applicability of JENDL-3 natural iron data for deep penetration in the shielding calculation is confirmed, as seen in the calculation of transmitted spectra at several depths and in the prediction of the calculated axial attenuation profiles. The obtained observations are: The agreement between calculation and experiment in the spectrum in the energy range including the 24-keV window is superior for the JENDL evaluation, it means the evaluation of the resonance parameters is very good for JENDL-3. From the evidence of C/E profiles in the In-115 reaction rates and the measured spectrum, some problems still remain in the assignments between elastic and inelastic scattering cross section in 600 keV to 1.2 MeV.

From the axial attenuation profile of S-32 and the spectrum, JENDL-3 provides stable results against the penetration depth than ENDF/B-IV or older versions of JENDL-3. The declining tendency along with the penetration depth is solved but modification seems to be too much. Inelastic scattering cross-section still seems to be checked for any of the evaluations. A further check is necessary.

From the attenuation profile of Au, the results by JENDL-3 or 3T are improved a little compared to that of JENDL-3PR1 but it does not yet reach to the level by ENDF/B-IV. Still some problems remain.

It is true that the flux underestimation in the unresolved resonance region comes from not only cross section uncertainties but also the multi-group approximation of shielding calculation. However, in the present work, the latter effect appears only in the neutron spectra in the limited energy range around 1 MeV, still more, at deep penetration position (see **Fig. 3.2-10**). Then, the similar observation was obtained in the MCNP results as follows.

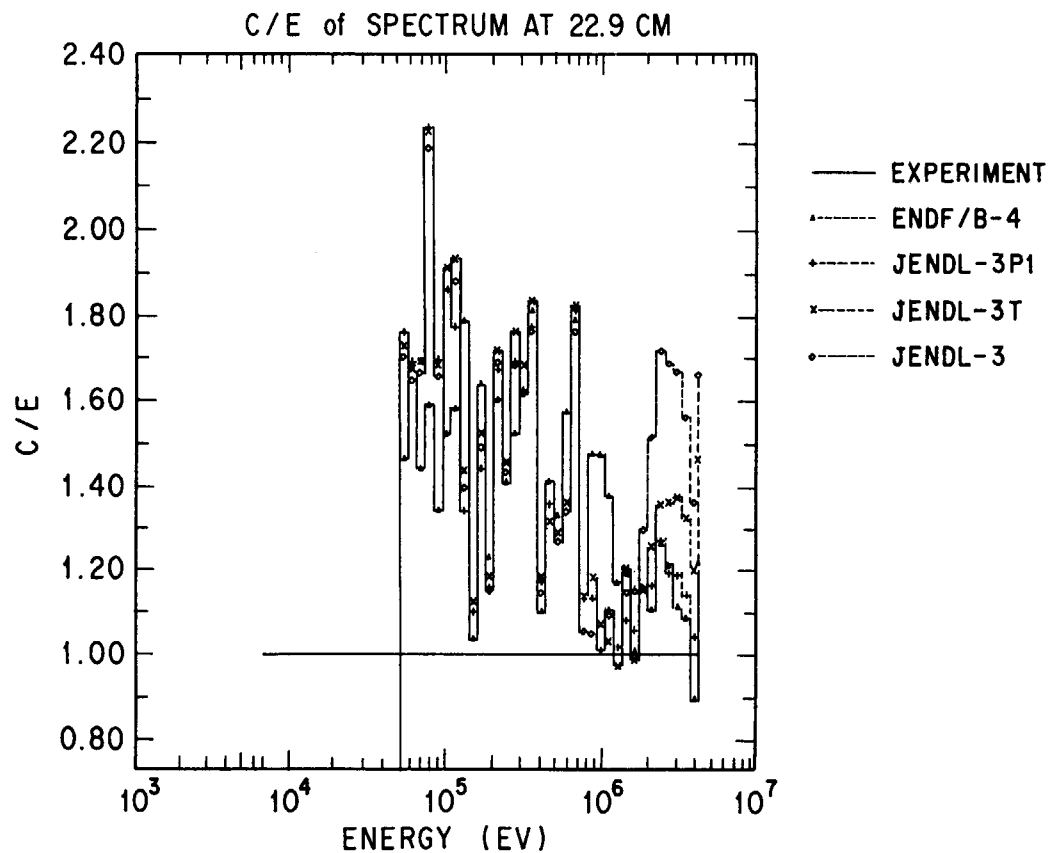
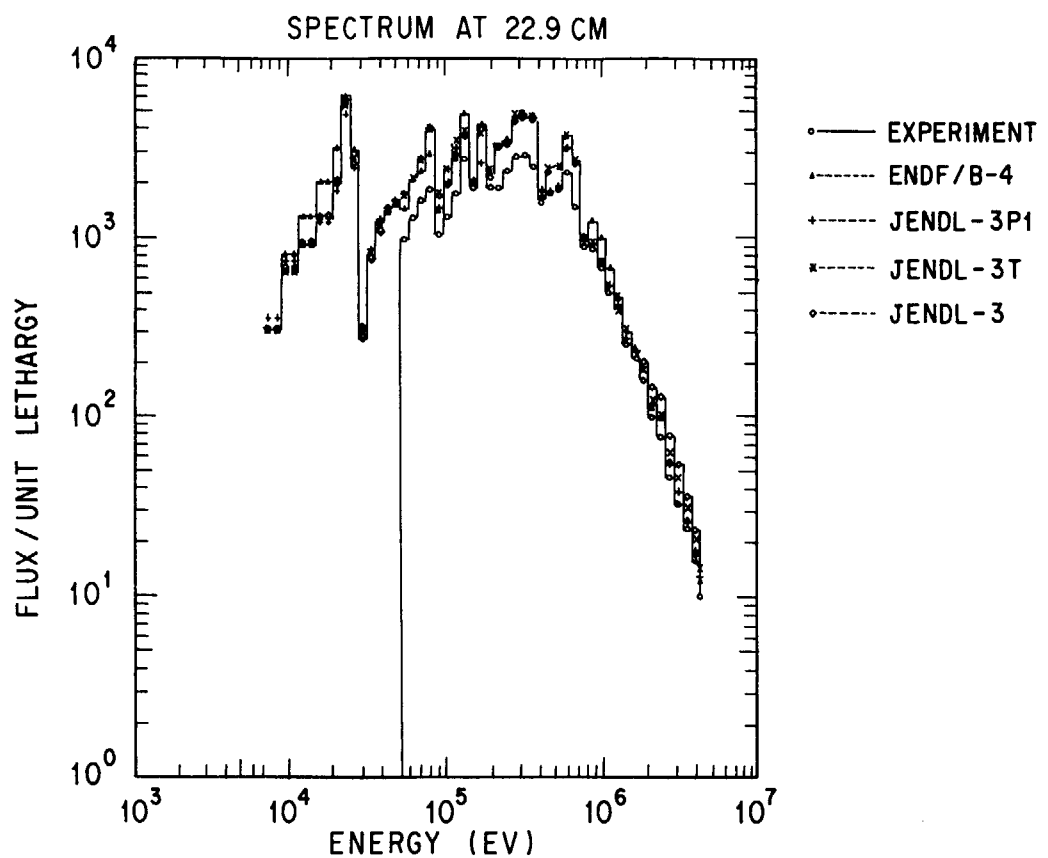


Fig. 3.2-7 Comparison of calculated flux profiles with the RADAK unfolded spectrum measurement and C/E values at the 22.9 cm position

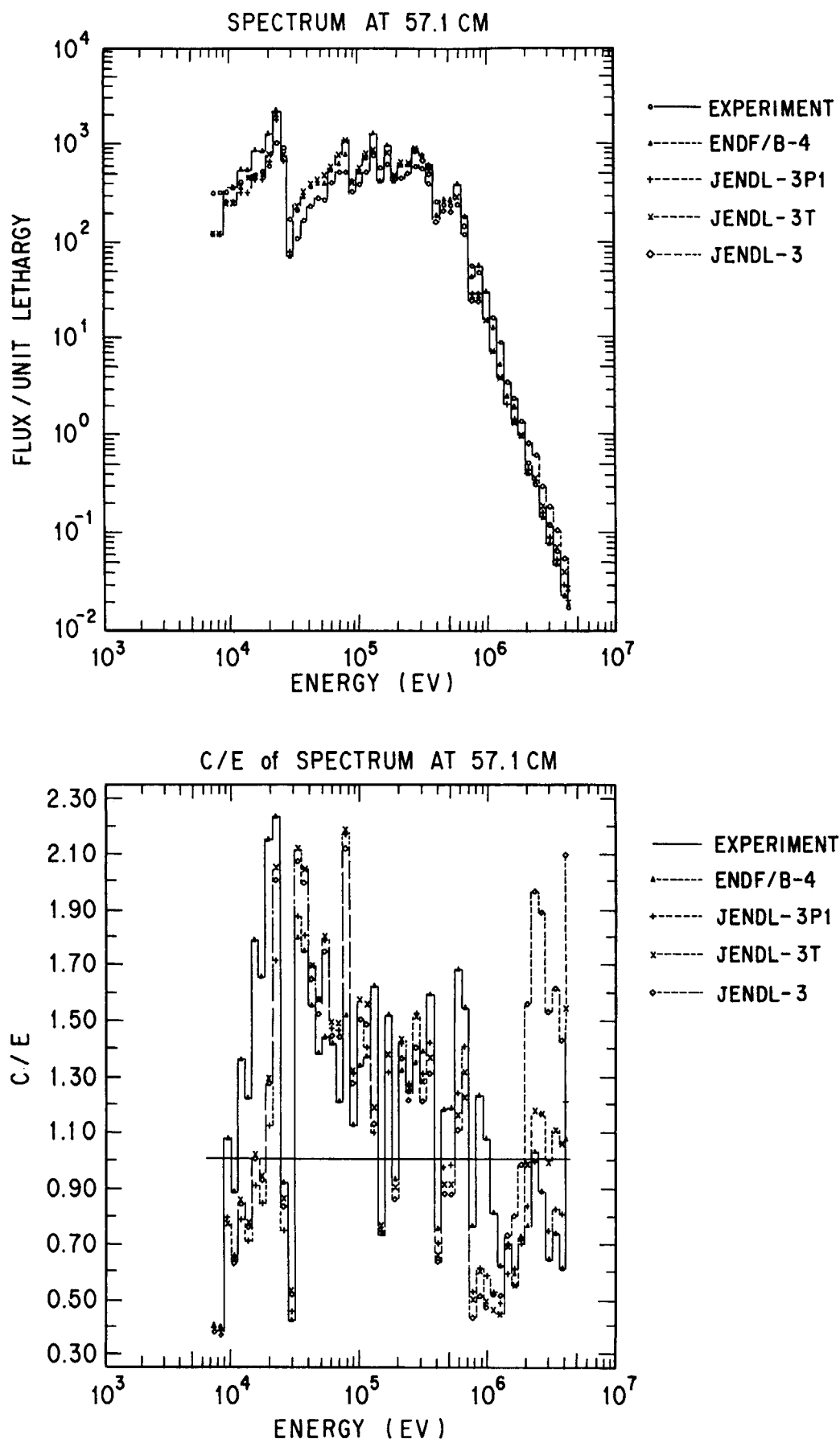


Fig. 3.2-8 Comparison of calculated flux profiles with the RADAK unfolded spectrum measurement and C/E values at the 57.1 cm position

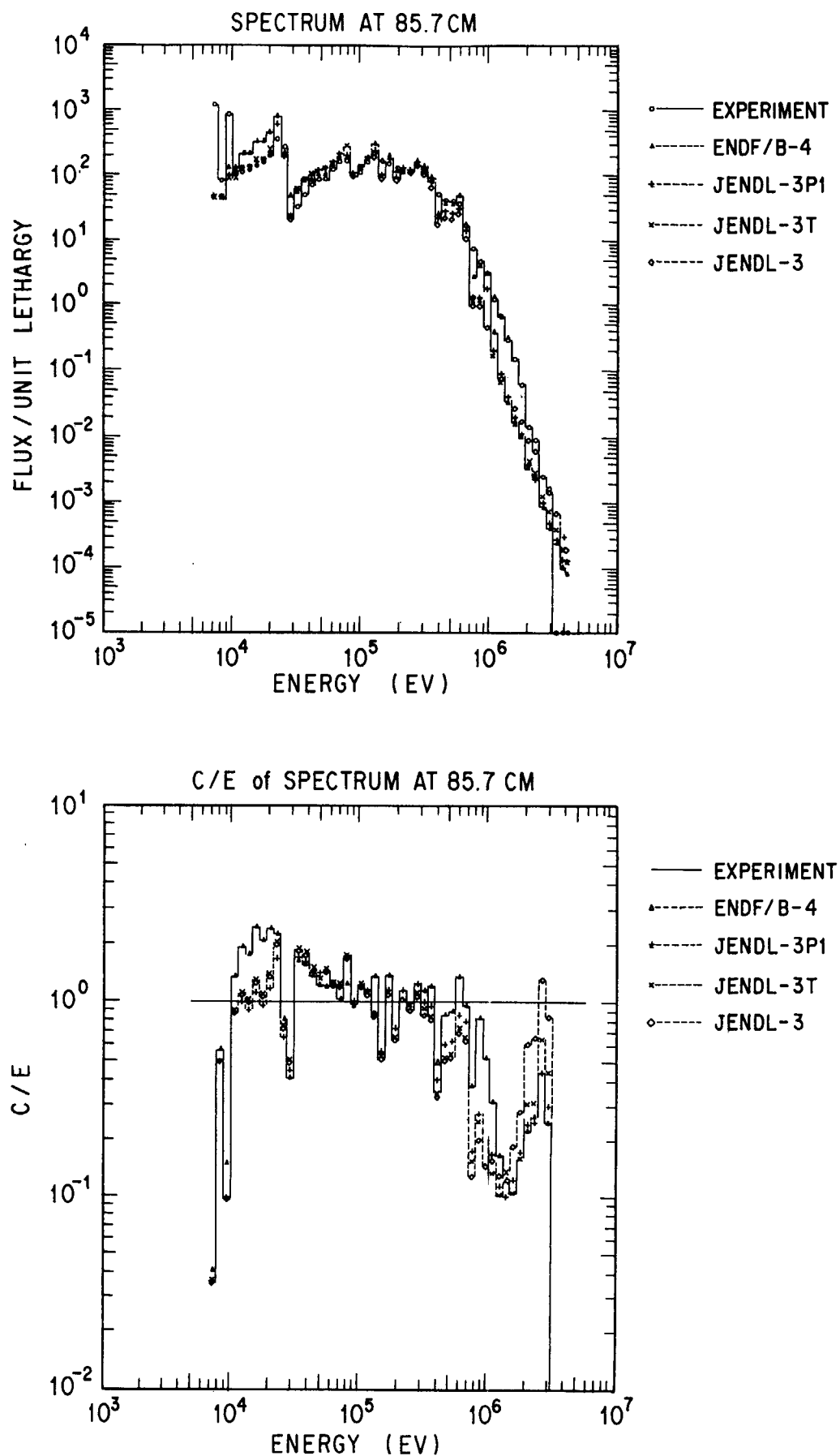


Fig. 3.2-9 Comparison of calculated flux profiles with the RADAK unfolded spectrum measurement and C/E values at the 85.7 cm position

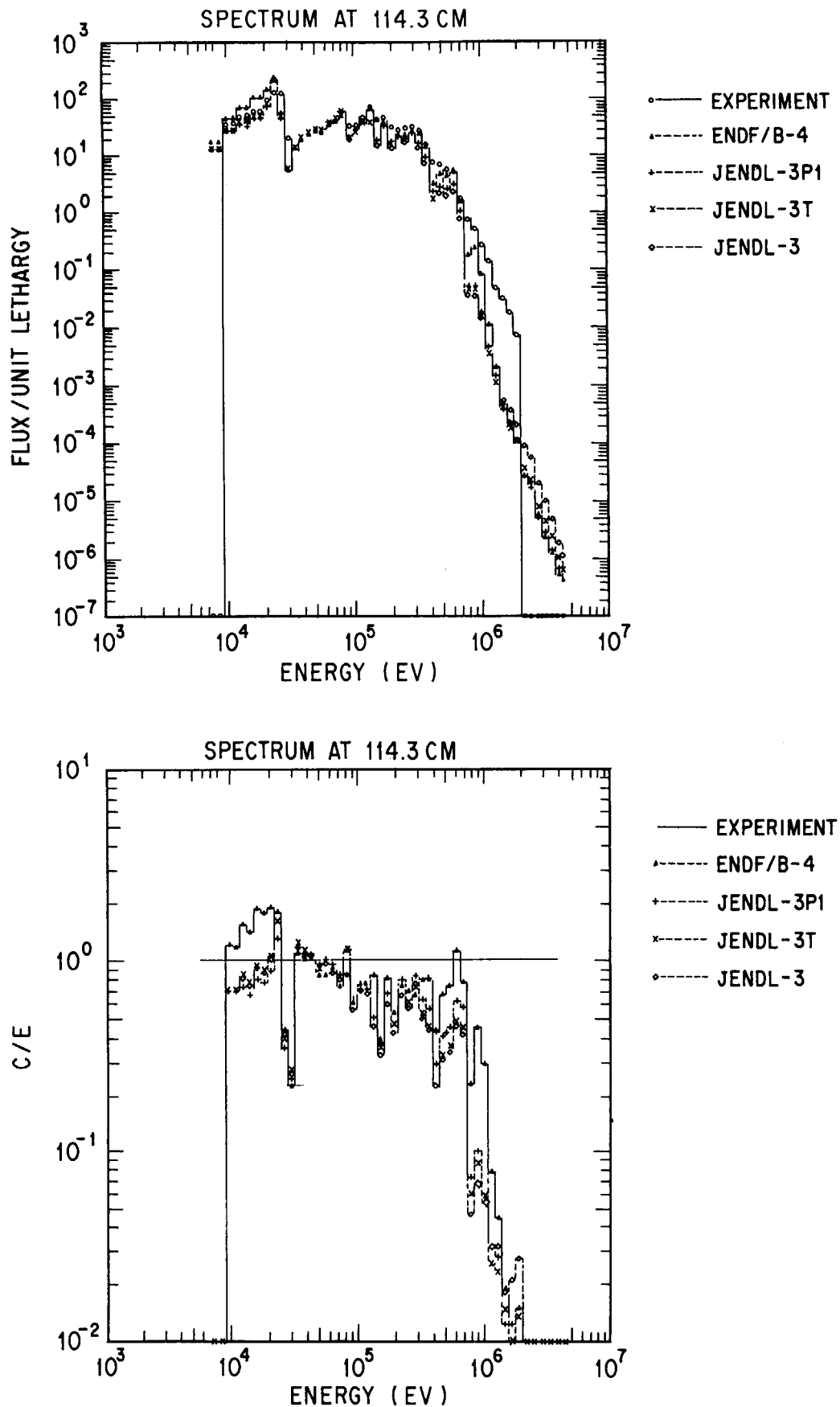


Fig. 3.2-10 Comparison of calculated flux profiles with the RADAK unfolded spectrum measurement and C/E values at the 114.3 cm position

3.2.4.2 Discussion of MCNP results

The comparison of the neutron energy spectra between the MCNP calculations with JENDL-3 and ENDF/B-IV and the measurements at each depth from 22.14 to 113.98 cm in the iron slabs are shown in **Figs. 3.2-11 to 3.2-14**. The FSDs in each energy bin range from 0.02 to 0.15 in both calculations. The results are summarized as follows:

- (i) On the whole, the calculated energy spectra by the MCNP code with JENDL-3 and with ENDF/B-IV agree fairly well with the experiment over the wide energy region as shown in **Figs. 3.2-11 through 3.2-14**.
- (ii) Especially, the calculated energy spectra with JENDL-3 agree more very closely than those with ENDF/B-IV in the energy range including the iron 24-keV window, and the spectra calculated with both of libraries agree closely with the experiments between 100 and 800 keV at the 56.83-cm depth, between 100 and 400 keV at the 85.41-cm depth, and between 100 and 310 keV at the 113.98-cm depth.
- (iii) Meanwhile, the calculated spectra with JENDL-3 denote a slight overestimation in the energy range between the iron 27-keV resonance and 100 keV, and a very distinct underestimation is observed above 800 keV at the 85.41-cm depth and above 900 keV at the 113.98-cm depth, as seen in **Figs. 3.2-13 and 3.2-14**, respectively.
- (iv) The over-shooting of calculated spectra compared to the experiments is observed at the 27-keV resonance (showing a valley of spectrum) and around 24 keV (peak) in calculations, as shown in **Figs. 3.2-12 to 3.2-14**. It does not necessarily mean that the evaluated data are wrong, because one major probable reason of this discrepancy is attributed to the smearing effect due to limited experimental resolution.

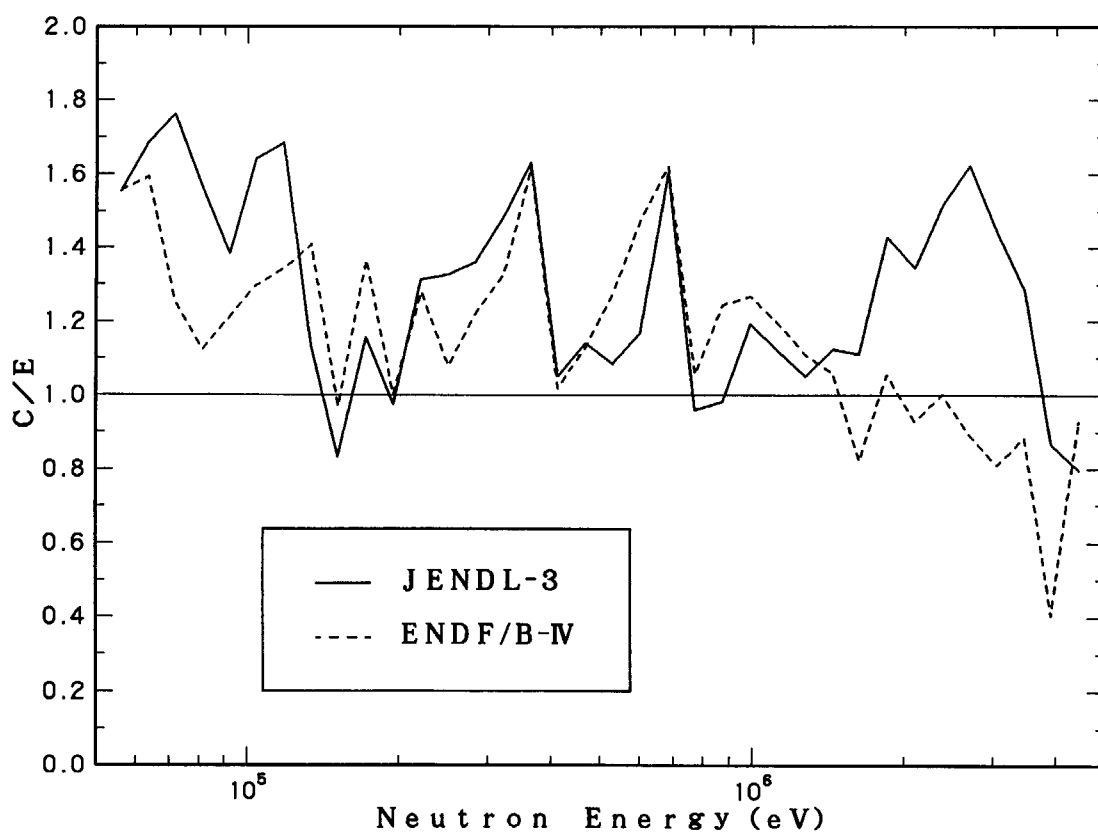
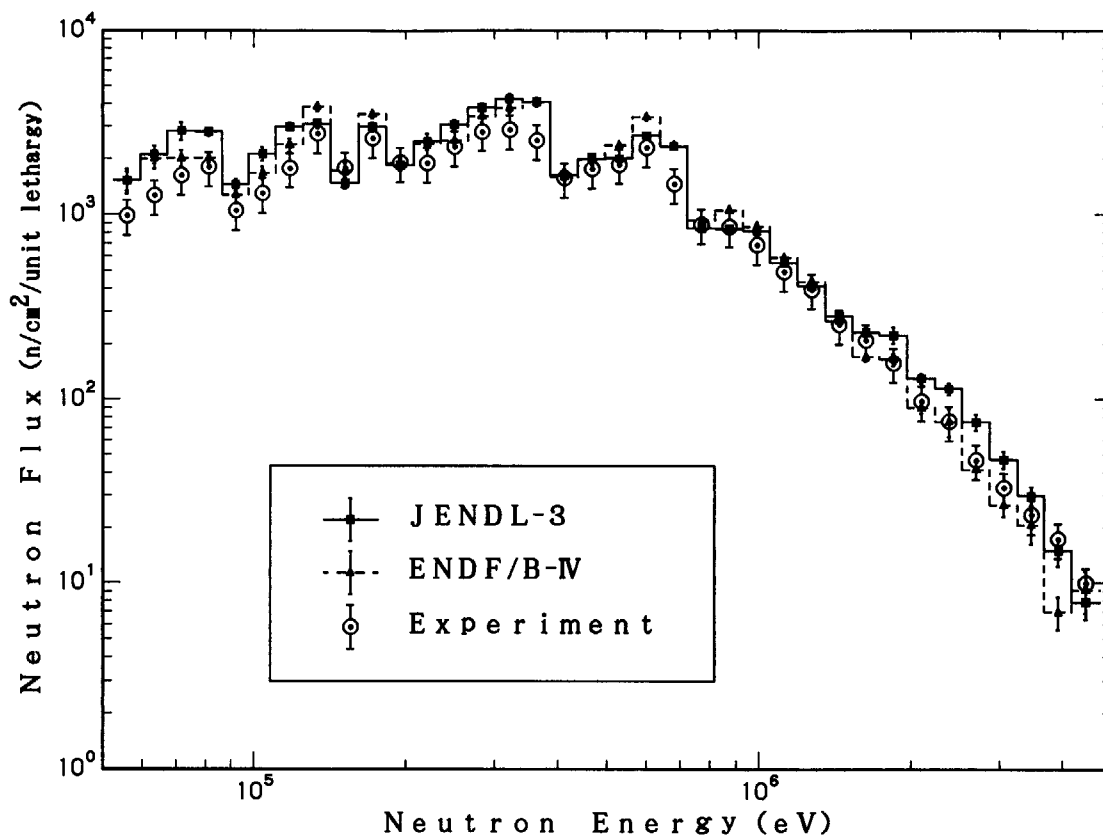


Fig. 3.2-11 Comparison of energy spectra between the MCNP calculation and measurement at the 22.54 cm depth in the shield and C/E values

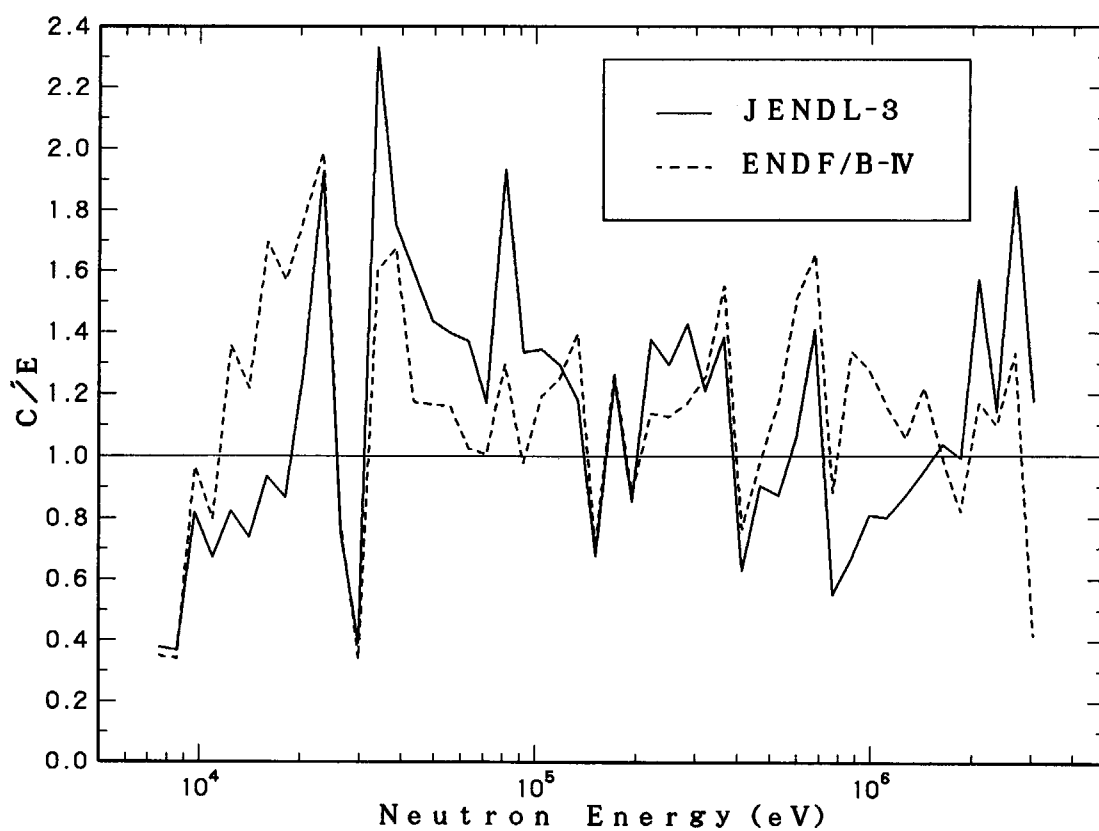
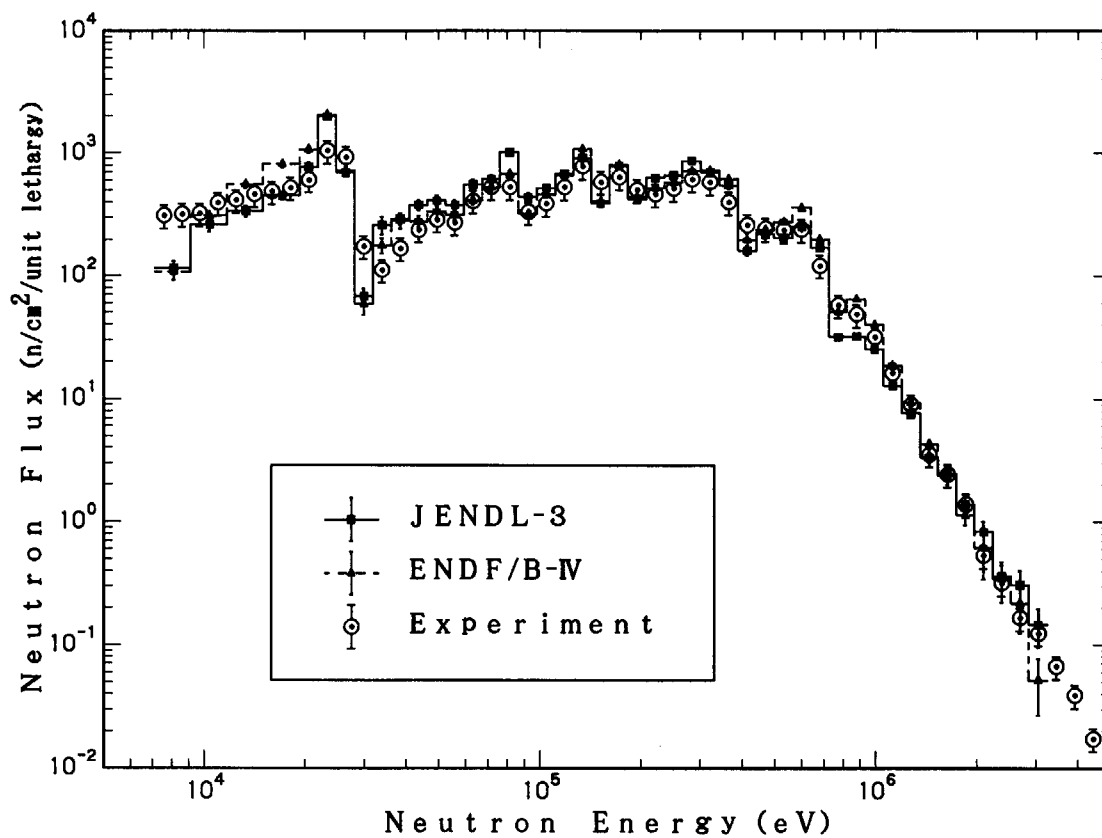


Fig. 3.2-12 Comparison of energy spectra between the MCNP calculation and measurement at the 56.83 cm depth in the shield and C/E values

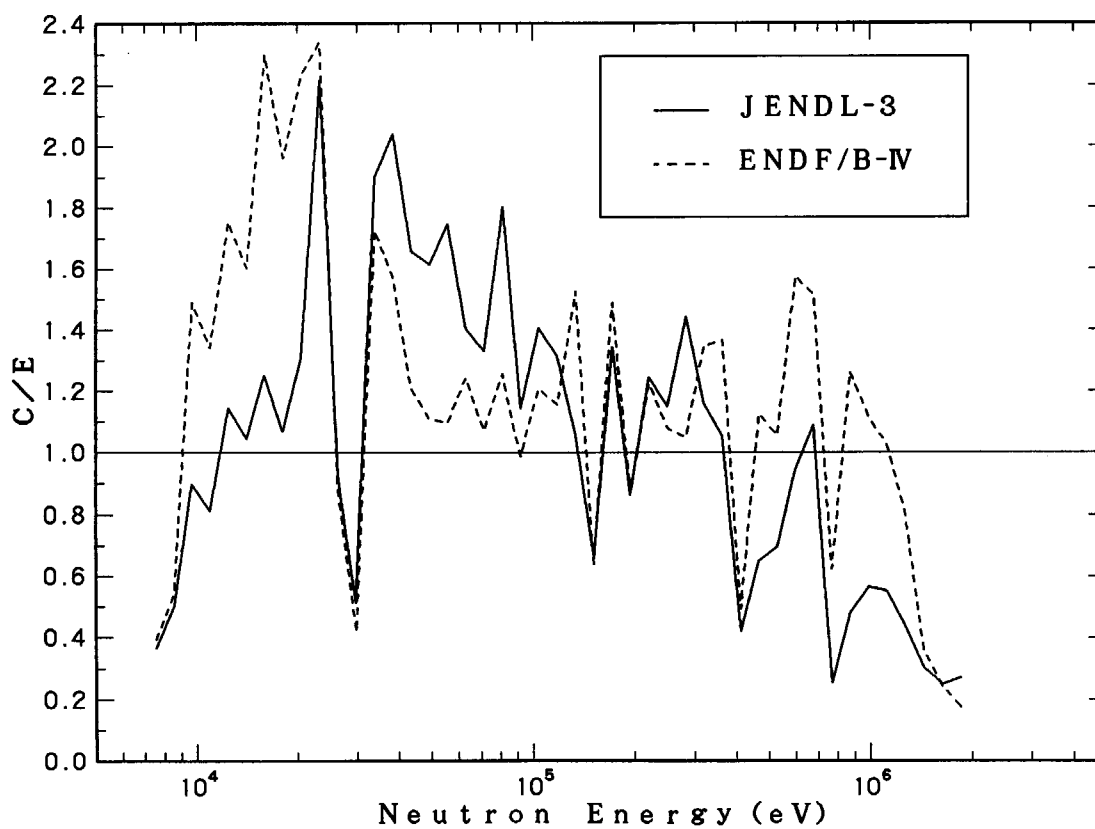
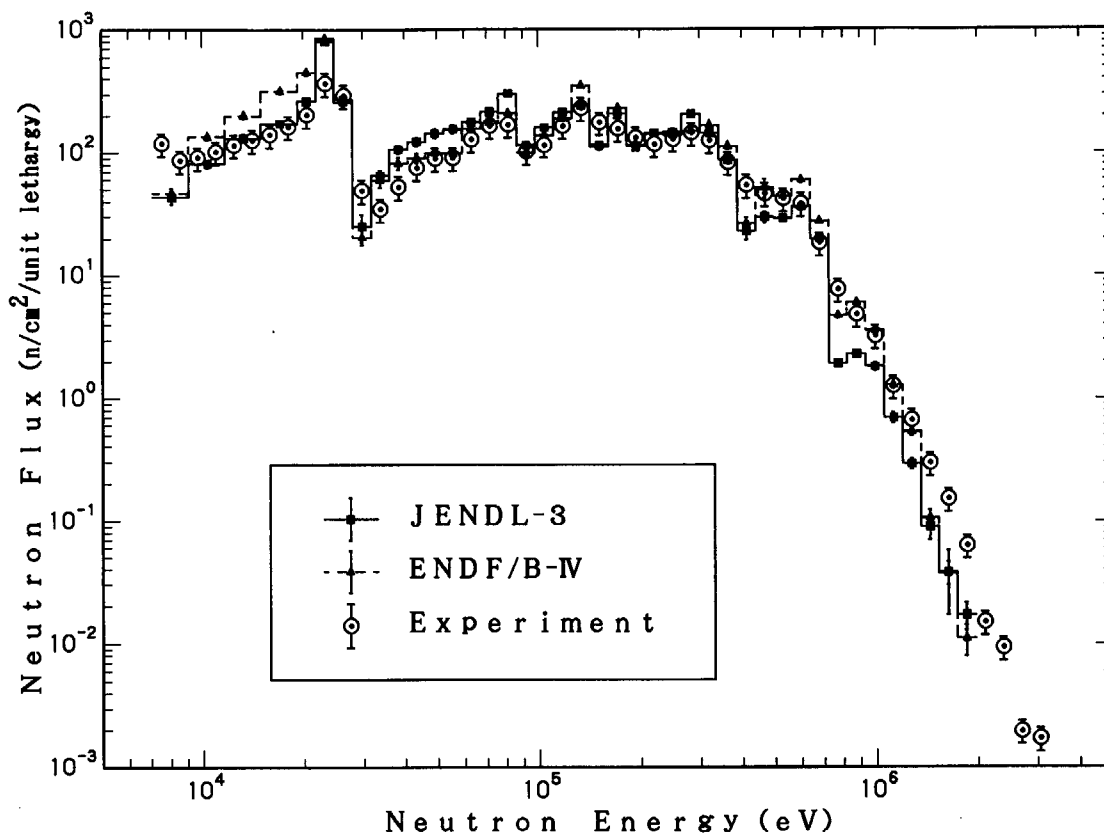


Fig. 3.2-13 Comparison of energy spectra between the MCNP calculation and measurement at the 85.41 cm depth in the shield and C/E values

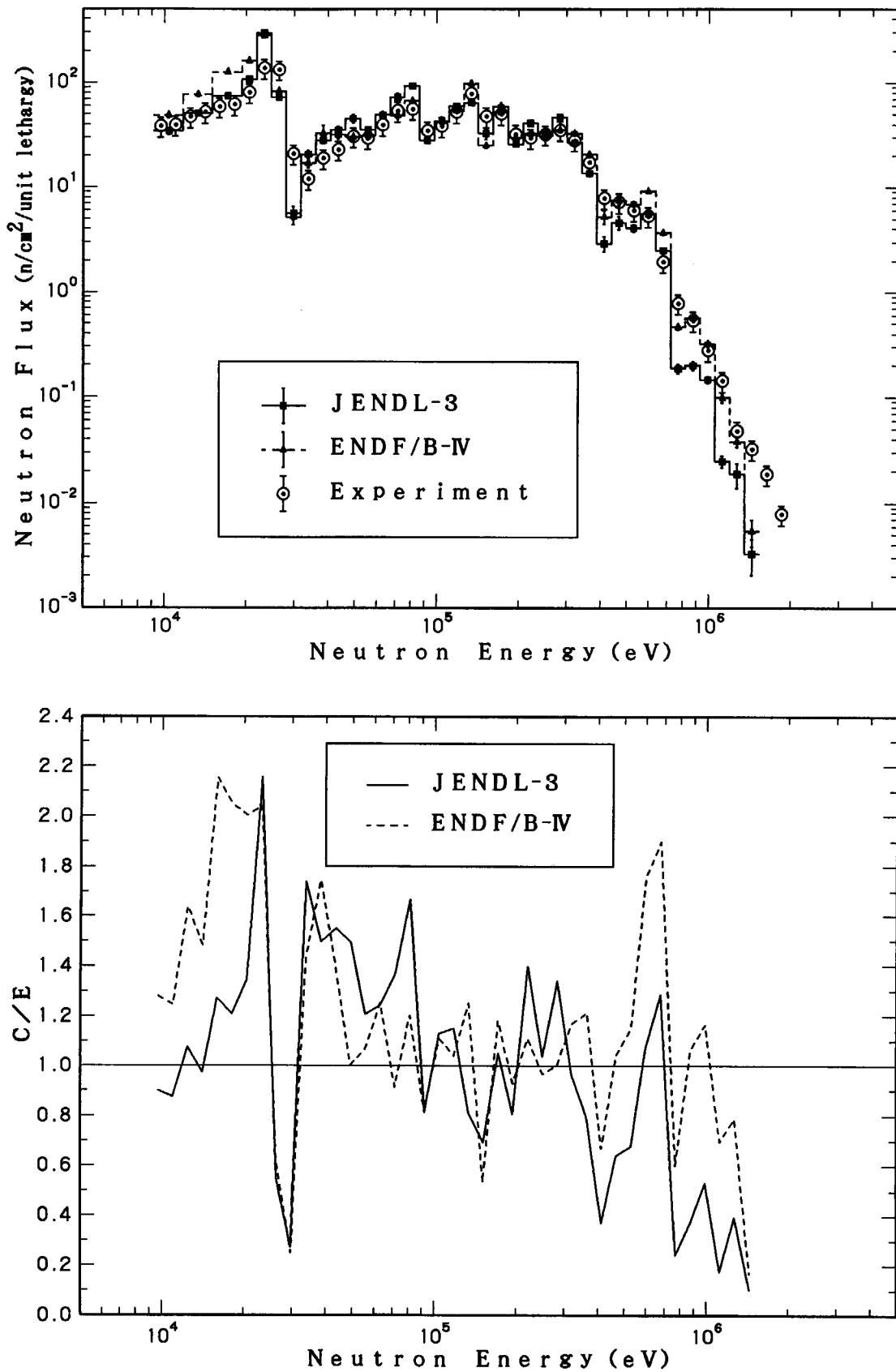


Fig. 3.2-14 Comparison of energy spectra between the MCNP calculation and measurement at the 113.98 cm depth in the shield and C/E values

3.3 ORNL Iron and Stainless Steel Experiments

3.3.1 Outline of Experiments

A series of deep-penetration neutron transmission measurements through iron slabs up to 36 in. thick and stainless steel slabs up to 18 in. thick was performed at the Tower Shielding Facility (TSF) of ORNL using a collimated beam from the reactor neutrons as the source³⁾. These measurements were made at various positions behind 60-in. square slabs, so that the effects of side leakage of neutrons were negligible even for a 36-in. thick sample of iron, since the beam was tightly collimated.

Figure 3.3-1 shows a schematic of the experimental geometry for the thickest sample. This collimator was used for all the measurements except those made behind 18 in. of stainless steel. The measurements behind 18 in. stainless steel were made using the reactor collimator shown in **Fig. 3.3-2**.

The thickness, density and composition of the individual slabs used in the experiment were accurately determined. The density of Type-304 stainless steel slabs was averaged at 7.86 grams/cm³ and that of iron slabs averaged at 7.79 grams/cm³. The average composition of the slabs is shown in **Table 3.3-1**.

Detailed measurements for the transmitted neutron energy spectra were made behind 12-in.-thick iron and 18-in.-thick stainless steel, covering the energy range above 80 keV, by using two types of spectrometers as follows:

- a) NE-213 scintillator, which determined energy spectra in the energy range between 800 keV and 15 MeV,
- b) Benjamin proton recoil spectrometer which determined energy spectra in the energy range between 80 keV and 1.5 MeV.

A set of three spherical BF₃ detectors surrounded by various thicknesses of polyethylene (0.5 to 4 in.) and an outside shell of cadmium was also used to obtain integral flux measurements behind iron and stainless steel. These "Bonner ball" detectors have response functions which peak in a different range in neutron energy. The descriptions of each Bonner ball are given in **Table 3.3-2**.

These measurements show that the tightly collimated source could be represented as a virtual point

Table 3.3-1 Composition of the slabs in atoms/barn-cm

Nuclide	Iron Slabs	Stainless Steel Slabs
Carbon	9.815×10^{-4}	—
Manganese	5.150×10^{-4}	1.14×10^{-3}
Iron	8.372×10^{-2}	5.995×10^{-2}
Chromium	—	1.686×10^{-2}
Nickel	—	7.90×10^{-3}

Table 3.3-2 Bonner ball description

Standard Bonner Ball Designation	Polyethylene Thickness (inch)	Polyethylene Density (grams/cm ³)	Diameter of Ball (inch)	Displacement of Center of Detection from Geometric Center (inch)*
3	0.515	0.951	3.09	0.9
6	1.91	0.925	5.88	1.8
10	3.90	0.951	9.86	3.0

* The detection of this displacement is toward the center of gravity of the hemispherical surface upon which the neutrons are incident.

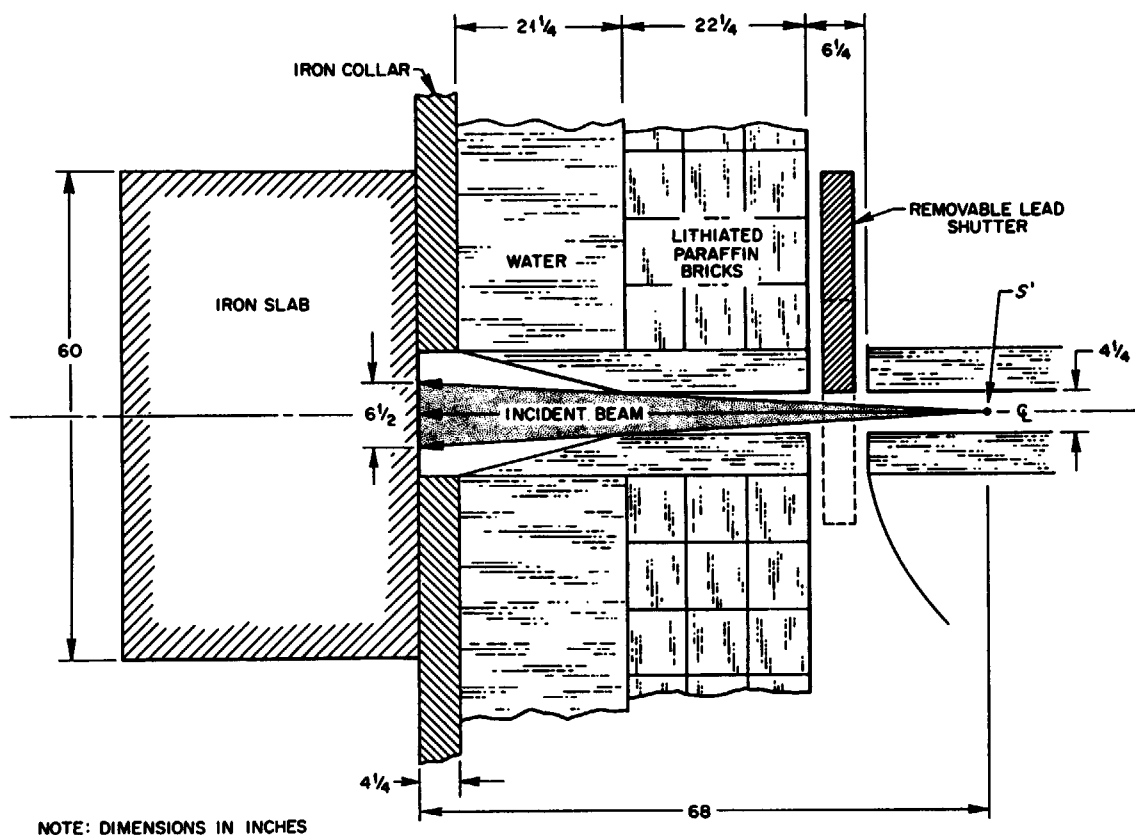


Fig. 3.3-1 Experimental configuration for the 4-1/4-in.-dia. collimator used for the measurements made behind iron slabs and 12-in.-thick stainless steel³⁾

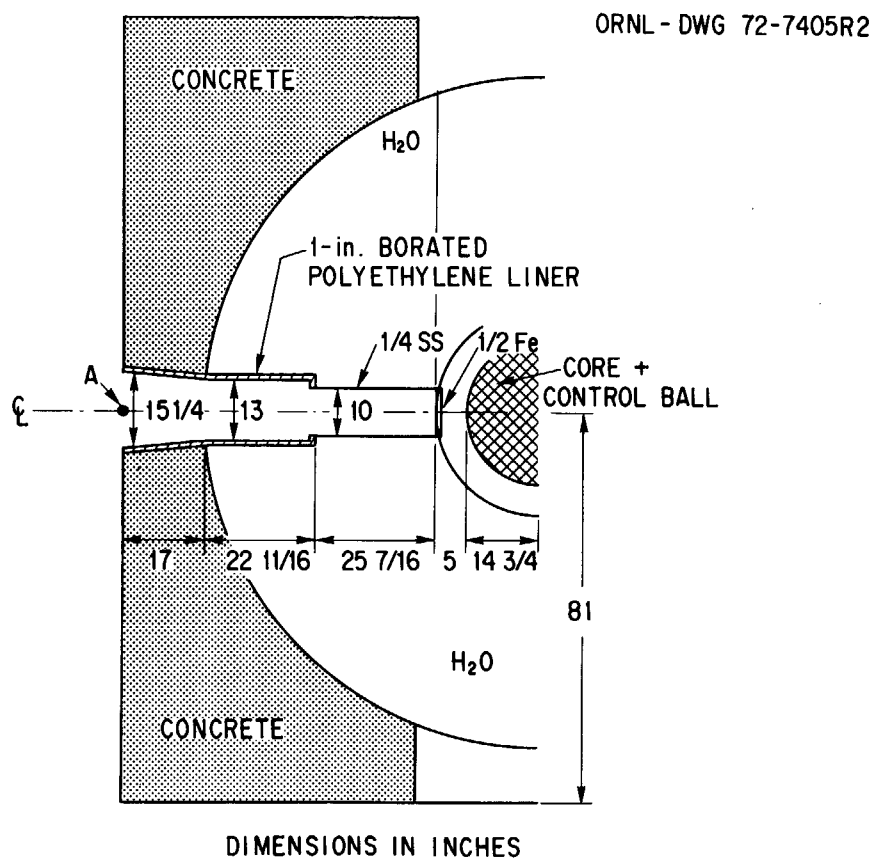


Fig. 3.3-2 Experimental configuration for the 15-1/4-in.-dia. collimator used for the measurements made behind 18-in.-thick stainless steel³⁾

anisotropic source located 68 in. inside the collimator from the edge of the iron collar (point S' shown in **Fig. 3.3-1**), with a uniform beam intensity over a diameter of about 6-1/2 in. at the mouth of the collimator and zero elsewhere.

The energy spectrum of source neutrons were absolutely determined by the spectrometer measurements for the centerline point located on the exit plane of the collimator as shown in **Fig. 3.3-3** for the energy region between 100 eV and 10 MeV. The accuracy of the incident spectrum was estimated to be within 10% above 200 keV and within 20% below 200 keV.

A summary of all the detector locations behind the iron and stainless steel slabs is shown in **Tables**

Table 3.3-3 Experimental configurations for the iron transmission measurements

Iron Slab Thickness (inch)	Detector Locations			Detector Type
	Centerline Distance Behind Slab (inch)	Radial Distance From Centerline (inch)	Observation Angle* with Respect to Centerline (degree)	
0.52	127	0	0	¹⁰ B Spectrometer
	123	33	15	
	90	90	45	
1.55	152	0	0	Bonner Balls
	146	39	15	
	107	107	45	
	126	0	0	¹⁰ B Spectrometer
	122	32.5	15	
	89	89	45	
4.05	158	42.5	15	NE-213 Spectrometer
	116	116	45	
6.06	162	0	0	NE-213 Spectrometer
12.13	141	0	0	Bonner Balls
	136	36.5	15	
	100	100	45	
	156	0	0	NE-213 Spectrometer
	150	40.5	15	
	110	110	45	
12.15	10	0	0	Benjamin Spectrometer
	10	12	50	
24.41	128	0	0	Bonner Balls
	124	33	15	
	90.5	90.5	45	
36.56	115	0	0	Bonner Balls
	111	30	15	
	81.5	81.5	45	

* The observation angle is defined as the angle between the centerline and the line connecting the detector and the midpoint of the emergent face of the slab. The vertex of this angle is the pivot point for the angular traverses.

Table 3.3-4 Experimental configurations for the stainless steel transmission measurements

Stainless Slab Thickness (inch)	Detector Locations			Detector Type
	Centerline Distance Behind Slab (inch)	Radial Distance From Centerline (inch)	Observation Angle* with Respect to Centerline (degree)	
12.17	141	0	0	Bonner Balls
	136	36.5	15	
	100	100	45	
	10	0	0	Benjamin Spectrometer
	10	12	50	
18.33 ⁺	12→140	0	0	Bonner Balls
	47.7	0	0	NE-213 Spectrometer
	12	0	0	Benjamin Spectrometer

* The observation angle is defined as the angle between the centerline and the line connecting the detector and the midpoint of the emergent face of the slab. The vertex of this angle is the pivot point for the angular traverses.

+ All measurements behind 18-in.-thick stainless steel were made using the collimator described in Fig. 3.3-2. The 3-in. and 6-in. Bonner balls were also of slightly different dimensions than those described in Table 3.3-2. See text.

3.3-3 and **3.3-4**, respectively. The Bonner ball positions were measured to the geometric center of each ball. For this collimator, the absolute spectrum at the point A in **Fig. 3.3-2** is approximately 7.4 times the spectrum shown in **Fig. 3.3-3**, with a virtual point source located 59.5 in. inside the collimator. This source spectrum is presented in a 100-group energy structure and can be readily interpolated to any other group structure. The 3- and 6-in. Bonner balls used behind the 18-in.-thick stainless steel were slightly different from those described in **Table 3.3-2**. The 3-in. Bonner ball has a polyethylene thickness of 0.47 in. and the 6-in. ball has a polyethylene thickness of 1.97 in. The density of the polyethylene is 0.951 grams/cm³ for both of 3-in. and 6-in. Bonner balls.

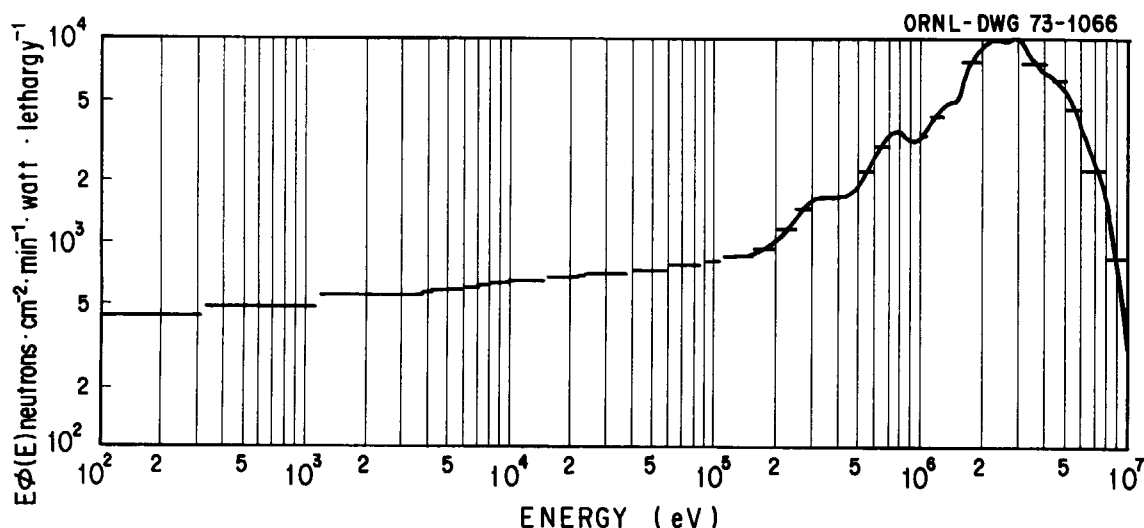


Fig. 3.3-3 Neutron beam source spectrum on the centerline at the outside edge of the 4-1/4-in.-dia. collimator

The effects of any transverse leakage combined with subsequent air and ground scattering were quantitatively measured for each foreground measurement by placing a thick hydrogenous shield about halfway between the detector and the back face of the slabs in such a way that neutrons leaking from the back face of the slabs could not reach the detector. These background neutrons were subtracted from all of the foreground measurements (i.e., measurements obtained in the absence of the hydrogenous shadow shield). It should be mentioned that the background estimated by the above procedure indicates an underestimation from the true background because of the neglect of subsequent air and ground scattering of neutrons which stopped in the additional shield of the background measurements, since the detectors have no collimator except for the ^{10}B spectrometer.

3.3.2 Calculation Method

3.3.2.1 Calculation method by DOT code

Seven geometries were analyzed for the iron slabs of 10.3 cm (4.05 in.), 30.8 cm (12.13 in.), 31.1 cm (12.25 in.), 62.0 cm (24.41 in.) and 92.9 cm (35.56 in.) thicknesses and for the stainless steel slabs of 30.9 cm (12.17 in.) and 46.6 cm (18.33 in.) thicknesses.

Figure 3.3-4 shows the R-Z calculational model for the five iron slabs in which the collimator was ignored. The iron slabs and collar were divided into 8 regions. The virtual point source was located at a distance of 172.72 cm from the surface of the iron slab.

Figures 3.3-5 and 3.3-6 show the R-Z calculational models for the stainless steel slabs of 30.9 cm and 46.6 cm thicknesses. The stainless steel slab of 30.9 cm thickness and the collar was divided into 8

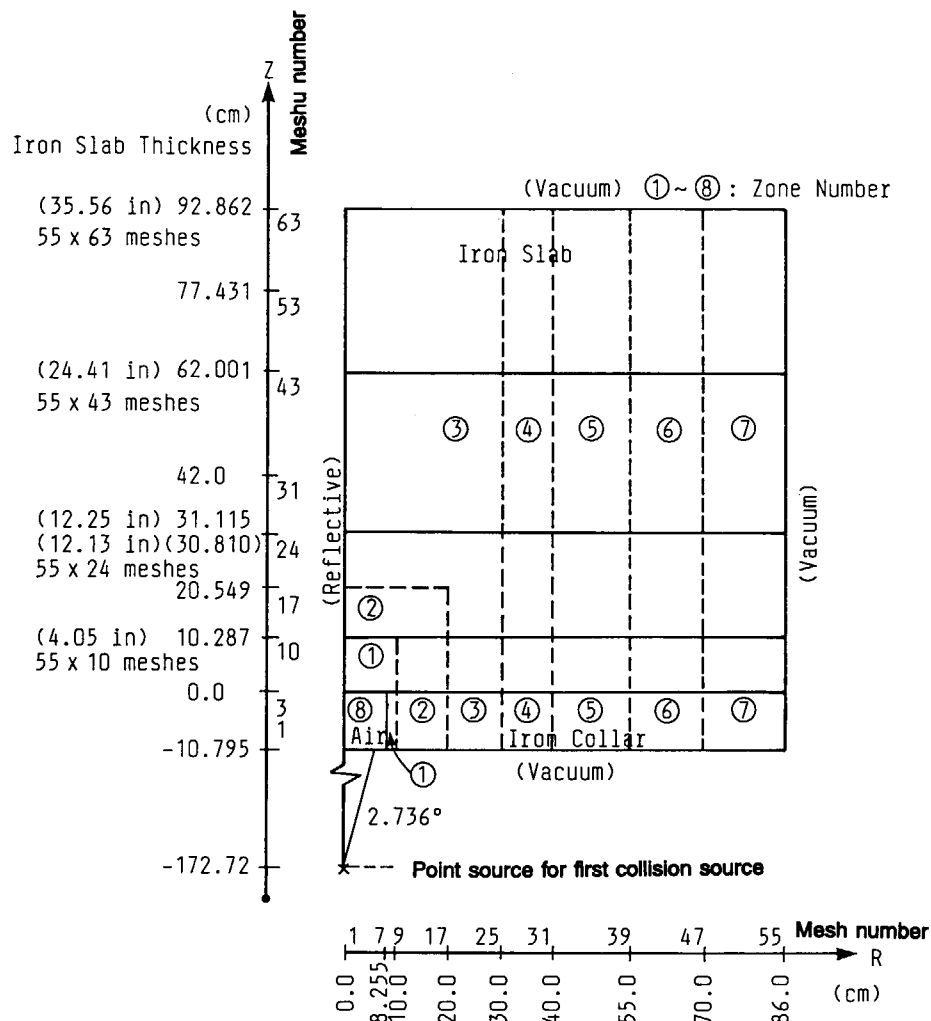


Fig. 3.3-4 Two-dimensional calculation model (iron slabs)

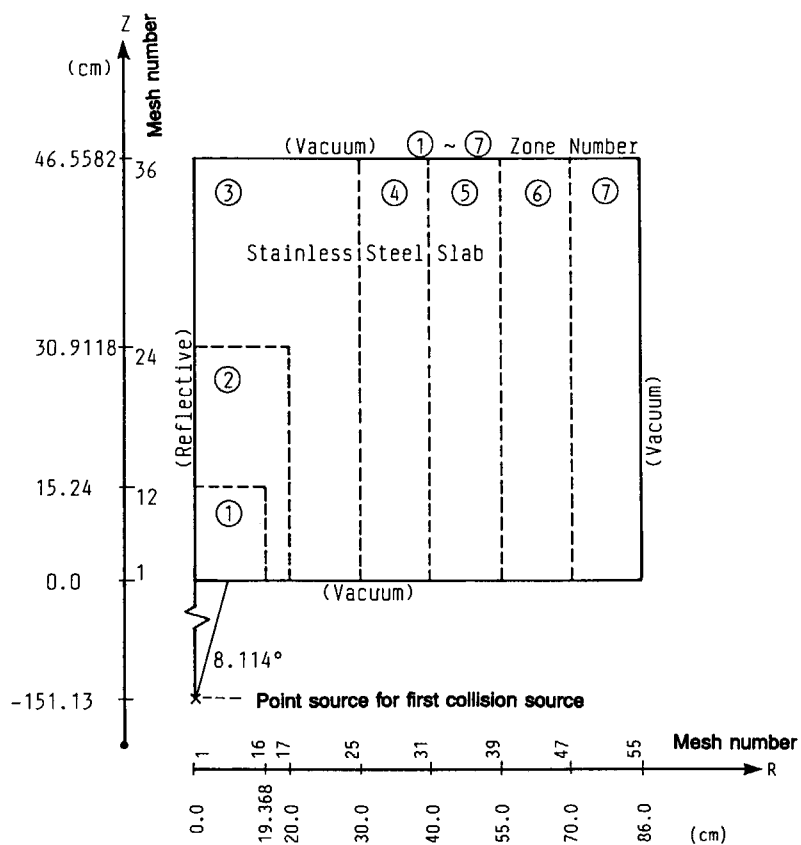


Fig. 3.3-6 Two-dimensional calculation model
(stainless steel 30.9 cm thickness)

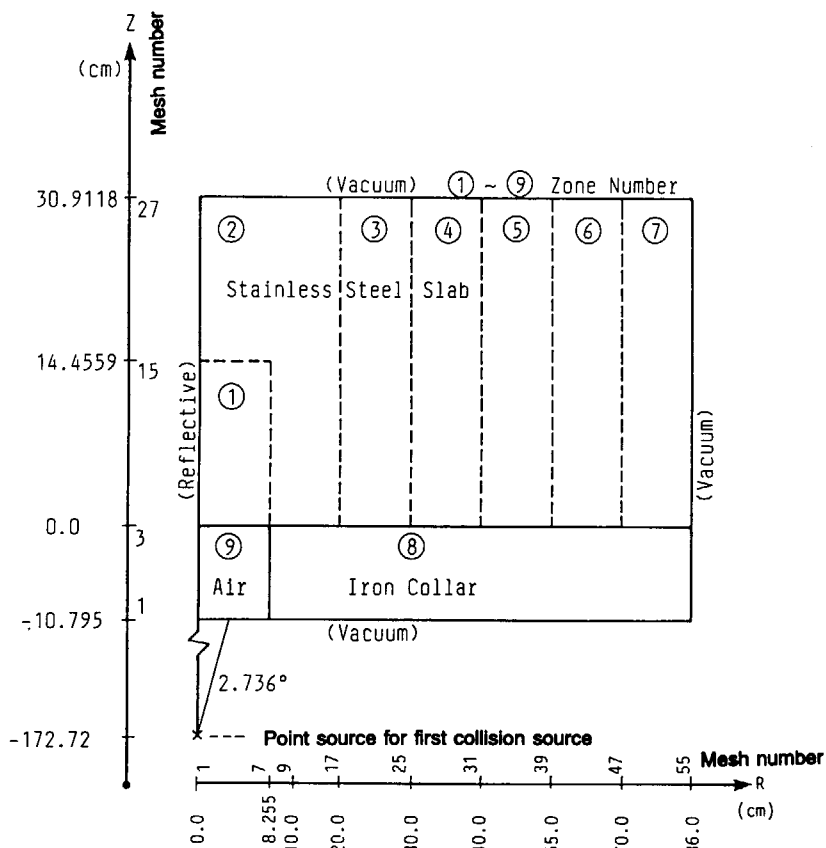


Fig. 3.3-5 Two-dimensional calculation model
(stainless steel 46.6 cm thickness)

regions and the virtual point source was located at the same distance from the iron slabs.

However, the stainless steel slab of 46.6 cm thickness was divided into 7 regions and the virtual point source was located at a distance of 151.13 cm from the surface of the stainless steel slab.

For these models, two-dimensional Sn transport calculations were carried out by DOT3.5¹³⁾ with an S8-P5 approximation and 100 energy groups in the JSSTD library²²⁾. **Table 3.3-5** shows the energy group structure. **Table 3.3-6** gives the 100-group response functions of Cd-covered BF₃, 3-in., 6-in., 10-in. Bonner balls used in the DOT3.5 calculations. The Bonner ball response functions in this table were converted from values given by Maerker et al.⁴¹⁾, using fission + 1/E spectrum as the weighting function. The external boundary angular fluxes computed by DOT3.5 were provided into the SPACETRAN code²¹⁾, which calculates the neutron energy spectra and the Bonner ball responses at the various detector positions behind the iron and stainless steel slabs.

3.3.2.2 Calculation method by MCNP code

As to the calculational model of the MCNP code¹⁷⁾, we closely followed the experimental configuration using the three-dimensional model. In the MCNP calculation, the following two methods were employed to reduce the fractional standard deviation (FSD) and to obtain results with sufficient accuracy. One is the Next Event Surface Crossing estimator (NESX estimator) and the other is the Weight Window Importance Sampling. Detailed description for these methods and selected parameters adopted in the calculation are summarized in Section 3.2.

Table 3.3-5 Energy group structure used in the ORNL iron and stainless steel benchmark calculations

No	Upper Energy (eV)	Lower Energy	No	Upper Energy (eV)	Lower Energy
1	1.6487E+07	1.4550E+07	51	3.1828E+04	2.8088E+04
2	1.4550E+07	1.2840E+07	52	2.8088E+04	2.4788E+04
3	1.2840E+07	1.1331E+07	53	2.4788E+04	2.1875E+04
4	1.1331E+07	1.0000E+07	54	2.1875E+04	1.9305E+04
5	1.0000E+07	8.8250E+06	55	1.9305E+04	1.7036E+04
6	8.8250E+06	7.7880E+06	56	1.7036E+04	1.5034E+04
7	7.7880E+06	6.8729E+06	57	1.5034E+04	1.1709E+04
8	6.8729E+06	6.0653E+06	58	1.1709E+04	9.1188E+03
9	6.0653E+06	5.3526E+06	59	9.1188E+03	7.1017E+03
10	5.3526E+06	4.7237E+06	60	7.1017E+03	5.5308E+03
11	4.7237E+06	4.1686E+06	61	5.5308E+03	4.3074E+03
12	4.1686E+06	3.6788E+06	62	4.3074E+03	3.3546E+03
13	3.6788E+06	3.2465E+06	63	3.3546E+03	2.6126E+03
14	3.2465E+06	2.8650E+06	64	2.6126E+03	2.0347E+03
15	2.8650E+06	2.5284E+06	65	2.0347E+03	1.5846E+03
16	2.5284E+06	2.2313E+06	66	1.5846E+03	1.2341E+03
17	2.2313E+06	1.9691E+06	67	1.2341E+03	9.6112E+02
18	1.9691E+06	1.7377E+06	68	9.6112E+02	7.4852E+02
19	1.7377E+06	1.5335E+06	69	7.4852E+02	5.8295E+02
20	1.5335E+06	1.3534E+06	70	5.8295E+02	4.5400E+02
21	1.3534E+06	1.1943E+06	71	4.5400E+02	3.5357E+02
22	1.1943E+06	1.0540E+06	72	3.5357E+02	2.7536E+02
23	1.0540E+06	9.3014E+05	73	2.7536E+02	2.1445E+02
24	9.3014E+05	8.2085E+05	74	2.1445E+02	1.6702E+02
25	8.2085E+05	7.2440E+05	75	1.6702E+02	1.3007E+02
26	7.2440E+05	6.3928E+05	76	1.3007E+02	1.0130E+02
27	6.3928E+05	5.6416E+05	77	1.0130E+02	7.8893E+01
28	5.6416E+05	4.9787E+05	78	7.8893E+01	6.1442E+01
29	4.9787E+05	4.3937E+05	79	6.1442E+01	4.7851E+01
30	4.3937E+05	3.8774E+05	80	4.7851E+01	3.7267E+01
31	3.8774E+05	3.4218E+05	81	3.7267E+01	2.9023E+01
32	3.4218E+05	3.0197E+05	82	2.9023E+01	2.2603E+01
33	3.0197E+05	2.6649E+05	83	2.2603E+01	1.7603E+01
34	2.6649E+05	2.3518E+05	84	1.7603E+01	1.3710E+01
35	2.3518E+05	2.0754E+05	85	1.3710E+01	1.0677E+01
36	2.0754E+05	1.8316E+05	86	1.0677E+01	8.3153E+00
37	1.8316E+05	1.6163E+05	87	8.3153E+00	6.4760E+00
38	1.6163E+05	1.4264E+05	88	6.4760E+00	5.0435E+00
39	1.4264E+05	1.2588E+05	89	5.0435E+00	3.9279E+00
40	1.2588E+05	1.1109E+05	90	3.9279E+00	3.0590E+00
41	1.1109E+05	9.8037E+04	91	3.0590E+00	2.3824E+00
42	9.8037E+04	8.6517E+04	92	2.3824E+00	1.8554E+00
43	8.6517E+04	7.6351E+04	93	1.8554E+00	1.4450E+00
44	7.6351E+04	6.7379E+04	94	1.4450E+00	1.1254E+00
45	6.7379E+04	5.9462E+04	95	1.1254E+00	8.7642E-01
46	5.9462E+04	5.2475E+04	96	8.7642E-01	6.8256E-01
47	5.2475E+04	4.6309E+04	97	6.8256E-01	5.3158E-01
48	4.6309E+04	4.0868E+04	98	5.3158E-01	4.1399E-01
49	4.0868E+04	3.6066E+04	99	4.1399E-01	1.5183E-01
50	3.6066E+04	3.1828E+04	100	1.5183E-01	3.5238E-04

Table 3.3-6 Bonner ball detector response functions

GROUP No.	Bonner Ball Detector Response Functions			
	Cd covered BF ₃	3 in.	6 in.	10 in.
1	1.76×10^{-5}	2.92×10^{-3}	1.91×10^{-1}	5.08×10^{-1}
2	5.95×10^{-5}	3.46×10^{-3}	2.30×10^{-1}	5.80×10^{-1}
3	9.08×10^{-5}	3.98×10^{-3}	2.65×10^{-1}	6.47×10^{-1}
4	1.00×10^{-4}	4.62×10^{-3}	3.11×10^{-1}	7.34×10^{-1}
5	1.12×10^{-4}	5.33×10^{-3}	3.59×10^{-1}	8.20×10^{-1}
6	1.25×10^{-4}	6.15×10^{-3}	4.13×10^{-1}	8.91×10^{-1}
7	1.42×10^{-4}	7.01×10^{-3}	4.62×10^{-1}	9.60×10^{-1}
8	1.68×10^{-4}	8.52×10^{-3}	5.26×10^{-1}	1.02
9	1.92×10^{-4}	9.96×10^{-3}	5.73×10^{-1}	1.07
10	1.89×10^{-4}	1.10×10^{-2}	6.14×10^{-1}	1.11
11	1.79×10^{-4}	1.22×10^{-2}	6.67×10^{-1}	1.13
12	1.64×10^{-4}	1.41×10^{-2}	7.18×10^{-1}	1.12
13	1.54×10^{-4}	1.63×10^{-2}	7.74×10^{-1}	1.12
14	1.58×10^{-4}	1.87×10^{-2}	8.45×10^{-1}	1.18
15	1.67×10^{-4}	2.14×10^{-2}	9.13×10^{-1}	1.20
16	1.77×10^{-4}	2.45×10^{-2}	9.84×10^{-1}	1.22
17	2.20×10^{-4}	2.79×10^{-2}	1.04	1.20
18	2.42×10^{-4}	3.16×10^{-2}	1.10	1.19
19	2.06×10^{-4}	3.57×10^{-2}	1.15	1.16
20	1.59×10^{-4}	4.02×10^{-2}	1.20	1.12
21	1.38×10^{-4}	4.52×10^{-2}	1.25	1.07
22	1.38×10^{-4}	5.06×10^{-2}	1.29	1.02
23	1.47×10^{-4}	5.65×10^{-2}	1.32	9.71×10^{-1}
24	1.63×10^{-4}	6.27×10^{-2}	1.35	9.17×10^{-1}
25	1.93×10^{-4}	6.95×10^{-2}	1.37	8.62×10^{-1}
26	2.33×10^{-4}	7.65×10^{-2}	1.38	8.08×10^{-1}
27	2.83×10^{-4}	8.39×10^{-2}	1.40	7.56×10^{-1}
28	3.42×10^{-4}	9.18×10^{-2}	1.40	7.07×10^{-1}
29	3.80×10^{-4}	1.00×10^{-1}	1.40	6.60×10^{-1}
30	3.89×10^{-4}	1.09×10^{-1}	1.40	6.17×10^{-1}
31	4.01×10^{-4}	1.17×10^{-1}	1.39	5.76×10^{-1}
32	4.45×10^{-4}	1.26×10^{-1}	1.39	5.38×10^{-1}
33	5.25×10^{-4}	1.35×10^{-1}	1.38	5.06×10^{-1}
34	5.98×10^{-4}	1.44×10^{-1}	1.37	4.75×10^{-1}
35	6.48×10^{-4}	1.52×10^{-1}	1.35	4.47×10^{-1}
36	6.87×10^{-4}	1.62×10^{-1}	1.34	4.22×10^{-1}
37	7.24×10^{-4}	1.71×10^{-1}	1.32	4.00×10^{-1}
38	7.63×10^{-4}	1.80×10^{-1}	1.31	3.80×10^{-1}
39	8.02×10^{-4}	1.89×10^{-1}	1.29	3.62×10^{-1}
40	8.44×10^{-4}	1.98×10^{-1}	1.27	3.46×10^{-1}
41	8.90×10^{-4}	2.06×10^{-1}	1.26	3.32×10^{-1}
42	9.41×10^{-4}	2.15×10^{-1}	1.25	3.19×10^{-1}
43	9.95×10^{-4}	2.23×10^{-1}	1.24	3.08×10^{-1}
44	1.05×10^{-3}	2.32×10^{-1}	1.22	2.98×10^{-1}
45	1.11×10^{-3}	2.40×10^{-1}	1.21	2.88×10^{-1}
46	1.18×10^{-3}	2.48×10^{-1}	1.19	2.80×10^{-1}
47	1.25×10^{-3}	2.56×10^{-1}	1.18	2.72×10^{-1}
48	1.33×10^{-3}	2.65×10^{-1}	1.18	2.66×10^{-1}
49	1.42×10^{-3}	2.30×10^{-1}	1.17	2.60×10^{-1}
50	1.51×10^{-3}	2.40×10^{-1}	1.16	2.54×10^{-1}

Table 3.3-6 (continued)

GROUP No.	Bonner Ball Detector Response Functions			
	Cd covered BF ₃	3 in.	6 in.	10 in.
51	1.60×10^{-3}	2.60×10^{-1}	1.15	2.49×10^{-1}
52	1.71×10^{-3}	2.80×10^{-1}	1.15	2.44×10^{-1}
53	1.81×10^{-3}	2.90×10^{-1}	1.14	2.40×10^{-1}
54	1.93×10^{-3}	3.10×10^{-1}	1.14	2.36×10^{-1}
55	2.06×10^{-3}	3.40×10^{-1}	1.13	2.32×10^{-1}
56	2.19×10^{-3}	3.40×10^{-1}	1.13	2.28×10^{-1}
57	2.40×10^{-3}	3.60×10^{-1}	1.12	2.23×10^{-1}
58	2.71×10^{-3}	3.80×10^{-1}	1.11	2.18×10^{-1}
59	3.07×10^{-3}	4.00×10^{-1}	1.11	2.12×10^{-1}
60	3.47×10^{-3}	4.20×10^{-1}	1.10	2.07×10^{-1}
61	3.92×10^{-3}	4.40×10^{-1}	1.09	2.02×10^{-1}
62	4.45×10^{-3}	4.60×10^{-1}	1.08	1.98×10^{-1}
63	5.02×10^{-3}	4.80×10^{-1}	1.08	1.94×10^{-1}
64	5.66×10^{-3}	5.00×10^{-1}	1.07	1.90×10^{-1}
65	6.45×10^{-3}	5.30×10^{-1}	1.07	1.86×10^{-1}
66	7.34×10^{-3}	5.60×10^{-1}	1.06	1.83×10^{-1}
67	8.32×10^{-3}	5.80×10^{-1}	1.05	1.79×10^{-1}
68	9.41×10^{-3}	6.00×10^{-1}	1.05	1.75×10^{-1}
69	1.06×10^{-2}	6.20×10^{-1}	1.04	1.71×10^{-1}
70	1.21×10^{-2}	6.70×10^{-1}	1.01	1.66×10^{-1}
71	1.37×10^{-2}	7.00×10^{-1}	1.02	1.64×10^{-1}
72	1.55×10^{-2}	7.20×10^{-1}	1.00	1.60×10^{-1}
73	1.76×10^{-2}	7.60×10^{-1}	9.91×10^{-1}	1.56×10^{-1}
74	2.00×10^{-2}	8.00×10^{-1}	9.84×10^{-1}	1.53×10^{-1}
75	2.25×10^{-2}	7.60×10^{-1}	9.55×10^{-1}	1.47×10^{-1}
76	2.43×10^{-2}	7.40×10^{-1}	8.84×10^{-1}	1.35×10^{-1}
77	2.67×10^{-2}	8.00×10^{-1}	8.60×10^{-1}	1.30×10^{-1}
78	3.21×10^{-2}	8.20×10^{-1}	9.08×10^{-1}	1.36×10^{-1}
79	3.74×10^{-2}	8.00×10^{-1}	9.22×10^{-1}	1.37×10^{-1}
80	4.26×10^{-2}	8.20×10^{-1}	9.09×10^{-1}	1.34×10^{-1}
81	4.78×10^{-2}	8.10×10^{-1}	8.84×10^{-1}	1.29×10^{-1}
82	5.25×10^{-2}	9.00×10^{-1}	8.40×10^{-1}	1.21×10^{-1}
83	6.15×10^{-2}	9.30×10^{-1}	8.51×10^{-1}	1.22×10^{-1}
84	7.01×10^{-2}	9.80×10^{-1}	8.38×10^{-1}	1.20×10^{-1}
85	7.93×10^{-2}	1.00	8.18×10^{-1}	1.16×10^{-1}
86	8.97×10^{-2}	1.00	7.96×10^{-1}	1.13×10^{-1}
87	1.01×10^{-1}	1.07	7.73×10^{-1}	1.09×10^{-1}
88	1.15×10^{-1}	1.10	7.50×10^{-1}	1.05×10^{-1}
89	1.30×10^{-1}	1.12	7.24×10^{-1}	1.01×10^{-1}
90	1.47×10^{-1}	1.15	6.97×10^{-1}	9.70×10^{-2}
91	1.65×10^{-1}	1.20	6.67×10^{-1}	9.27×10^{-2}
92	1.86×10^{-1}	1.20	6.34×10^{-1}	8.78×10^{-2}
93	2.08×10^{-1}	1.20	5.97×10^{-1}	8.25×10^{-2}
94	2.30×10^{-1}	1.12	5.51×10^{-1}	7.60×10^{-2}
95	2.48×10^{-1}	1.11	4.92×10^{-1}	6.77×10^{-2}
96	2.53×10^{-1}	1.00	4.12×10^{-1}	5.66×10^{-2}
97	2.31×10^{-1}	8.30×10^{-1}	3.05×10^{-1}	4.17×10^{-2}
98	1.47×10^{-1}	5.00×10^{-1}	1.59×10^{-1}	2.21×10^{-2}
99	0.00	0.00	0.00	0.00
100	0.00	0.00	0.00	0.00

3.3.3 Results by DOT Calculation

3.3.3.1 Iron

The calculated values by using the DOT3.5 and SPACETRAN codes were compared with the experimental data for the off-center geometry. **Table 3.3-7** shows the calculated results and the C/E values for the Bonner ball detectors and the integrated fluxes by the NE-213 and the Benjamin spectrometers. The C/E values for the Bonner ball detectors are as follows:

iron slab of 30.8 cm (12.13 in.) thickness: 0.94-1.26,

iron slab of 62.0 cm (24.41 in.) thickness: 0.90-1.12,

iron slab of 92.9 cm (36.56 in.) thickness: 0.67-1.00.

The C/E values for the NE-213 spectrometer are as follows:

iron slab of 10.3 cm (4.05 in.) thickness: 1.24-1.32,

iron slab of 30.8 cm (12.13 in.) thickness: 0.85-0.91.

The C/E value for the Benjamin spectrometer is as follows:

iron slab of 31.1 cm (12.25 in.) thickness: 1.34.

The calculations are in agreement with the experimental data within 30%.

Figures 3.3-7 to 3.3-10 compare the neutron energy spectra with JENDL-3 and JENDL-3T above 0.8 MeV with the measured values by the NE-213 spectrometer at $\phi_d=15$ deg. and $\phi_d=45$ deg. behind the slabs of 10.3 cm and 30.8 cm thicknesses. From these figures, no significant difference is found between JENDL-3 and JENDL-3T in the energy range from 800 keV to 2 MeV. However, a significant difference is shown in the energy range between 2 and 10 MeV. Namely, JENDL-3 overestimated neutron spectrum more than JENDL-3T.

Figure 3.3-11 shows a comparison of the neutron energy spectra calculated with JENDL-3 and JENDL-3T with the measured values by the Benjamin spectrometer at $\phi_d=50$ deg. behind the slab of 31.1 cm thickness in the energy range between 80 keV and 1.5 MeV. From this figure, no significant difference is found between JENDL-3 and JENDL-3T in the energy range from 80 keV to 1.5 MeV. The agreement between calculation and experiment is very good in the energy range from 100 keV to 1.5 MeV. However, in the energy range between 80 keV and 100 keV, JENDL-3 and JENDL-3T overestimated the spectra in comparison with the experimental results.

3.3.3.2 Stainless Steel

The calculated values by using the DOT3.5 and SPACETRAN codes were compared with experimental data. **Table 3.3-8** shows the calculated results and C/E values for the Bonner ball detector responses and for the integrated fluxes by the NE-213 and the Benjamin spectrometers. The C/E values for the Bonner ball detectors are from 0.98 to 1.25. The C/E value for the Benjamin spectrometer is 1.03. The agreement between calculations and experiments is very good.

Figure 3.3-12 compares the calculated neutron energy spectra with the measured values by the Benjamin spectrometer at $\phi_d=50$ deg. behind the slab of 30.9 cm thickness in the energy range between 48 keV and 1.5 MeV.

Table 3.3-7 Calculated results and C/E values of the ORNL iron experiments

Iron Slab Thickness (cm)	Detector Locations (cm)			Detector Type	Measured Values				Calculated Values				C/E (Calculated/Measured)			
	Centerline Distance behind Slab	Radial Distance from Centerline	Observation Angle with Respect to Centerline (deg.)		Bonner Balls (Neutrons/cm ² /min/W)		Other Detectors	Bonner Balls (Neutrons/cm ² /min/W)		Other Detectors	Bonner Balls		Other Detectors			
					3 in.	6 in.		10 in.	3 in.		6 in.	10 in.				
10. 287 (4. 05 in.)	401. 32 (158 in.)	107. 95 (42. 5 in.)	15	NE-213 Spectrometer	—	—	—	1. 74	—	—	—	2. 161	—	—	—	1. 24
	294. 64 (116 in.)	294. 64 (116 in.)	45		—	—	—	0. 846		—	—	—	1. 118	—	—	—
30. 810 (12. 13 in.)	354. 44 (139. 5 in.)	92. 71 (36. 5 in.)	15	Bonner Balls	0. 577	3. 54	1. 58	—	0. 578	4. 47	1. 82	—	1. 00	1. 26	1. 15	—
	254. 00 (100 in.)	254. 00 (100 in.)	45		0. 411	2. 39	1. 04		0. 385	2. 94	1. 17		0. 94	1. 23	1. 13	
	381. 00 (150 in.)	102. 87 (40. 5 in.)	15	NE-213 Spectrometer	—	—	—	0. 265	—	—	—	0. 240	—	—	—	0. 91
	279. 40 (110 in.)	279. 40 (110 in.)	45		—	—	—	0. 157	—	—	—	0. 134	—	—	—	0. 85
31. 115 (12. 25 in.)	25. 40 (10 in.)	30. 48 (12 in.)	50	Benjamin Spectrometer	—	—	—	74. 5	—	—	—	99. 6	—	—	—	1. 34
62. 001 (24. 41 in.)	314. 96 (124 in.)	83. 82 (33 in.)	15	Bonner Balls	0. 367	1. 70	0. 600	—	0. 329	1. 78	0. 537	—	0. 90	1. 05	0. 90	—
	229. 87 (90. 5 in.)	229. 87 (90. 5 in.)	45		0. 245	1. 13	0. 405		0. 238	1. 26	0. 376		0. 97	1. 12	0. 93	
92. 862 (36. 56 in.)	281. 94 (111 in.)	76. 20 (30 in.)	15	Bonner Balls	0. 181	0. 700	0. 227	—	0. 133	0. 574	0. 151	—	0. 73	0. 82	0. 67	—
	207. 01 (81. 5 in.)	207. 01 (81. 5 in.)	45		0. 128	0. 475	0. 151		0. 111	0. 477	0. 124		0. 87	1. 00	0. 82	

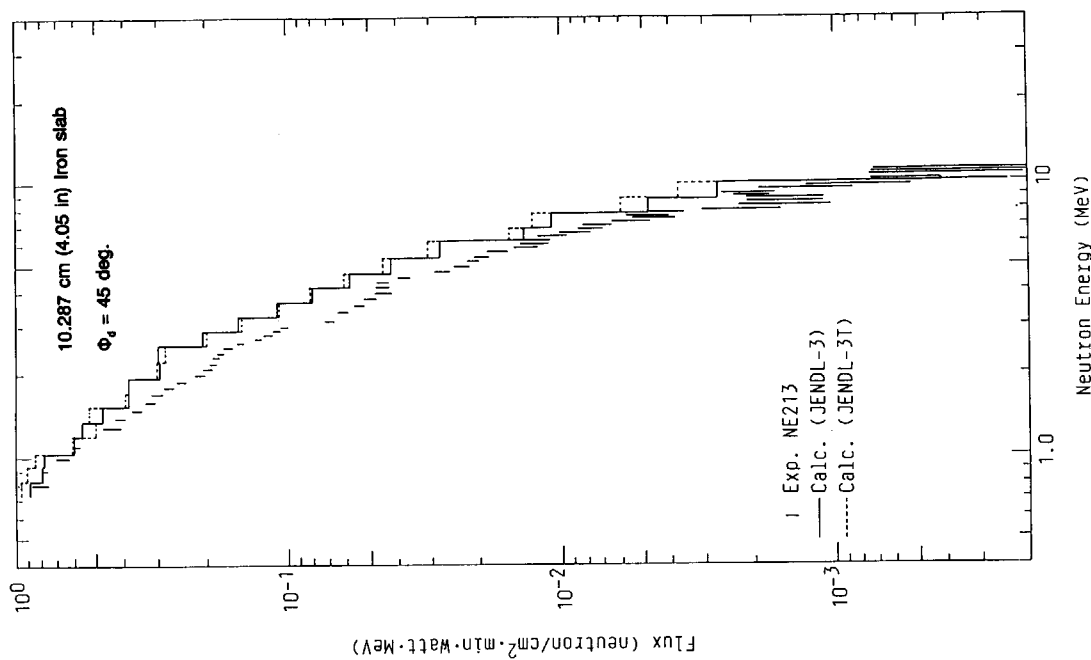


Fig. 3.3-8 Neutron energy spectrum at ($r=294.64$ cm, $z=294.64$ cm) behind 10.287-cm (4.05-in.) thick iron slab

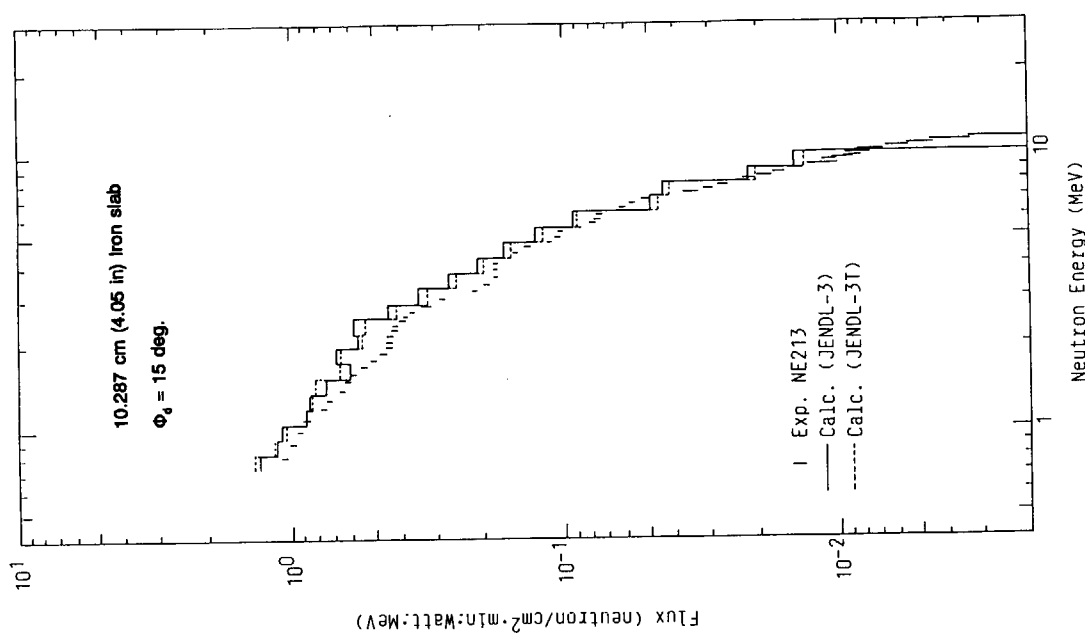


Fig. 3.3-7 Neutron energy spectrum at ($r=401.32$ cm, $z=107.95$ cm) behind 10.287-cm (4.05-in.) thick iron slab

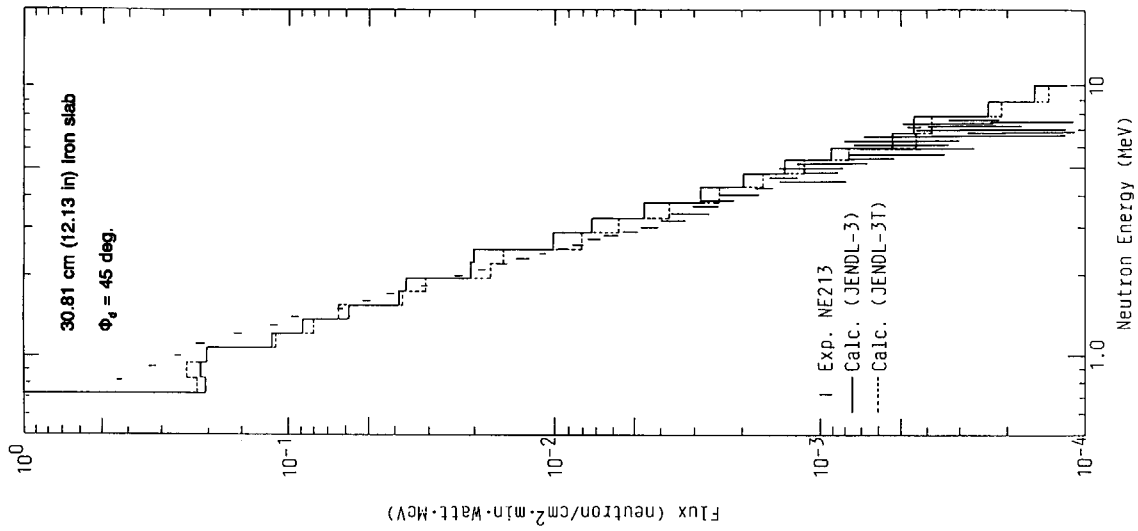


Fig. 3.3-10 Neutron energy spectrum at ($r=279.4$ cm, $z=279.4$ cm) behind 30.81-cm (12.13-in.) thick iron slab

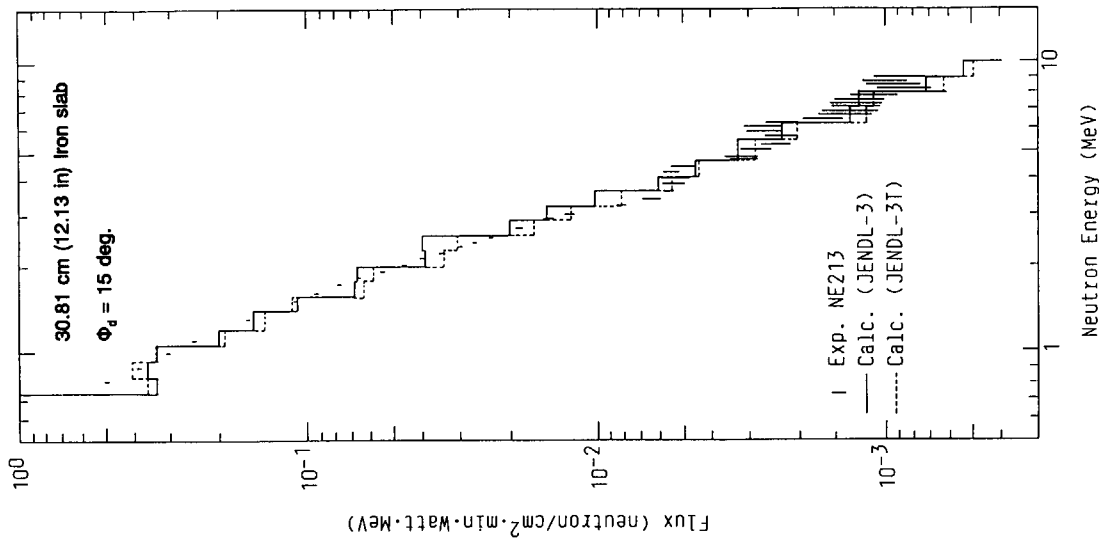


Fig. 3.3-9 Neutron energy spectrum at ($r=381.0$ cm, $z=102.87$ cm) behind 30.81-cm (12.13-in.) thick iron slab

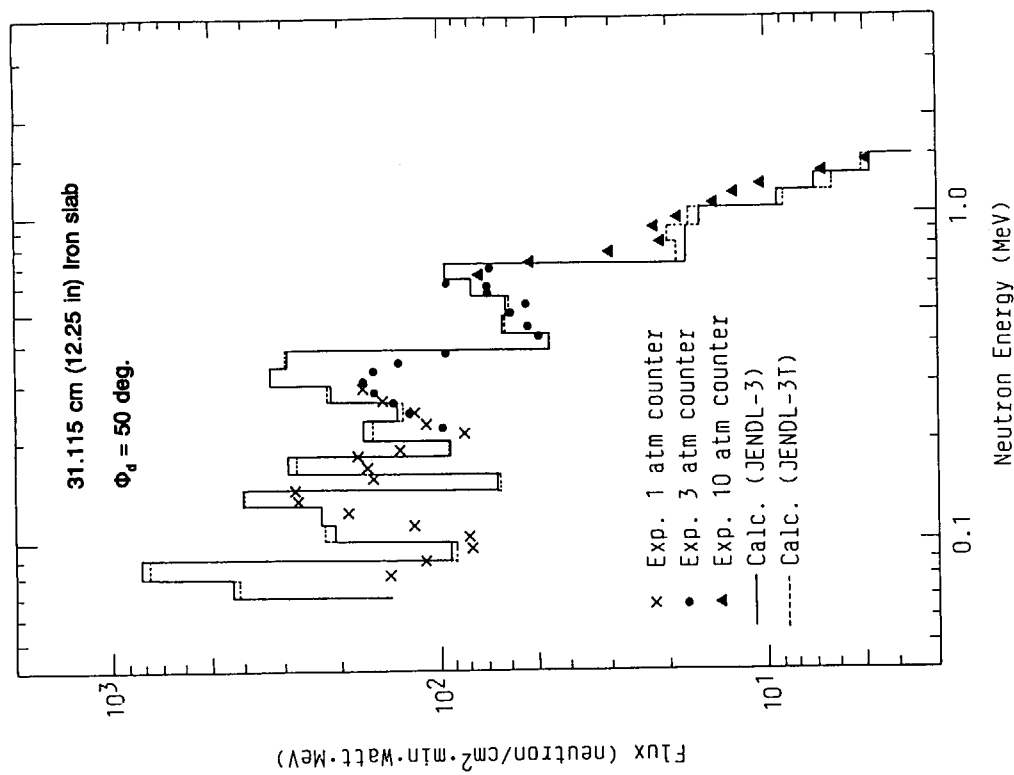


Fig. 3.3-11 Neutron energy spectrum at ($r=25.4$ cm, $z=30.48$ cm) behind 31.115-cm (12.25-in.) thick iron slab

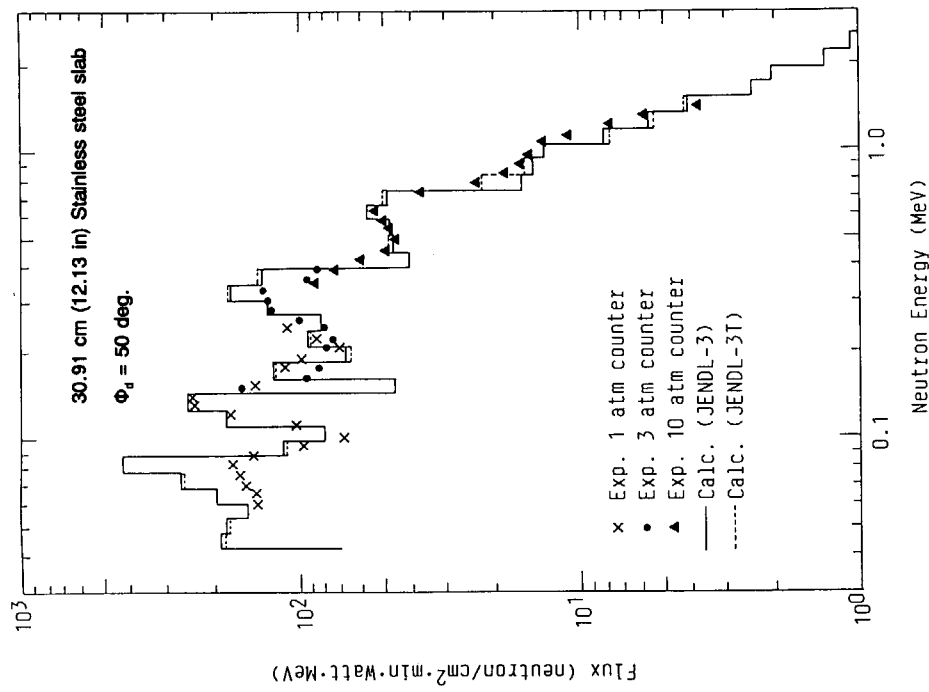


Fig. 3.3-12 Neutron energy spectrum at ($r=25.4$ cm, $z=30.48$ cm) behind 30.91-cm (12.17-in.) thick stainless steel slab

Table 3.3-8 Calculated results and C/E values of the ORNL stainless steel experiments

Stainless Steel Slab Thickness (cm)	Detector Locations (cm)			Detector Type	Measured Values				Calculated Values				C/E (Calculated/Measured)			
	Centerline Distance behind Slab	Radial Distance from Centerline	Observation Angle with Respect to Centerline (deg.)		Bonner Balls (Neutrons/cm ² /min/W)			Other Detectors	Bonner Balls (Neutrons/cm ² /min/W)			Other Detectors	Bonner Balls			Other Detectors
					3 in.	6 in.	10 in.	3 in.	6 in.	10 in.	3 in.	6 in.	10 in.	3 in.	6 in.	
30.91 (12.17 in.)	345.44 (136 in.)	92.71 (36.5 in.)	15	0.496	2.74	1.28	—	0.488	3.34	1.37	—	0.98	1.22	1.07	—	
	254.00 (100 in.)	254.00 (100 in.)	45	0.327	1.77	0.797		0.327	2.21	0.877		1.00	1.25	1.11		
	25.40 (10 in.)	30.48 (12 in.)	50				58.4				60.2				1.03	

3.3.4 Results by MCNP Calculation

Comparisons of the neutron energy spectra between 60 keV and 1.5 MeV and above 800 keV on the centerline behind the 12-in.-thick iron slab between the measurements and MCNP calculations with JENDL-3 and ENDF/B-IV are shown in **Figs. 3.3-13** and **3.3-14**, respectively. The FSDs in each energy bin range from 0.033 to 0.089 and from 0.022 to 0.135 in **Figs. 3.3-13** and **3.3-14**, respectively. The results are summarized as follows:

- (i) The calculated energy spectra with JENDL-3 and with ENDF/B-IV show fairly good agreement with the measurements above about 100 keV, while the spectra in the energy range around 75 keV are considerably overestimated in comparison with the experiments as shown in **Fig. 3.3-13**.
- (ii) For the fast neutron spectrum above 3 MeV, the calculations with JENDL-3 agree more closely with the experiments than that with ENDF/B-IV in **Fig. 3.3-14**. Meanwhile, a considerable underestimation is observed in the calculated spectrum with JENDL-3 in the energy range between 1 and 3 MeV as shown in **Fig. 3.3-14**.

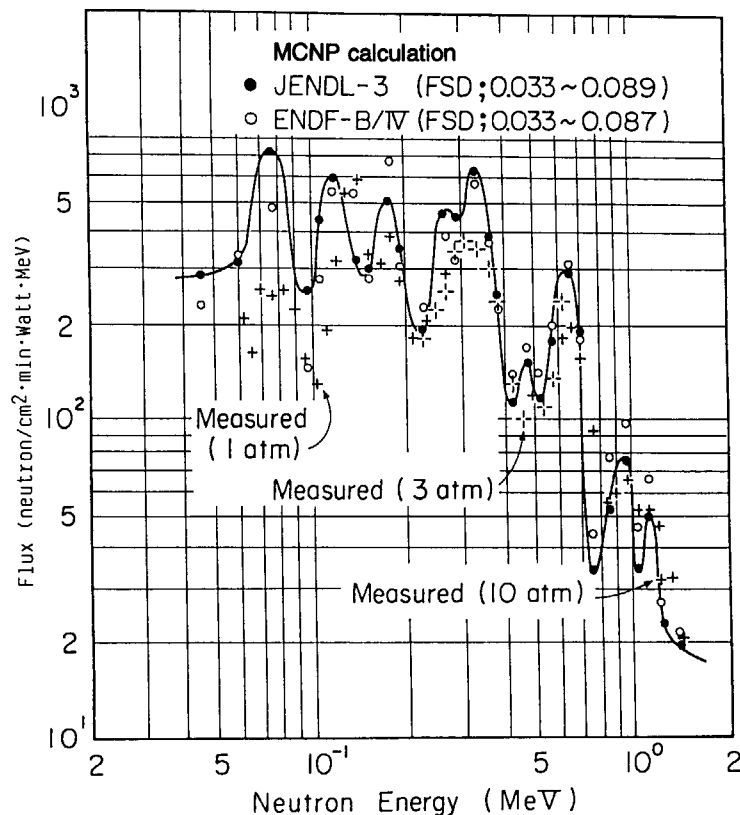


Fig. 3.3-13 Comparison of energy spectra between the MCNP calculation and measurement in the energy range from 60 keV to 1.5 MeV on the centerline behind 12-in.-thick iron slab

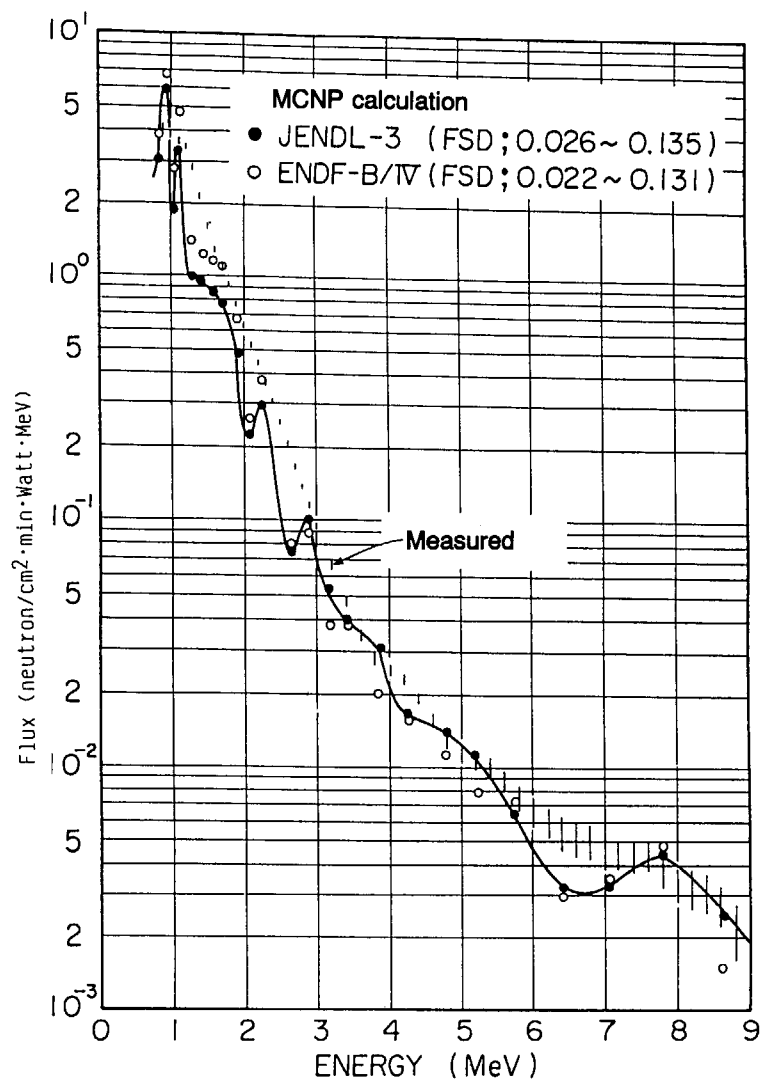


Fig. 3.3-14 Comparison of energy spectra between the MCNP calculation and measurement above 800 keV on the centerline behind 12-in.-thick iron slab

3.4 KfK Iron Experiments

3.4.1 Outline of Experiments

This experiment⁶⁾ is provided for measuring leakage neutron energy spectra from six kinds of iron spheres using a proton recoil counter and a ^3He -Si diode spectrometer. A ^{252}Cf neutron source was located at the center of the sphere. The energy spectra of source neutrons were measured and evaluated using both spectrometers. The iron spheres used in the experiments were constructed with pure iron (C: 0.07w/o, Mn: 0.05w/o, P: 0.009w/o, S: 0.007w/o). Diameters of the iron spheres were 15, 20, 25, 30, 35 and 40 cm, respectively.

The experimental configuration is shown in Fig. 3.4-1. In the measurement for the proton recoil counter, the background was estimated using a shadow cone. Energy spectra of neutrons were obtained using the unfolding technique with the SPEC4 code. In the measurement for the ^3He -Si diode spectrometer, the measured data were corrected by using the reaction rates of $\text{Si}(n, d)$, $\text{Si}(n, p)$ reactions and the background subtraction. Energy spectra of neutrons were also obtained with the Bluhm unfolding technique.

3.4.2 Calculation Method

As for the calculation model, one-dimensional geometry of sphere was applied. The shell source condition at 0.88 cm from the center of sphere was provided. The configuration is shown in Fig. 3.4-2. The energy spectra of source neutrons used in the calculation are given in Table 3.4-1 together with the adopted energy group structure.

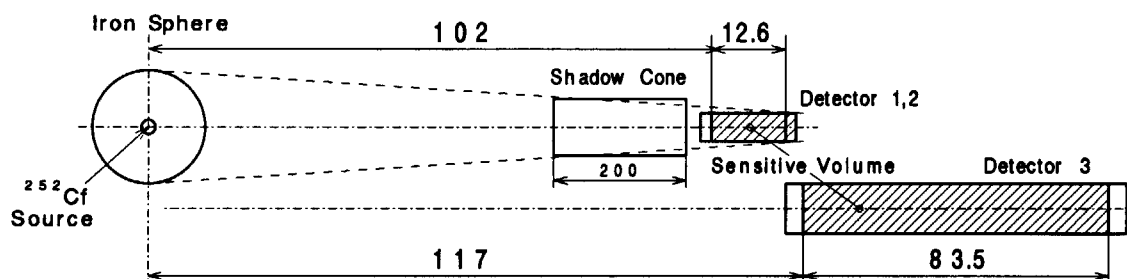


Fig. 3.4-1 Configuration of the KfK iron benchmark experiment

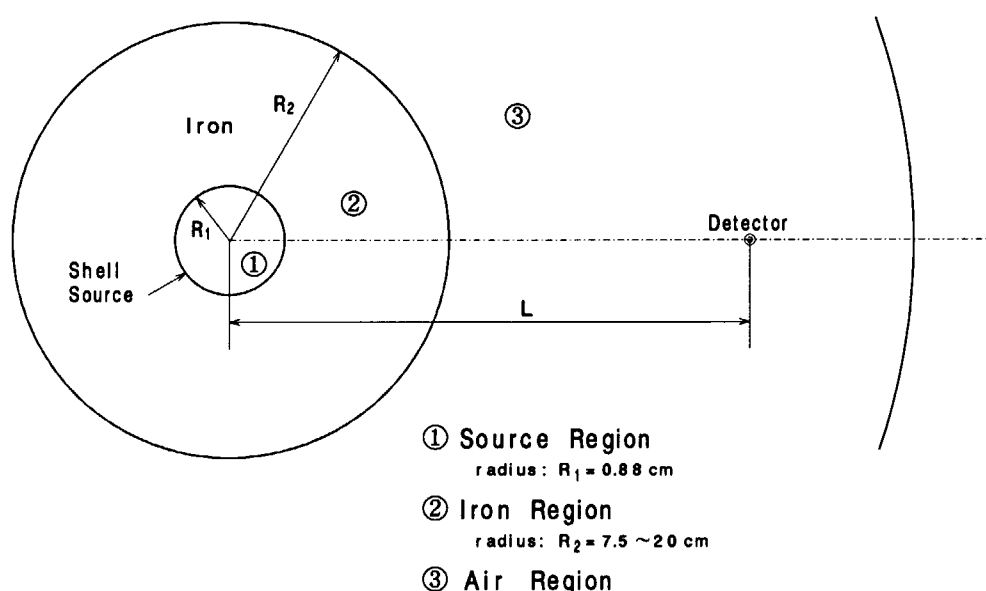


Fig. 3.4-2 Calculation model for the KfK iron benchmark problem

Table 3.4-1 Energy group structure and the energy spectrum of ^{252}Cf neutron source used in the KfK benchmark calculation

No.	Upper Energy (eV)	Lower Energy	Source Fraction	No.	Upper Energy (eV)	Lower Energy	Source Fraction
1	1.00000E+7*	8.82497E+6	6.39894E-3	61	4.08677E+4	3.43067E+4	0.0
2	8.82497E+6	7.78801E+6	7.76003E-3	62	3.43067E+4	3.18278E+4	0.0
3	7.78801E+6	6.87289E+6	1.04851E-2	63	3.18278E+4	2.85124E+4	0.0
4	6.87289E+6	6.06531E+6	2.73713E-2	64	2.85124E+4	2.69866E+4	0.0
5	6.06531E+6	5.35261E+6	2.45428E-2	65	2.69866E+4	2.60584E+4	0.0
6	5.35261E+6	4.72367E+6	2.33215E-2	66	2.60584E+4	2.47875E+4	0.0
7	4.72367E+6	4.16862E+6	5.68139E-2	67	2.47875E+4	2.41755E+4	0.0
8	4.16862E+6	3.67879E+6	4.66636E-2	68	2.41755E+4	2.35786E+4	0.0
9	3.67879E+6	3.24652E+6	5.26699E-2	69	2.35786E+4	2.18749E+4	0.0
10	3.24652E+6	2.86505E+6	5.55357E-2	70	2.18749E+4	1.93045E+4	0.0
11	2.86505E+6	2.59240E+6	3.34858E-2	71	1.93045E+4	1.50344E+4	0.0
12	2.59240E+6	2.38521E+6	2.69217E-2	72	1.50344E+4	1.11936E+4	0.0
13	2.38521E+6	2.36525E+6	3.98368E-3	73	1.11936E+4	9.11882E+3	0.0
14	2.36525E+6	2.30685E+6	1.96078E-2	74	9.11882E+3	7.10174E+3	0.0
15	2.30685E+6	2.12248E+6	5.38028E-2	75	7.10174E+3	5.53084E+3	0.0
16	2.12248E+6	1.92050E+6	4.50166E-2	76	5.53084E+3	4.30743E+3	0.0
17	1.92050E+6	1.73774E+6	4.36170E-2	77	4.30743E+3	3.70744E+3	0.0
18	1.73774E+6	1.53355E+6	5.18680E-2	78	3.70744E+3	3.35463E+3	0.0
19	1.53355E+6	1.35335E+6	4.83538E-2	79	3.35463E+3	3.03539E+3	0.0
20	1.35335E+6	1.19433E+6	4.47098E-2	80	3.03539E+3	2.74654E+3	0.0
21	1.19433E+6	1.05399E+6	4.05644E-2	81	2.74654E+3	2.61259E+3	0.0
22	1.05399E+6	9.58472E+5	2.80825E-2	82	2.61259E+3	2.48517E+3	0.0
23	9.58472E+5	8.20850E+5	4.08594E-2	83	2.48517E+3	2.24867E+3	0.0
24	8.20850E+5	7.24398E+5	2.86993E-2	84	2.24867E+3	2.03468E+3	0.0
25	7.24398E+5	6.39279E+5	2.51562E-2	85	2.03468E+3	1.58461E+3	0.0
26	6.39279E+5	5.64161E+5	2.19203E-2	86	1.58461E+3	1.23410E+3	0.0
27	5.64161E+5	4.97871E+5	1.90040E-2	87	1.23410E+3	9.61117E+2	0.0
28	4.97871E+5	4.39369E+5	1.63284E-2	88	9.61117E+2	7.48518E+2	0.0
29	4.39369E+5	3.87742E+5	1.40160E-2	89	7.48518E+2	5.82947E+2	0.0
30	3.87742E+5	3.68832E+5	5.05534E-3	90	5.82947E+2	4.53999E+2	0.0
31	3.68832E+5	3.42181E+5	6.93383E-3	91	4.53999E+2	3.53575E+2	0.0
32	3.42181E+5	3.33733E+5	2.19792E-3	92	3.53575E+2	2.75364E+2	0.0
33	3.33733E+5	3.01974E+5	8.02277E-3	93	2.75364E+2	2.14454E+2	0.0
34	3.01974E+5	2.98500E+5	8.50695E-4	94	2.14454E+2	1.67017E+2	0.0
35	2.98500E+5	2.97199E+5	3.18571E-4	95	1.67017E+2	1.30073E+2	0.0
36	2.97199E+5	2.94518E+5	6.56486E-4	96	1.30073E+2	1.01301E+2	0.0
37	2.94518E+5	2.87246E+5	1.78067E-3	97	1.01301E+2	7.88932E+1	0.0
38	2.87246E+5	2.74607E+5	3.09486E-3	98	7.88932E+1	6.14421E+1	0.0
39	2.74607E+5	2.66491E+5	1.93321E-3	99	6.14421E+1	4.78512E+1	0.0
40	2.66491E+5	2.50972E+5	3.67562E-3	100	4.78512E+1	3.72665E+1	0.0
41	2.50972E+5	2.35177E+5	3.64307E-3	101	3.72665E+1	2.90232E+1	0.0
42	2.35177E+5	2.07543E+5	6.18960E-3	102	2.90232E+1	2.26033E+1	0.0
43	2.07543E+5	1.85924E+5	4.63585E-3	103	2.26033E+1	1.76035E+1	0.0
44	1.85924E+5	1.61635E+5	4.95484E-3	104	1.76035E+1	1.37096E+1	0.0
45	1.61635E+5	1.48464E+5	2.57576E-3	105	1.37096E+1	1.06770E+1	0.0
46	1.48464E+5	1.39120E+5	1.76272E-3	106	1.06770E+1	8.31529E+0	0.0
47	1.39120E+5	1.31019E+5	1.49160E-3	107	8.31529E+0	6.47595E+0	0.0
48	1.31019E+5	1.29715E+5	2.35770E-4	108	6.47595E+0	5.04348E+0	0.0
49	1.29715E+5	1.22773E+5	1.25515E-3	109	5.04348E+0	3.92786E+0	0.0
50	1.22773E+5	1.11090E+5	4.56954E-3	110	3.92786E+0	3.05902E+0	0.0
51	1.11090E+5	9.80366E+4	1.69349E-3	111	3.05902E+0	2.38237E+0	0.0
52	9.80366E+4	8.65170E+4	1.49451E-3	112	2.38237E+0	1.85539E+0	0.0
53	8.65170E+4	8.27100E+4	4.40815E-4	113	1.85539E+0	1.44498E+0	0.0
54	8.27100E+4	7.94669E+4	3.75521E-4	114	1.44498E+0	1.12535E+0	0.0
55	7.94669E+4	7.63509E+4	3.60803E-4	115	1.12535E+0	8.76425E-1	0.0
56	7.63509E+4	7.19046E+4	5.14839E-4	116	8.76425E-1	6.82560E-1	0.0
57	7.19046E+4	6.73795E+4	5.23964E-4	117	6.82560E-1	5.31579E-1	0.0
58	6.73795E+4	5.94622E+4	5.78953E-8	118	5.31579E-1	4.13994E-1	0.0
59	5.94622E+4	5.24752E+4	0.0	119	4.13994E-1	1.09624E-1	0.0
60	5.24752E+4	4.08677E+4	0.0	120	1.09624E-1	3.30660E-5	0.0

*1.0E+7 means 1.0×10^7 .

Table 3.4-2 Nuclide compositions for the KfK iron experiments

Nuclide	Atomic number density ($\times 10^{24}$ atoms/cm ³)		
	Source region	Iron region	Air region
N	—	—	4.25E-5
O	2.60 E-3*	—	1.13E-5
Mg	3.90 E-3	—	—
Al	1.055E-1	—	—
Si	8.00 E-4	—	—
Fe	—	8.464E-2	—
Zr	2.94 E-2	—	—
Sn	4.00 E-4	—	—

*2.60E-3 means 2.6×10^{-3} .

Cross sections were prepared using the RADHEAT-V4 code system¹⁵⁾ with 32 angular meshes of the DDX form. The energy group structure of neutrons which consists of 120 groups was adopted in this calculation. The energy group structure is the same as the SSL90A library²³⁾ described in Section 2.2.2. The nuclide compositions of each material are shown in **Table 3.4-2**. For the evaluated nuclear data, JENDL-3 was used as the standard nuclear data, and ENDF/B-IV was also used for comparison.

The neutron transport calculation was performed by the DIAC code¹²⁾, which is a one-dimensional S_N -transport code in the RADHEAT-V4 code system. The DIAC code directly uses the cross sections of the DDX form, so that the angular flux can be accurately computed, since no approximation is used such as the low order Legendre expansion. The angular fluxes calculated at the surface of the iron sphere were converted to the leakage currents integrated over 4π directions, then these were directly compared with the measured data. The mesh spacings in the calculation were selected between 0.5 and 1 cm.

3.4.3 Results by DIAC Calculation

The calculated energy spectra of neutrons for each iron thickness with JENDL-3 and ENDF/B-IV are shown in **Figs. 3.4-3** to **3.4-8**, compared with the measured data using the proton recoil counter in the energy range between 63.25 keV and 5.238 MeV and ³He-Si diode spectrometer between 100 keV and 8 MeV. The neutron fluxes are normalized to the $4\pi r^2 \times$ leakage currents per source neutron per unit lethargy. The measured data by the ³He-Si diode spectrometer show slight discrepancies from those by the proton recoil measurements whose method is more established than that of the ³He-Si spectrometer, so that the data by the ³He-Si spectrometer are ignored.

From these figures, the neutron energy spectra in the energy range between 100 keV and 1 MeV calculated with JENDL-3 and with ENDF/B-IV are in good agreement regarding the spectral shape for resonances. The C/E values for the selected neutron energy ranges are shown in **Tables 3.4-3** and **3.4-4**. The error in the C/E table is estimated from the experimental error. The C/E values for the integrated flux in the energy range between 63.25 keV and 1 MeV are distributed from 0.95 to 1.17 with JENDL-3, and from 0.95 to 1.13 with ENDF/B-IV. The C/E values for the integrated flux in the energy range between 1 and 5.238 MeV are distributed from 1.27 to 1.35 with JENDL-3, and from 1.21 to 1.24 with ENDF/B-IV. The C/E values for the total neutrons in the whole measured energy range between 63.25 keV and 5.238 MeV are distributed from 1.20 to 1.25 with JENDL-3, and from 1.15 to 1.18 with ENDF/B-IV.

As the experimental error was estimated to be 25%, it can be said that both the results with JENDL-3 and ENDF/B-IV are in good agreement. However, the neutron energy spectrum below the 24 keV window with JENDL-3 is different from that with ENDF/B-IV. The difference decreases as penetration

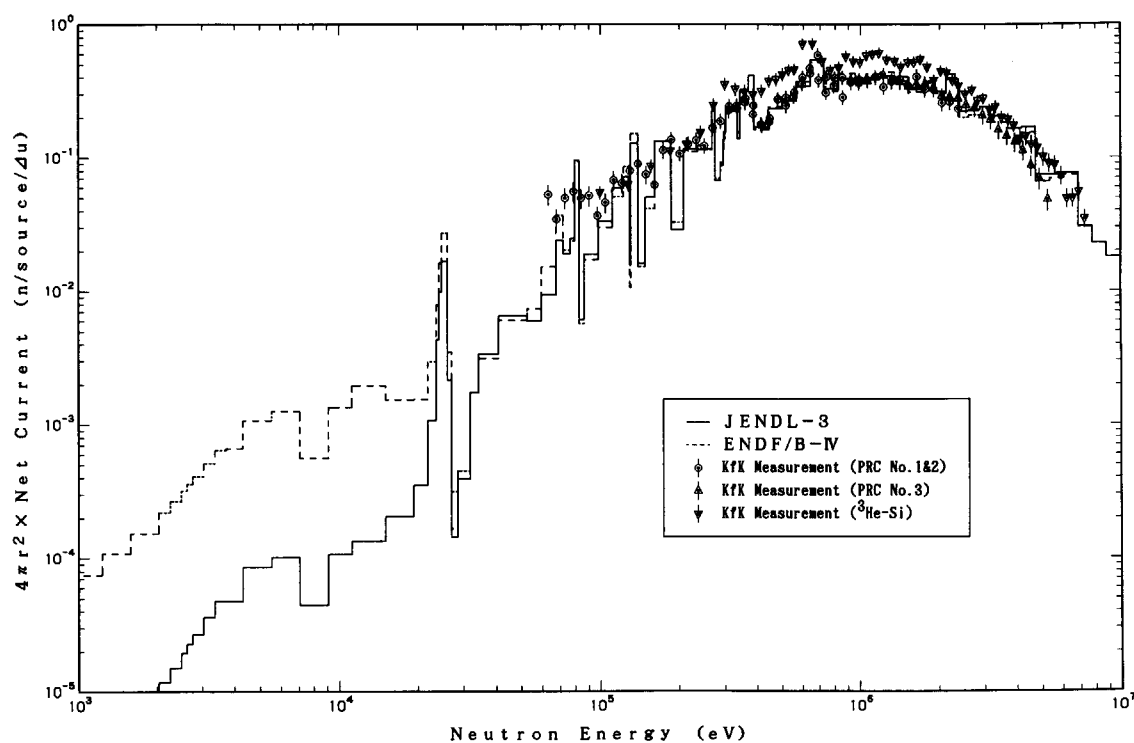


Fig. 3.4-3 Energy spectra of neutrons from the KfK iron sphere having a 15 cm diameter

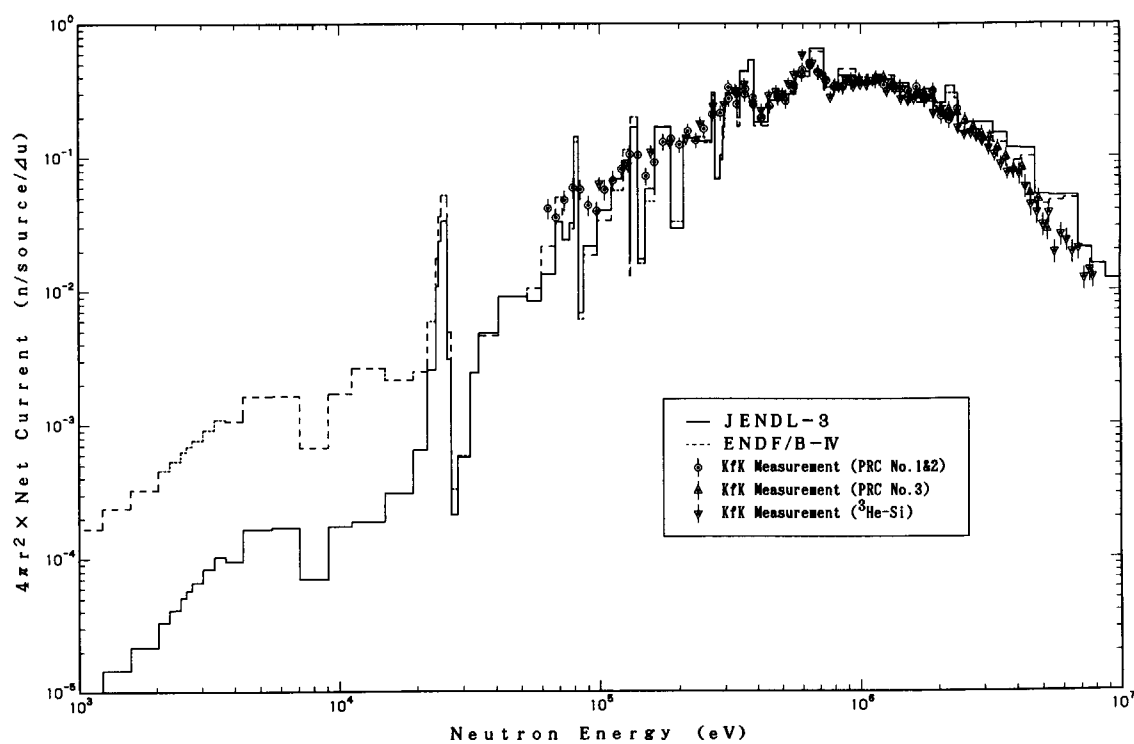


Fig. 3.4-4 Energy spectra of neutrons from the KfK iron sphere having a 20 cm diameter

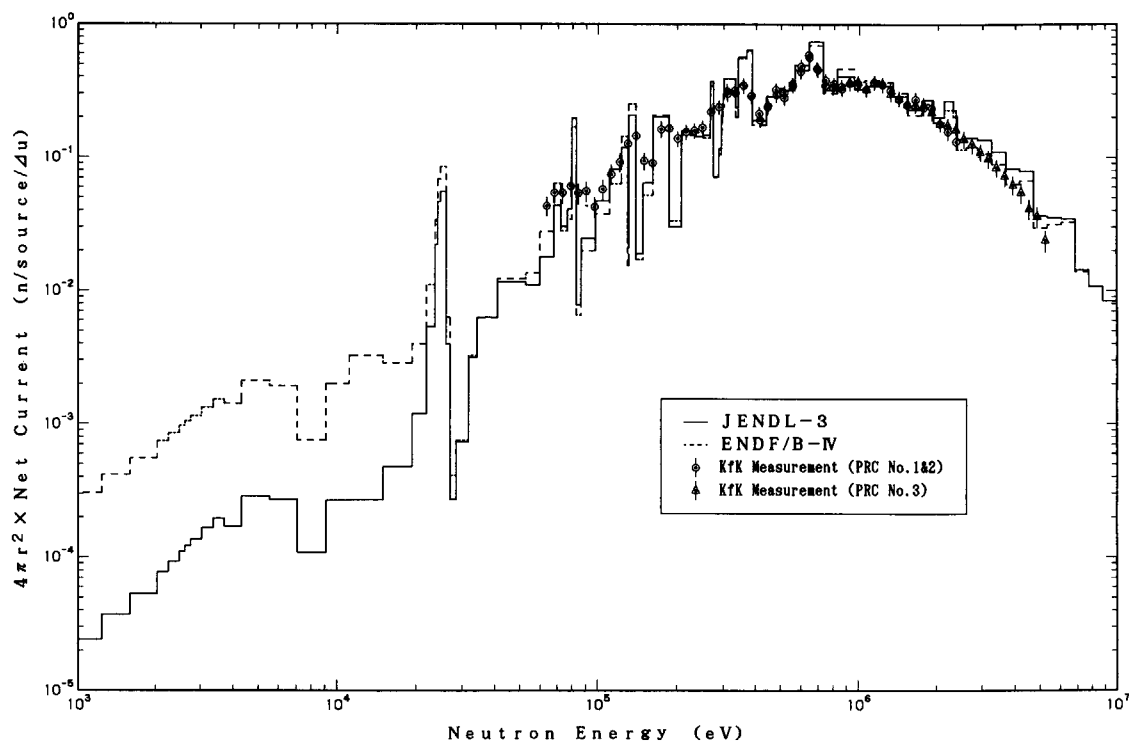


Fig. 3.4-5 Energy spectra of neutrons from the KfK iron sphere having a 25 cm diameter

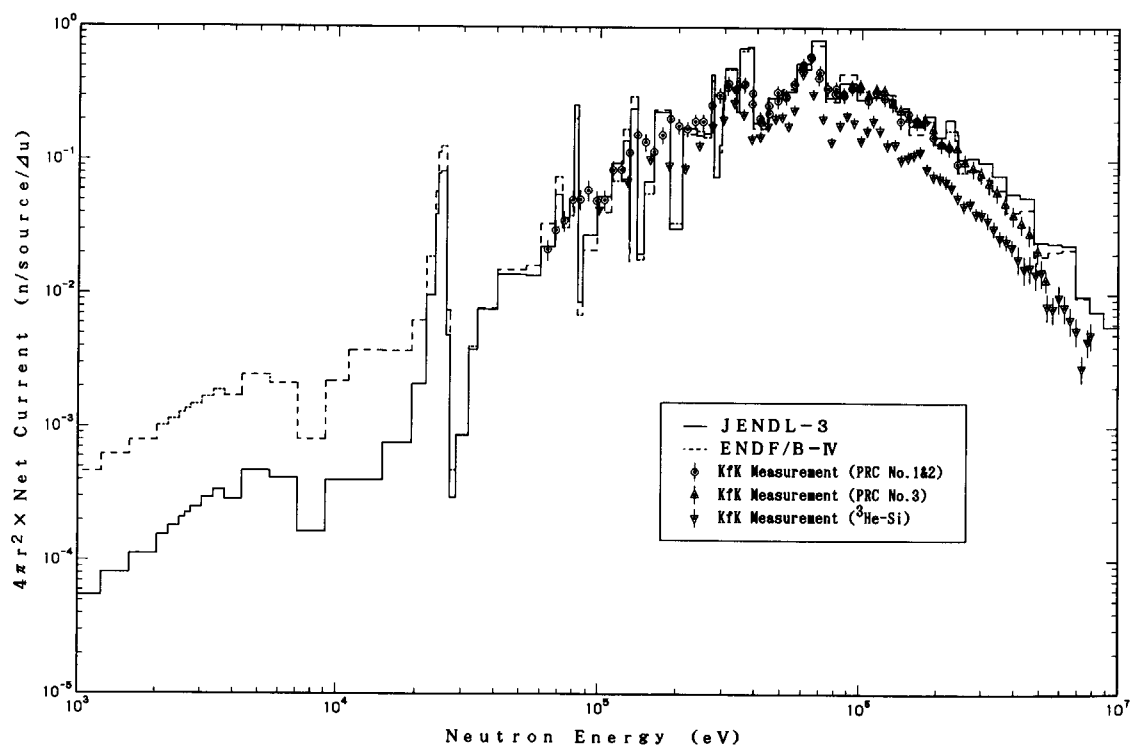


Fig. 3.4-6 Energy spectra of neutrons from the KfK iron sphere having a 30 cm diameter

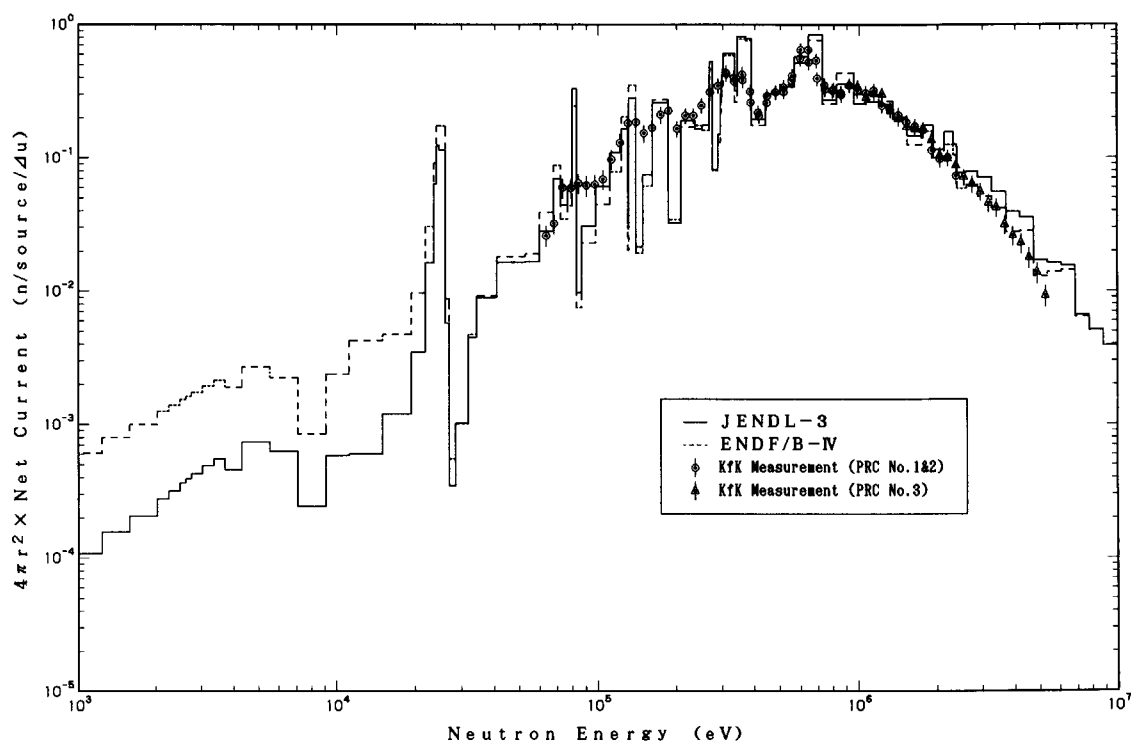


Fig. 3.4-7 Energy spectra of neutrons from the KfK iron sphere having a 35 cm diameter

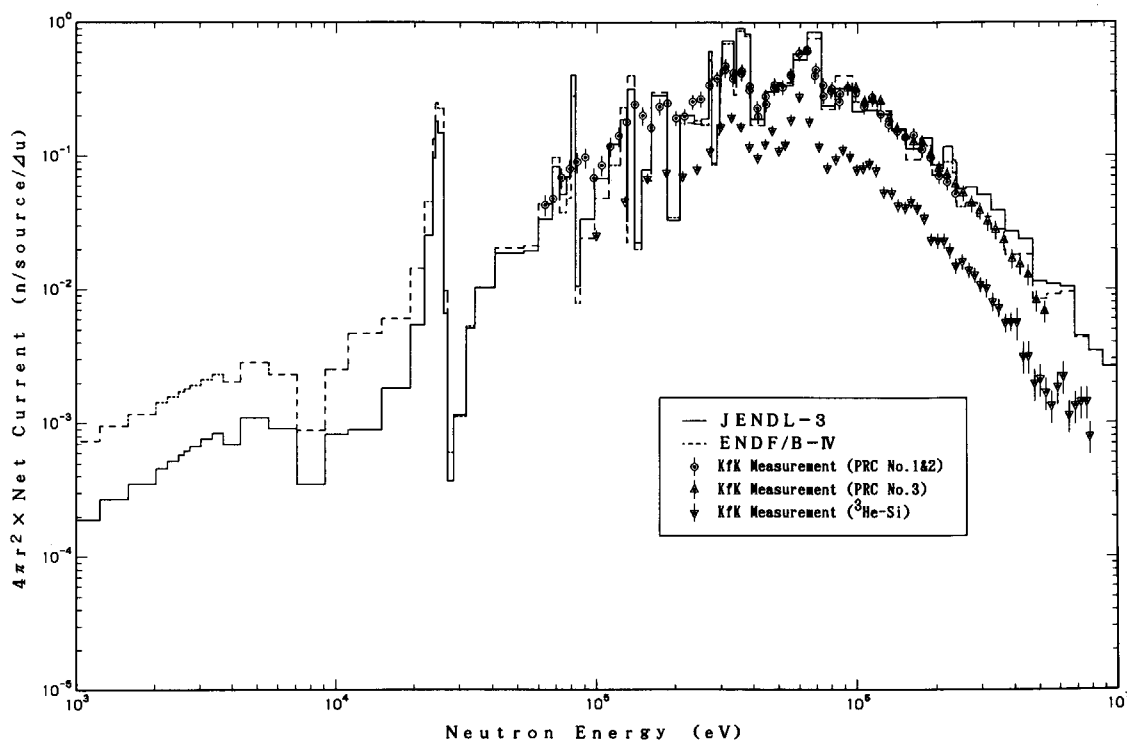


Fig. 3.4-8 Energy spectra of neutrons from the KfK iron sphere having a 40 cm diameter

depth increases. The decreasing tendency is attributed to the increasing multiple elastic scattering with penetration. The difference would indicate the evaluation for the discrete inelastic scattering cross sections is different from each other; however, we cannot determine which is an adequate evaluation, since there is no measured data below the 27 keV-resonance in the KfK experiments.

Table 3.4-3 C/E values for selected energy ranges from 63.25 keV to 5.238 MeV for the KfK iron experiments

Energy Range (eV)	$6.325 \times 10^4 \sim 1.000 \times 10^6$		$1.000 \times 10^6 \sim 5.238 \times 10^6$		$6.325 \times 10^4 \sim 5.238 \times 10^6$	
Diameter of Iron Sphere (cm)	C/E		C/E		C/E	
	JENDL-3	ENDF/B-IV	JENDL-3	ENDF/B-IV	JENDL-3	ENDF/B-IV
15	0.953 ^{+0.133} -0.104	0.952 ^{+0.133} -0.104	1.270 ^{+0.206} -0.155	1.210 ^{+0.196} -0.148	1.198 ^{+0.188} -0.143	1.151 ^{+0.181} -0.137
20	1.042 ^{+0.146} -0.114	1.031 ^{+0.144} -0.113	1.305 ^{+0.208} -0.158	1.229 ^{+0.196} -0.149	1.231 ^{+0.189} -0.145	1.174 ^{+0.181} -0.138
25	1.101 ^{+0.154} -0.120	1.081 ^{+0.151} -0.118	1.316 ^{+0.208} -0.158	1.228 ^{+0.194} -0.147	1.243 ^{+0.189} -0.145	1.178 ^{+0.179} -0.137
30	1.137 ^{+0.159} -0.124	1.109 ^{+0.155} -0.121	1.346 ^{+0.210} -0.160	1.247 ^{+0.194} -0.148	1.261 ^{+0.188} -0.145	1.191 ^{+0.178} -0.137
35	1.144 ^{+0.161} -0.125	1.109 ^{+0.156} -0.122	1.330 ^{+0.205} -0.156	1.228 ^{+0.189} -0.145	1.242 ^{+0.183} -0.141	1.172 ^{+0.173} -0.133
40	1.167 ^{+0.165} -0.128	1.127 ^{+0.159} -0.124	1.347 ^{+0.205} -0.157	1.242 ^{+0.190} -0.145	1.250 ^{+0.183} -0.141	1.180 ^{+0.173} -0.134

Table 3.4-4 C/E values for selected energy ranges from 63.25 keV to 1.0 MeV for the KfK iron experiments

Energy Range (eV)	$6.325 \times 10^4 \sim 1.000 \times 10^5$		$1.000 \times 10^5 \sim 5.000 \times 10^5$		$5.000 \times 10^5 \sim 1.000 \times 10^6$	
Diameter of Iron Sphere (cm)	C/E		C/E		C/E	
	JENDL-3	ENDF/B-IV	JENDL-3	ENDF/B-IV	JENDL-3	ENDF/B-IV
15	0.454 ^{+0.093} -0.066	0.499 ^{+0.102} -0.073	0.952 ^{+0.139} -0.107	0.925 ^{+0.135} -0.104	0.958 ^{+0.131} -0.103	0.966 ^{+0.132} -0.103
20	0.625 ^{+0.128} -0.091	0.656 ^{+0.134} -0.095	1.024 ^{+0.150} -0.116	0.981 ^{+0.143} -0.111	1.054 ^{+0.144} -0.113	1.056 ^{+0.144} -0.113
25	0.738 ^{+0.151} -0.107	0.730 ^{+0.149} -0.106	1.119 ^{+0.164} -0.127	1.057 ^{+0.155} -0.120	1.097 ^{+0.150} -0.118	1.096 ^{+0.149} -0.117
30	1.089 ^{+0.223} -0.158	1.005 ^{+0.206} -0.146	1.169 ^{+0.171} -0.133	1.091 ^{+0.160} -0.124	1.122 ^{+0.153} -0.120	1.119 ^{+0.153} -0.120
35	1.104 ^{+0.226} -0.160	0.953 ^{+0.195} -0.138	1.174 ^{+0.173} -0.134	1.082 ^{+0.159} -0.123	1.128 ^{+0.154} -0.121	1.125 ^{+0.153} -0.121
40	0.989 ^{+0.203} -0.144	0.801 ^{+0.164} -0.116	1.200 ^{+0.177} -0.137	1.095 ^{+0.162} -0.125	1.150 ^{+0.157} -0.123	1.151 ^{+0.157} -0.123

FERDOR code and those of about 70 keV to 1.5 MeV were derived by the SPEC-4 code from the Benjamin spectrometer results.

In **Table 3.5-1**, atomic number densities used in the analyses are given. It should be noted that contents of impurity, hydrogen, silicon and magnesium are given as maximum values.

3.5.2 Calculation Method

The present analyses were made for two thick sodium samples of 304.7 cm (10 ft) and 455.8 cm (15 ft) in length. Calculations of neutron fluxes in samples were carried out using DOT3.5¹³⁾ with the calculational condition given in **Table 3.5-2**, using the 100-group cross sections processed by PROF-GROUCH-G/B¹⁴⁾. The calculations were also done by using the cross sections generated with RADHEAT-V4¹⁵⁾ to make an intercomparison of the results with a different evaluated nuclear data file such as JENDL-2, -3 and ENDF/B-IV. **Figures 3.5-3** and **3.5-4** show the two-dimensional R-Z

Table 3.5-1 Atomic number densities for materials used
in the ORNL sodium benchmark experiments
(unit : atoms/cm³)

Elements	Sodium	Aluminum	Concrete
H	3.387×10^{19}	—	1.213×10^{22}
C	—	—	2.491×10^{21}
O	7.114×10^{18}	—	4.476×10^{22}
Na	2.473×10^{22}	—	1.045×10^{21}
Al	—	6.024×10^{22}	2.570×10^{21}
Si	—	—	1.197×10^{22}
K	$2.183 \times 10^{18*}$	—	$8.035 \times 10^{20**}$
Ca	$5.679 \times 10^{18*}$	—	$2.893 \times 10^{21**}$
Fe	—	—	8.028×10^{20}

N. B. *) Substituted with Si in the analysis.

**) Substituted with ENDF/B-IV data in the analysis.

Table 3.5-2 DOT3.5 calculational condition

Items	Condition
Number of groups	100 (JSD-1000 type group structure)
Cross sections	Processed by PROF-GROUCH-G/B with/without hydrogen Processed by RADHEAT-V4 without hydrogen (for comparison with the results using JENDL-2 and ENDF/B-IV)
Approximation	S8-P5 (S8-P3 for comparison with other library)
Model	Two-dimensional R-Z model (Figs. 3.5-3 and -4) 10-ft sample : 213.36 cm radius \times 324.65 cm long 15-ft sample : 213.36 cm radius \times 475.78 cm long
Number of spatial meshes	10-ft sample : 25 \times 38 meshes 15-ft sample : 25 \times 56 meshes
Neutron source	First collision source from a virtual point source located at a 131.13 cm distance from the sodium tank
Flux convergence criterion	Flux error < 1%
Solving mode	Weighted difference scheme
Acceleration	Rebalancing technique (in WWESOL)

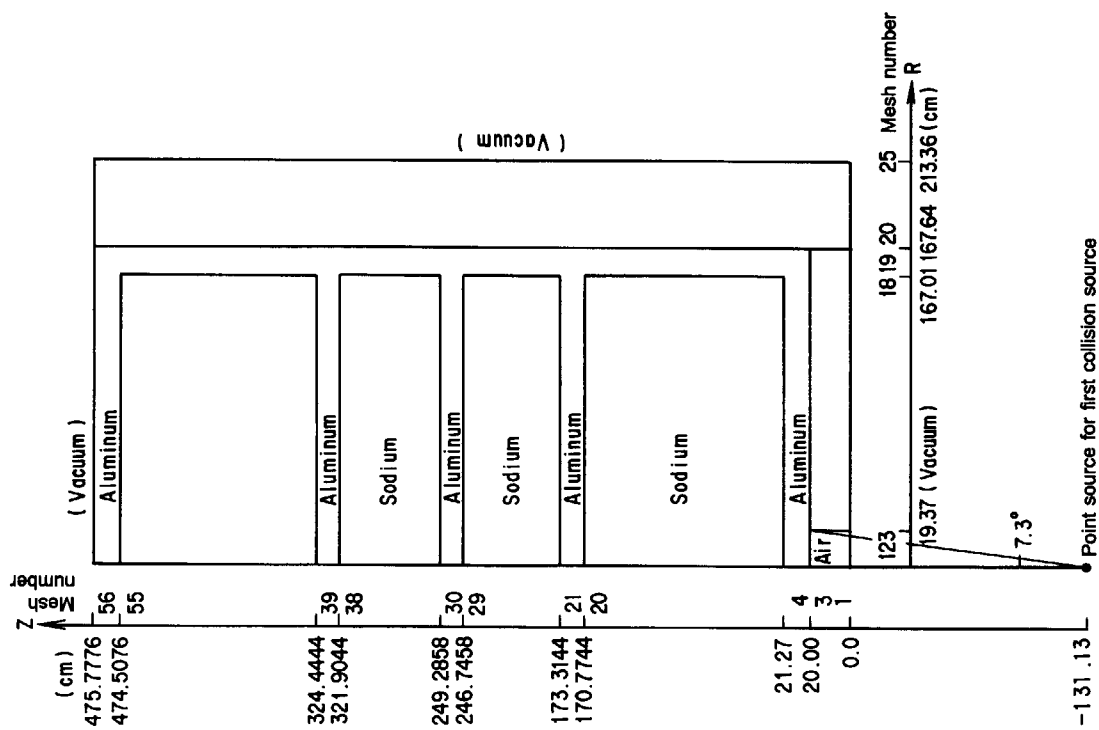


Fig. 3.5-4 Calculational RZ model of 15-ft-thick sodium

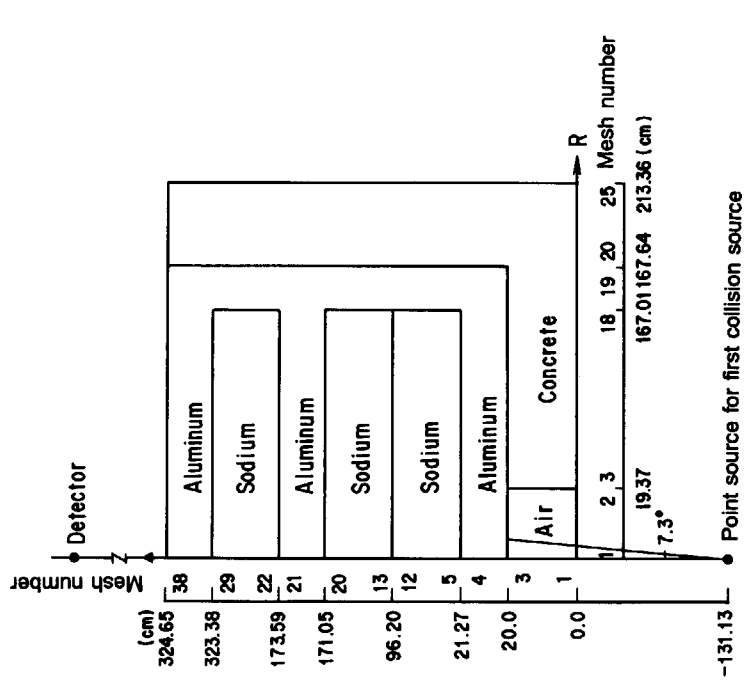


Fig. 3.5-3 Calculational RZ model of 10-ft-thick sodium

models which were composed of 25×38 meshes for 10-ft-thick sample and of 25×56 meshes for 15-ft-thick sample. To remedy the ray-effect due to a collimated beam source, we employed a treatment of the first collision source from a virtual point isotropic source at $Z = -131.13$ cm.

The neutrons at the detector behind the sample were estimated from the angular fluxes obtained with DOT3.5 and with the line-of-sight method by using the SPACETRAN code²¹⁾. Since the sizes of Bonner ball detectors were so large that effective detection centers were given at a slightly forward position from the real detector center as follows:

Detector type	: Cd covered BF ₃	3 in. Bonner	6 in. Bonner	10 in. Bonner	
Effective Center	:	-1.52 cm	-2.29 cm	-4.57 cm	-7.62 cm

The 100-group response functions of the Bonner ball detectors are the same as those used for the analyses of the ORNL iron benchmark experiments³⁾, which were described in Section 3.3.

3.5.3 Results

Since the content of impurity of hydrogen in the sodium was uncertain, the analyses using cross sections processed by PROF-GROUCH-G/B were performed with two kinds of macroscopic cross sections for sodium, considering the impurity of hydrogen with the reported maximum content and ignoring it, while the analyses by RADHEAT-V4 were made ignoring hydrogen impurity. The calculated results showed the effect of hydrogen to decrease the neutron transmission through strong slowing down of the fast neutrons.

Figure 3.5-5 shows the calculated and measured neutron spectra at 12 in. behind the 10-ft-thick

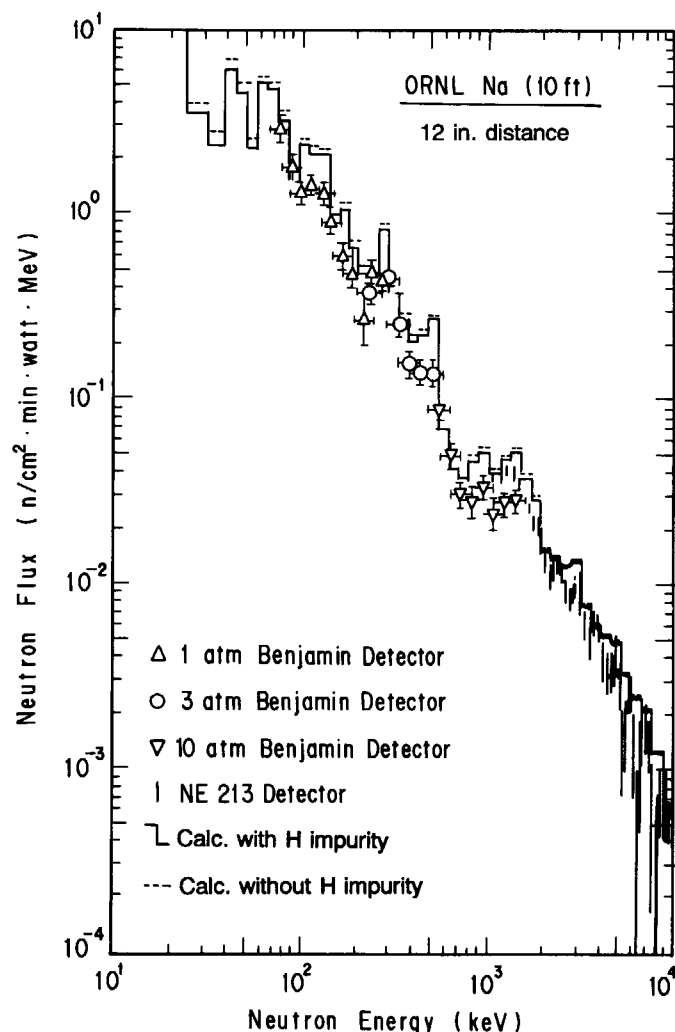


Fig. 3.5-5 Neutron spectra at 12 in. behind 10-ft-thick sodium

sodium sample. The calculated results with considering the impurity of hydrogen are slightly larger than the measured data: the C/E value ranges from 1.0 to 1.3. The calculation ignoring it still overestimates the fast neutron fluxes. The effect of hydrogen is larger in the lower energy regions than MeV neutron energy: Flux differences are -5% to 6% above 1 MeV, 12% to 15% in the keV region, 10% to 20% below 100 eV and 240% for thermal region.

The results for the Bonner ball detectors behind the 10-ft-thick sample are summarized in **Table 3.5-3**. In the case without hydrogen impurity, the results with PROF-GROUCH-G/B cross sections agree with those of RADHEAT-V4 within 3%, and two different code systems turned out reliable. **Figures 3.5-6** and **3.5-7** show the axial and radial traverse of the Bonner ball responses. As for axial traverse, the experimental values exist between the calculations with extreme two hydrogen contents. They show the similar profile uniformly decreasing with the distance from the sample. However, the radial traverse has a turning point near $R=24$ in. outside of which discrepancy between the experiments and calculations is prominent. The turning point can be related to the first collision source boundary and the underestimation may come from the approximation of source distribution. Another reason of the discrepancy may be attributed to an ambiguity of background correction, judging from the abrupt fall of the measured counts from $R=60$ in. to 72 in. Accordingly, data validation was made by taking account of the axial traverse data along main axis. **Figure 3.5-8** shows the C/E values for the axial traverse of the Bonner ball responses. The C/E values averaged over the data except for the nearest point (6 in.) data which are discrepant from the other data are given in **Table 3.5-4**.

The results for the 15-ft-thick sample are given in **Table 3.5-5** and **Figs. 3.5-9** through **3.5-11**. Excellent agreement with the experimental data is observed in **Fig. 3.5-9** for the results considering

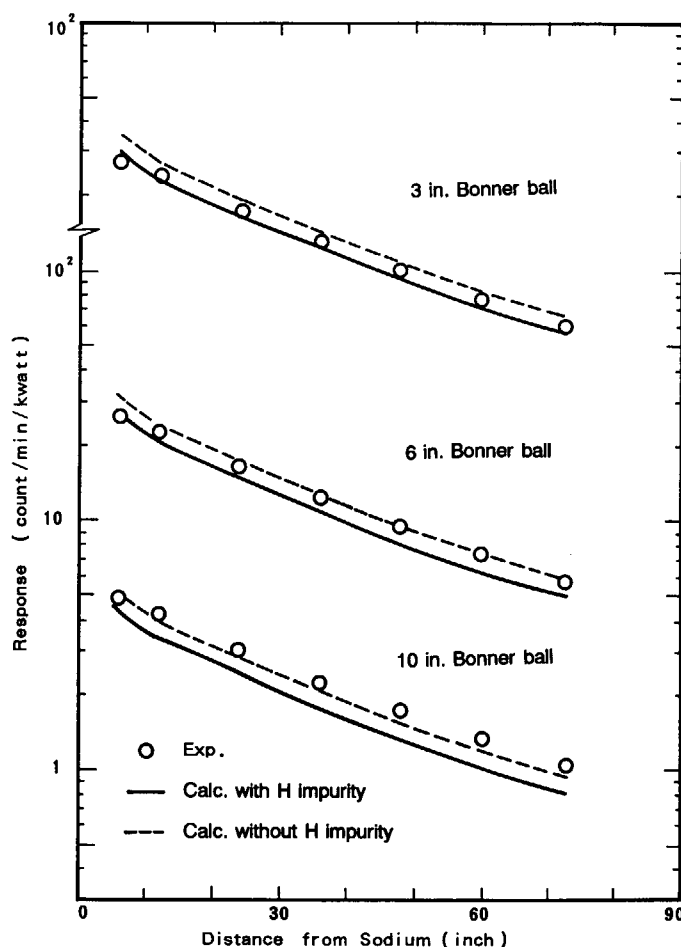


Fig. 3.5-6 Axial traverse of Bonner ball responses behind 10-ft-thick sodium

Table 3.5-3 Comparison of Bonner ball responses behind 10-ft-thick sodium and their C/E values

(unit : counts/min/Watt)

	Position		Measured value				Calc. PROF-GROUCH-G/B				Calc. PROF-GROUCH-G/B (without H)				Calc. RADHEAT-V4 (without H)			
	R	Z	3"	6"	10"	BF ₃ /Cd	3"	6"	10"	BF ₃ /Cd	3"	6"	10"	BF ₃ /Cd	3"	6"	10"	BF ₃ /Cd
1	0	6"	27.5	26.7	4.90	3.08	30.0 (1.09)	27.1 (1.01)	4.43 (0.90)	3.10 (1.01)	34.2 (1.24)	30.9 (1.16)	5.02 (1.02)	3.47 (1.13)	34.9 (1.27)	31.7 (1.19)	5.15 (1.05)	3.53 (1.15)
2	0	12"	23.5	22.8	4.17	2.66	22.9 (0.97)	20.5 (0.90)	3.33 (0.80)	2.39 (0.90)	26.2 (1.11)	23.5 (1.03)	3.79 (0.91)	2.68 (1.01)	26.8 (1.14)	24.1 (1.06)	3.89 (0.93)	2.73 (1.03)
3	0	24"	17.3	16.7	3.01	1.96	16.86 (0.97)	14.99 (0.90)	2.49 (0.83)	1.77 (0.90)	19.28 (1.11)	17.19 (1.03)	2.76 (0.92)	1.990 (1.02)	19.70 (1.14)	17.62 (1.06)	2.83 (0.94)	2.02 (1.03)
4	0	36"	13.0	12.6	2.26	1.50	12.20 (0.94)	10.78 (0.86)	1.739 (0.77)	1.29 (0.86)	13.96 (1.07)	12.37 (0.98)	1.982 (0.88)	1.451 (0.97)	14.27 (1.10)	12.69 (1.01)	2.03 (0.90)	1.476 (0.98)
5	0	48"	10.1	9.52	1.71	1.14	9.29 (0.92)	8.18 (0.86)	1.320 (0.77)	0.98 (0.86)	10.64 (1.05)	9.40 (0.99)	1.505 (0.88)	1.108 (0.97)	10.87 (1.08)	9.64 (1.01)	1.544 (0.90)	1.128 (0.99)
6	0	60"	7.78	7.41	1.33	0.888	7.15 (0.92)	6.29 (0.85)	1.012 (0.76)	0.76 (0.86)	8.20 (1.05)	7.22 (0.97)	1.155 (0.87)	0.857 (0.97)	8.38 (1.08)	7.41 (1.00)	1.185 (0.89)	0.872 (0.98)
7	0	72.4"	6.07	5.78	1.03	0.707	5.67 (0.93)	4.98 (0.86)	0.801 (0.78)	0.604 (0.85)	6.50 (1.07)	5.72 (0.99)	0.914 (0.89)	0.681 (0.96)	6.65 (1.10)	5.87 (1.02)	0.938 (0.91)	0.693 (0.98)
8	0	2"	30.6	—	—	3.55	39.0 (1.27)	35.3 (—)	5.78 (—)	4.02 (1.13)	44.4 (1.45)	40.4 (—)	6.55 (—)	4.49 (1.26)	45.4 (1.48)	41.4 (—)	6.72 (—)	4.57 (1.29)
9	12"	2"	28.8	—	—	3.36	28.3 (0.98)	25.5 (—)	4.14 (—)	2.95 (0.88)	32.4 (1.13)	29.2 (—)	4.70 (—)	3.31 (0.99)	33.1 (1.15)	29.9 (—)	4.83 (—)	3.36 (1.00)
10	24"	2"	25.3	—	—	2.95	24.5 (0.97)	21.8 (—)	3.50 (—)	2.58 (0.87)	28.1 (1.11)	25.0 (—)	3.99 (—)	2.90 (0.98)	28.7 (1.13)	25.6 (—)	4.10 (—)	2.95 (1.00)
11	36"	2"	20.3	—	—	2.39	13.8 (0.68)	12.02 (—)	1.909 (—)	1.475 (0.62)	15.86 (0.78)	13.86 (—)	2.19 (—)	1.667 (0.70)	16.2 (0.80)	14.2 (—)	2.25 (—)	1.697 (0.71)
12	48"	2"	14.0	—	—	1.69	7.31 (0.52)	6.26 (—)	0.984 (—)	0.798 (0.47)	8.44 (0.60)	7.24 (—)	1.132 (—)	0.906 (0.54)	8.63 (0.62)	7.44 (—)	1.163 (—)	0.923 (0.55)
13	60"	2"	7.34	—	—	0.909	3.03 (0.41)	2.54 (—)	0.398 (—)	0.340 (0.37)	3.51 (0.48)	2.95 (—)	0.459 (—)	0.388 (0.43)	3.59 (0.49)	3.03 (—)	0.472 (—)	0.395 (0.43)
14	72"	2"	0.64	—	—	0.083	0.867 (1.35)	0.723 (—)	0.1133 (—)	0.0983 (1.18)	1.004 (1.57)	0.838 (—)	0.1306 (—)	0.1123 (1.35)	1.029 (1.61)	0.861 (—)	0.1343 (—)	0.115 (1.39)

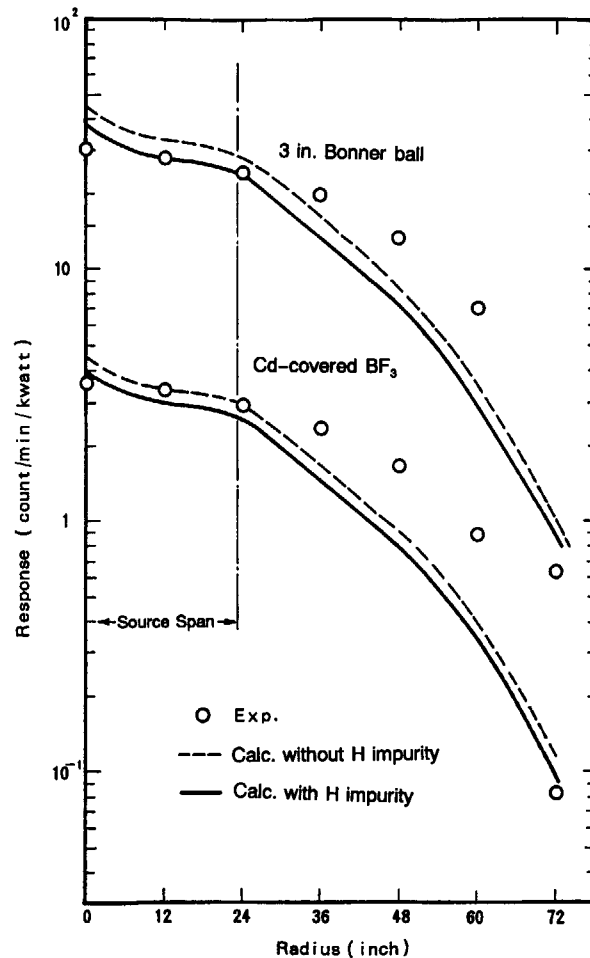


Fig. 3.5-7 Radial traverse of Bonner ball responses at 24 in. distant behind 10-ft-thick sodium

Table 3.5-4 Average C/E values of Bonner ball responses

Sodium thickness	Hydrogen content	Cd-covered BF_3	3-in.	6-in.	10-in.
10 ft.	Maximum	0.87	0.94	0.87	0.79
	Ignored	1.00	1.10	1.03	0.91
15 ft.	Maximum	0.91	0.98	0.90	0.79
	Ignored	1.21	1.33	1.22	1.07

hydrogen impurity. **Figure 3.5-10** shows the radial traverse of 3 in. Bonner ball responses. In the figure, triangle denotes the experimental values corrected for background by assuming the background was 25 counts/min/kwatt which was reported for the data on the center axis. It shows good agreement with the calculations with hydrogen impurity. It is also found by comparing the C/E values with those for 10-ft-thick sample that the effect of hydrogen becomes larger. For the axial traverse, calculated response shows a faster decrease in the range of 6 in. to 24 in. from the sample than the experiments. This tendency is obvious in the C/E value distributions given in **Fig. 3.5-11**. The average C/E values are given in **Table 3.5-4**. The C/E values in the case of considering hydrogen impurity are as much as those obtained for the 10-ft-thick sample and are near unity. Even in the worst case neglecting hydrogen, JENDL-3 predicted neutron transmission within sodium layer up to 15-ft thickness with an accuracy of 30%.

It is natural to think that one reason of the overestimation of the transmitted neutron fluxes is the

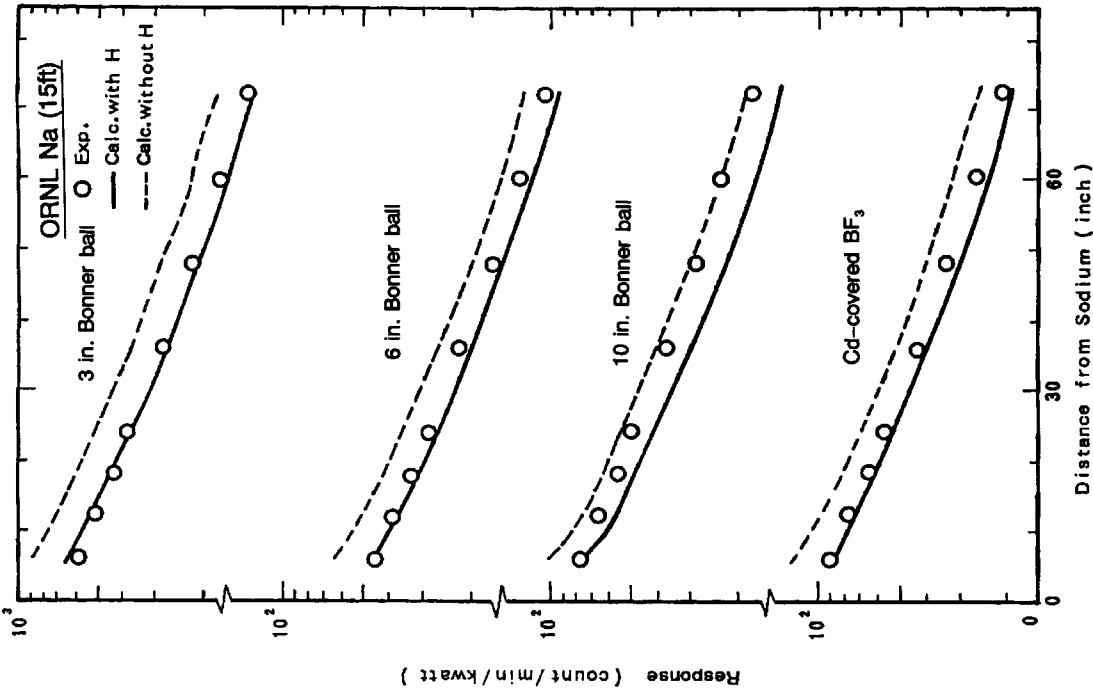


Fig. 3.5-9 Axial traverse of Bonner ball responses behind the 15-ft-thick sodium

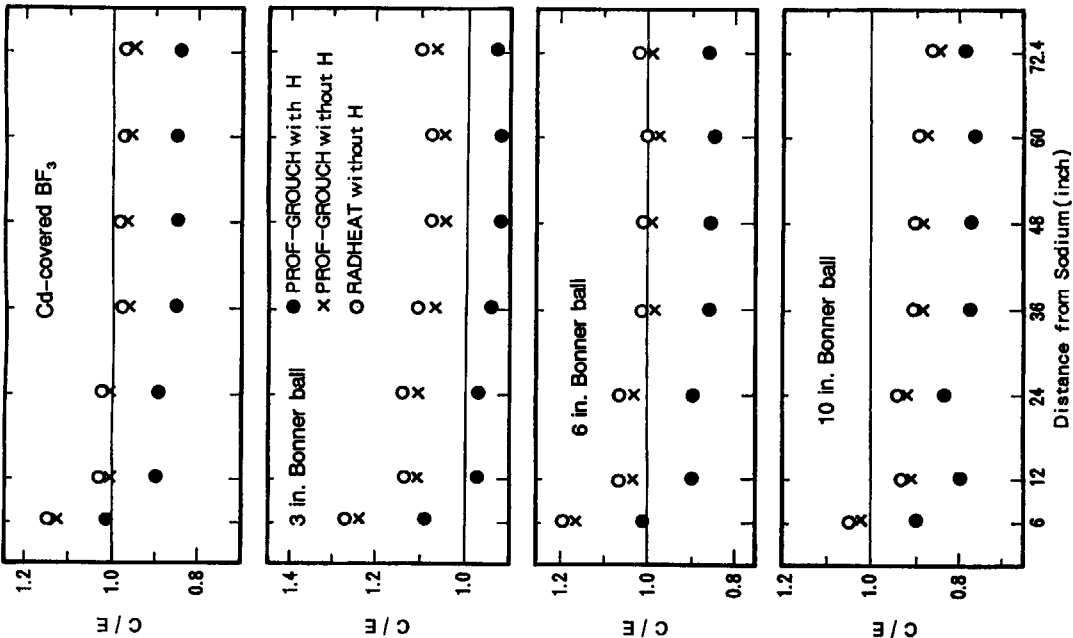


Fig. 3.5-8 Comparison of C/E values for Bonner ball responses in the case of 10-ft-thick sodium

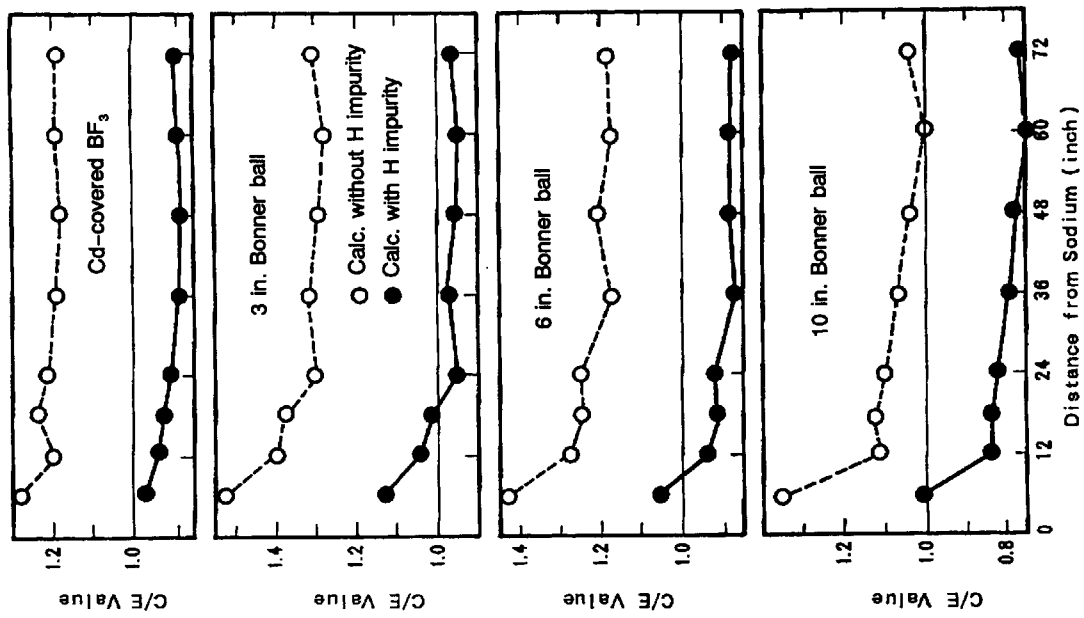


Fig. 3.5-11 Comparison of C/E values for Bonner ball responses in the case of 15-ft-thick sodium

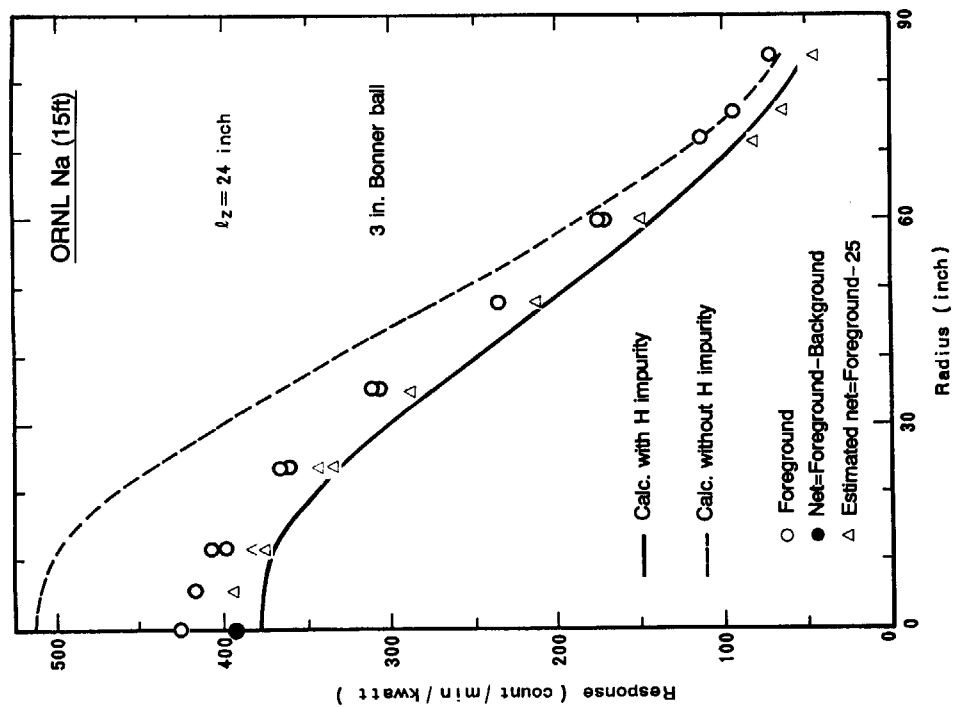


Fig. 3.5-10 Radial traverse of 3 in. Bonner ball responses at 24 in. distant behind 15-ft-thick sodium

Table 3.5-5 Comparison of Bonner ball responses behind 15-ft-thick sodium and their C/E values

Position		PROF-GROUCH-G/B						PROF-GROUCH-G/B (without H)						RADHEAT-V4 (without H)						RADHEAT-V4 (1.05 times density, without H)					
		R	Z	3"	6"	10"	BF ₃ /Cd	3"	6"	10"	BF ₃ /Cd	3"	6"	10"	BF ₃ /Cd	3"	6"	10"	BF ₃ /Cd	3"	6"	10"	BF ₃ /Cd		
1	0			0.663 (1.13)	0.482 (1.06)	0.0777 (1.01)	0.0890 (0.97)	0.859 (1.47)	0.623 (1.38)	0.100 (1.30)	0.115 (1.25)	0.894 (1.53)	0.651 (1.44)	0.105 (1.36)	0.119 (1.29)	0.552 (0.94)	0.391 (0.86)	0.0624 (0.81)	0.0760 (0.83)						
2	0		12"	0.525 (1.04)	0.370 (0.94)	0.0549 (0.83)	0.0716 (0.94)	0.680 (1.34)	0.479 (1.22)	0.0708 (1.07)	0.0923 (1.21)	0.708 (1.40)	0.500 (1.28)	0.0740 (1.11)	0.0918 (1.20)	0.436 (0.86)	0.299 (0.76)	0.0441 (0.66)	0.0610 (0.80)						
3	0		18"	0.446 (1.01)	0.311 (0.92)	0.0472 (0.84)	0.0611 (0.93)	0.579 (1.32)	0.402 (1.19)	0.0609 (1.08)	0.0789 (1.20)	0.603 (1.38)	0.420 (1.25)	0.0636 (1.13)	0.0819 (1.24)	0.371 (0.85)	0.251 (0.74)	0.0378 (0.67)	0.0520 (0.79)						
4	0		24"	0.379 (0.96)	0.267 (0.92)	0.0406 (0.82)	0.0521 (0.91)	0.492 (1.25)	0.345 (1.19)	0.0524 (1.05)	0.0672 (1.18)	0.513 (1.30)	0.361 (1.25)	0.0548 (1.10)	0.0698 (1.22)	0.315 (0.80)	0.215 (0.74)	0.0324 (0.65)	0.0443 (0.78)						
5	0		36"	0.278 (0.98)	0.193 (0.87)	0.0291 (0.79)	0.0384 (0.89)	0.361 (1.27)	0.250 (1.13)	0.0376 (1.02)	0.0495 (1.15)	0.377 (1.32)	0.261 (1.18)	0.0393 (1.07)	0.0514 (1.20)	0.231 (0.81)	0.155 (0.70)	0.0233 (0.63)	0.0325 (0.76)						
6	0		48"	0.212 (0.96)	0.148 (0.89)	0.0221 (0.77)	0.0293 (0.89)	0.275 (1.25)	0.192 (1.15)	0.0285 (1.00)	0.0378 (1.15)	0.287 (1.30)	0.201 (1.21)	0.298 (1.04)	0.0393 (1.19)	0.176 (0.80)	0.119 (0.78)	0.176 (0.62)	0.0248 (0.75)						
7	0		60"	0.164 (0.95)	0.114 (0.88)	0.0171 (0.74)	0.0226 (0.89)	0.212 (1.23)	0.148 (1.14)	0.0220 (0.96)	0.0292 (1.15)	0.221 (1.28)	0.154 (1.18)	0.0230 (1.00)	0.0303 (1.20)	0.135 (0.78)	0.0915 (0.70)	0.0136 (0.59)	0.0191 (0.75)						
8	0		72"	0.131 (0.97)	0.0908 (0.88)	0.0136 (0.77)	0.0181 (0.90)	0.170 (1.26)	0.118 (1.15)	0.0175 (0.99)	0.0234 (1.15)	0.177 (1.31)	0.123 (1.19)	0.0183 (1.04)	0.0243 (1.20)	0.108 (0.80)	0.0729 (0.71)	0.0108 (0.61)	0.0153 (0.76)						

(unit : counts/min/Watt)

(unit : counts/min/Watt)

uncertainty of cross sections or sodium density. **Table 3.5-5** also shows the results of calculation with macroscopic cross sections provisionally increased by 5% which is likely maximum uncertainty of sodium total cross section. The C/E values are decreased by 33-41% from those for the calculations with the RADHEAT-V4 cross section without hydrogen impurity. The results shows that the overestimation of fluxes by about 10% can be explained with cross section underestimation by 1.2-1.5%. However, since the deviation of cross sections from true values must be at random, the true effect of the cross-section uncertainty may be smaller than the values mentioned above.

Comparison of neutron spectra indicates the reliability of JENDL-3 in the high energy region above 70 keV, although it is limited to the 10-ft-thick sample. The C/E value was 1.0-1.3 in the case with the maximum content of hydrogen impurity. As the content of hydrogen impurity is decreased, fast neutron fluxes increase; the uncertainty of hydrogen impurity brings errors of about 10% in maximum into the fast neutron fluxes above 10 keV.

Most responses of Bonner ball detectors are contributed by slow neutrons below 10 keV, because the sodium sample was so long that fast neutrons were moderated to lower energy. Therefore, the C/E values of the Bonner ball responses become a measure of reliability for low energy. The C/E values in the case with the maximum hydrogen content are 0.79 to 0.94 for 10-ft-thick sample and 0.79 to 0.98 for 15-ft-thick sample. Considering the actual hydrogen impurity could be fewer than the maximum value, the C/E values may be closer to unity.

Table 3.5-6 compares the average C/E values for the Bonner ball response calculated with different libraries, using group cross sections without hydrogen impurity. The JENDL-3 result is the closest to unity. Since the C/E values in the actual hydrogen content should become lower than the value in the table, JENDL-3 is considered to be the most reliable data to calculate the neutron fluxes, at least in the energy region below 10 keV neutrons which give a dominant contribution to the Bonner ball responses.

Accordingly, it can be said that the JENDL-3 sodium cross sections give reliable neutron fluxes transmitted through the thick sodium sample. This characteristics can be expected for a thinner sodium sample.

Table 3.5-6 Average C/E values of Bonner ball responses for 10-ft-thick sodium. The analyses were made using P3 cross sections generated with RADHEAT-V4, ignoring hydrogen impurity

Detector	JENDL-3	JENDL-2	ENDF/B-IV
Cd-covered BF ₃	1.0	0.7	0.8
3-in. Bonner Ball	1.1	0.8	0.9
6-in. Bonner Ball	1.05	0.9	0.9
10-in. Bonner Ball	1.0	0.9	0.85

3.6 RPI Graphite Experiments

3.6.1 Outline of Experiments

The neutron energy spectra from a fission source in graphite were measured⁷⁾. General arrangement of experiments is shown in **Fig. 3.6-1**. Graphite stack for neutron spectrum measurement is given in **Fig. 3.6-2**. Neutron source generator was a depleted uranium target at the center of the graphite stack. The composition of each material is shown in **Table 3.6-1**. Twenty-eight MeV electrons from an electron linear accelerator were shot into the target. The energy distribution of neutron source was similar to a fission spectrum. The normalized total leakage spectrum from the target surface is given in **Table 3.6-2**, and cumulative probability for source angular distribution is given in **Table 3.6-3**. Neutron angular spectra were measured using the time-of-flight method at several points of the graphite. A liquid scintillator of $5.08 \text{ cm} \phi \times 5.08 \text{ cm}$ long (NE211) or $12.7 \text{ cm} \phi \times 12.7 \text{ cm}$ long was used for measurements

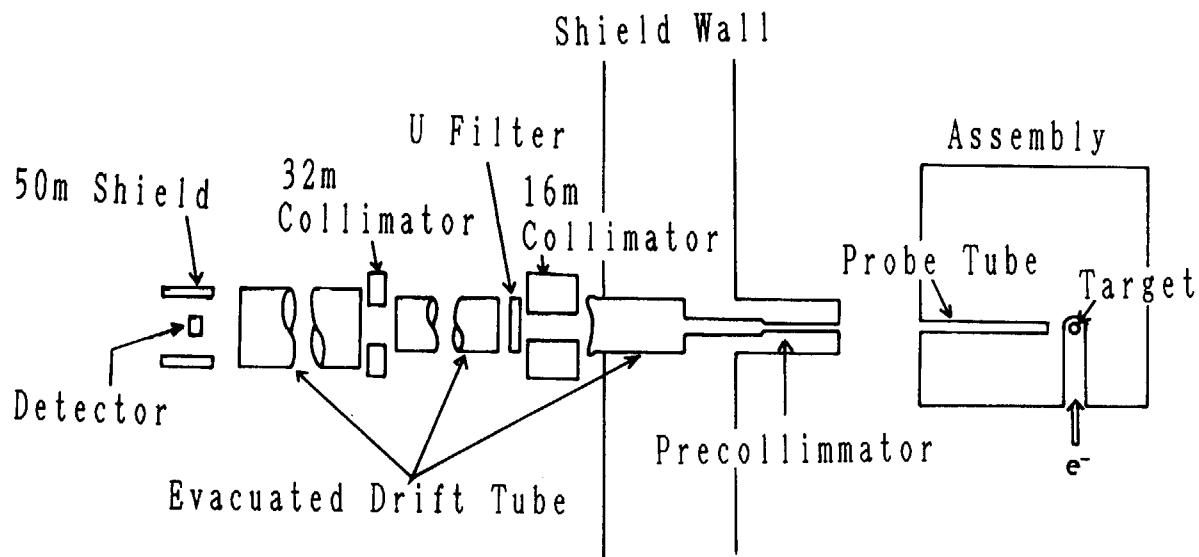


Fig. 3.6-1 Schematic experimental layout⁷⁾

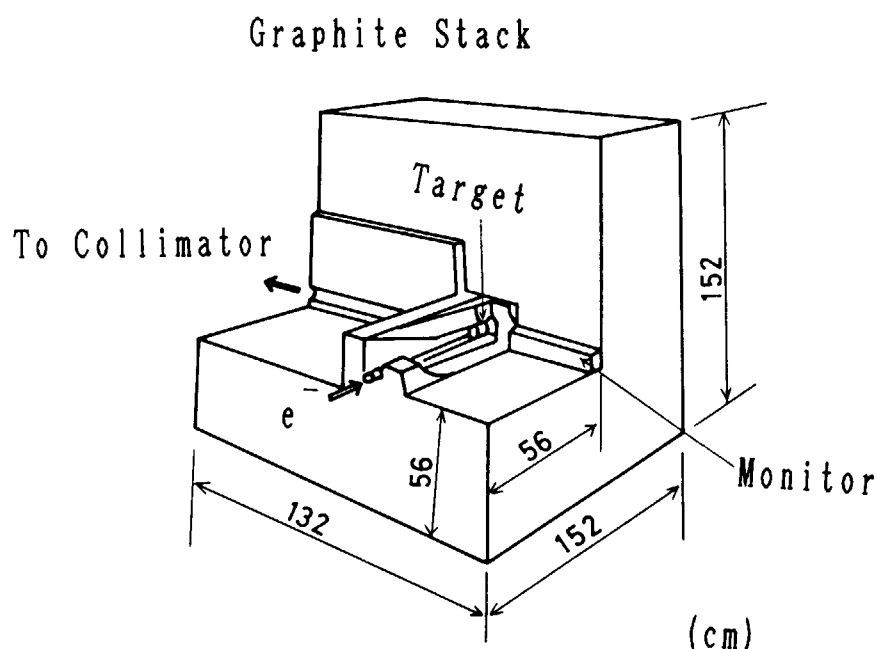


Fig. 3.6-2 Graphite stack for neutron spectrum measurement⁷⁾

Table 3.6-1 Composition of materials

Region	Nuclide	Atomic density (atom/cm ³)
Target	U-238	4.796+22*
	U-235	1.071+20
Cooling water & iron	H	4.965+22
	O	2.482+22
	Fe	2.187+22
Air	N	4.250+19
	O	1.130+19
Graphite	C	8.330+22

*) Read as 4.796×10^{22} .

above 0.8 MeV. The geometry of source region can be modeled by sphere as described **Fig.3.6-3**. The results of experiment were normalized to a reaction rate of $^{32}\text{S}(n,p)^{32}\text{P}$ reaction. The neutron source was given as the leakage spectrum at the depleted uranium target and normalized in the same way. Therefore, the comparisons of experiments and calculated results can be absolutely made.

3.6.2 Calculation Method

The calculation was made by using a spherical model and a one-dimensional discrete ordinate code ANISN¹¹⁾ with 100 energy groups and S32-P5. The calculation model is shown in **Fig. 3.6-4**. The neutron source was modeled as a shell source just outside the uranium target. The cross-section library is JSSTD-100 obtained from JSSTD-120²²⁾, but the nitrogen included in the air was neglected.

Generally, angular fluxes of discrete directions are given from the Sn calculation. Angular fluxes of desired directions are obtained by inter/extrapolation using 32nd order Legendre expansion.

3.6.3 Results

The calculated and experimental results are compared with each other in **Figs. 3.6-5 to 3.6-15** (Unit of vertical axis of **Figs. 3.6-5 to 3.6-8** is different from one of **Figs. 3.6-9 to 3.6-15**, to set adapt to the original paper.). The calculated results are in good agreement with the experiment in the energy range between 600 keV and 9 MeV, except for the angular flux at 0 degrees. At 0 degrees, the S32-P5 approximation may not be sufficient, since calculated angular flux has a very sharp forward peak. Angular distributions of neutron flux at $R=50.8$ cm and $E=1$ MeV, 2 MeV, 5 MeV are shown in **Figs. 3.6-16 to 3.6-18**, respectively. The forward peak is shown in the energy above 1 MeV, but the forward peak does not appear at 1 MeV. On the other hand, the calculated energy distribution of angular flux at 0 degree, $R=50.8$ cm is in good agreement with the experiment for the energy below 1 MeV, but some discrepancies can be seen for energy above 1 MeV. This can be understood by the consideration that the 32nd Legendre expansion of the angular flux cannot express the sharp forward peak. Therefore, we did not adopt the results of 0 degrees for the evaluation.

Table 3.6-2 Normalized total leakage spectrum from target

Energy(eV)	N(E)	Energy(eV)	N(E)
2.28+5*	9.3922-7	1.430+6	2.2159-7
2.39+5	8.8415-7	1.480+6	2.0672-7
2.51+5	9.2784-7	1.550+6	1.9265-7
2.64+5	8.8965-7	1.610+6	1.8116-7
2.78+5	9.0278-7	1.680+6	1.6438-7
2.94+5	8.4926-7	1.760+6	1.5583-7
3.10+5	8.6542-7	1.840+6	1.4496-7
3.28+5	8.9883-7	1.920+6	1.3060-7
3.48+5	9.3518-7	2.010+6	1.2216-7
3.69+5	9.6676-7	2.110+6	1.1287-7
3.92+5	8.7166-7	2.220+6	1.0589-7
4.18+5	9.1609-7	2.330+6	9.7190-8
4.47+5	9.1462-7	2.450+6	8.1821-8
5.13+5	8.4449-7	2.580+6	7.9492-8
5.52+5	8.4412-7	2.730+6	7.4866-8
5.95+5	7.8868-7	2.880+6	6.4034-8
6.43+5	7.4499-7	3.050+6	5.9922-8
6.98+5	6.7266-7	3.230+6	5.2762-8
7.60+5	6.0840-7	3.440+6	4.7438-8
7.76+5	6.9065-7	3.660+6	4.1711-8
7.99+5	6.2970-7	3.900+6	3.7708-8
8.23+5	6.0179-7	4.170+6	3.2373-8
8.75+5	5.3166-7	4.460+6	2.7960-8
9.03+5	5.0926-7	4.790+6	2.4145-8
9.32+5	4.6667-7	5.160+6	2.0418-8
9.62+5	4.3767-7	5.570+6	1.7128-8
9.94+5	4.0022-7	6.030+6	1.4151-8
1.03+6	3.8773-7	6.560+6	1.0589-8
1.06+6	3.6298-7	7.150+6	7.7620-9
1.10+6	3.4389-7	7.830+6	5.5002-9
1.14+6	3.2553-7	8.600+6	3.4433-9
1.18+6	3.0435-7	9.500+6	2.1226-9
1.22+6	2.8540-7	1.055+7	1.1408-9
1.27+6	2.6264-7	1.179+7	5.7095-9
1.32+6	2.4446-7	1.325+7	2.7828-9
1.37+6	2.3201-7	1.552+7	1.0453-9

*) Read as 2.28×10^5 .

Table 3.6-3 Cumulative probability for source angular distribution

E (MeV)	COS (θ)								
	1.00-0.99	0.99-0.875	0.875-0.750	0.750-0.625	0.625-0.500	0.500-0.375	0.375-0.250	0.250-0.125	0.125-0.0
15.00-10.00	0.37515	0.94507 ^{*)}	0.98778	0.99932	1.00000	1.00000	1.00000	1.00000	1.00000
10.00- 6.70	0.33607	0.86961	0.92311	0.94178	0.99883	1.00000	1.00000	1.00000	1.00000
6.70- 4.49	0.31717	0.87134	0.94723	0.97849	0.99208	0.99749	0.99952	1.00000	1.00000
4.49- 3.01	0.29114	0.82415	0.91232	0.95396	0.97613	0.98740	0.99332	0.99762	1.00000
3.01- 2.02	0.28429	0.80479	0.89597	0.94233	0.96926	0.98280	0.98957	0.99594	1.00000
2.02- 1.35	0.26970	0.77257	0.87008	0.92375	0.95728	0.97561	0.98558	0.99449	1.00000
1.35- 0.82	0.22590	0.69746	0.81994	0.89410	0.94317	0.97010	0.98376	0.99410	1.00000
0.821- 0.49	0.16473	0.58862	0.74387	0.84549	0.91607	0.95609	0.97677	0.99171	1.00000
0.498- 0.30	0.12122	0.49596	0.66771	0.78725	0.87424	0.93058	0.96545	0.98850	1.00000
0.302- 0.20	0.09054	0.42435	0.60527	0.73822	0.83941	0.91234	0.96142	0.98687	1.00000

*) Probability is a cumulative value, i.e., the value is added the probability of interval $\cos(\theta) = 1.00$ to 0.99.

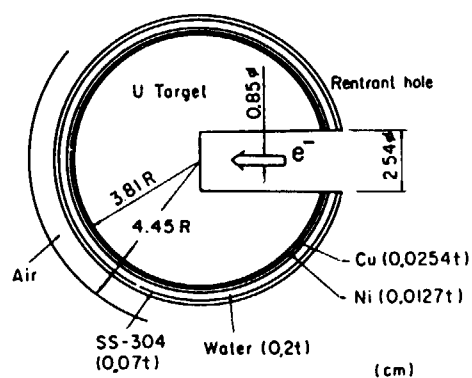
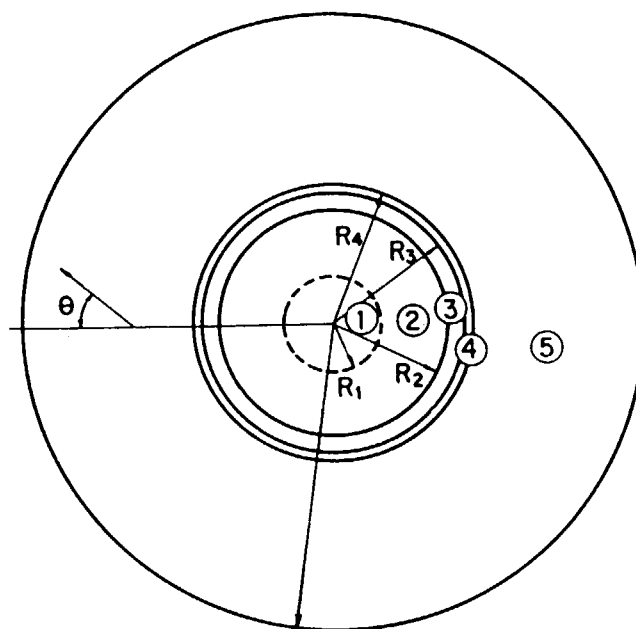


Fig. 3.6-3 Depleted uranium target



- | | |
|--|-------------------------|
| ① Depleted U Target
(photoneutron source) | $R_1 = 0.85 \text{ cm}$ |
| ② Depleted U Target | $R_2 = 3.81 \text{ cm}$ |
| ③ Water + Fe | $R_3 = 4.12 \text{ cm}$ |
| ④ Air | $R_4 = 4.45 \text{ cm}$ |
| ⑤ Graphite | $R_5 = 80.0 \text{ cm}$ |

Fig. 3.6-4 Calculational model for one-dimensional sphere geometry

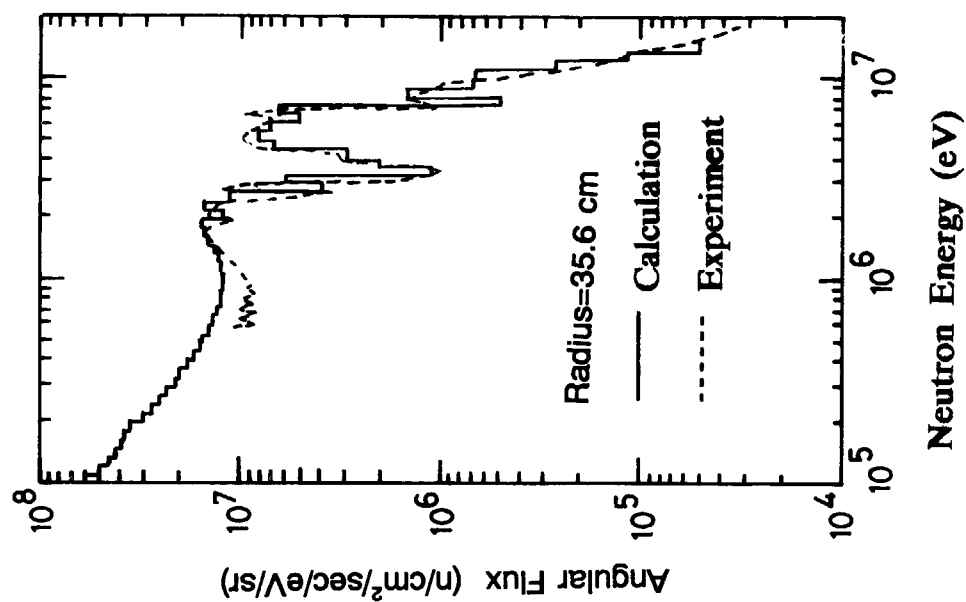


Fig. 3.6-6 Fast neutron angular spectra at 0 deg. and $r=35.6\text{cm}$

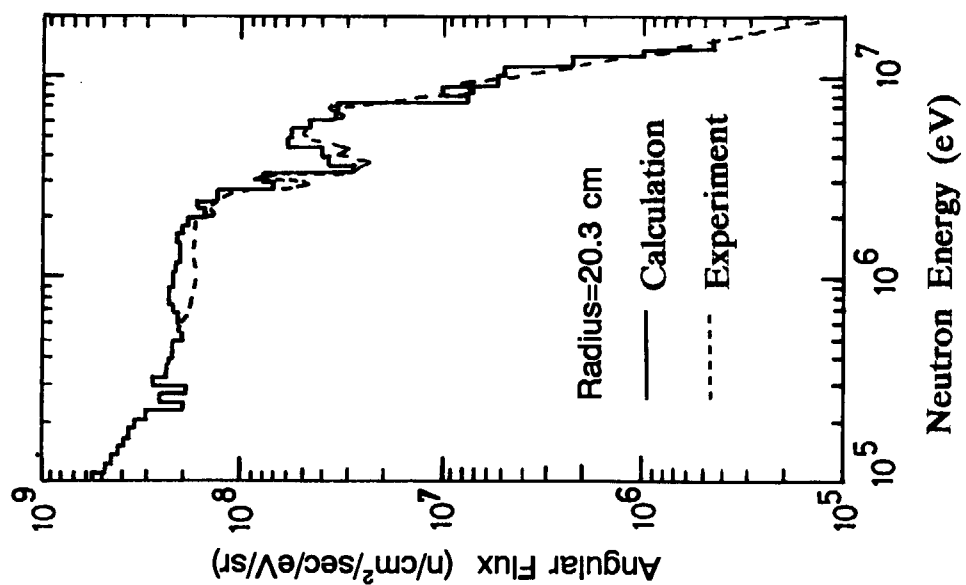
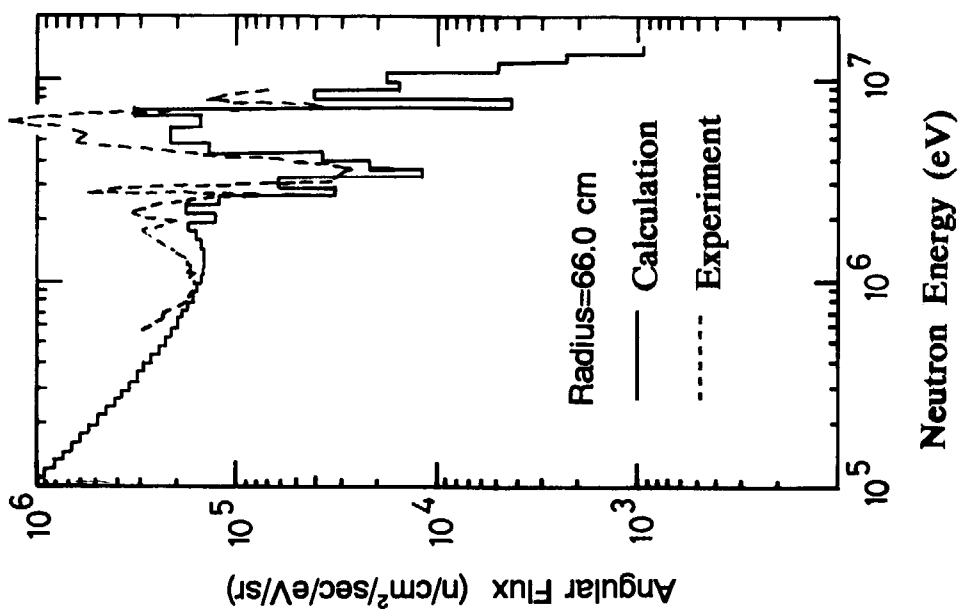
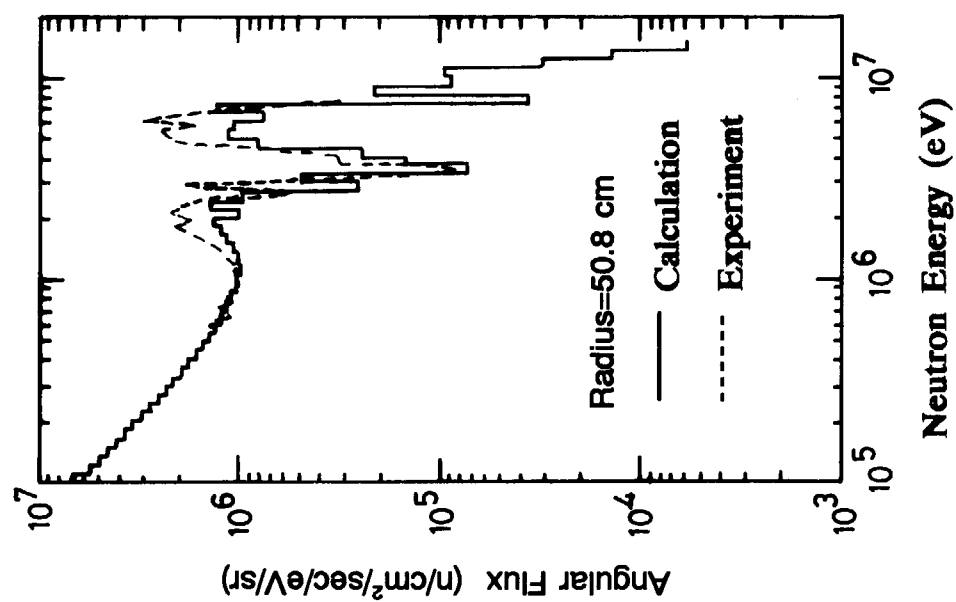


Fig. 3.6-5 Fast neutron angular spectra at 0 deg. and $r=20.3\text{cm}$

Fig. 3.6-8 Fast neutron angular spectra at 0 deg. and $r=66.0\text{cm}$ Fig. 3.6-7 Fast neutron angular spectra at 0 deg. and $r=50.8\text{cm}$

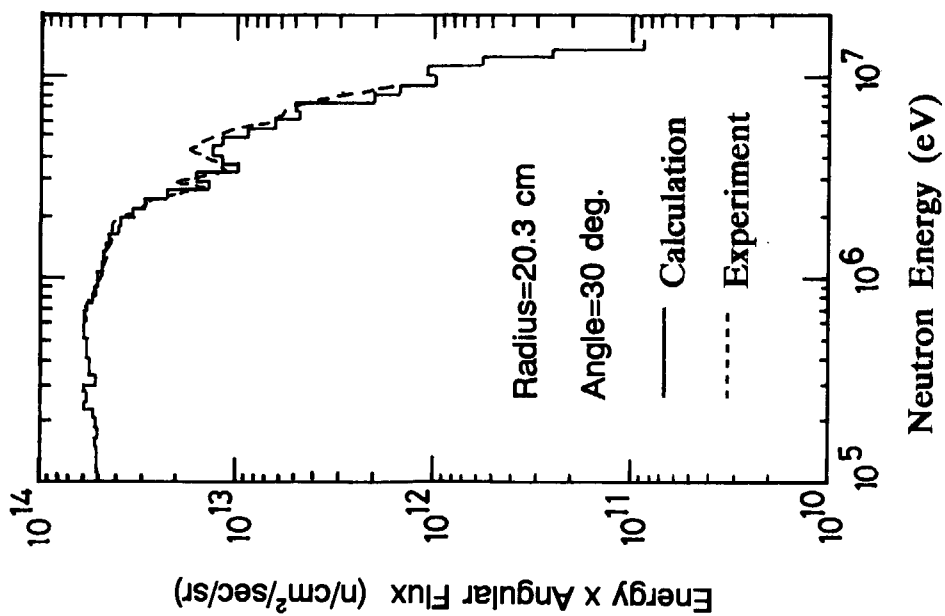


Fig. 3.6-9 Neutron angular spectra at 30 deg. and $r=20.3\text{cm}$

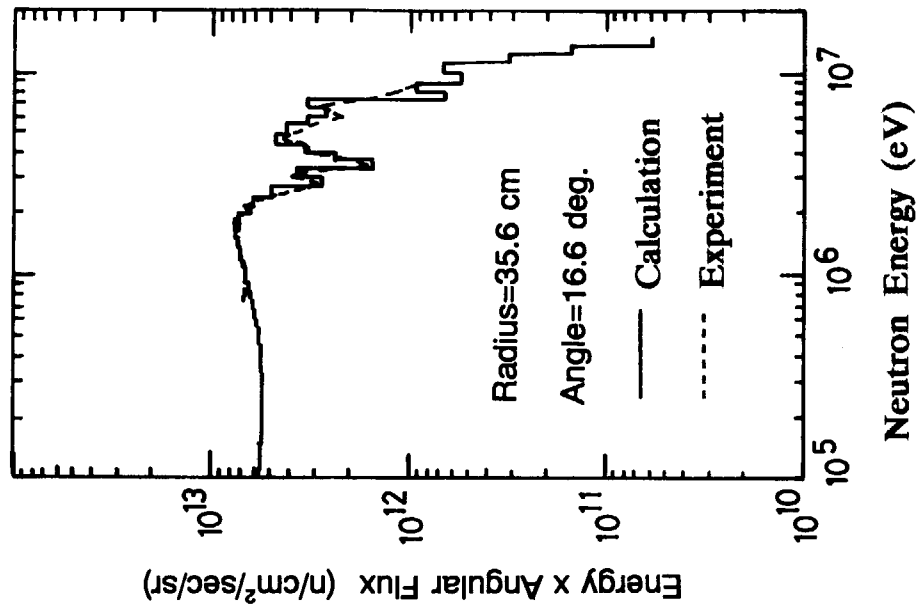
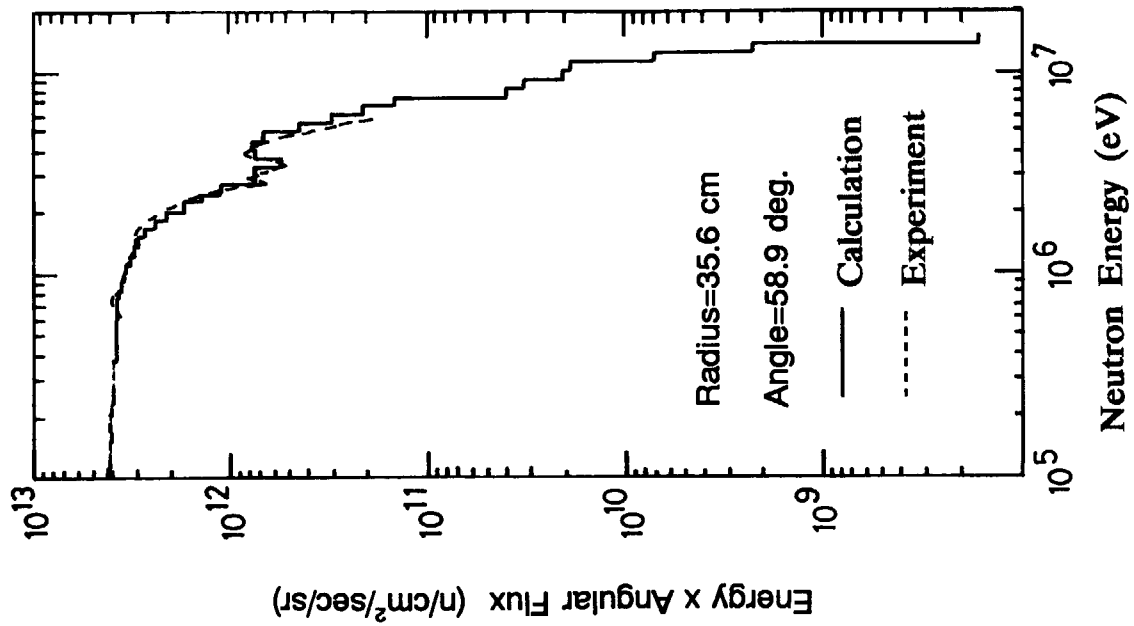
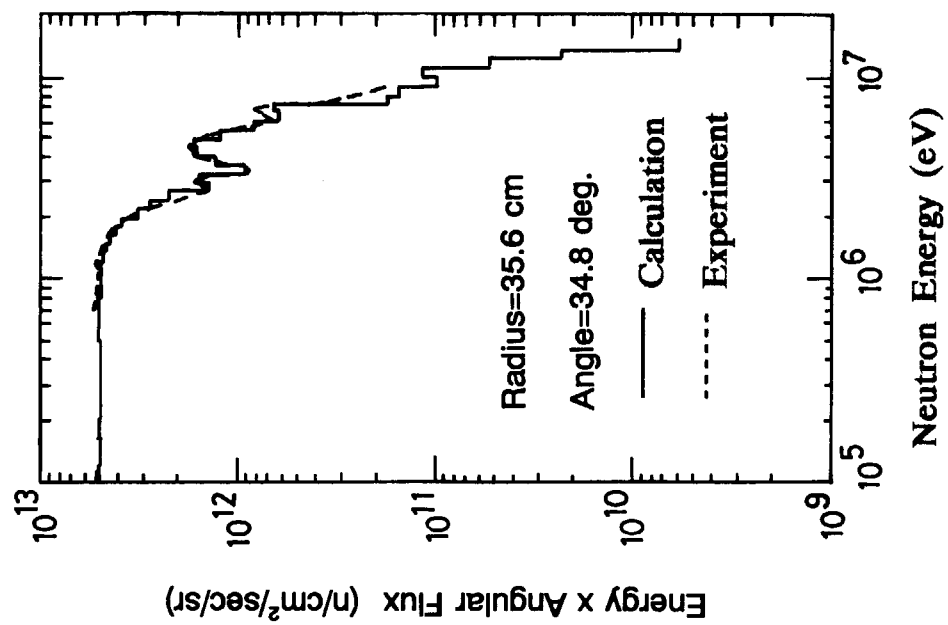


Fig. 3.6-10 Neutron angular spectra at 16.6 deg. and $r=35.6\text{cm}$

Fig. 3.6-12 Neutron angular spectra at 58.9 deg. and $r=35.6\text{cm}$ Fig. 3.6-11 Neutron angular spectra at 34.8 deg. and $r=35.6\text{cm}$

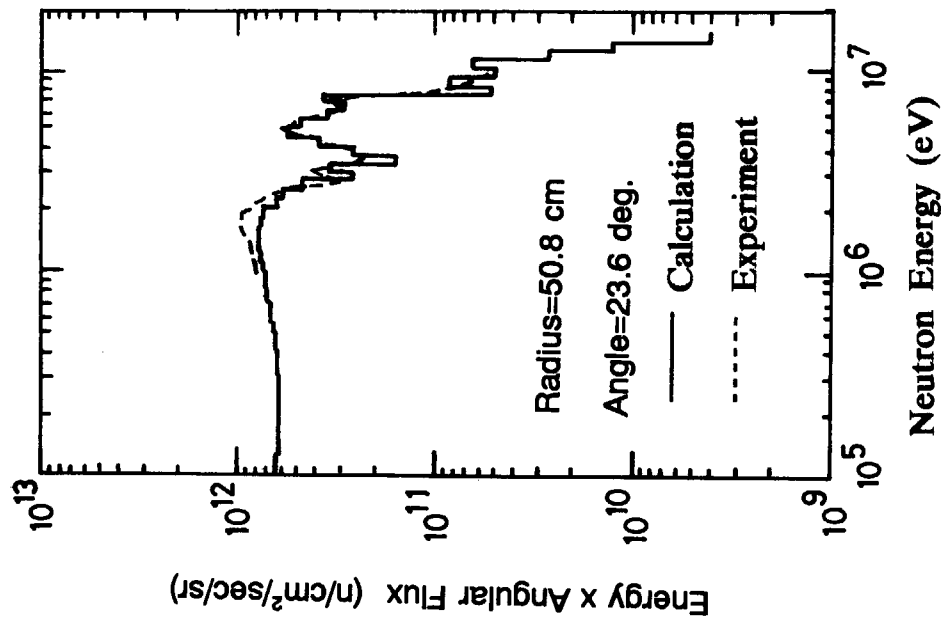


Fig. 3.6-14 Neutron angular spectra at 23.6 deg. and $r=50.8$ cm

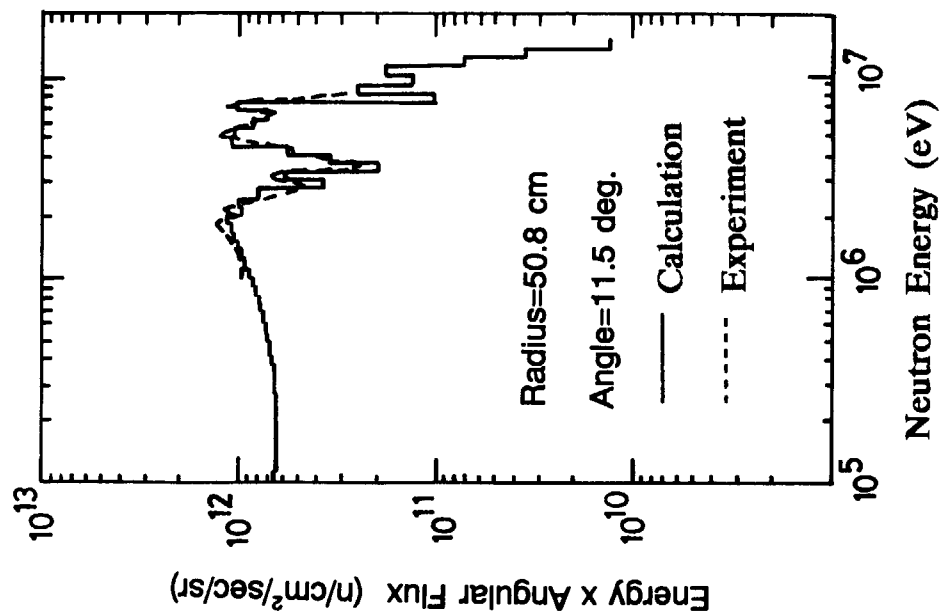


Fig. 3.6-13 Neutron angular spectra at 11.5 deg. and $r=50.8$ cm

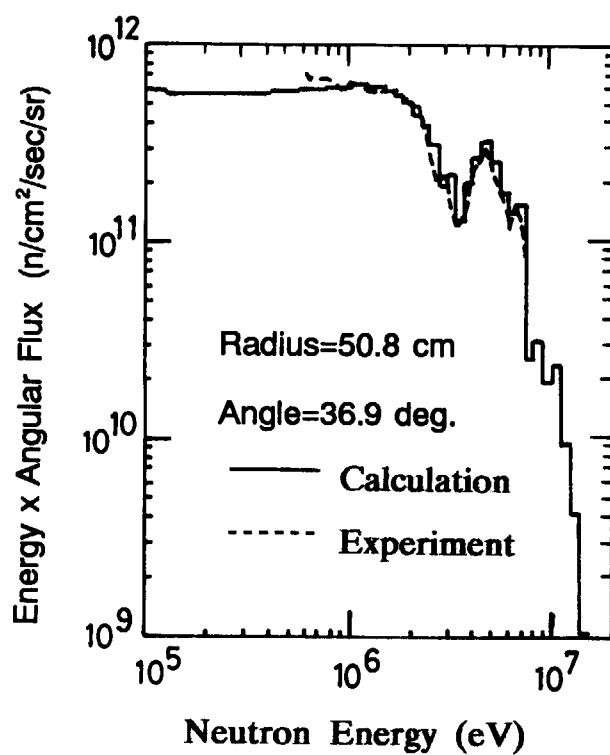


Fig. 3.6-15 Neutron angular spectra at 36.9 deg. and $r=50.8\text{cm}$

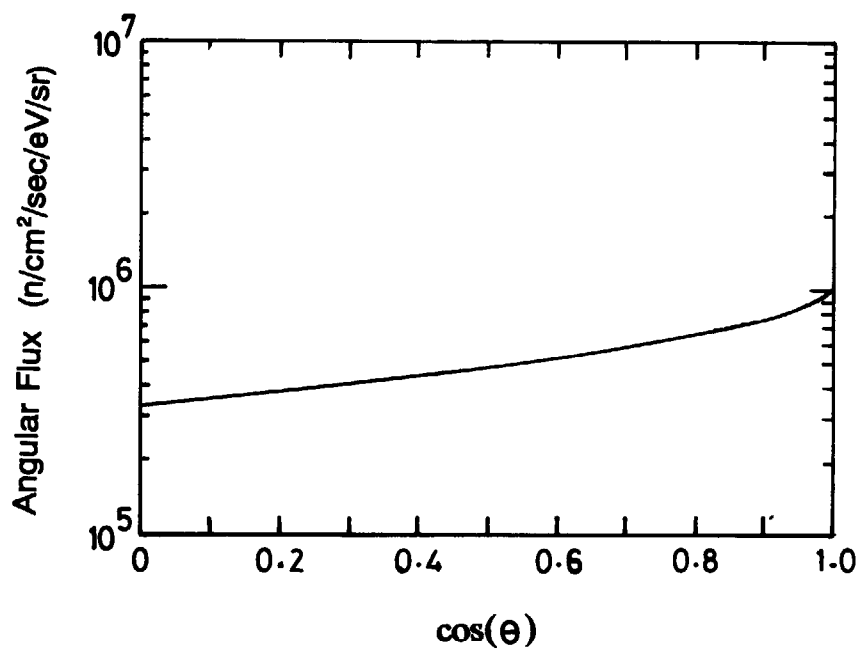


Fig. 3.6-16 Flux angular distribution at $r=50.8\text{ cm}$, $E=1.0\text{ MeV}$

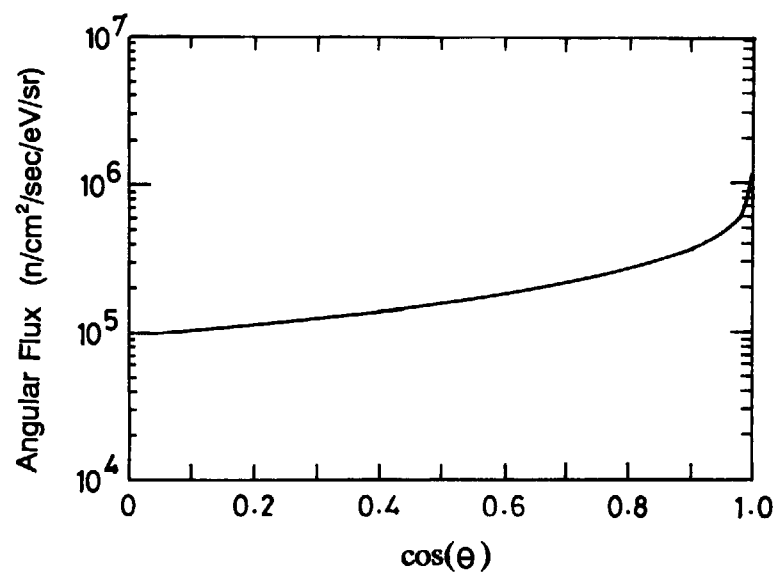


Fig. 3.6-17 Flux angular distribution at $r=50.8$ cm, $E=2.0$ MeV

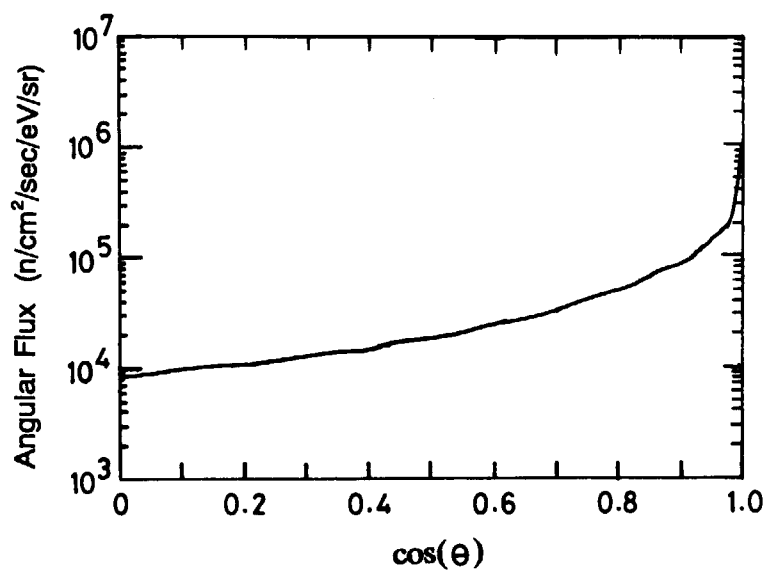


Fig. 3.6-18 Flux angular distribution at $r=50.8$ cm, $E=5.0$ MeV

3.7 ORNL Graphite Experiments

3.7.1 Outline of Experiments

Neutron transmission experiments⁸⁾ through graphite blocks were performed at the Tower Shielding Facility of the Oak Ridge National Laboratory. The multi-layer experimental configurations are shown in Fig. 3.7-1. The neutron source through a 32 inch dia. collimator from the TSR-II reactor with a spectrum modifier was provided to simulate the typical leakage neutron energy spectrum from the radial blanket of a sodium cooled fast-breeder reactor (LMFBR). The spectrum modifier was followed by a mockup of the stainless steel shield of LMFBR near-core radial shields and six layers of 10.16 cm thick graphite blocks.

Measurements were made on the centerline of neutron beam by using BF_3 Bonner ball detectors with different thicknesses of polyethylene covers, NE-213 and Benjamin neutron spectrometers. The Bonner ball detectors were placed 30 cm behind the outermost layer and after each measurement following layers were set for the next measurement. The spectrometers were located at 36.3 cm behind the six graphite layers backed with 6.5 cm thick B_4C and 15.24 cm thick lead layers.

3.7.2 Calculation Method

A two-dimensional Sn code DOT3.5¹³⁾ was used in the analyses, approximating the square (152.4 cm \times 152.4 cm) slabs in R-Z geometry. The JSSTD-100 library²²⁾, based on JENDL-3, was applied to computations. Preceding DOT3.5 calculations with S12-P3 and 21 energy groups, one-dimensional ANISN¹¹⁾ calculations with S16-P5 and the original 100 energy groups of JSSTD-100 were performed to obtain neutron spectra for collapsing cross-section data for all material layers. The count rates of Bonner ball detectors were evaluated at the effective detection centers which were given at slightly forward positions from the real detector centers as shown in Section 3.5.2.

3.7.3 Results

The calculated results of Bonner ball count rates are tabulated as calculation-to-experiment ratios in

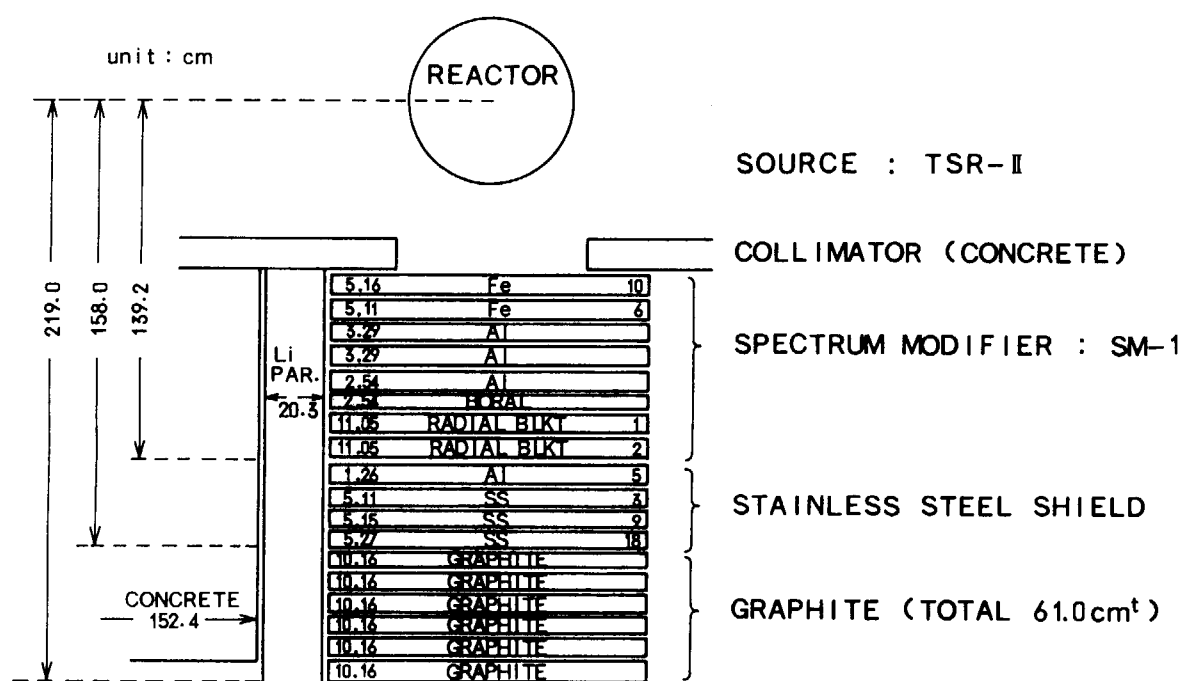


Fig. 3.7-1 Configuration of the ORNL graphite benchmark experiment

Table 3.7-1. For a comparison with existing other evaluated nuclear data files, the calculated results using the same analysis method but different only in cross-section libraries are also shown in the table. One library is JSDJ2 based on JENDL-2 and the other library is JSMD based on ENDF/B-IV. These libraries were generated with use of MINX⁴²⁾, while JSSTD-100 based on JENDL-3 was generated by using PROF-GROUCH-G/B¹⁴⁾. Analyses using the mixed macroscopic cross-section data of JSSTD-100 for graphite and of JSDJ2 for the other materials were made for a comparison. It was confirmed that the one-dimensional calculations with the collapsed 21-energy-group libraries give lower count rates by about 5% than those with the original 100-energy-group libraries.

The results with JENDL-3 are a little greater than unity throughout any graphite thickness except for bare and cadmium covered Bonner ball detectors. The overestimation tendency is reduced as the transmission in graphite increases. In general, the calculated results with JENDL-3 are higher than those with ENDF/B-IV. At a 10.16 cm thickness, the calculated results with ENDF/B-IV show the best agreement with the experimental results. At a 60.96 cm thickness, the calculated results with JENDL-3 show the best agreement within 2 or 3% (except for bare and cadmium covered Bonner ball detectors), and those with JENDL-2 show underestimation more than 10%. At a 30.48 cm thickness, the calculated results with JENDL-3 show better agreement with the experiments than those with JENDL-2. The calculated results between the mixed library (JENDL-3 for graphite and JENDL-2 for the other materials) and JENDL-2 agree with each other. This agreement is also affirmed by good similarity with the carbon total cross sections between both files.

The calculated results of neutron energy spectrum are shown in Fig. 3.7-2. The energy spectrum with the mixed library is higher than the spectrum with JENDL-2 in the energy region lower than 1 MeV and shows comparatively good agreement with the measured spectrum.

It is found from the C/E value of the Bonner ball responses that JENDL-3 gives superior results than JENDL-2 at graphite thickness of more than 10.16 cm. However, a comparison of the energy spectra calculated with JENDL-3 and the JENDL-2-and-3-mixed library indicates that cross-section data of the other elements used in the spectrum modifier composed of the UO₂ blanket region or stainless steel

Table 3.7-1 C/E values of Bonner ball responses calculated with DOT3.5
for the ORNL graphite benchmark experiments

Graphite Thickness (cm)	Library	C/E Values of Various Bonner Ball Detectors					
		Bare	Cd	3 in.	5 in.	8 in.	10 in.
10.16	JENDL-3	1.16	1.01	1.18	1.09	1.06	1.09
	JENDL-3*	1.02	0.87	1.02	0.94	0.91	0.94
	JENDL-2	0.95	0.90	1.04	0.96	0.92	0.95
	ENDF/B-IV	0.96	0.90	1.10	1.03	1.00	1.03
30.48	JENDL-3	0.98	0.92	1.07	1.04	1.02	1.02
	JENDL-3*	0.84	0.79	0.92	0.89	0.87	0.87
	JENDL-2	0.84	0.81	0.94	0.91	0.88	0.88
60.96	JENDL-3	0.85	0.85	1.01	1.02	1.03	1.02
	JENDL-3*	0.73	0.73	0.87	0.87	0.88	0.87
	JENDL-2	0.73	0.76	0.90	0.90	0.89	0.88
	ENDF/B-IV	0.65	0.81	0.96	0.95	0.93	0.91

N. B. JENDL-3 : The JSSTD-100 library

JENDL-3* : The JSSTD-100 library for graphite
and the JSDJ2 library for the other materials

JENDL-2 : The JSDJ2 library

ENDF/B-IV : The JSMD library

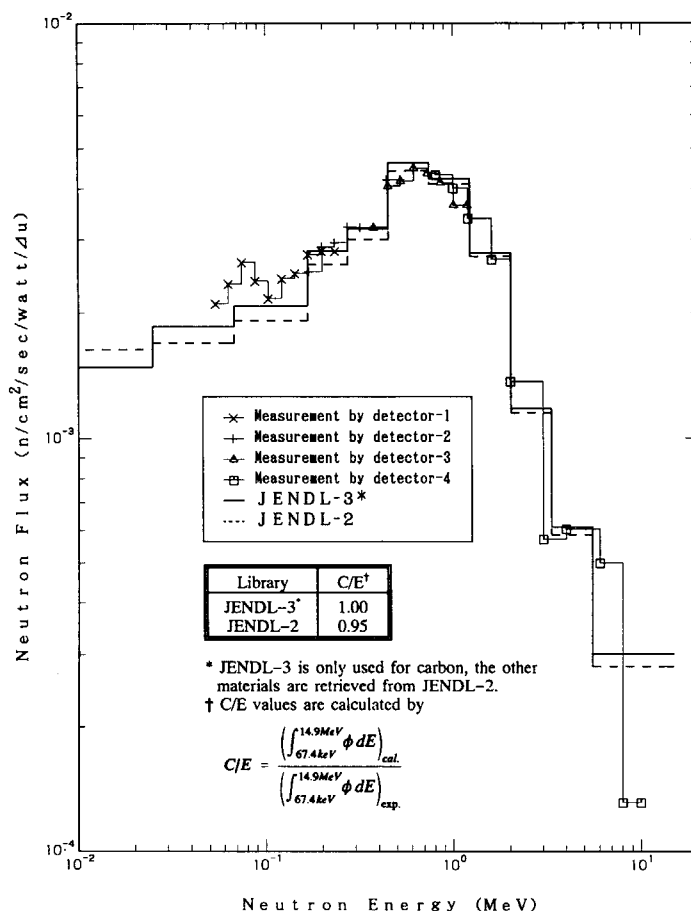


Fig. 3.7-2 Comparison of neutron energy spectra of the ORNL graphite experiment (36.3 cm behind the slabs of graphite 60.96 cm + B₄C 6.5 cm + lead 15.24 cm)

slab strongly affect the formation of the transmitted neutron energy spectrum. So, as far as neutron transmission in graphite region, JENDL-3 gives similar accuracy with ENDF/B-IV for the integral fluxes by the Bonner balls and a little better accuracy than ENDF/B-IV for the high energy spectrum above 67 keV.

3.8 LLNL Iron and Graphite Experiments

3.8.1 Outline of Experiments

Neutron emission spectra for spherical targets bombarded with a centered, D-T neutron source were measured for many elements and compounds⁹⁾. These measurements were provided to check on the neutron transport codes and evaluation of the neutron cross sections. The high energy spectra between 2 and 15 MeV were measured using the collimated flight paths at 30 and 120 deg., while the low energy spectra were measured at 26 deg. in the center of a large enclosure. At those angles, the source neutron energies were 14.97, 13.65 and 15.00 MeV, respectively. A schematic drawing of the experimental configuration is shown in **Fig. 3.8-1**.

The neutron detector used for the high energy measurements was a 5.08-cm-dia. by 5.08-cm-long, NE213 liquid scintillator contained in a thin aluminum cylinder. The detector was located at 766.0 cm from the center of the iron spheres for the 30-deg. measurements and at 975.2 cm for the 120 deg. measurements. For the low energy measurements, a 5.1-cm-dia. by 1.9-cm-thick ⁶Li glass detector was used, and was located at 801.4 cm from the tritium target. The detector was supported by strings in the center of a large concrete enclosure (**Fig. 3.8-1**) to minimize the outscatter-inscatter effect.

The iron targets were solid spheres of 4.46, 13.41, and 22.30-cm radii, which correspond to 0.9, 2.9, and 4.8 mfp, also, the graphite targets were of 10.16 and 20.96-cm radii, which correspond to 1.3 and 2.9 mfp, for 14-MeV neutrons. A schematic drawing of the iron target is shown in Fig. 3.8-2.

3.8.2 Calculation Method

The continuous energy Monte Carlo code MCNP¹⁷⁾ was employed in this problem and the NESX³⁹⁾ estimator as shown in Fig. 3.2-2 was used in the TALLYD routine of the MCNP code for analyzing the LLNL-Sphere neutron benchmark experiments. In the NESXE routine, neutrons of which entered into

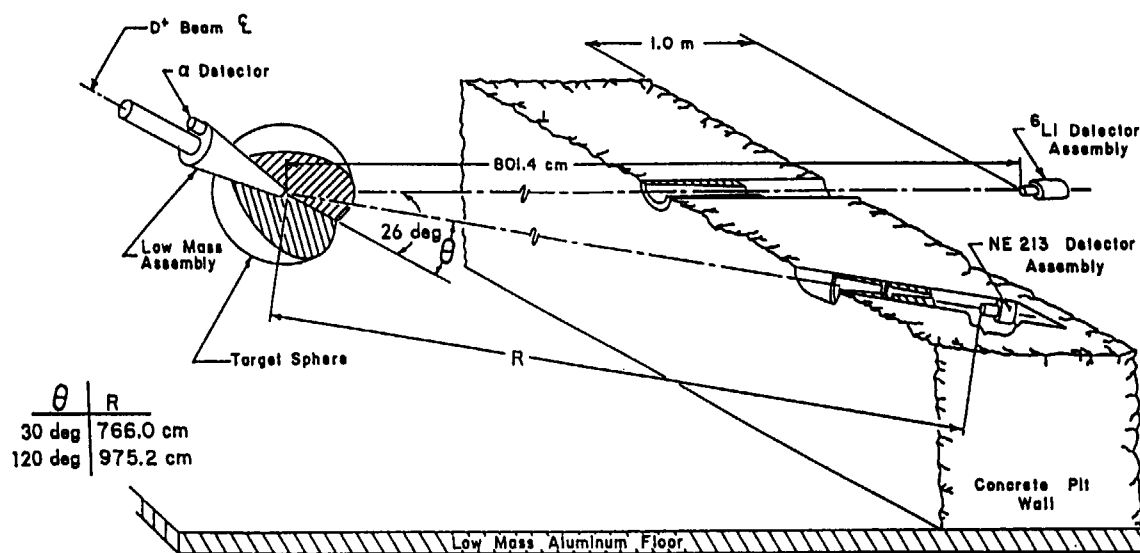
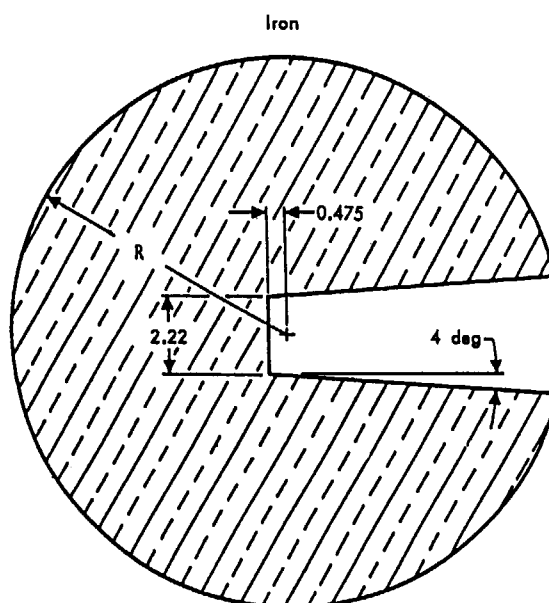


Fig. 3.8-1 Schematic drawing of the experimental setup⁹⁾



(unit: in cm)

λ	R
0.9	4.46
2.9	13.41
4.8	22.40

Fig. 3.8-2 Geometry of the spherical iron targets⁹⁾

measuring angle ± 5 deg. were scored. As described in **Fig. 3.8-2**, there is a void hole in the rear side of the iron sphere. Accordingly, even though the hole geometry was taken into account in the Monte Carlo calculations, the results in the rear direction (at 120 deg.) is irrelevant for the test of cross sections. Therefore, the calculations were carried out only measuring angle at the 30 deg. The calculated fluxes have been smoothed in each energy interval with an energy-dependent Gaussian response function.

3.8.3 Results

3.8.3.1 Iron

The comparison of angular fluxes between the measured and MCNP results for 0.9, 2.9, and 4.8 mfp (mean-free-path) thicknesses of iron-spheres are shown in **Figs. 3.8-3**, **3.8-4**, and **3.8-5**, respectively.

For the three different iron-spheres, there are no significant difference between the measured angular fluxes and the calculations with JENDL-3¹⁾. However, a little bit of underestimation is observed between 7 and 13 MeV for all the calculations. The cause of the underestimation between 7 and 10 MeV was likely due to underestimation of the continuum inelastic scattering cross section given for the ⁵⁶Fe excited levels above 4.5 MeV, particularly pre-equilibrium component, and also between 11 and 13 MeV was due to that of inelastic scattering cross sections directly exciting to the discrete levels below 4.5 MeV.

3.8.3.2 Carbon

The comparison of angular fluxes between measured and MCNP calculations for 1.3 and 2.9 mfp thicknesses of carbon-spheres are shown in **Figs. 3.8-6**, and **3.8-7**, respectively.

The peak of source neutrons around 15 MeV indicates good agreement between the measured results and the MCNP calculations. However, the peak locations of the scattered neutrons have slipped slightly in both figures. It is not clear whether the discrepancy is caused from the experimental results or nuclear data in JENDL-3.

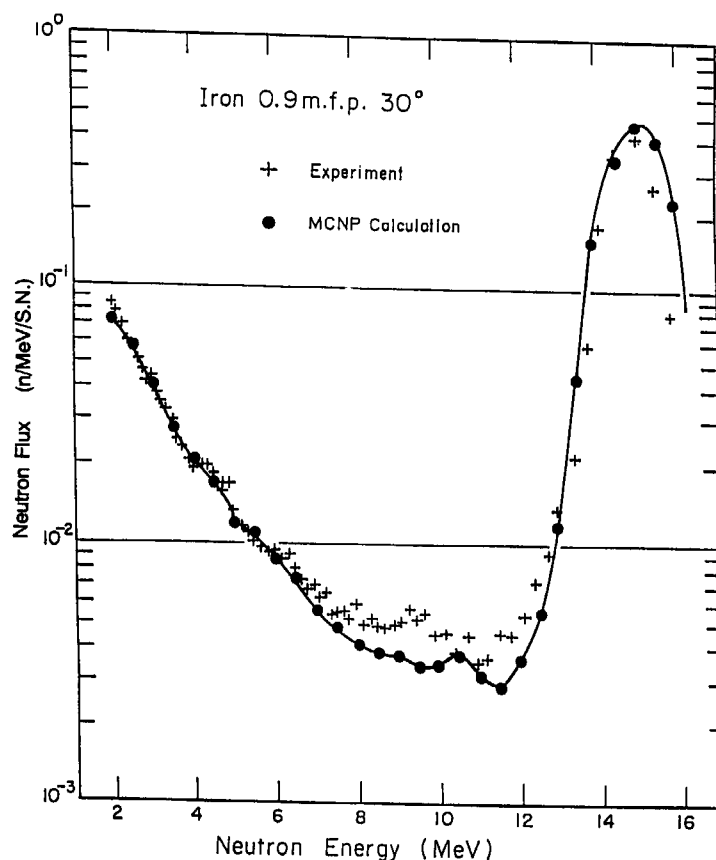


Fig. 3.8-3 Comparison of energy spectrum between the LLNL experiments and the MCNP calculations with JENDL-3 for 0.9 mfp ($r=4.46$ cm) of iron at 30°

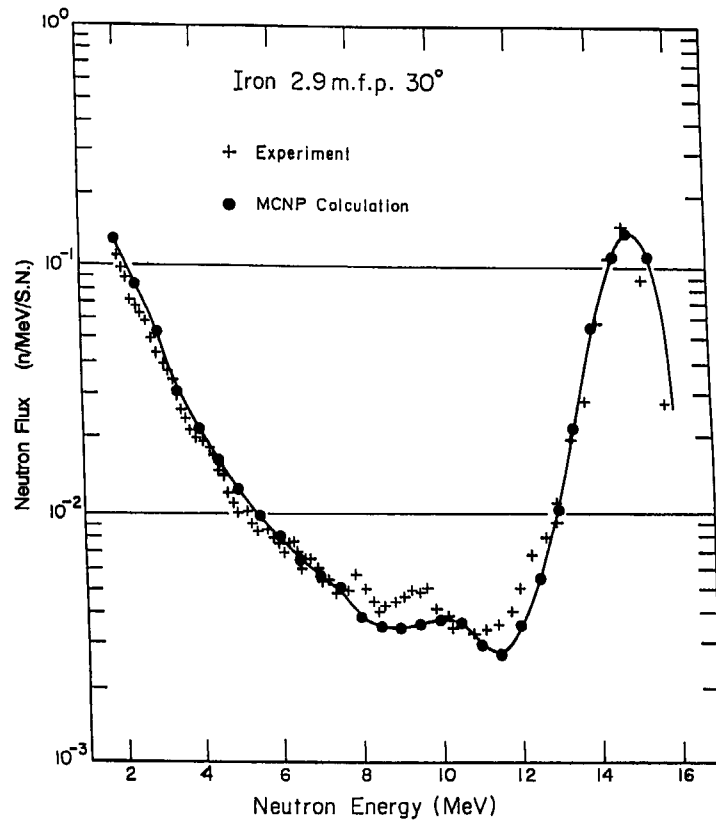


Fig. 3.8-4 Comparison of energy spectrum between the LLNL experiments and the MCNP calculations with JENDL-3 for 2.9 mfp ($r=13.41$ cm) of iron at 30°

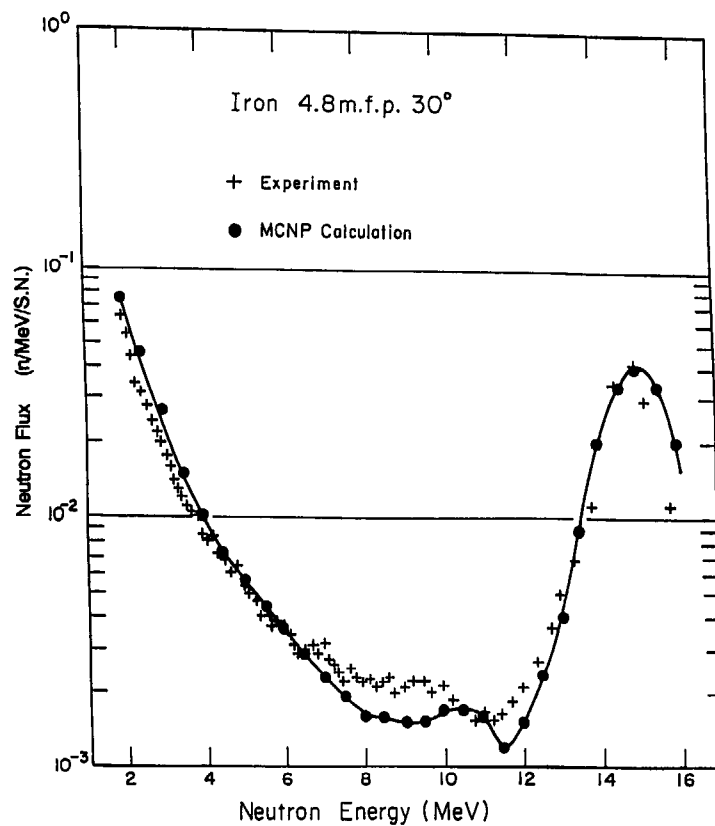


Fig. 3.8-5 Comparison of energy spectrum between the LLNL experiments and the MCNP calculations with JENDL-3 for 4.8 mfp ($r=22.30$ cm) of iron at 30°

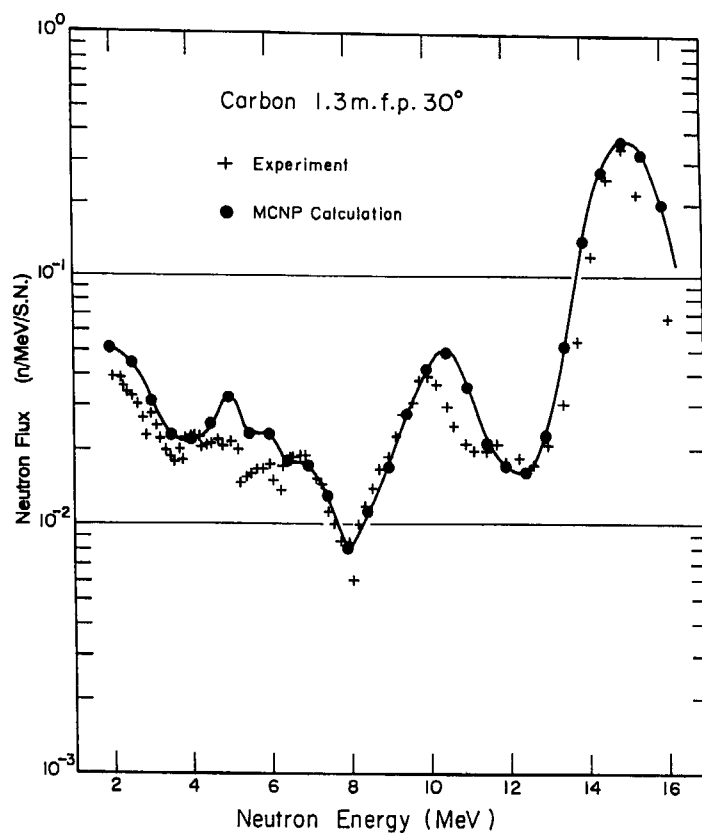


Fig. 3.8-6 Comparison of energy spectrum between the LLNL experiments and the MCNP calculations with JENDL-3 for 1.3 mfp ($r=10.16$ cm) of carbon at 30°

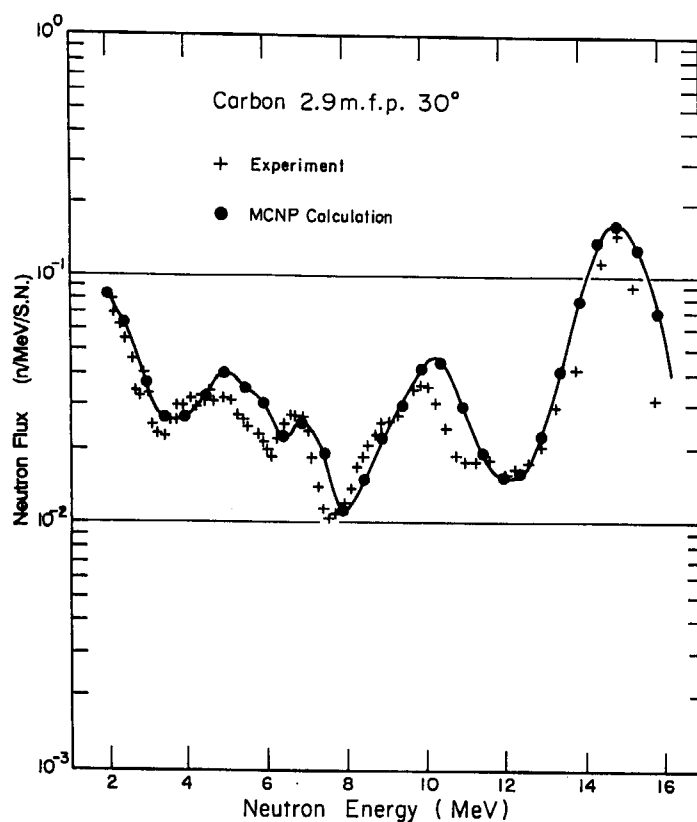


Fig. 3.8-7 Comparison of energy spectrum between the LLNL experiments and the MCNP calculations with JENDL-3 for 2.9 mfp ($r=20.96$ cm) of carbon at 30°

3.9 JAERI-FNS Experiments

3.9.1 Outline of Experiments

The angular neutron fluxes from the slab assemblies were measured as functions of slab thickness and measuring angle to evaluate neutron cross sections and check the neutron transport codes for fusion neutronics¹⁰⁾.

Figure 3.9-1 shows the experimental layout in the target room. The radius of the assembly was set at 31.5 cm, corresponding to 5-6 mean-free-paths for 14 MeV neutrons, such that the neutron flux attenuated to 1% when passing through the material in the radial direction. In the FNS experimental series, the graphite assemblies of 5.06, 20.24 and 40.48-cm-thick, also, the beryllium assemblies of 5.08 and 15.24-cm-thick were employed. The slab assemblies used in the FNS experimental series were made in a pseudo-cylindrical shape. This geometry was adopted to simplify the calculation as much as possible, and it can be modeled for a two-dimensional code. The pseudo-cylinder was composed of blocks of a standard size of 5.06 cm side length as shown in **Fig. 3.9-2**, supported by square aluminum tubes 5.08 cm in size. The assembly was placed at a distance of 20 cm from the neutron source. The detector-collimator system determined the area on the rear-surface of slab and the solid angle by which the angular neutron flux was defined. The area was designed to be about 5.0 cm in diameter by choosing the sizes of the detector and collimator opening. The detector-collimator system was placed on the dual rotating deck. The detector-collimator system was placed on the dual rotating deck.

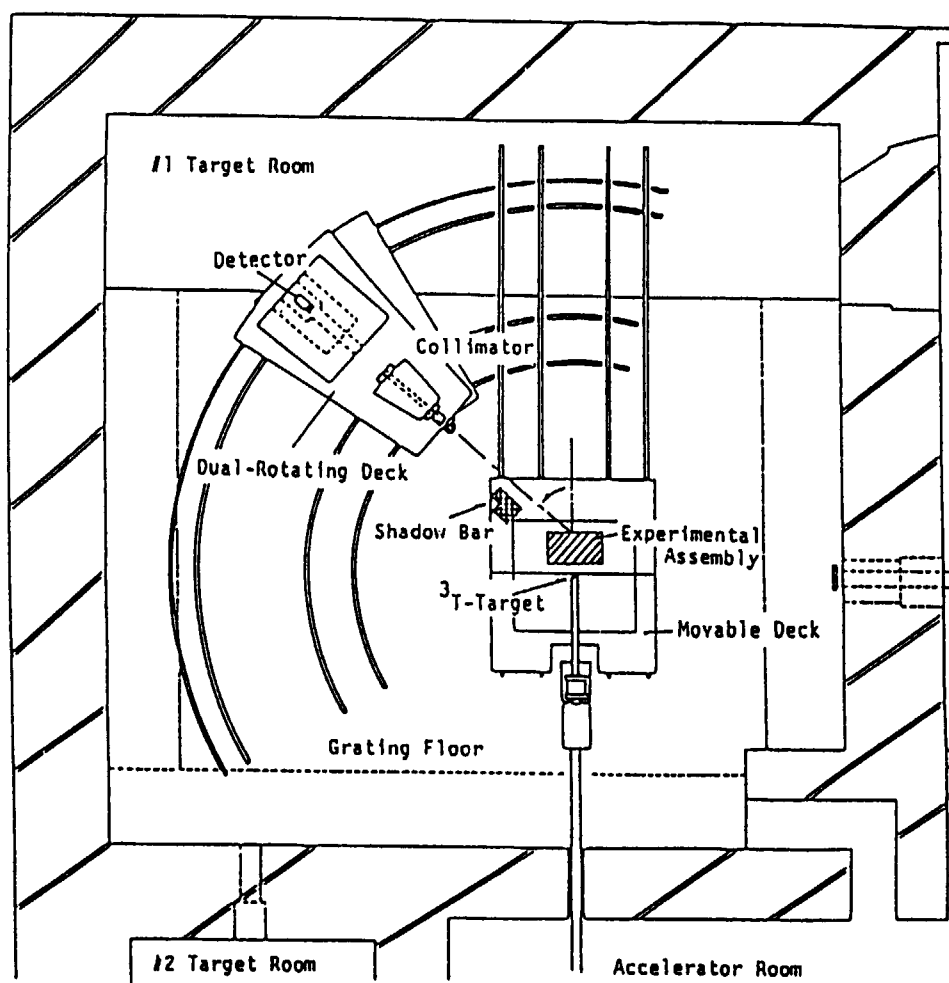


Fig. 3.9-1 Layout of target, assembly, collimator and detector¹⁰⁾

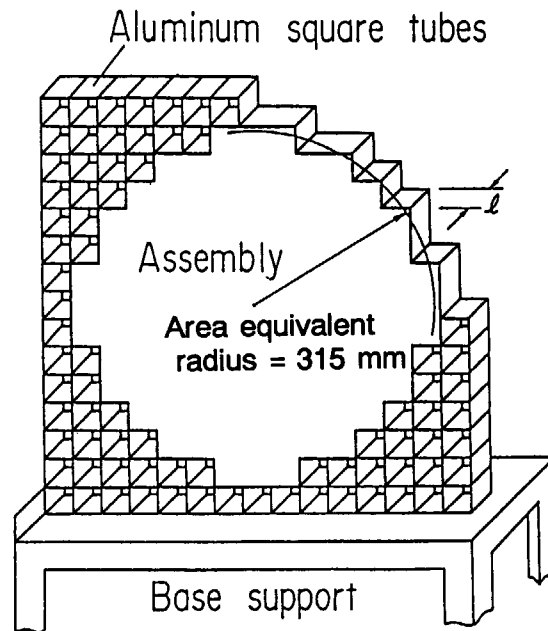


Fig. 3.9-2 Experimental assembly with pseudo-cylindrical shape made of rectangular blocks

3.9.2 Calculation Method

The particle scoring routine TALLYD in the MCNP code was steeply modified to take into account the experimental configuration of the JAERI-FNS neutron angular flux benchmark experiments, as shown in **Fig. 3.9-3**. Due to the modification of the TALLYD routine, neutrons which passed through the narrow collimator could be scored at a point on the detector surface. Accordingly, the experimental configuration of the JAERI-FNS benchmark experiments was faithfully reproduced in the MCNP Monte Carlo calculations. The values of solid angles, effective measured areas and flight paths were employed from Ref. (10).

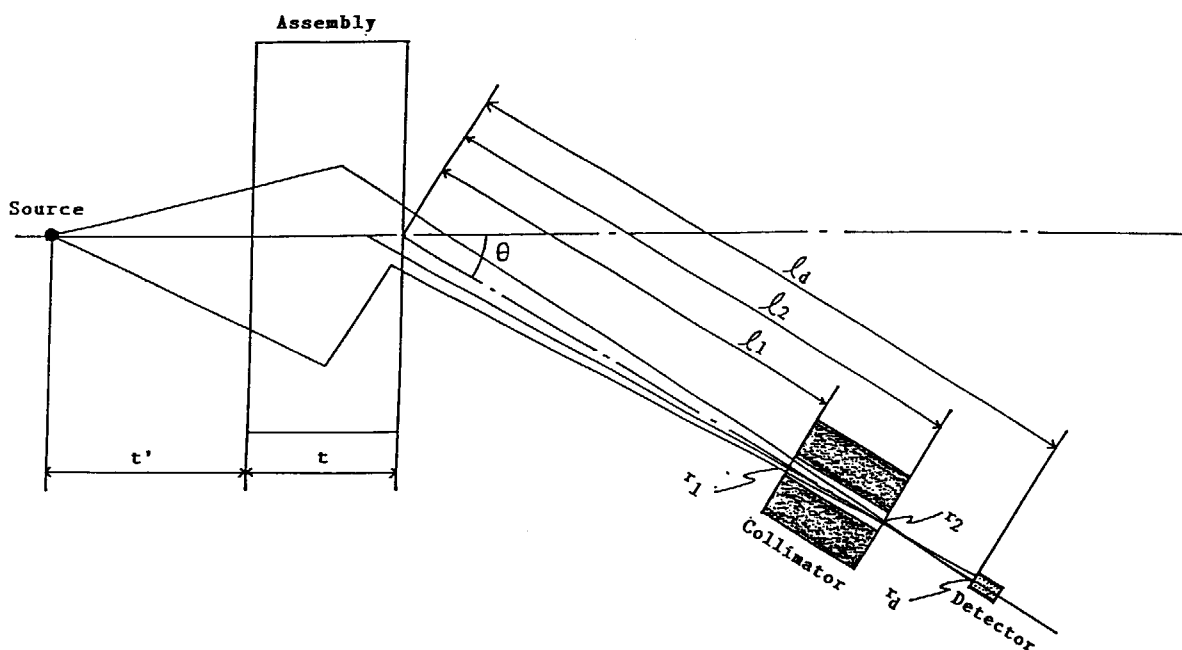


Fig. 3.9-3 Calculational model of the FNS experiment by using modified subroutine TALLYD in the MCNP code

3.9.3 Results

3.9.3.1 Beryllium

The calculated-to-experimental value ratios (C/E) for integrated fluxes of beryllium and comparisons of angular fluxes between the experiments and the MCNP calculations for the 15.24-cm-thick slab are summarized in **Figs. 3.9-4** and **3.9-5(a)~5(e)** for five measuring angles, respectively. The FSDs for the angular fluxes are also described in each figure.

- (1) As a whole, the C/E values integrated over 10 MeV are excellent, indicating approximately 1.0 for the measuring angles, except only for the angle 41.8 deg. At 41.8 deg., the C/E value is 0.86; meanwhile, the C/E values with ENDF/B-IV decrease as the measuring angle increases, that is, 0.95 at 0.0 deg., 0.84 at 24.9 deg., 0.80 at 41.8 deg. and 0.72 at 66.8 deg. The C/E values, integrated over 0.01 MeV, are between 0.98 and 1.08 with JENDL-3, and are between 0.91 and 0.96 with ENDF/B-IV.
- (2) As shown in **Fig. 3.9-5(d)**, the elastic-scattering peak at 14.5 MeV at the measuring angle of 41.8 deg. is obviously underestimated for both libraries, but the angular fluxes below the peak agree very well with the experiment. The underestimation tendency is consistent with the DDX data measured at OKTAVIAN⁴³⁾, while both libraries reproduce well the angular distributions of elastic scattering neutrons compared⁴⁴⁾ with the experiments reported from the other laboratories.
- (3) Except for the measuring angle of 41.8 deg., the calculated angular fluxes with JENDL-3 are in good agreement with the measured fluxes over the wide energy region, including the elastic-scattering peak.

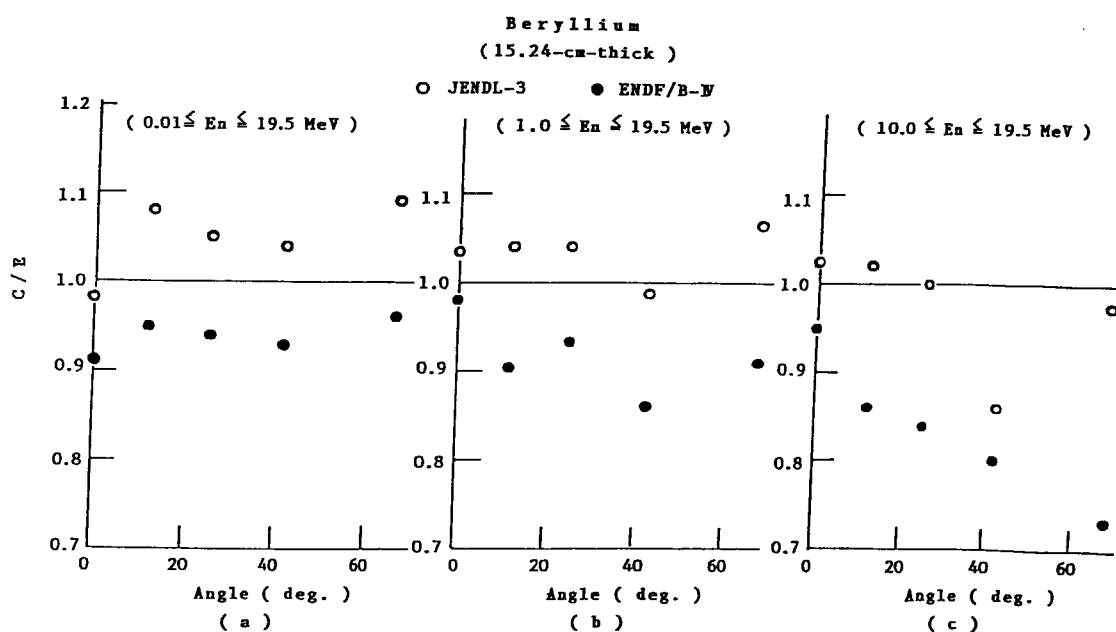


Fig. 3.9-4 MCNP Calculation/Experiment (C/E) ratio of fluxes integrated over three energy regions for the 15.24-cm-thick assembly;
(a) above 0.01 MeV, (b) above 1.0 MeV, (c) above 10.0 MeV

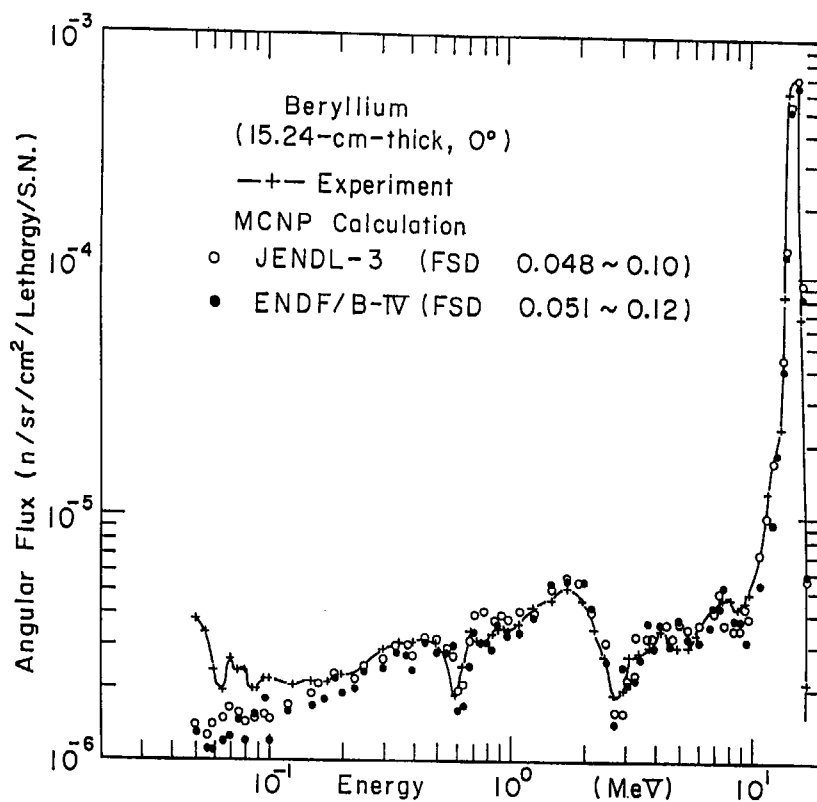


Fig. 3.9-5 Comparison of beryllium angular fluxes between the FNS experiments and the MCNP calculations with JENDL-3 and ENDF/B-IV for 15.24-cm-thick; (a) 0.0 deg.

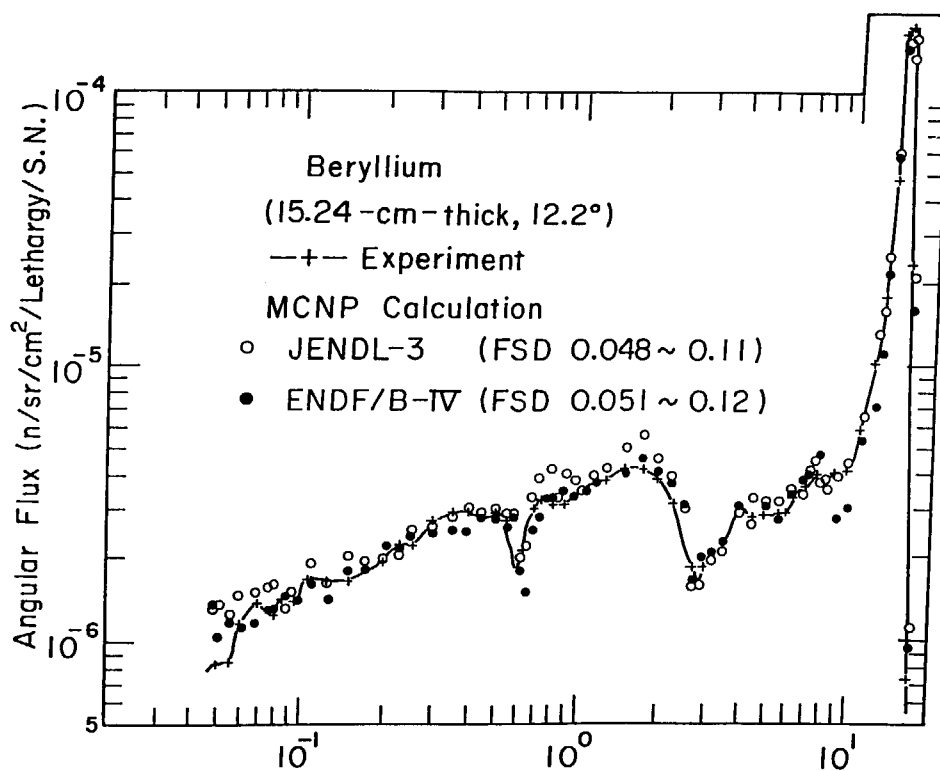


Fig. 3.9-5 (b) 12.2 deg.

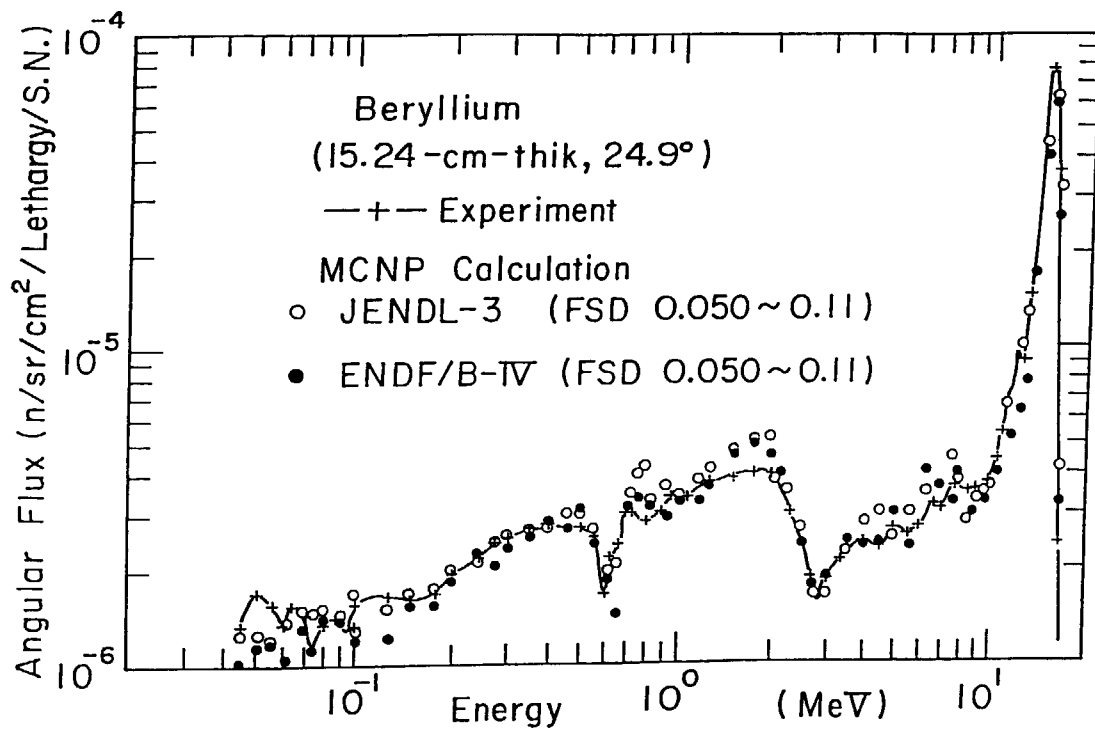


Fig. 3.9-5 (c) 24.9 deg.

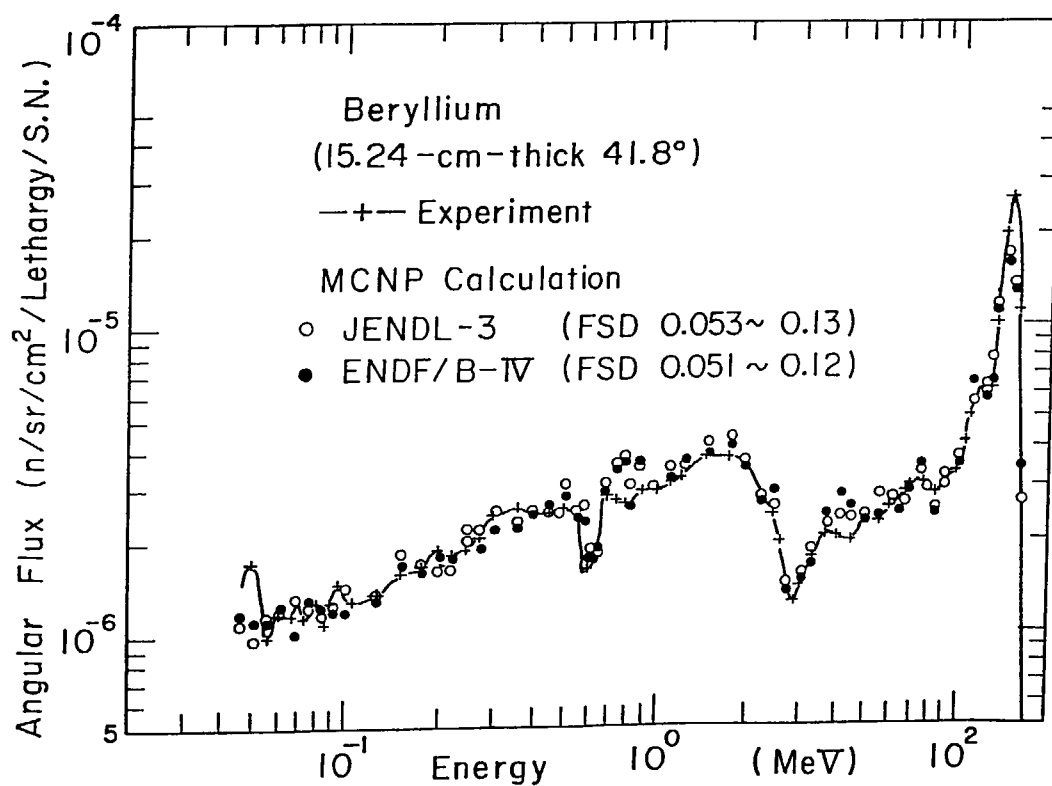


Fig. 3.9-5 (d) 41.8 deg.

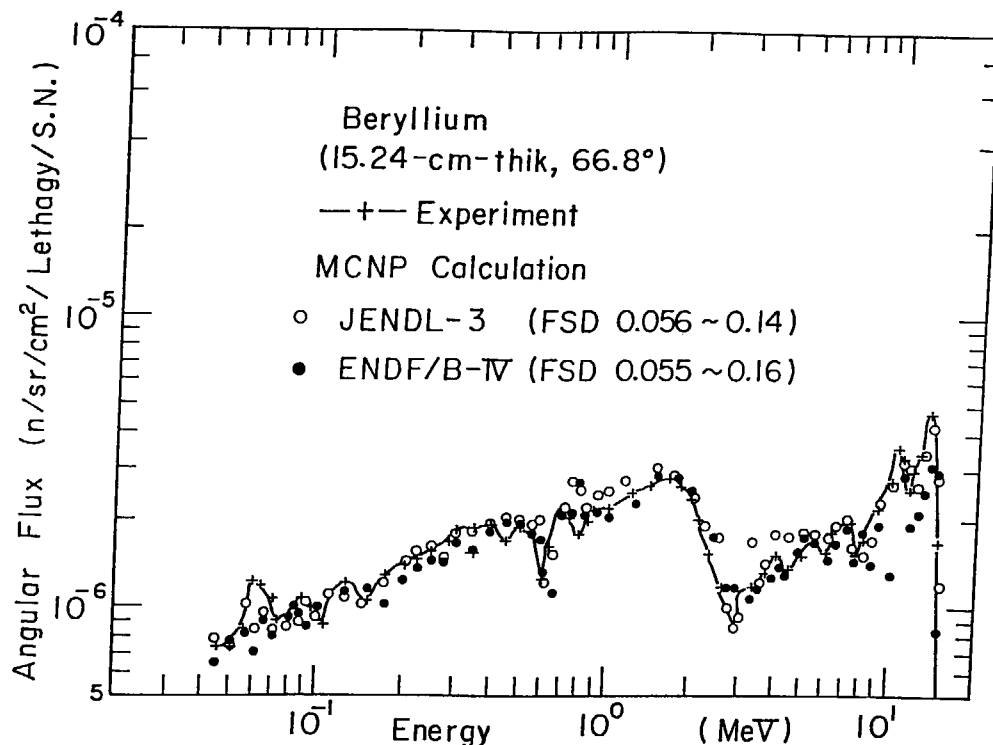


Fig. 3.9-5 (e) 66.8 deg.

3.9.3.2 Graphite

The C/E values for the energetically integrated fluxes for the 20.24-cm-thick slab are shown in Fig. 3.9-6. Figs. 3.9-7(a) through 3.9-7(e) show a comparison of angular fluxes between the experiments and the MCNP calculations for each measuring angle from 0.0 deg. to 66.8 deg. The FSDs for the angular fluxes are also described in each figure.

- (1) The C/E values, integrated over 0.5, 1.0 and 10 MeV with both libraries, are in excellent agreement within 1.0 ± 0.1 at all the measuring angles. However the values with JENDL-3 show a trend of "larger than 1.0". On the contrary, a trend of "less than 1.0" is shown with ENDF/B-IV.
- (2) In the angular fluxes shown in Figs. 3.9-7(a)~3.9-7(e), the elastic-scattering peak at each measuring angle indicates excellent agreement with the experiment, except at the deepest angle of 66.8 deg.; only at the 0.0 deg., uncollided neutrons are included in the peak. At the 66.8 deg., the calculated elastic-scattering peak value at 12.5 MeV is larger than the measured one by a factor of 1.8.

At the deepest measuring angle of 66.8 deg., the elastic and other peaks observed in the experiments are lower than the calculated ones. This discrepancy might come from the experiments at 66.8 deg. which imposed large experimental errors because of the lower counting statistics of the measurements.

- (3) Especially at several peaks and dips between 2.5 and 11.0 MeV, caused by the inelastic scattering, the calculated results with JENDL-3 showed better agreement than that with ENDF/B-IV at all the measuring angles.

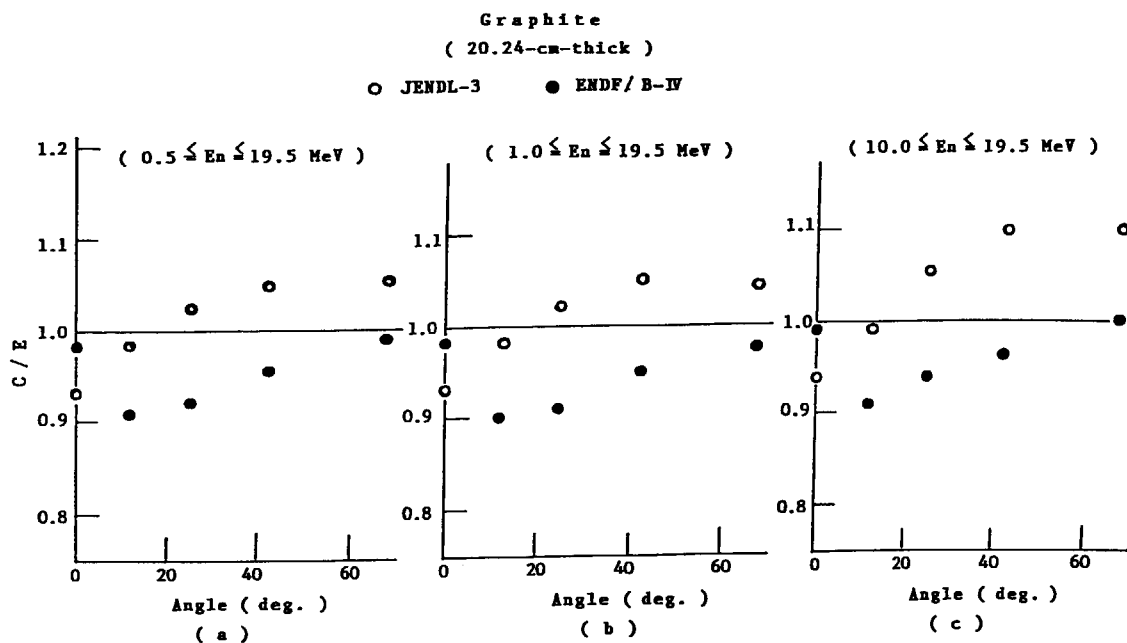


Fig. 3.9-6 MCNP Calculation/Experiment (C/E) ratio of fluxes integrated over three energy regions for the 20.24-cm-thick assembly;
(a) above 0.01 MeV, (b) above 1.0 MeV, (c) above 10.0 MeV

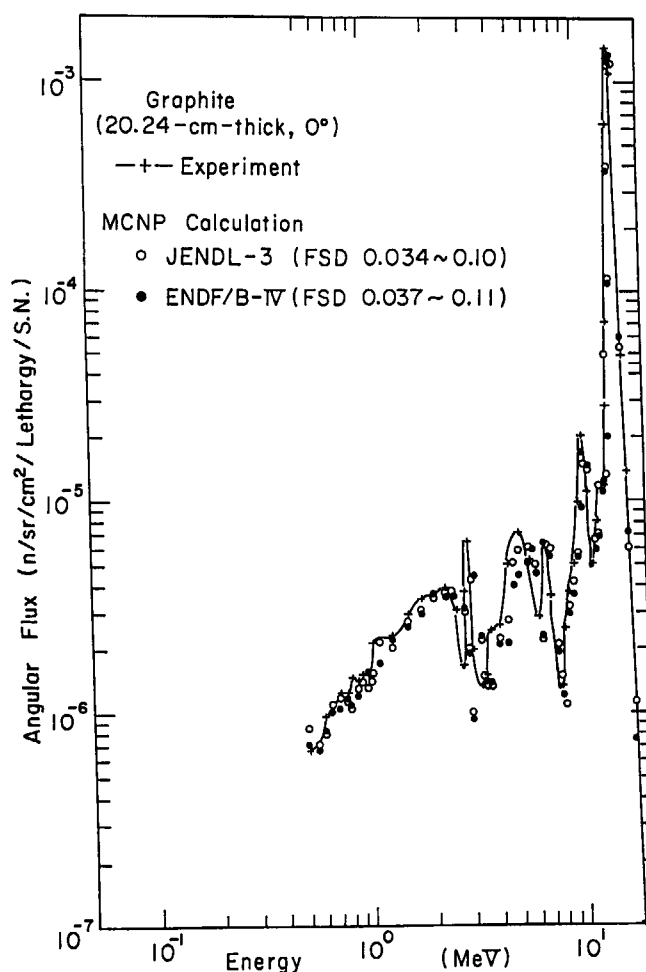


Fig. 3.9-7 Comparison of graphite angular fluxes between the FNS experiments and the MCNP calculations with JENDL-3 and ENDF/B-IV for 20.24-cm-thick; (a) 0.0 deg.

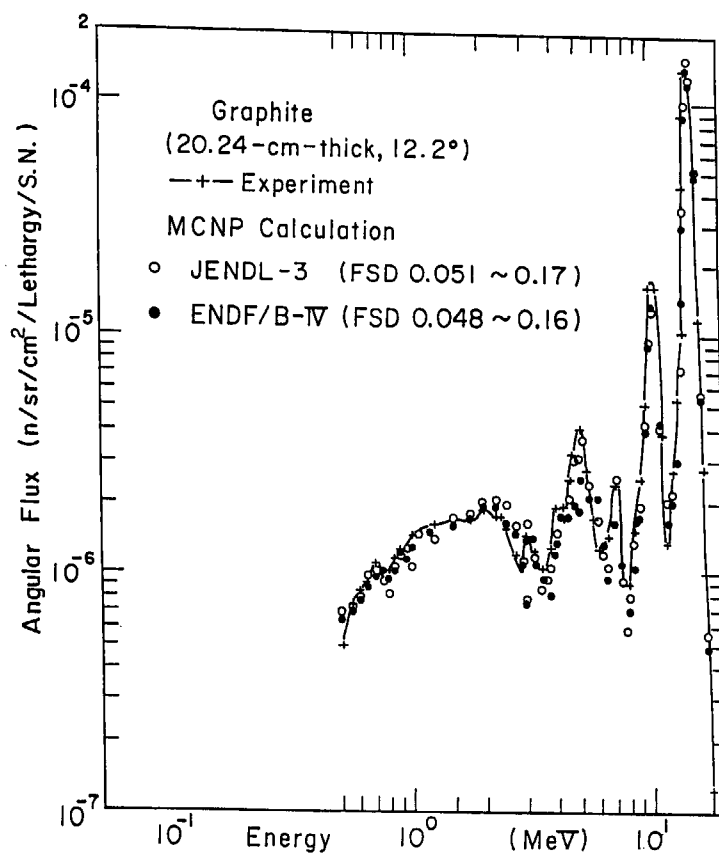


Fig. 3.9-7 (b) 12.2 deg.

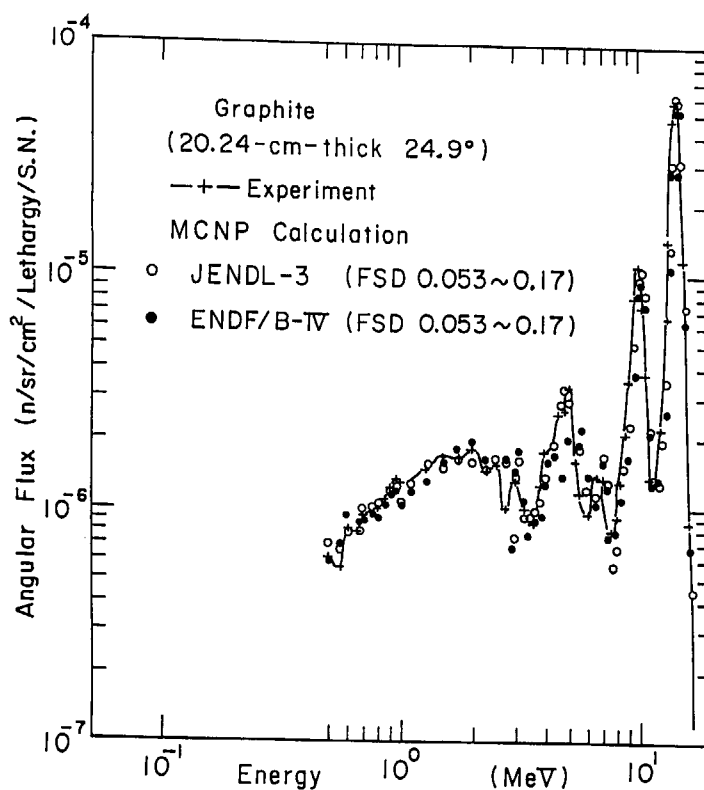


Fig. 3.9-7 (c) 24.9 deg.

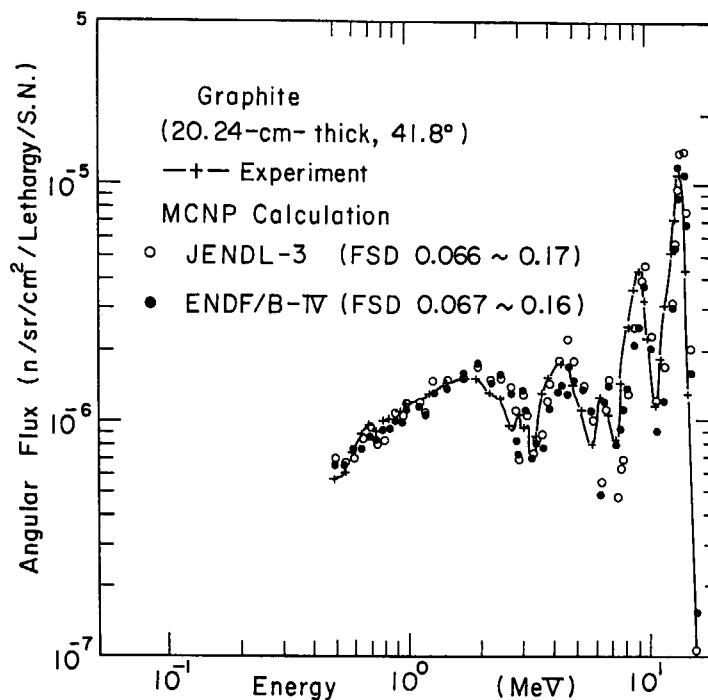


Fig. 3.9-7 (d) 41.8 deg.

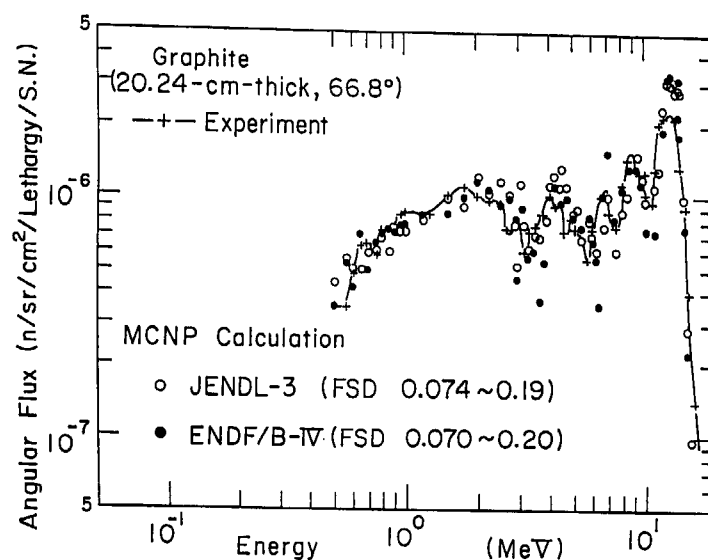


Fig. 3.9-7 (e) 66.8 deg.

4. Discussions

4.1 Iron

From the check of total cross sections by the Broomstick experiment, the total cross-section minima of natural iron in JENDL-3 are too large in the energy range between 1 and 3 MeV, so that the C/E value for the transmitted neutrons is small by about 30%. The higher energy part in JENDL-3 shows a better result than ENDF/B-IV since the total cross section above 3 MeV has been revised in JENDL-3 revision 1 (1990).

For deep penetration problems, the ASPIS and ORNL benchmarks provide good information. From these results, overall applicability of JENDL-3 for natural iron has been confirmed for the deep penetration in the shielding calculation. The agreement between calculation and experiment in the spectrum just below the 24 keV window is superior for the JENDL-3 evaluation. It means the evaluation of the resonance parameters of iron including the 24 keV window range is very good for JENDL-3.

However, some problems still remain in the assignments between elastic and inelastic scattering cross sections in the energy range between 600 keV and 3 MeV. For the ASPIS benchmark, the result by the DOT3.5 calculation shows underestimation between 600 keV and 1.2 MeV. The MCNP result also shows the same tendency between 400 keV and 1.2 MeV at 85.41 cm depth. For the ORNL iron and stainless steel benchmarks, the underestimation also appears between 700 keV and 3 MeV in the MCNP calculation. The underestimation of JENDL-3 between 1 and 3 MeV corresponds to the underestimation in the Broomstick benchmark analysis.

For a relatively thin transmission problem, the KfK benchmark provides good information. The calculated neutron leakage spectra in the energy range between 100 keV and 1 MeV with JENDL-3 and with ENDF/B-IV show good agreement for the spectral shape regarding the resonance structure. The C/E values for the various energy ranges distribute from 0.95 to 1.35 with JENDL-3, from 0.95 to 1.24 with ENDF/B-IV, respectively. The results of JENDL-3 are slightly higher than those of ENDF/B-IV. The difference between JENDL-3 and ENDF/B-IV in the spectrum below the 24 keV window appear more clearly than in the ASPIS and ORNL benchmarks, since the inelastic scattering has major contribution to form the neutron leakage spectrum below 24 keV. However, any measurement below 24 keV was not reported in the KfK experiment, and it is not possible to say which evaluation is adequate so far. On the other hand, the results for Cd-covered gold foils in the ASPIS experiments (see **Fig. 3.2-6**) indicate a possibility that inelastic scattering cross section data of ENDF/B-IV is better than JENDL-3.

For D-T neutron source problem, the LLNL Hansen's benchmark provides good information. From the result calculated with the MCNP code, good agreement is obtained for the once collided elastic peak including uncollided source neutrons and the multiple scattering region, except for the energy region between 7.5 and 12.5 MeV. In this region, a slight underestimation is shown in the calculation results with JENDL-3.

Figure 4.1-1 shows the total cross sections of natural iron in JENDL-3 and ENDF/B-IV in the energy range between 1 and 1.1 MeV. Various experimental data are also plotted for a comparison. It is clearly shown that the total cross section in JENDL-3 follows well the experimental data, while ENDF/B-IV has a keener resonance structure than the experimental one. **Figure 4.1-2** shows the elastic and total inelastic scattering cross sections of natural iron in JENDL-3 and ENDF/B-IV for the same energy region. The sharp resonance structure in the inelastic reaction clearly appears in ENDF/B-IV compared with that in JENDL-3. Keener structure should be essentially considered in the cross section evaluation with estimating the energy resolution in the cross-section measurements, since the difference in the

resonance structure strongly affects the estimation of the resonance self-shielding factor.

Figures 4.1-3 and 4.1-4 also show similar differences in the energy range between 800 keV and 1 MeV. For the inelastic scattering cross section below 860 keV, JENDL-3 contains the contribution from the ^{57}Fe low-lying discrete level, so that the difference between JENDL-3 and ENDF/B-IV is clearly shown.

For the energy below 100 keV, a comparison of the total cross sections of natural iron between JENDL-3 and ENDF/B-IV is shown in **Fig. 4.1-5**. Various experimental data are also plotted for comparison. In this figure, JENDL-3 follows well the recent experimental data, so that the neutron energy spectra at the 24 keV window are reproduced very well in the benchmark analyses, while the total cross-section minima around 82 keV window are rather small in JENDL-3.

A considerable difference in the total cross section is shown below the 24 keV window between JENDL-3 and ENDF/B-IV, however the spectrum difference between JENDL-3 and ENDF/B-IV in the KfK benchmark analysis cannot be explained only by the difference in the total cross sections. The neutron spectrum in the energy region is formed by the competitive processes between direct inelastic scattering and multiple elastic scattering. **Figures 4.1-6 and 4.1-7** show the group-wise cross sections for the elastic and total inelastic scattering in the JSSTD library²²⁾. For the energy above 2 MeV, ENDF/B-IV has larger inelastic cross sections compared with those in JENDL-3, so that the slowing down neutrons below 24 keV directly coming from the inelastic scattering of source neutrons will be a major contribution to form the neutron spectrum in the KfK experiment.

From these results, the iron data in JENDL-3 should be verified for the elastic and inelastic scattering cross sections including the resonance structure in the energy range between 600 keV and 3 MeV. JENDL-3 has a tendency that the elastic scattering cross sections are relatively large in the energy range between 1 and 3 MeV, and the inelastic scattering cross sections are relatively small in the energy range between 2 and 6 MeV.

We have concluded that the quality of JENDL-3 is as good as ENDF/B-IV, while it is superior to ENDF/B-IV in resolved resonance parameters.

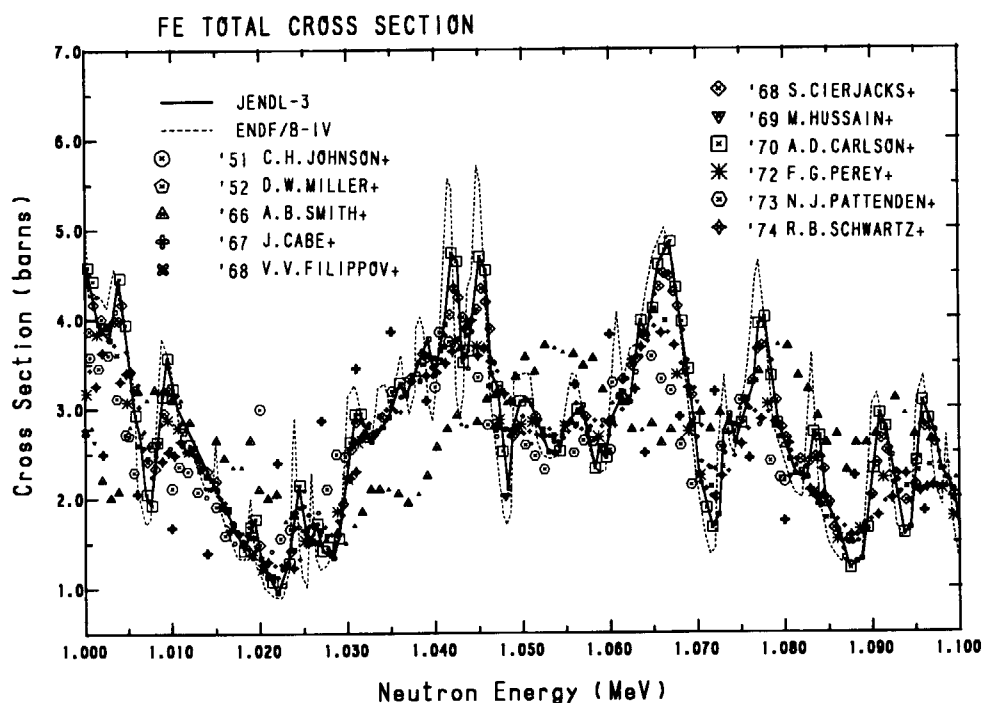


Fig. 4.1-1 Comparison of total cross sections for natural iron between JENDL-3 and ENDF/B-IV in the energy range from 1 MeV to 1.1 MeV

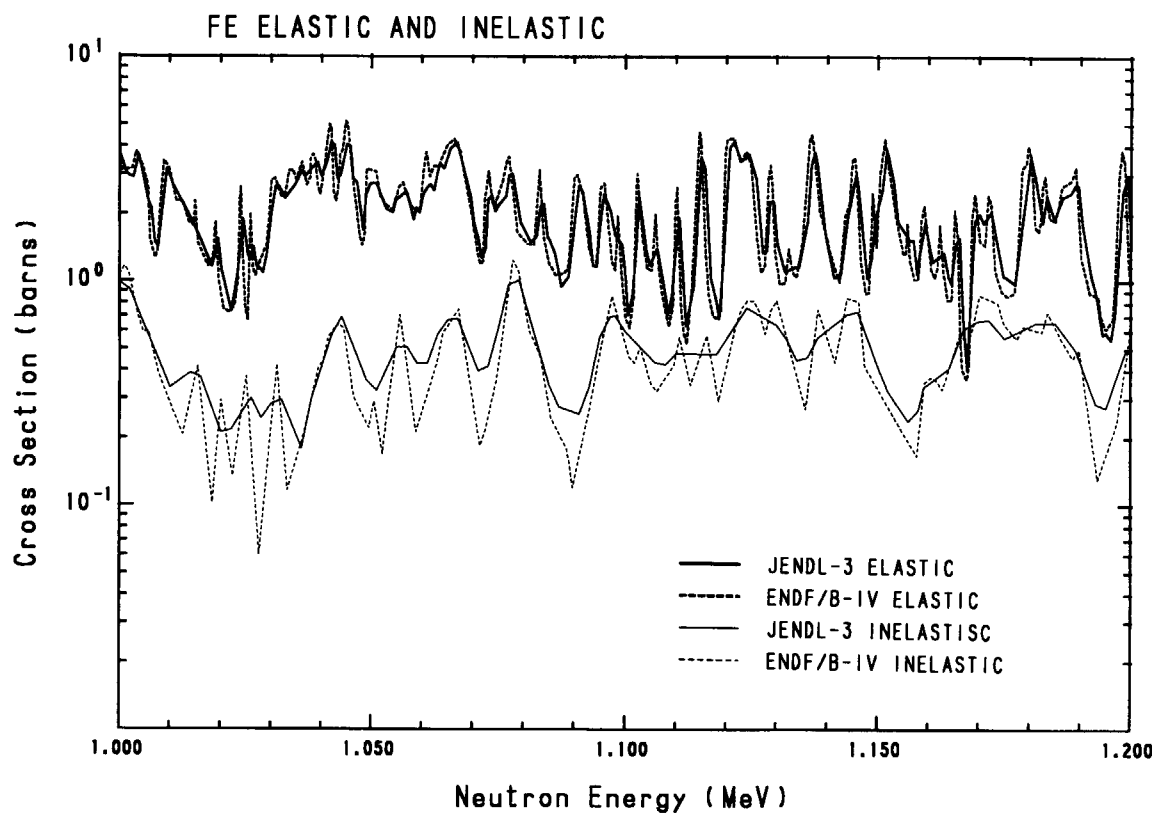


Fig. 4.1-2 Comparison of elastic and total inelastic scattering cross sections for natural iron between JENDL-3 and ENDF/B-IV (1 - 1.2 MeV)

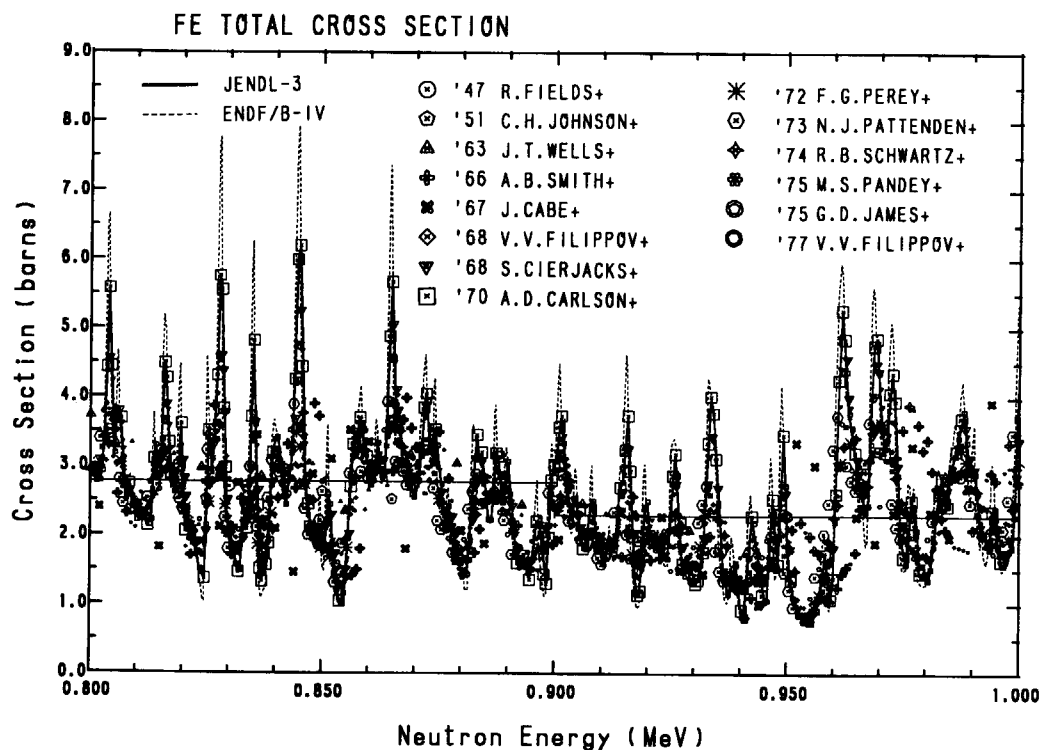


Fig. 4.1-3 Comparison of total cross sections for natural iron between JENDL-3 and ENDF/B-IV in the energy range from 800 keV to 1 MeV

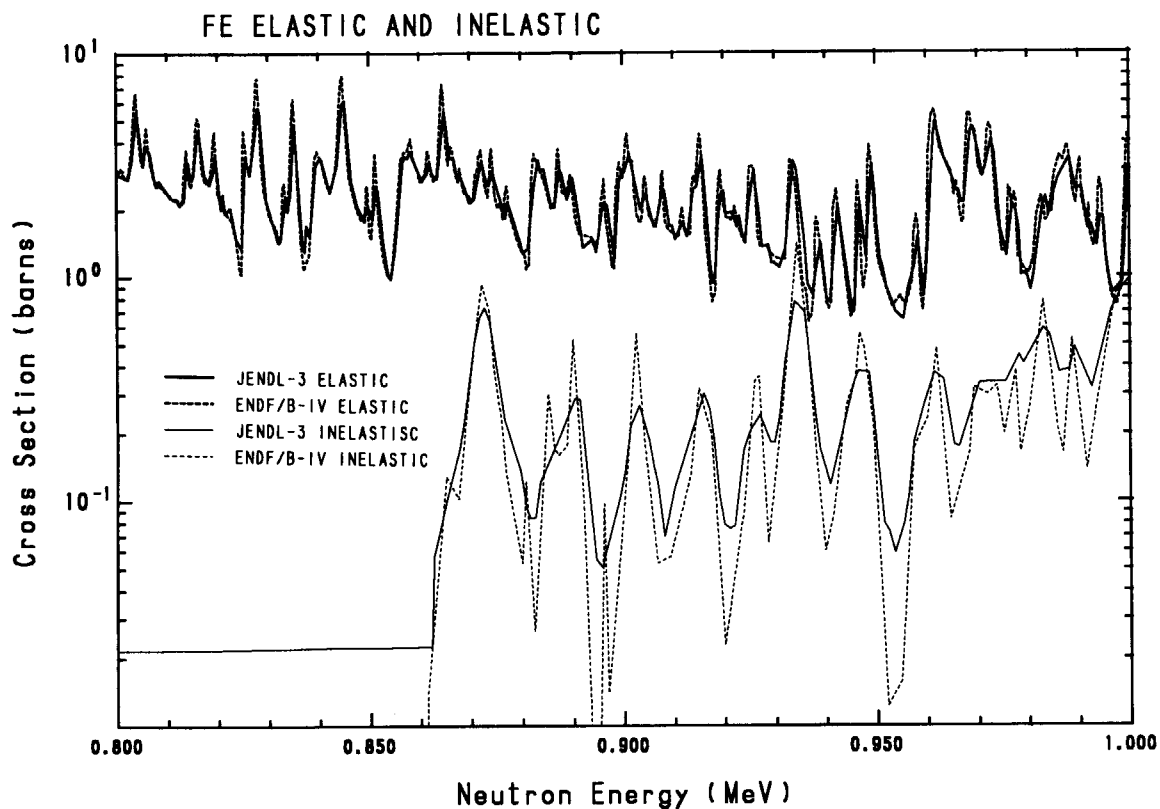


Fig. 4.1-4 Comparison of elastic and total inelastic scattering cross sections for natural iron between JENDL-3 and ENDF/B-IV (0.8 - 1.0 MeV)

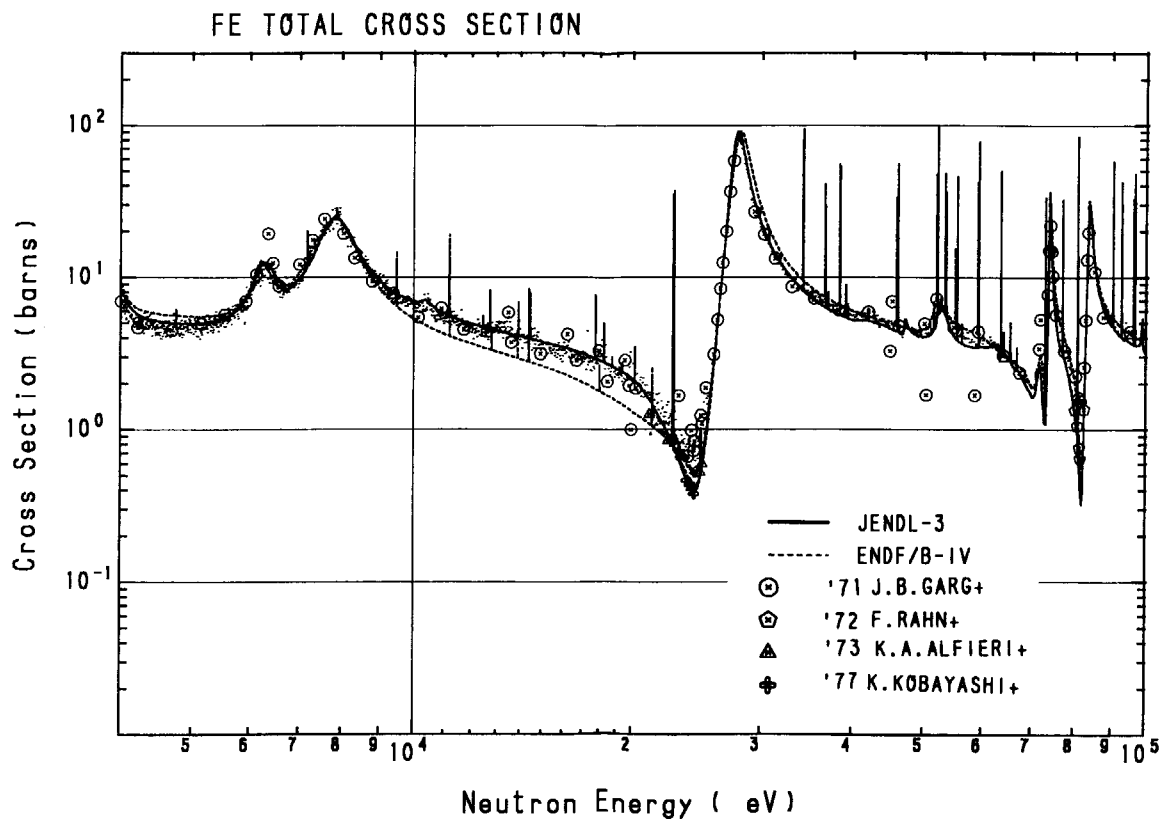


Fig. 4.1-5 Comparison of total cross sections for natural iron between JENDL-3 and ENDF/B-IV in the energy range from 4 keV to 100 keV

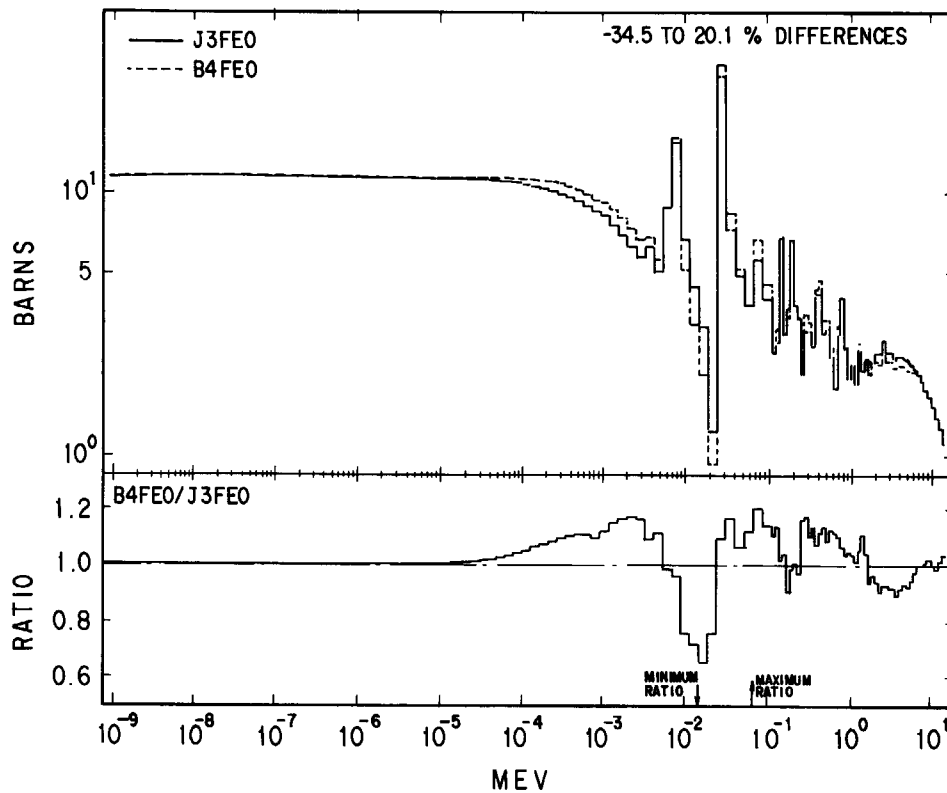


Fig. 4.1-6 Comparison of group-wise elastic scattering cross sections for natural iron between JENDL-3 and ENDF/B-IV in the JSSTD library

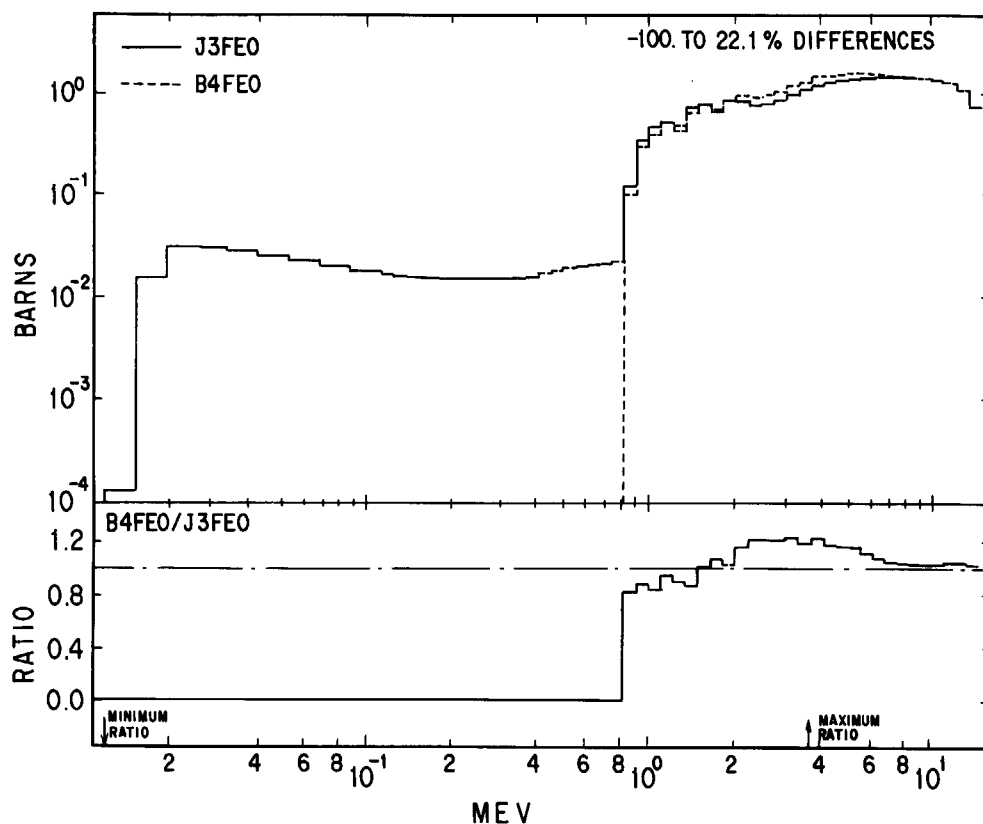


Fig. 4.1-7 Comparison of group-wise inelastic scattering cross sections for natural iron between JENDL-3 and ENDF/B-IV in the JSSTD library

4.2 Sodium

Sodium cross sections were tested with the analyses of the Broomstick experiments³⁵⁾ and the ORNL transmission experiments⁴⁾ for a thick sodium sample.

In the Broomstick experiment analysis, JENDL-3 gives about 20% higher transmission from 2 to 10 MeV and ENDF/B-IV gives better results. The analyses of the ORNL transmission experiments for 10 and 15-ft long samples have clarified that JENDL-3 can reproduce fast neutron spectrum above 70 keV with $C/E = 1.0 - 1.3$, and the responses for 3 - 10 in. dia. Bonner ball detectors and cadmium covered BF_3 counter with the average $C/E = 0.79 - 0.98$, in the case calculated with a maximum content of hydrogen impurity in the sodium sample. The results are influenced by the hydrogen contents; the case without hydrogen gives $C/E = 0.91 - 1.10$ and $1.07 - 1.33$ for 10 and 15-ft-thick samples, respectively. In this case, ENDF/B-IV and JENDL-2 underestimate the Bonner ball responses for 10-ft thick sample by 10-20% and 10-30%, respectively. It is due to the fact that sodium samples contained hydrogen to some degree, so that the C/E values may be closer to the results obtained with hydrogen. Accordingly, JENDL-3 which gives the highest and closest-to-unity C/E values is seen as being better than ENDF/B-IV.

However, there are some problems in the sodium cross sections of JENDL-3. The overestimation of MeV neutron transmission is commonly observed in the calculated neutron spectra for the Broomstick experiments and the ORNL transmission experiments using a 10-ft-thick sodium sample, as described in Section 3.5. These fast neutron fluxes are the most sensitive to the total cross section. **Figure 4.2-1** compares the sodium total cross sections of JENDL-3 in the energy range between 1 and 10 MeV with the evaluated data of JENDL-2 and ENDF/B-IV as well as the experimental data. All evaluated data exist within the scattered experimental data, but ENDF/B-IV is a few percent larger than JENDL-2 and -3 above 7 MeV. Therefore, a slight modification in the total cross section above several MeV can diminish the overestimation of neutron transmission, although there are likely to be ambiguities in the sodium density and some calculation errors.

The calculation with a one-dimensional Sn transport code ANISN¹¹⁾ for the ORNL transmission experiments⁴⁾ shows that axial distributions of neutron fluxes calculated by JENDL-2 deviate from those by JENDL-3 and ENDF/B-IV along with the distance from the source. The deviation is more prominent for the neutron spectra at the exit of sodium sample, as shown in **Fig. 4.2-2**. These differences come from the difference in inelastic scattering cross sections, as shown in **Fig. 4.2-3**; JENDL-2 data are based on the theoretical calculation and the others are on the experimental data. Larger inelastic scattering cross sections cause too large neutron moderation. The neutron fluxes calculated with JENDL-3 and ENDF/B-IV are close to each other in the sodium sample, but they are slightly different near the exit of the sodium sample. Such differences mainly come from the difference in the angular distributions of elastically scattered neutrons between JENDL-3 and ENDF/B-IV. This effect should bring about the difference in neutron fluxes behind the sample, calculated with the SPACETRAN code²¹⁾.

As far as the present analyses, it has been concluded that JENDL-3 is the most applicable to the shielding calculations for fission-like neutron source problems.

The present analyses for the thick sodium sample could clarify the degree of the calculation accuracy for slow neutron more than fast neutron. In actual design, the mixed configuration of sodium and shielding materials such as stainless steel and boron carbide becomes a problem. In that problem, slow neutrons are absorbed more by shielding material, so the accuracy of fast neutron fluxes is much more important. To solve such problem, shielding mockup experiments are desirable and have been made at ORNL^{8, 45)}, Cadarache⁴⁶⁾ and Winfrith⁴⁷⁾. The JASPER project⁸⁾ is one of the representative shielding mockup experiments for LMFBR. It is very important for improving the integral tests for sodium cross sections to analyze the much more experiments containing sodium layers.

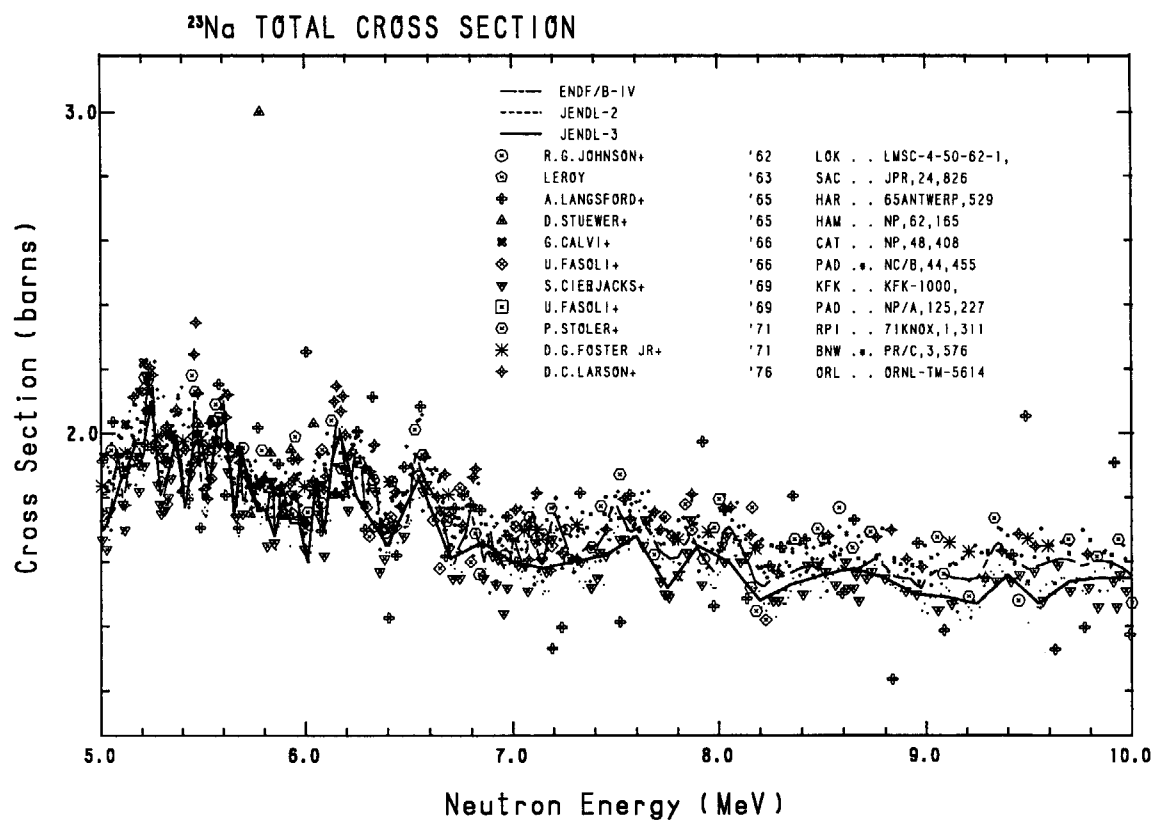


Fig. 4.2-1 Comparison of evaluated and experimental total cross sections for sodium

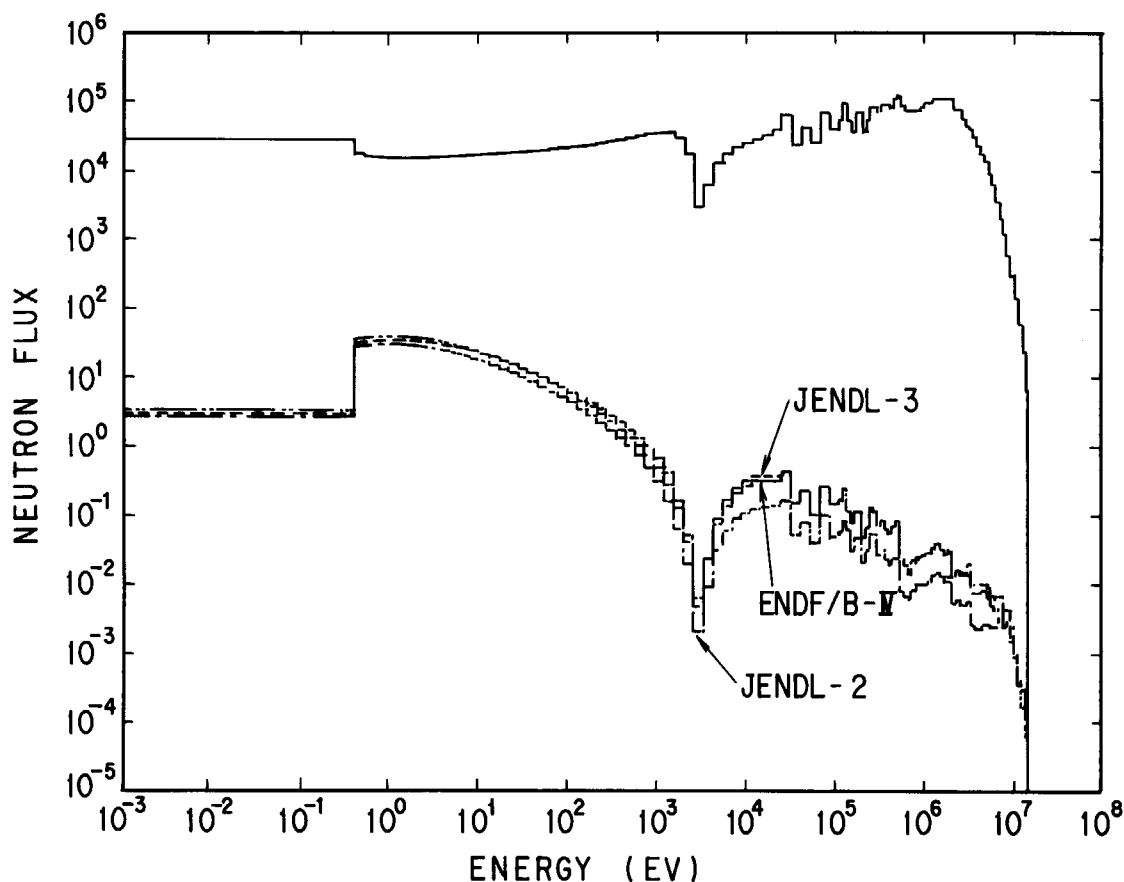


Fig. 4.2-2 Comparison of neutron spectra at the source and the opposite side positions

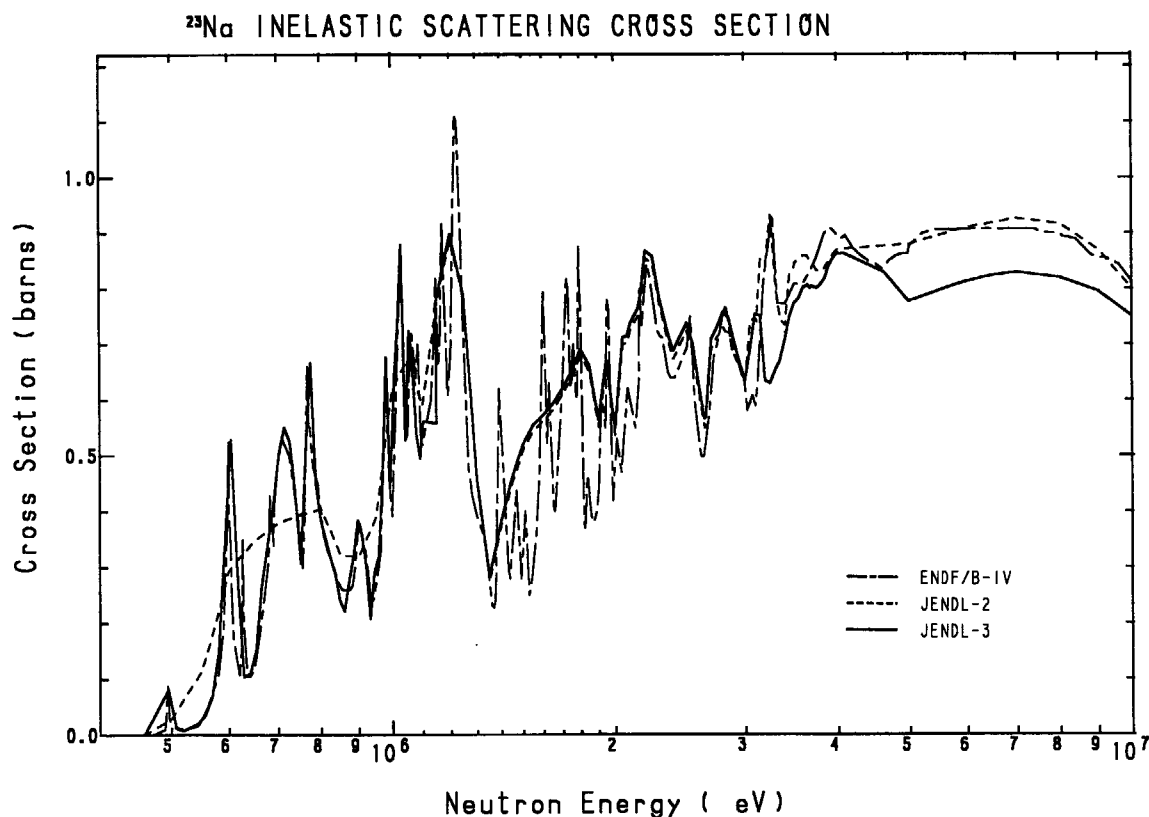


Fig. 4.2-3 Comparison of inelastic scattering cross section for sodium of JENDL-3 with JENDL-2 and ENDF/B-IV

4.3 Graphite

The carbon cross sections of JENDL-3 were checked by benchmark calculations for the RPI experiments, ORNL experiments and JAERI-FNS experiments, at energy range between 70 keV and 14 MeV.

We could carry out an accurate calculation for the RPI experiments, since the geometry could be modeled as a one-dimensional sphere. However, the angular flux at 0 degrees could not be expressed accurately in this study. The calculated angular flux gives good agreement with the measured data. The carbon cross section of JENDL-3 is highly applicable for the penetration problem at energy range from 600 keV to 9 MeV.

The ORNL experiments include the spectrum modifier in front of graphite slabs. The calculated results are affected by the spectrum modifier, i.e., they are strongly affected by other materials than carbon. From the viewpoint of C/E, JENDL-3 shows superior results to JENDL-2, at more than 10.16 cm thickness of graphite. However, comparing the calculated flux distributions in the graphite between JENDL-3 and the mixed library, it is clarified that the difference in the C/E values with JENDL-3 from those with a mixed library, JENDL-2 or ENDF/B-IV is induced by the difference of cross-section data for the other elements used in the spectrum modifier composed of the UO_2 blanket region or stainless steel slab. So, as far as neutron transmission in graphite, JENDL-3 gives a similar accuracy for integral flux and a little better accuracy for high energy spectrum than JENDL-2.

For the JAERI-FNS TOF experiments, the angular fluxes calculated with JENDL-3 indicate a much better agreement than those with ENDF/B-IV. Especially at several peaks and dips due to the inelastic scattering of the D-T source neutrons appearing between 2.5 and 11.0 MeV can be realized at all measuring angles. However, only at the angle of 66.8 deg., the once elastic collided peak at 12.5 MeV was considerably overestimated with both libraries. Accordingly, there is a possibility that the peak might be

underestimated in the experiment because of low counting statistics. On the whole, the C/E values integrated over 0.5, 1.0, and 10 MeV with JENDL-3 and ENDF/B-IV were in agreement within 10% for all the measuring angles. However, the values with JENDL-3 indicated a tendency of larger than 1.0 ; on the contrary, smaller than 1.0 with ENDF/B-IV.

In conclusion, the carbon cross sections in JENDL-3 are reliable for the energy range from 70 keV to 14 MeV.

4.4 Oxygen

For this material, only the Broomstick experiment was analyzed. This experiment is for checking the minima of the total cross section in MeV energy range (800keV to 11MeV). No transport calculation is required for the analysis. The result is analytically calculated from the cross-section data. Therefore only the information about total cross-section minima is concerned. Cross-section shapes for ENDF/B-IV and JENDL-3 are given in Fig. 4.4-1.

Concerning the overall predictability for the shape of transmitted fluxes JENDL-3 is as good as other evaluations (JENDL-3 T, ENDF/B-IV), although all evaluations show systematically small underestimation of transmitted fluxes (See Fig. 3.1-2). This tendency suggests that the minima of the total cross section available in all evaluations is a little bit shallow, i.e., depth of the minima is not enough. In Fig. 4.4-1, deeper minima of the cross sections are given for ENDF/B-IV, giving better results than JENDL-3 (See Fig. 3.1-2).

The quality of JENDL-3 is stepped up from the previous version of JENDL (JENDL-3T) especially in the energy range from 0.2 to 0.4 MeV. However, in the 6 to 8 MeV range, ENDF/B-IV produces better results than JENDL-3. A slight modification (deeper minima of total cross-section) will give better results for this energy range for JENDL-3.

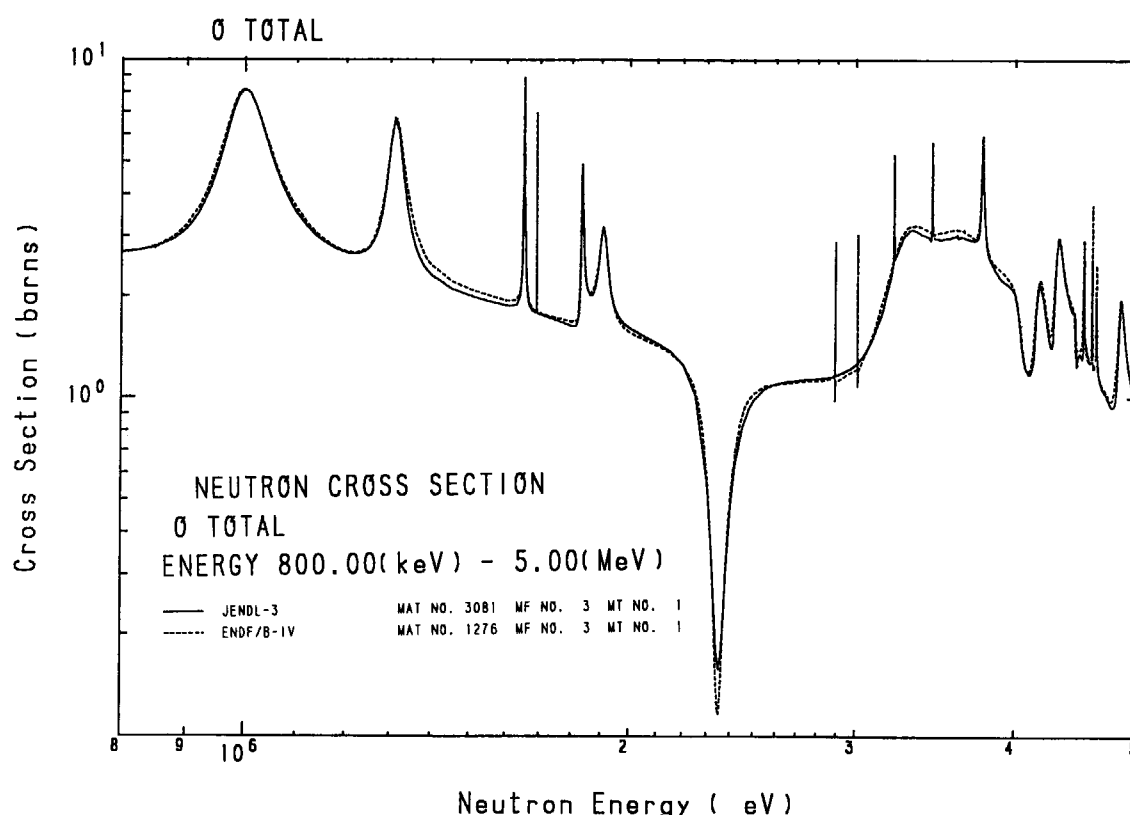


Fig. 4.4-1 Total cross section of oxygen for JENDL-3 and ENDF/B-IV

4.5 Stainless Steel

The stainless steel is composed of iron, chromium and nickel. Iron is the main component of the stainless steel. From this reason, the calculated results of stainless steel are similar to those of iron. However, the degree of overestimation of neutron fluxes behind the stainless steel slab in the energy range between 48 and 90 keV is smaller than in the case of iron. This flux overestimation comes from too small minima of iron total cross section in JENDL-3 at the off-resonance energies, as shown in **Fig. 4.1-5**; the cross section minima give the flux peaks as a result of the window effect. In the case of stainless steel, cross sections of nickel and chromium bury the minima of iron cross section off the resonances and the underestimation of macroscopic total cross section at minima becomes reduced. Accordingly, the results for stainless steel are better than those for iron.

4.6 Beryllium

For the beryllium cross sections, the angular fluxes calculated with JENDL-3 agree very well with the JAERI-FNS TOF experiments, over all the measured energy regions, except for the elastic peak of the measuring angle at 41.8 deg. and neutron fluxes between 0.7 and 8 MeV at the angles below 24 deg. At the 41.8 deg. the elastic scattering peak at 14.5 MeV is underestimated with JENDL-3 and also with ENDF/B-IV. The underestimation tendency is consistent with the DDX (energy-angle doubly differential cross section) data measured at OKTAVIAN⁴³⁾, while both libraries reproduce well the angular distributions of elastic scattered neutrons compared with the experiments reported from the other laboratories. Therefore, further experimental investigation is needed to solve the problems for elastic scattering around 40 deg. Overestimation of neutron fluxes between 0.7 and 8 MeV at smaller angles means that there are uncertainties of DDX for forward scattering angles in JENDL-3. The C/E values integrated over 0.01 MeV are between 0.98 and 1.09 for all of the measuring angles. Those values integrated over 10 MeV are approximately unity, except for the C/E value of 0.86 at 41.8 deg. with JENDL-3.

5. Conclusion

The integral tests of neutron cross sections for beryllium, graphite, oxygen, sodium, iron and stainless steel in JENDL-3 have been performed to verify applicability for use of shielding designs and analyses of fission reactor and fusion neutronics.

As for the benchmark analyses, five measurements for fission-like neutron source problem and two measurements for D-T neutron source problem have been employed. The analyses have been performed using one-dimensional S_N -transport codes, ANISN, DIAC, a two-dimensional one, DOT 3.5, with more than 100 energy groups, and a continuous energy Monte Carlo code, MCNP. The calculation models for each benchmark analysis have been carefully determined to obtain sufficient accuracy for checking the neutron nuclear data. The group-wise and point-wise cross sections adopted in this study have been generated using the state-of-the-art cross-section processing code systems, PROF-GROUCH-G/B, RADHEAT-V4 and NJOY83.

The calculated results with JENDL-3 have been compared with the experimental data and with those calculated using the other nuclear data files of JENDL-2 and ENDF/B-IV. The results of benchmark analyses for the same material have been also compared systematically with one another, and the problems in cross-section evaluation have been clarified in the discussions. A summary of individual materials is as follows:

(1) For beryllium, the cross section evaluation of JENDL-3 is fairly good for the D-T neutron source problem, except for the angular distribution of the elastic scattering cross section around 40 deg., (2) For carbon, the cross section evaluation of JENDL-3 is very good for the different benchmark analyses of fission-like and D-T neutron source problems, (3) For oxygen, the quality of JENDL-3 is almost the same as ENDF/B-IV, but the total cross section is rather large in the energy range between 2 and 8 MeV, (4) For sodium, the cross-section evaluation of JENDL-3 is better than JENDL-2 and ENDF/B-IV for the fission-like neutron source problem, but the total cross section is rather small for 6 to 10 MeV, (5) For iron, the cross-section evaluation of JENDL-3 is excellent for the resonance parameters including 24 keV window, and overall applicability has been confirmed for deep penetration in the shielding calculation. However, some problems still remain in the assignments between elastic and inelastic scattering cross sections in the energy range between 600 keV and 3 MeV.

The feedback information obtained from the present integral test will be soon reflected in JENDL-3.2⁴⁸⁾.

Acknowledgments

The present work was performed under constant encouragement and interest of the members of the Japanese Nuclear Data Committee. The authors would like to thank them for their invaluable help. They would like to express their thanks to Dr. Hirokazu Tsunoda of Mitsubishi Research Institute for his useful discussions regarding analysis of the benchmark problems, and to Dr. Tsuneo Nakagawa of Nuclear Data Center, JAERI for preparation of the cross-section library and plotting various graphs. They are very much indebted to Dr. Yasuyuki Kikuchi of Nuclear Data Center, JAERI for his guidance and support during the course of this work.

References

- 1) Shibata K., Nakagawa T., Asami T., et al.: "Japanese Evaluated Nuclear Data Library, Version-3 - JENDL-3 -, " JAERI-1319 (1990).
- 2) Straker E. A.: "Experimental Evaluation of Minima in Total Cross Sections of Several Shielding Materials, " ORNL-TM-2242 (1968).
- 3) Maerker R. E. and Muckenthaler F. J.: "A Benchmark Experiment for Neutron Transport in Iron and Stainless Steel, " Nucl. Sci. Eng., **52**, 227-246 (1973).
- 4) Maerker R. E., Muckenthaler F. J. and Childs R. E.: "The ORNL Benchmark Experiment for Neutron Transport in Thick Sodium, " Nucl. Technol., **22**, 275-297 (1974).
- 5) Carter M. D. and Packwood A.: "The Winfrith Benchmark Experiment in Iron-Experimental Results, " Proc. of the Specialists' Meeting on Sensitivity Studies and Shielding Benchmarks, Paris, October 1975, pp. 111-119, OECD (1975).
- 6) Werle H., Kappeler F. and Kuhn D.: "Measurements of Neutron Leakage Spectra from Iron Sphere with a ^{252}Cf Source in the Center, " NEACRP-U-73, p. 8 (1976).
- 7) Profio A. E., Antúnez H. M. and Huffman D. L.: "The Neutron Spectrum from a Fission Source in Graphite, " Nucl. Sci. Eng., **35**, 91-103 (1969).
- 8) Ohtani N., Suzuki S., Shirakata K., et al.: "Benchmark Experiment and Analysis of Neutron Penetration through FBR Radial Shield Mockups. " Proc. 7th Int. Conf. on Radiation Shielding, Bournemouth, September 1988, Vol. II, p. 433 (1988); see also Ingersoll D.T. and Ohtani N.: "JASPER-US and Japan Shielding Program for Experimental Research, " Proc. of ANS Topical Conf. on Theory and Practices in Radiation Protection and Shielding, Knoxville, April 1987, Vol. 2, p. 346 (1987).
- 9) Hansen L. F., Wong C., Komoto T., et al.: "Measurements of the Neutron Spectra from Materials Used in Fusion Reactors and Calculations Using the ENDF/B-III and -IV Neutron Libraries, " Nucl. Sci. Eng., **27**, 35 (1976).
- 10) Oyama Y. and Maekawa H.: Nucl. Sci. Eng., **97**, 220 (1987); Oyama Y., Yamaguchi S. and Maekawa H.: J. Nucl. Sci. Technol., **25**, 419 (1988); see also Oyama Y., Yamaguchi S. and Maekawa H.: "Experimental Results of Angular Neutron Flux Spectra Leaking from Slabs of Fusion Reactor Candidate Materials (I), " JAERI-M 90-092 (1990).
- 11) Engle W. W. Jr.: "A Users Manual for ANISN, A One Dimensional Discrete Ordinates Transport Code With Anisotropic Scattering, " K-1963 (1967).
- 12) Yamano N., Koyama K. and Minami K.: J. Nucl. Sci. Technol., **16**, 919 (1979).
- 13) Rhodes W. A. and Mynatt F. R.: "The DOT-III Two-Dimensional Discrete Ordinate Transport Code, " ORNL-TM-4280 (1973).
- 14) Hasegawa A.: "Development of a Processing Code System PROF-GROUCH-G/B, " private communication.
- 15) Yamano N., Minami K., Koyama K., et al.: "RADHEAT-V4: A Code System to Generate Multi-group Constants and Analyze Radiation Transport for Shielding Safety Evaluation, " JAERI-1316 (1989).
- 16) Bondarenko I. I., (ed.): "Group Constants for Nuclear Reactor Calculations, " Consultant Bureau, New York (1964).
- 17) Briesmeister J. F., (ed.): "MCNP - A General Monte Carlo Code for Neutron and Photon Transport, " LA-7396-M, revised 2 (1986).
- 18) MacFarlane R. E., Muir D. W. and Boicourt R. M.: "The NJOY Nuclear Data Processing System,

- " LA-9303-M (ENDF-324) (1982).
- 19) Garber D., Dunford C. and Pearlstein S.: "ENDF102 Data Formats and Procedures for the Evaluated Nuclear Data File ENDF, " BNL-NCS-50496 (1975).
 - 20) Nakagawa T.: "Summary of JENDL-2 General Purpose File, " JAERI-M 84-103 (1984).
 - 21) Cramer S. N. and Solomito M.: "SPACETRAN III - Dose Calculations at Detectors at Various Distances from the Surface of a Cylinder, " ORNL/RSIC CCC-120 (1973).
 - 22) Hasegawa A.: "Development of a Common Nuclear Group Constants Library System: JSSTD-295 n-104 γ Based on JENDL-3 Nuclear Data Library, " Proc. of Int. Conf. on Nuclear Data for Science and Technology, Jülich, May 1991, p. 232, Springer-Verlag (1992).
 - 23) Yamano N., Tabara T., Takano M., et al.: "Production and Accuracy Evaluation of Standard Group Constants for Safety Analysis of Radiation Shielding, " JAERI-M 90-183 (1990) [in Japanese].
 - 24) Kosako K., Oyama Y. and Maekawa H.: "FSXLIB-J3:MCNP Continuous Energy Cross Section Library Based on JENDL-3, " JAERI-M 91-187 (1991) [in Japanese].
 - 25) Nakazawa M., et al.: "Proposal on Post-JENDL-3 Activity Program for Japanese Nuclear Data Committee, " JAERI-M 87-025, p. 9 (1987).
 - 26) Straker E. A., Stevens P. N., Irving D. C. and Cain V. R.: "The MORSE Code - A Multi-group Neutron and Gamma Ray Monte Carlo Transport Code, " ORNL-4585 (1970).
 - 27) Koyama K., Minami K., Taji Y., et al.: "RADHEAT-V3, A Code System for Generating Coupled Neutron and Gamma-Ray Group Constants and Analyzing Radiation Transport, " JAERI-M 7155 (1977).
 - 28) Koyama K., Okumura Y., Furuta K., et al.: "Multi-group Cross-Section Sets for Shielding Materials, " JAERI-M 6928 (1977) [in Japanese].
 - 29) Yamano N.: "JSD1000 : Multi-Group Cross-Section Sets for Shielding Materials, " JAERI-M 84-038 (1984).
 - 30) Berger M. H. and Hubbell J. H.: "PHOTX V2.0, " DLC-136/PHOTX, Available from RSIC.
 - 31) Ford III, W. E. and Wallace D. H.: "POPOP4, A Code for Converting Gamma-Ray Spectra to Secondary Gamma-Ray Production Cross Sections, " CTC-12 (1969).
 - 32) Storm E. and Israel H. I.: Nuclear Data Tables, **A7**, 565 (1970).
 - 33) Maerker R. E.: "SDT1. Iron Broomstick Experiment-An Experimental Check of Neutron Total Cross Sections, " ORNL-TM-3867 (Revised) (1972).
 - 34) Maerker R. E.: "SDT2. Oxygen Broomstick Experiment -An Experimental Check of Neutron Total Cross Sections, " ORNL-TM-3868 (Revised) (1972).
 - 35) Maerker R. E.: "SDT4. Sodium Broomstick Experiment -An Experimental Check of Neutron Total Cross Sections, " ORNL-TM-3870 (Revised) (1972).
 - 36) Asami, T.: "An Outline of JENDL-3T, " JAERI-M 88-065, p. 4 (1988); see also
Nakagawa, T.: "Evaluation of Nuclear Data for Heavy Nuclides, " *ibid.*, p.10;
Mizumoto, M.: "Nuclear Data Evaluation for Medium and Heavy Nuclei, " *ibid.*, p. 29;
Kawai, M. and FPND Sub-WG: "Evaluation of FP Cross Sections for JENDL-3, " *ibid.*, p.57;
Chiba, S.: "Evaluation of the Fusion-Related Neutron Nuclear Data for JENDL-3 - Nuclear Data in the Very Light Mass Region Stored in JENDL-3T -, " *ibid.*, p. 75.
 - 37) Carter M. D., McCracken A. K. and Packwood A.: "The Winfrith Iron Benchmark Experiment, A Compilation of Previously Published Results for Use in the International Comparison of Shielding Data-Sets Sponsored by NEA, " AEE Winfrith (1982).
 - 38) Suzuki T., Hasegawa A., Mori T. and Ise T.: "BERMUDA-2DN: A Two-Dimensional Neutron Transport Code, " JAERI-M 82-190 (1982) [in Japanese].
 - 39) Ueki K., Inoue M. and Maki Y.: Nucl. Sci. Eng., **84**, 271-284 (1983).
 - 40) Reactor Physics Constants: "Constants Related to Interpretation of Experimental Data, " Argonne National Laboratory, ANL-5800 (1963).

- 41) Maerker R. E., Williams L. R., Mynatt F. R., et al.: "Response Functions for Bonner Ball Neutron Detectors, " ORNL-TM-3451 (1971).
- 42) Weisbin C. R., Soran P. D., MacFarlane R. E., et al.: "MINX: A Multi-group Interpretation of Nuclear Xsections from ENDF/B, " LA-6486-MS (1976).
- 43) Takahashi A., Ichimura E., Sasaki Y., et al.: "Double and Single Differential Neutron Emission Cross Sections at 14.1 MeV - Volume I -, " OKTAVIAN Report A-87-03, Osaka University (1987).
- 44) Ueki K., Ohashi, A. and Kawai, M.: J. Nucl. Sci. Technol., **30**, 339 (1993).
- 45) Disney R. K.: "Radiation Protection/Shield Design - A Need for A System Approach -, " Proc. of 5th Int. Conf. on Reactor Shielding, Knoxville, April 1977, p. 157, Science Press (1977).
- 46) Calamand D., Despretz A., Raneurel H., et al.: "Results of Neutron Propagation in Steel Sodium Mixtures with Various Source Spectra on HARMONIE and TAPIRO, " *ibid.*, p. 795 (1977); see also Calamand D., Erdmann W., Nimal J. C., et al.: "The JASON Experimental Program for New Shielding Concepts and Streaming Effect, " Proc. of ANS Topical Conf. on Theory and Practices in Radiation Protection and Shielding, Knoxville, April 1987, Vol. 2, p. 333 (1987).
- 47) Avery A. F. and Curtis G. C.: "Neutron Attenuation Studies in Fast Reactor Shielding, " Proc. Int. Conf. on Physics Problems of Reactor Shielding, Harwell, September 1967, Vol. 2, p. 515, UKAEA (1968).
- 48) Kawai M., Hasegawa A., Ueki K., et. al.: "Systematic Shielding Benchmark Tests of JENDL-3 and Their Feedback to Nuclear Data Evaluation, " Proc. of Int. Symp. on Nuclear Data Evaluation Methodology, BNL, October 1992, p. 180, World Scient. Pub. Co. Pte. Ltd. (1993).